

# **Self-Assembly and Optical Properties of Phenyleneethynylene and BODIPY Based $\pi$ -Systems**

By

**GOURAB DAS**

10CC14A39001

A thesis submitted to the  
Academy of Scientific and Innovative Research  
for the award of the degree of  
**DOCTOR OF PHILOSOPHY**  
in  
**SCIENCE**

Under the supervision of  
**Prof. A. AJAYAGHOSH**



**CSIR-National Institute for Interdisciplinary Science and Technology (CSIR-NIIST)  
Thiruvananthapuram - 695 019**



**Academy of Scientific and Innovative Research  
AcSIR Headquarters, CSIR-HRDC Campus  
Sector 19, Kamla Nehru Nagar,  
Ghaziabad, Uttar Pradesh - 201 002, India**

**April 2021**

*Dedicated to My Beloved  
Baba, Maa and Suchismita*



## राष्ट्रीय अंतर्विषयी विज्ञान तथा प्रौद्योगिकी संस्थान

वैज्ञानिक तथा औद्योगिक अनुसंधान परिषद्  
इंडस्ट्रियल इस्टेट पी.ओ., पाप्पनकोड, तिरुवनंतपुरम, भारत-695 019

**CSIR-NATIONAL INSTITUTE FOR INTERDISCIPLINARY SCIENCE & TECHNOLOGY (CSIR-NIIST)**

Council of Scientific & Industrial Research  
Industrial Estate P.O., Pappanamcode, Thiruvananthapuram, India-695 019

डॉ. ए. अजयघोष एकान्त, एफटीडब्ल्यूएस  
निदेशक



Dr. A. Ajayaghosh FNA, FTW  
Director

31-03-2021

### CERTIFICATE

*This is to certify that the work incorporated in this Ph. D. thesis entitled, "Self-Assembly and Optical Properties of Phenyleneethynylene and BODIPY Based  $\pi$ -Systems", submitted by Mr. Gourab Das to the Academy of Scientific and Innovative Research (AcSIR) in partial fulfilment of the requirements for the award of the Degree of Doctor of Philosophy in Sciences, embodies original research work carried out by the student. We further certify that this work has not been submitted to any other University or Institution in part or full for the award of any degree or diploma. Research materials obtained from other sources and used in this research work have been duly acknowledged in the thesis. Images, illustrations, figures, tables etc., used in the thesis from other sources, have also been duly cited and acknowledged.*

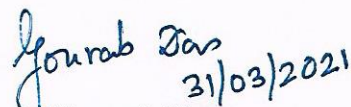
*Gourab Das*  
31/03/2021  
Gourab Das

*A. Ajayaghosh*  
31-3-2021  
A. Ajayaghosh

(Thesis Supervisor)

## STATEMENTS OF ACADEMIC INTEGRITY

I Gourab Das, a Ph. D. student of the Academy of Scientific and Innovative Research (AcSIR) with Registration No. 10CC14A39001 hereby undertake that, the thesis entitled “**Self-Assembly and Optical Properties of Phenyleneethynylene and BODIPY Based  $\pi$ -Systems**” has been prepared by me and that the document reports original work carried out by me and is free of any plagiarism in compliance with the UGC Regulations on “*Promotion of Academic Integrity and Prevention of Plagiarism in Higher Educational Institutions (2018)*” and the CSIR Guidelines for “*Ethics in Research and in Governance (2020)*”.

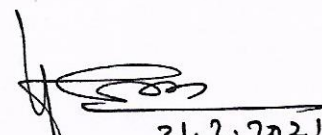
  
Gourab Das  
31/03/2021

March 31<sup>st</sup>, 2021

Thiruvananthapuram

---

It is hereby certified that the work done by the student, under my supervision, is plagiarism-free in accordance with the UGC Regulations on “*Promotion of Academic Integrity and Prevention of Plagiarism in Higher Educational Institutions (2018)*” and the CSIR Guidelines for “*Ethics in Research and in Governance (2020)*”.

  
31.3.2021

Prof. A. Ajayghosh

March 31<sup>st</sup>, 2021

Thiruvananthapuram



## DECLARATION

I, Gourab Das, bearing AcSIR Registration No. 10CC14A39001 declare that my thesis entitled, “**Self-Assembly and Optical Properties of Phenyleneethynylene and BODIPY Based  $\pi$ -Systems**” is plagiarism free in accordance with the UGC Regulations on “*Promotion of Academic Integrity and Prevention of Plagiarism in Higher Educational Institutions (2018)*” and the CSIR Guidelines for “*Ethics in Research and in Governance (2020)*”.

I would be solely held responsible if any plagiarised content in my thesis is detected, which is violative of the UGC regulations 2018.

  
Gourab Das

March 31<sup>st</sup>, 2021

Thiruvananthapuram

## ACKNOWLEDGEMENTS

It is with great pleasure that I extend my deep sense of gratitude to Prof. A. Ajayaghosh, my thesis supervisor, for suggesting the research problem, for his valuable guidance, support, motivation and encouragement, leading to the successful completion of this work.

I would like to express my gratitude to late Prof. M. V. George for being an inspiration.

I thank Dr. Suresh Das (former Director) and the present Director Dr. A. Ajayaghosh of CSIR-National Institute for Interdisciplinary Science and Technology (CSIR-NIIST), Thiruvananthapuram, for providing the necessary facilities for carrying out this work.

My sincere thanks are also due to:

- ✓ Dr. V. K. Praveen, Senior Scientist (CSTD) for all his support, guidance, motivation and fruitful discussion throughout my Ph. D. work.
- ✓ Dr. V. Karunakaran, Dr. C. H. Suresh, Dr. R. Luxmi Varma and Dr. Mangalam S. Nair, present and former AcSIR co-ordinators.
- ✓ Dr. K. N. Narayanan Unni, Dr. V. Karunakaran and Dr. Vijayakumar C., Doctoral Advisory Committee (DAC) members and the whole AcSIR faculty for the successful completion of the course work.
- ✓ Dr. P. Sujatha Devi, Dr. R. Luxmi Varma, Dr. K. R. Gopidas, present and former Heads of the Chemical Sciences and Technology Division (CSTD).
- ✓ Dr. J. D. Sudha, Dr. Rakesh K. Mishra, Dr. Sunil Varughese, Dr. Jubi John, Dr. Kaustabh Kumar Maiti and Dr. Sreejith Shankar for their support and discussion.
- ✓ Dr. Biswapriya Deb, Dr. Joshy Joseph, Dr. K. Yoosaf, Dr. Suraj Soman, Dr. Ishita Neogi, Dr. Adersh Asok, Dr. Manas Panda and Dr. Animesh Samanta, present and former scientists of the Photosciences and Photonics Section, for their help and support.
- ✓ Mr. Chandrakanth C. K., Mr. Kiran J. S., Mr. Robert Philip and Mr. Vishnu Gurjar for general help.
- ✓ Mr. Kiran Mohan for TEM analysis, Mr. Harish Raj V. for SEM analysis, Mrs. Saumini Matthew, Mr. Saran P., Mr. Gokul R. for NMR, Mrs. Viji S. for mass spectral analyses, Mr. Vibhu Darshan, Mr. Ashwin Maheswar for AFM and Mr. Peer Mohamed for Rheological studies.

- ✓ Mr. Akhil P., Ms. Drishya Elizebath K., Mr. Vijay B. Banakar, Dr. Jith C. J., Ms. Rasitha R., Ms. Anjali Anand, Ms. Sarikalekshmi K., Ms. Anisha P., Ms. Aarathi Krishna, Ms. Julie Mole, Ms. Angitha Francy, Ms. Betzy Ritha K., Ms. Sneha K. K., Ms. Saithya P., Ms. Shanu A. S. for their support.
- ✓ Dr. B. Vedhanarayanan, Dr. Rahul Dev Mukhopadhyay and Dr. R. Thirumalai for their support and advice.
- ✓ Dr. Anees P., Dr. Sandeep A., Dr. Vishnu S. Nair, Dr. Divya Susan Philips, Dr. Sandeep C., Dr. Samrat Ghosh, Dr. Sudheesh K. V., Dr. Arindam Mal, Dr. Mohamed Hifsudheen B. M., Dr. Satyajit Das, Dr. Saranya Giridharan, Mr. S. Vijayakumar, Mr. Sandip Chakraborty, Ms. Anjali N., Ms. Indulekha M., Mr. S. Lingamoorthy, Mr. Dipak Patra, Ms. Priyanka A. S., Ms. Lekshmi L., former and present group members for their help and cooperation.
- ✓ Dr, Sumesh Babu K., Dr. Sandeepa K. V., Mr. Virat G., Mr. Basavaraja, Mr. Vikas G. and Mr. Ajay krishna M. S., my roommates.
- ✓ Former and present members of CSTD and friends at CSIR-NIIST, for their help and support.
- ✓ Mrs. Vinitha Praveen, Sthuthi and Chuchu, for giving me all supports during my stay at Thiruvananthapuram.
- ✓ All my teachers for their encouragement at different stages of my academic career.
- ✓ Mr. Amit Kundu, my chemistry teacher, for inspiring me to take the challenges in chemistry during my school days.
- ✓ Dr. Suchismita Saha, for her support and motivation.
- ✓ Council of Scientific and Industrial Research (CSIR) and Department of Science and Technology (DST) for Research fellowship.

I am deeply and forever indebted to my baba and maa for their constant source of love, inspiration and blessings. Finally, I would like to thank my kaku, kakima, friends and relatives for their excellent support and encouragement. Above all, I thank the Almighty for all blessings.

**Gourab Das**

## TABLE OF CONTENTS

Certificate		i
Statements of Academic Integrity		ii
Declaration		iii
Acknowledgements		iv
Table of Contents		vi
List of Abbreviations		ix
Preface		xii
<b>CHAPTER 1</b>	<b>Self-Assembly of Phenyleneethynylene Based <math>\pi</math>-Systems</b>	<b>1-59</b>
1.1	Abstract	1
1.2	Introduction	2
1.2.1	Supramolecular Polymers	2
1.2.2	Ring-Chain Supramolecular Polymerization	4
1.2.3	Isodesmic Supramolecular Polymerization	4
1.2.4	Cooperative Supramolecular Polymerization	6
1.3	Thermodynamic and Kinetic Aspects of Supramolecular Polymerization	7
1.3.1	Equilibrium Versus Non-Equilibrium Supramolecular Assemblies	8
1.3.2	Metastable Versus Kinetically Trapped Supramolecular Assemblies	9
1.3.3	Consecutive and Competitive Pathways	10
1.4	Self-Assembly of $\pi$ -Conjugated Systems	11
1.5	Linear PEs	13
1.5.1	Short PEs (Containing Three Phenyl Rings)	13
1.5.2	Long PEs (Containing Five or More Phenyl Rings)	24
1.5.3	Metal Complexes of Linear PEs	31
1.6	Triangular PEs	37
1.6.1	Mechanistic Details and Amplification of Chirality Effect in Supramolecular Polymerization	37
1.7	Amides and Retroamides of Linear and Triangular PEs	46
1.8	PEs Attached to BODIPY	49
1.9	Origin, Objectives and Approach to the Thesis	55
1.10	References	56

<b>CHAPTER 2</b>	<b>Self-Assembly Induced Enhanced Emission in Phenyleneethynylene Derived <math>\pi</math>-Gelators</b>	<b>60-104</b>
2.1	Abstract	60
2.2	Introduction	61
2.3	Results and Discussion	69
2.3.1	Synthesis of PE Derivatives	69
2.3.2	Photophysical Studies	71
2.3.3	Morphological Characterization	76
2.3.4	Gelation Studies	78
2.3.5	FT-IR Studies	81
2.3.6	WAXS Studies	83
2.3.7	SIEE Studies	85
2.4	Conclusions	88
2.5	Experimental Section: Synthesis	89
2.6	Description on Experimental Techniques	97
2.7	References	100
<b>CHAPTER 3</b>	<b>Distinct Morphology and Optical Properties of a Y-Shaped BODIPY Self-Assembly</b>	<b>105-167</b>
3.1	Abstract	105
3.2	Introduction	106
3.3	Results and Discussion	115
3.3.1	Synthesis of BODIPY Derivatives	115
3.3.2	Photophysical Properties and Self-Assembly	118
3.3.3	Morphological Characterization	126
3.3.4	Self-Assembly of Chiral BODIPY Derivative	129
3.3.5	The Origin of Multiple Emission: Energy Migration Studies	131
3.3.6	Effect of Noncovalent Interactions	138
3.4	Conclusions	144
3.5	Experimental Section: Synthesis	145
3.6	Description on Experimental Techniques	157
3.7	References	161



<b>CHAPTER 4</b>	<b>Spindle-Shaped Supramolecular Co-polymers with Controlled Excitation Energy Transfer</b>	<b>168-210</b>
4.1	Abstract	168
4.2	Introduction	169
4.3	Results and Discussion	179
4.3.1	Synthesis of BODIPY and PE Derivative	179
4.3.2	Structural Aspects of Y-Shaped BODIPY and PE	180
4.3.3	Photophysical Properties and Self-Assembly	182
4.3.4	Co-Assembly Studies of BODIPY and PE (1:1 ratio)	187
4.3.5	Importance of BODIPY Monomers in Co-Polymerization	191
4.3.6	Importance of PE Monomers in Co-Polymerization	193
4.3.7	Excitation Energy Migration in Poly(PE)	195
4.3.8	Control over the Extent of Energy Migration in Co-Assembly	197
4.4	Conclusions	201
4.5	Experimental Section: Synthesis	202
4.6	Description on Experimental Techniques	204
4.7	References	206
	Abstract of the Thesis	211
	List of Publications	212
	List of Conference Presentations	214

## List of Abbreviations

$\alpha_{agg}$	Fraction of aggregate / Degree of aggregation
1D	One-dimensional
2D	Two-dimensional
AFM	Atomic force microscopy
AIE	Aggregation induced emission
AIEE	Aggregation induced enhanced emission
AuNPs	Gold nanoparticles
BODIPY	4,4-difluoro-4-bora-3a-4a-diaza-s-indacene
BOP	benzotriazol-1-yloxytris(dimethylamino)phosphonium hexafluorophosphate
CD	Circular dichroism
CGC	Critical gelator concentration
cm	Centimeter
CS	Chitosan
DLS	Dynamic light scattering
DMF	<i>N,N</i> -Dimethylformamide
equiv.	Equivalent
ESI-MS	Electrospray ionization mass spectrometry
FT-IR	Fourier-transform infrared
g	Gram
G'	Storage modulus
G''	Loss modulus
h	Hour
H-bonding	Hydrogen bonding
H-bonds	Hydrogen bonds
HOMO	Highest occupied molecular orbital
HRMS	High resolution mass spectrometry
IRF	Instrument response function
$I_{em}$	Intensity of emission
K	Kelvin
$k_r$	Radiative decay rate constant
$k_{nr}$	Non-radiative decay rate constant

LD	Linear dichroism
LUMO	Lowest unoccupied molecular orbital
M	Molar
mm	Millimeter
m.p.	Melting point
MALDI-TOF	Matrix-assisted laser desorption ionization time-of-flight
MCH	Methylcyclohexane
MHz	Mega hertz
min	Minute
mL	Milliliter
mmol	Millimole
mol	Mole
NDI	Naphthalene diamide
NIR	Near-infrared
nm	Nanometer
NMR	Nuclear magnetic resonance
ns	Nanosecond
OPM	Optical polarizing microscopy
PE	<i>p</i> -Phenyleneethynylene
PBI	Perylene bisimide
pH	Hydrogen ion concentration at logarithmic scale
PL	Photoluminescence
ps	Picosecond
PV	<i>p</i> -Phenylenevinylene
r.t.	Room temperature
s	Second
SAXS	Small angle X-ray scattering
SEM	Scanning electron microscopy
SIEE	Self-assembly induced enhanced emission
t	Time
T	Temperature
TCSPC	Time Correlated Single Photon Counting
$T_e$	Elongation temperature

TA	Tartaric acid
TEM	Transmission electron microscopy
TEG	Triethylene glycol
THF	Tetrahydrofuran
TLC	Thin layer chromatography
TRES	Time resolved emission spectroscopy
TMS	Tetramethylsilane
UV	Ultra-violet
vis	Visible
WAXS	Wide angle X-ray scattering
XRD	X-ray diffraction
Å	Angstrom
°C	Degree Celsius
$\Delta H^\circ$	Standard enthalpy
$\Delta S^\circ$	Standard entropy
$\Delta G^\circ$	Standard Gibbs free energy
$\Delta \epsilon$	Molar extinction coefficient
$\epsilon$	Ellipcity
$\Phi_F$	Fluorescence quantum yield
$\lambda$	Wavelength
$\lambda_{\text{abs}}$	Wavelength of absorption
$\lambda_{\text{em}}$	Wavelength of emission
$\lambda_{\text{ex}}$	Wavelength of excitation
$\lambda_{\text{max}}$	Wavelength of maximum intensity
$\mu\text{m}$	Micrometer
$\mu\text{L}$	Microliter
$\tau$	Lifetime
$\tau_{\text{av}}$	Average lifetime
$\gamma$	Strain amplitude

## PREFACE

The field of polymer chemistry had taken a new leap in 1920, when Hermann Staudinger came up with a brilliant concept stating that polymeric substances are the long chains of short repeating molecular units linked through covalent bonds. Though covalent polymers have showed their efficiency in various aspects of human life for the last several decades, they face limitations in terms of their irreversible nature leading to the inability to self-heal and disintegrate posing environmental threat. Unlike covalent polymers, the prevalence of non-covalent interactions makes supramolecular polymers reversible, modular, adaptive, and stimuli-responsive. At the early stages of the development of supramolecular polymers, researchers were mainly focused on creating systems under thermodynamic equilibrium, where the system remains at the global minimum of the energy landscape. During the last decade, the focus of this exciting research area has shifted to understanding the pathway complexity in supramolecular polymerization, living supramolecular polymerization, and transient assemblies. In this regard, a variety of  $\pi$ -systems have been explored to develop proper design principles and structure-property relationships. The first chapter gives a brief summary of the recent advancements in the area of supramolecular polymers by discussing the self-assembly behavior of phenyleneethynylene (PE) and PE-linked BODIPYs. In this context, importance has been given to their formation mechanism, diversity in morphology, intriguing ground and excited state properties and applications.

In the second chapter, we have shown the self-assembly induced modulation of the emission of the amide functionalized PE chromophores bearing linear achiral (**1**) or branched chiral (**2**) alkoxy chains.<sup>1</sup> Self-assembled structures of both **1** and **2** from *n*-decane exhibited enhanced emission with  $\Phi_F$  values of 0.34 and 0.25, respectively, whereas these molecules were less-emissive in chloroform ( $\Phi_F = 0.02$ ). Formation of entangled blue-emissive fibers for **1** and supercoiled helical blue-emissive fiber bundles for **2** has been confirmed from TEM and



fluorescence microscopy studies. Above a critical concentration (8.8 mM for **1** and 23.6 mM for **2** in *n*-decane), self-assembly of both **1** and **2** led to gelation of linear and cyclic nonpolar solvents. Moreover, a significant shift in the emission towards longer wavelength was noticed from solution state to aggregates to the gel state. The observed self-assembly induced enhanced emission (SIEE) phenomenon in compounds **1** and **2** can be attributed to the restriction of rotation of the PE chromophores in the gel state. Comparison of the optical properties between the gels of **1** and **2** revealed relatively stronger emission with the former having achiral side chains.

In the third chapter, we have demonstrated creation and control of distinct supramolecular architectures and their energy landscapes for the reversible control of the excited-state emission processes through cascade energy transfer, facilitated by an unprecedented solvent effect.<sup>2</sup> In MCH, a Y-shaped BODIPY derivative self-assembled to form an unusual spherical architecture of 400-1200 nm size, exhibiting a single emission at 540 nm upon 475 nm excitation through a normal excitation deactivation process. However, in *n*-decane, the same BODIPY derivative formed 2D supramolecular sheets, exhibiting multiple emission peaks at 540, 610, 650, 725 and 790 nm with 475 nm excitation due to cascade energy transfer. Furthermore, reversible control on the morphology and excitation energy transfer has been obtained by suitably varying the solvent composition or by ultrasound stimulation, resulting in enhanced near-infrared emission with a large pseudo Stokes shift of 7105 cm<sup>-1</sup>.

In the fourth chapter, formation of spindle-shaped supramolecular polymers by thermodynamically controlled supramolecular copolymerization of two distinct Y-shaped **BODIPY** and **PE** monomers, forming 2D and 1D supramolecular polymers, respectively are described.<sup>3</sup> The cooling curves derived from the temperature-dependent UV-vis absorption study clearly discerned that copolymerization of a 1:1 mixture of **BODIPY** and **PE** to elongated spindle-like co-assemblies (aspect ratio ~4-7) is initially driven by nucleation-elongation of

**BODIPY**, followed by the secondary nucleation of **PE** monomers. The importance of initial nucleation of **BODIPY** monomers in forming spindle structure with controlled length has been further confirmed by varying the composition of **BODIPY** and **PE** to a 3:1 ratio, which restricted the growth and exhibited circular spindles having an aspect ratio of 1-2.5. Furthermore, it has been demonstrated that when the initial nucleation occurs through 1D assembly forming **PE** monomers by changing the composition of **BODIPY** and **PE** to 1:3, the aspect ratio ( $\geq 13-15$ ) for the final structure of the supramolecular co-assembly could not be controlled. Finally, with the help of time resolved emission spectroscopy (TRES) studies, we have established that the hetero-energy migration taking place from **PE** donors to **BODIPY** acceptors within the copolymeric assemblies could control the cascade homo-energy transfer process occurring in poly(**BODIPY**).

## References

1. Enhanced Emission in Self-Assembled Phenyleneethynylene Derived  $\pi$ -Gelators. **Das, G.**; Thirumalai, R.; Vedhanarayanan, B.; Praveen, V. K.; Ajayaghosh, A. *Adv. Opt. Mater.* **2020**, *8*, 2000173.
2. Tweaking of an Unusual Spherical BODIPY Assembly to Two-Dimensional Supramolecular Sheets Facilitates Domino-Type Energy Transfer Assisted Multiple Emission. **Das, G.**; Cherumukkil, S.; Padmakumar, A.; Banakar, V. B.; Praveen, V. K.; Ajayaghosh, A. *Angew. Chem. Int. Ed.* **2021**, *60*, DOI: 10.1002/anie.202015390.
3. Spindle-Shaped Supramolecular Co-Polymers with Controlled Excitation Energy Transfer by Co-Polymerizing 2D- and 1D-Assembly Forming  $\pi$ -System Monomers. **Das, G.**; Vedhanarayanan, B.; Padmakumar, A.; Praveen, V. K.; Ajayaghosh, A. (Manuscript under preparation)

---

# Self-Assembly of Phenyleneethynylene Based $\pi$ -Systems

---

### 1.1. Abstract

*Nature has been a source of inspiration to understand the complexities and functional properties of molecular assemblies and supramolecular polymers. Unlike covalent polymers, the prevalence of non-covalent interactions makes supramolecular polymers reversible, modular, adaptive, and stimuli-responsive. At the early stages of the development of supramolecular polymers, researchers were mainly focused on creating systems under thermodynamic equilibrium, where the system remains at the global minimum of the energy landscape. During the last decade, the focus of this exciting research area has shifted to understanding the pathway complexity in supramolecular polymerization, living supramolecular polymerization, and transient assemblies. In this regard, a variety of  $\pi$ -systems have been explored to develop proper design principles and structure-property relationships. Due to their intriguing optoelectronic properties, PE, a member of extended  $\pi$ -systems, has played a pivotal role in this progress. In this chapter, we have summarized the recent developments in the field of supramolecular polymers by discussing the self-assembly behaviors of*

*PEs in the context of their formation mechanism, diversity of morphology, intriguing ground and excited-state properties and applications. Finally, the objectives and the approach of the investigations leading to the current thesis work has been described.*

## **1.2. Introduction**

### **1.2.1. Supramolecular Polymers**

In 1920, the field of polymer chemistry had taken a new leap when Hermann Staudinger came up with a brilliant concept stating that polymeric substances are the long chains of short repeating molecular units linked through covalent bonds.<sup>[1,2]</sup> Though polymers have underpinned their efficacy in various aspects of human life for the last several decades, they face limitations in terms of their irreversible nature leading to the inability to self-heal and disintegrate posing environmental threat. In this context, breakthroughs in the field of supramolecular chemistry have shown how reversible and directional secondary interactions can lead to polymeric materials of a high degree of internal order with self-healing and self-recovery properties.<sup>[3-6]</sup> In general, the size and dimensions of supramolecular polymers depends on the nature and strength of the non-covalent bonds involved in the polymerization process, the concentration of monomers and experimental conditions such as solvent, temperature and so on.<sup>[7]</sup> The main advantages attributed to supramolecular polymers over the conventional polymers are purity and processability. Though the elegance and functional aspects of naturally occurring supramolecular polymers such as G-actin and tubulin, acting as building-blocks for the scaffolding of cells were an inspiration for researchers to venture into the field of supramolecular polymers. In this context, a real breakthrough in creating artificial

supramolecular polymers was the development of 2-ureido-4[1H]-pyrimidinone (UPy) monomers in 1997.<sup>[7,8]</sup> The monomeric unit of UPy can form quadruple H-bonds and two of these self-complementary monomeric units can self-assemble to form supramolecular polymers with a relatively long lifetime of the bonds (0.1–1 seconds) essential for making networks with true polymeric properties.<sup>[8]</sup>

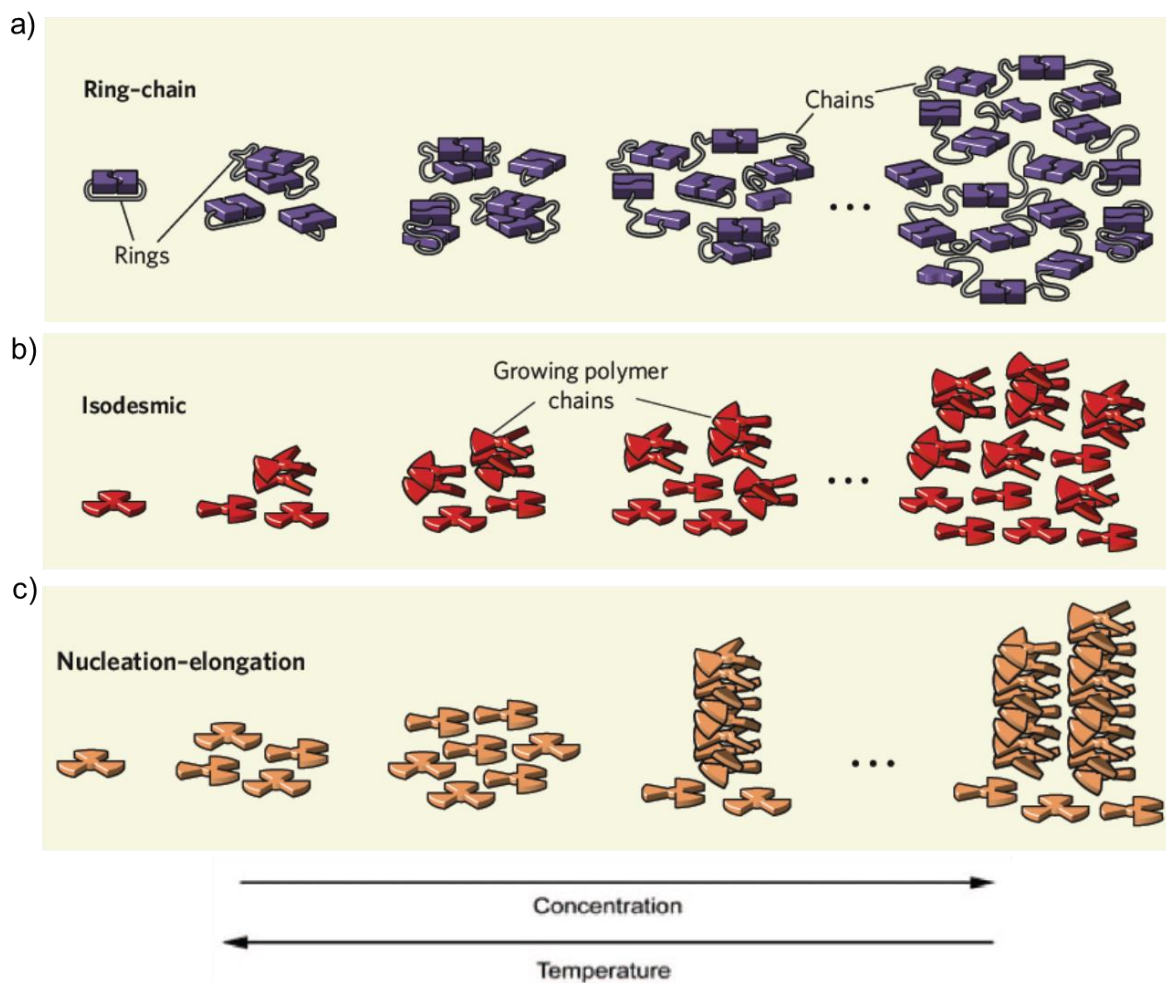


**Figure 1.1.** Different growth mechanisms for the formation of supramolecular polymeric assemblies from the monomeric units: (a) ring-chain; (b) isodesmic and (c) cooperative (nucleation-elongation) supramolecular polymerization. (Adapted with permission from Ref 7).

The extensive amount of works carried out in the research field of supramolecular polymeric assemblies demonstrates how the chemical information encoded in the



monomeric structure can influence the self-assembly process into well-defined supramolecular architectures. As a part of this continuing research effort, several mechanistic models to understand the self-assembly process have been developed. The supramolecular polymerization processes are classified into three different growth mechanisms: ring-chain, isodesmic and nucleation-elongation (cooperative) mechanisms (**Figure 1.1**).<sup>[7,9-13]</sup>

### 1.2.2. Ring-Chain Supramolecular Polymerization

The ring-chain polymerization mechanism is applicable only for the ditopic monomeric systems where an equilibrium exists between the closed ring of the monomers and the linear chains (**Figure 1.1a**).<sup>[5a,7]</sup> In this case, the ends of small supramolecular polymers always prefer to form a ring structure below a critical concentration instead of finding another monomer to participate in chain elongation. The formation of ring-chain supramolecular polymers is very rarely reported in the literature.<sup>[5a]</sup> For example, at lower concentrations, bifunctional UPy derivatives form cyclic dimers in solution following ring-chain supramolecular polymerization.<sup>[5a]</sup> However, in most cases, the supramolecular polymerization can be addressed either by isodesmic or nucleation-elongation mechanism (**Figure 1.1b,c**).

### 1.2.3. Isodesmic Supramolecular Polymerization

The isodesmic or equal K model is applicable to the polymerization process where the rate constant in each step remains unaltered (**Figure 1.2a**), indicating that the length of

the polymer chain cannot affect the strength of the secondary interactions at the time of addition of the monomer units to the growing end of the polymer chains.<sup>[5a,7,9]</sup> Moreover, the process of successive addition of the monomers results in a constant decrease in the free energy of the overall system (**Figure 1.2b**). For example, the  $C_3$ -symmetrical PV (**C<sub>3</sub>PV**) when cooled from 363 to 283 K in toluene at a controlled rate of 1 K/min, follows an isodesmic pathway (**Figure 1.2c**).<sup>[5b]</sup> Some of the biological processes like serpin polymerization<sup>[5c]</sup> and conversion of FtsZ proteins (protein encoded by the *ftsZ* gene) into the Z-ring during cell-division<sup>[5d]</sup> also follow isodesmic pathway.

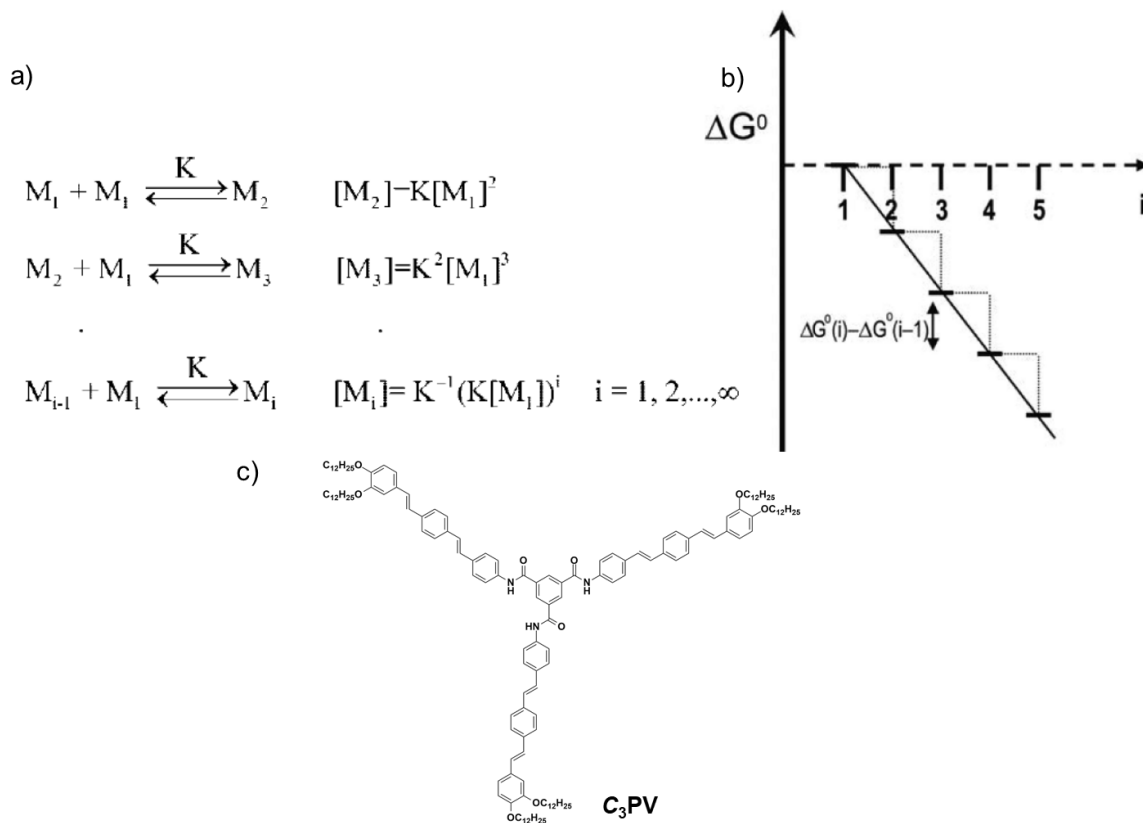


**Figure 1.2.** (a) General scheme for the isodesmic supramolecular polymerization of the monomers (M). (b) Energy diagram for an isodesmic supramolecular polymerization. The abscissa in this plot represents the size of the oligomer ( $i$ ), whereas the ordinate measures the free energy  $\Delta G^\circ$  in arbitrary units. (c) Molecular structure of **C<sub>3</sub>PV** following isodesmic supramolecular polymerization pathway. (Adapted with permission from Ref 5).

### 1.2.4. Cooperative Supramolecular Polymerization

The cooperative (nucleation-elongation) supramolecular polymerization process involves two distinct phases (**Figure 1.3**), an energetically uphill slow nucleation process (association constant  $\sim K_n$ ) followed by an energetically downhill rapid elongation process with an association constant of  $K_e$ , ( $K_n \ll K_e$ ).<sup>[5a,9,14]</sup> In this case, the

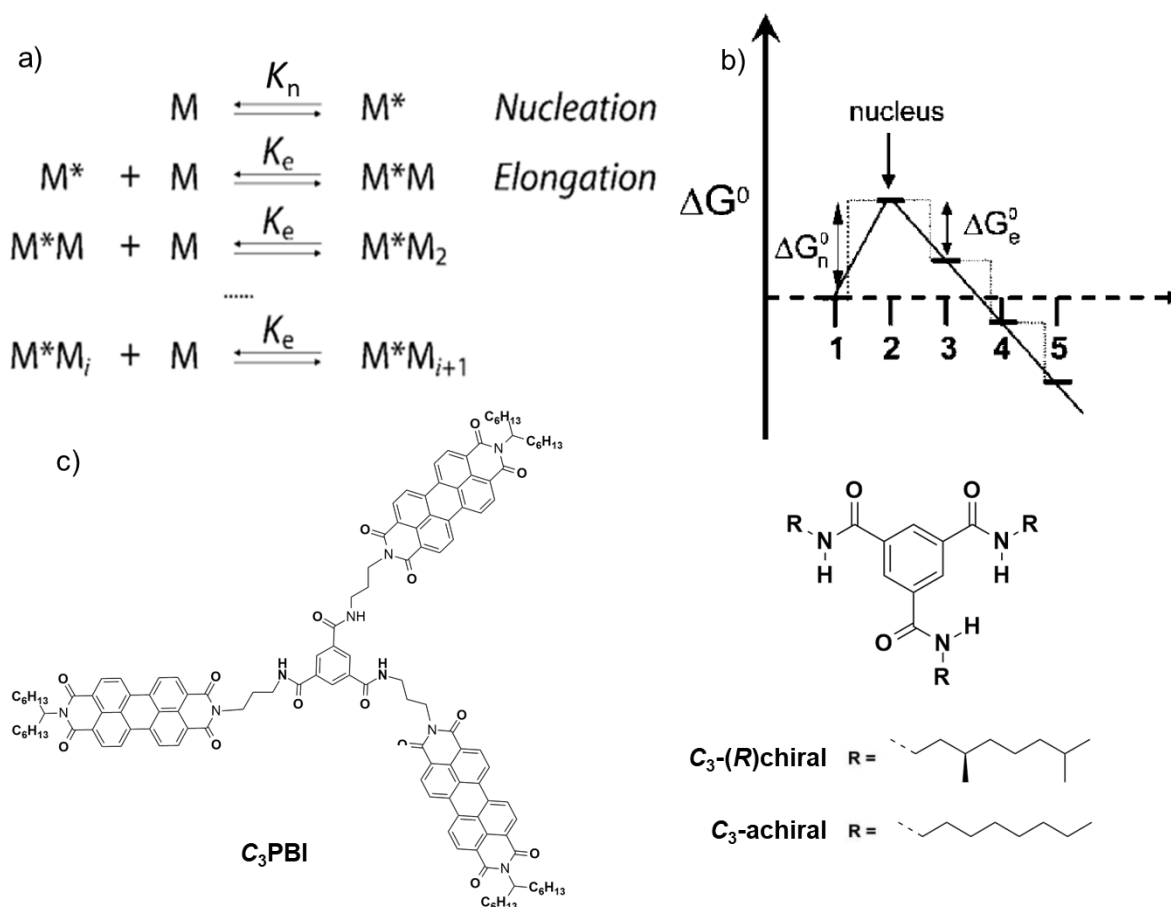


**Figure 1.3.** (a) General scheme for the cooperative supramolecular polymerization, demonstrating the formation of a stable nucleus from the monomers M followed by elongation to supramolecular polymer. (b) Energy diagram of a cooperative supramolecular polymerization. The abscissa in this plot represents the size of the oligomer ( $i$ ), whereas the ordinate measures the free energy  $\Delta G^\circ$  in arbitrary units. (c) Molecular structures of **C<sub>3</sub>PBI**, **C<sub>3</sub>-(R)chiral**, **C<sub>3</sub>-achiral** following cooperative supramolecular polymerization pathway. (Adapted with permission from Ref 5).

formation of the stable nucleus is crucial for further addition of the monomers to accelerate the growth of the polymeric chains. **Figure 1.3a** demonstrates a general scheme associated with the self-assembly mechanism of cooperative supramolecular polymerization.<sup>[5a]</sup> For example, growth of actin monomers into filaments follows a cooperative path.<sup>[5e]</sup> Most of the  $C_3$ -symmetrical benzene trisamide derivatives such as **C<sub>3</sub>PBI**, **C<sub>3</sub>-(R)chiral**, **C<sub>3</sub>-achiral** are known to self-assemble through a cooperative nucleation–elongation mechanism (**Figure 1.3c**).<sup>[5b,5f]</sup>

### 1.3. Thermodynamic and Kinetic Aspects of Supramolecular Polymerization

Detailed understanding of the formation mechanism of supramolecular polymeric assemblies has allowed researchers to investigate the pathway complexity phenomena

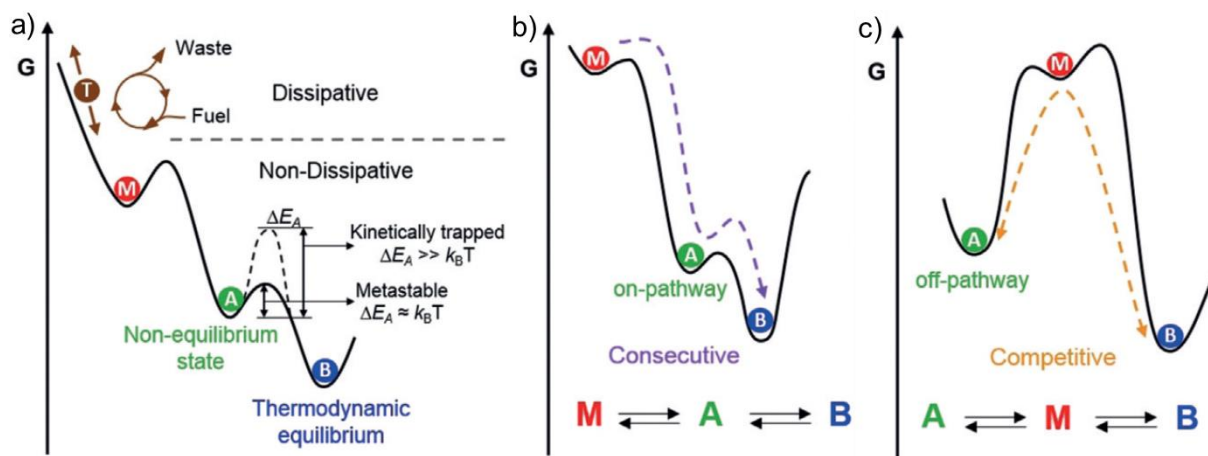


**Figure 1.4.** Energy landscapes illustrating the different concepts for the characterization of various supramolecular assemblies: (a) dissipative versus non-dissipative and equilibrium versus non-equilibrium states, (b) consecutive and (c) competitive pathway. (Adapted with permission from Ref 15).

dealing with a multitude of aspects by which supramolecular polymers can be classified into different categories.<sup>[15,16]</sup> In this regard, detailed studies have shown that the self-assembling conditions can decide the formation and stability of supramolecular polymers and their transformation from one state to the other.<sup>[16-19]</sup> In this section, we discuss the classification and differentiation of various types of supramolecular assemblies obtained under different experimental conditions within a system by giving preference to their standard Gibbs free energy (**Figure 1.4**).

### 1.3.1. Equilibrium Versus Non-Equilibrium Supramolecular Assemblies

In an energy landscape diagram, the systems which remain in the global energy minimum are mainly considered as the system under thermodynamic equilibrium (B in **Figure 1.4a**). At this condition, the system can still be dynamic with the monomers equilibrating continuously between solution and aggregates without any time-dependent changes. As a result, these systems are highly stable and do not require any external inputs to maintain them in this state. The dependence of energy landscape on various parameters such as concentration, temperature, and solvent composition may influence the formation of equilibrium species.<sup>[5a,6,20,21]</sup> Any other species that do not follow the above-mentioned conditions is considered kinetic, non-equilibrium supramolecular assemblies (**Figure 1.4a**).<sup>[16,20]</sup> However, these structures are prone to spontaneous conversion by which they can overcome the activation energy barrier and gradually evolve into equilibrium assemblies with time or in the presence of external stimuli. All of the above set of conditions come under the boundary of non-dissipative equilibrium

or non-equilibrium state.<sup>[15,16]</sup> Supramolecular polymers can also form under dissipative non-equilibrium conditions (**Figure 1.4a**), where the monomers (M) have low or no propensity to self-assemble because of their high thermodynamic stability. In this case, the supramolecular polymerization process is an uphill process and requires constant input of energy to maintain the supramolecular assembly that is transient in nature.<sup>[15,16,22]</sup> The absence of the external supply of energy leads to spontaneous dissipation of the energy of the system to fall into a thermodynamic global minimum, which either corresponds to the initial monomeric state or a completely different chemical or conformational state.

### 1.3.2. Metastable Versus Kinetically Trapped Supramolecular Assemblies

The presence of an activation energy barrier in the energy landscape retards the spontaneous formation of thermodynamically stable supramolecular polymers. The magnitude of this energy barrier plays a decisive role in distinguishing kinetic species into either metastable or kinetically trapped supramolecular assemblies (**Figure 1.4a**).<sup>[14,16,23]</sup> If the energy barrier for the transformation is relatively low (not greater than  $k_B T$ ), the system can slowly convert to form a stable species at room temperature and within an observable time scale (ranging from minutes to several months), which signifies the unstable assembly as a metastable supramolecular assembly (**Figure 1.4a**). On the contrary, if the energy barrier for the transformation is relatively higher, the system can get trapped in a particular state and take a prolonged time for the conversion process, thereby signifying the formation of kinetically trapped supramolecular

assemblies (**Figure 1.4a**). In general, kinetically trapped supramolecular assemblies reside in a local energy minimum unless and until affected by a suitable external stimulus to overcome the energy barrier.

### 1.3.3. Consecutive and Competitive Pathways

Conversion of supramolecular assemblies from one state to the other can take place through various pathways. Therefore, it is important to understand and categorize the formation mechanism of each assembly in the energy landscape diagram of a complex system.<sup>[24]</sup> The term "consecutive" deals with a pathway in which a species (trapped state) undergo a slow conversion to a relatively more stable species by structural rearrangement or by forming higher-ordered architectures (**Figure 1.4b**). On the other hand, when the transformation occurs through the disassembly of the initially formed species to monomers followed by their reorganization to a comparatively more stable assembly, the pathway is considered as "competitive" (**Figure 1.4c**). Monitoring the time-dependent changes of these assemblies at different concentrations is the most important experiment to distinguish these two complex pathways. Acceleration in the aggregate-to-aggregate transformation with an increase in concentration confirms the conversion time to be shorter, and hence the pathway is consecutive. However, in the competitive pathway, the time taken for the interconversion increases upon increasing the concentration as a greater number of less-stable species disintegrate into free, aggregation-prone monomers before their reorganization into a more stable assembly.

## 1.4. Self-Assembly of $\pi$ -Conjugated Systems

In the last couple of decades,  $\pi$ -conjugated systems have gained a lot of interest because of their intriguing functional properties noticed during the exploration of their ground and excited-state properties. Different research groups working in supramolecular chemistry worldwide analyzed the self-assembly behavior of various  $\pi$ -conjugated systems and categorized them into different types of supramolecular assemblies as described in the previous section.<sup>[14,15,20]</sup> For example, Miyajima, Aida, and co-workers demonstrated the living chain-growth supramolecular polymerization of a kinetically trapped monomer of amide-appended thioalkyl chain substituted  $C_5$ -symmetric corannulene, **1** (**Figure 1.5a**).<sup>[25]</sup> The monomer, conformationally restricted by intramolecular H-bonding, was unable to take part in intermolecular H-bond mediated polymerization under ambient conditions. Interestingly, addition of the initiator **2** (**Figure 1.5a**), an *N*-methylated analogue of the monomer, to a solution of **1** resulted in controlled supramolecular polymerization as in the case of living chain-growth polymerization. Later, Sugiyasu, Takeuchi and co-workers have demonstrated porphyrin-based monomers, **3** (**Figure 1.5b**) self-assembled to nanoparticles and then gradually converted into nanofibers with time following a consecutive self-assembly pathway.<sup>[26]</sup> The conversion of particles to fibers was found accelerating upon addition of a small aliquot of seeds of one-dimensional (1D) fibers to the solution.



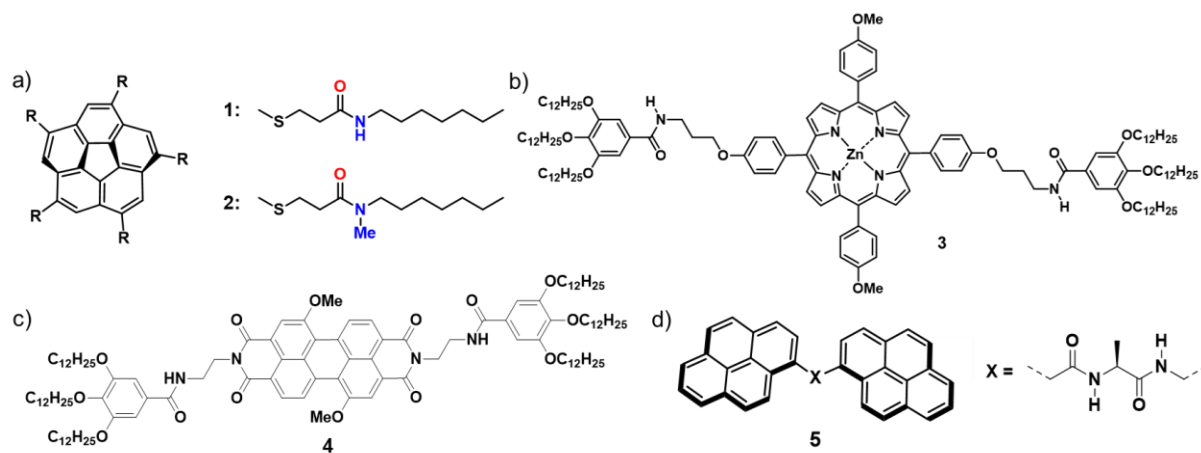


**Figure 1.5.** Self-assembly of some of the reported  $\pi$ -conjugated systems: (a) amide-appended thioalkyl chain substituted C<sub>5</sub>-symmetric corannulene, (b) porphyrin based monomer bearing H-bonding moieties and long alkyl chains, (c) dimethoxy substituted perylene bisimide and (d) amino acid based diamide bearing a pyrene unit at each of the terminus. (Adapted with permission from Ref 25,26,28 and 29).

The process was found to be similar to the amyloid fibril formation observed in prion infection in biological systems,<sup>[27]</sup> where the misfolded proteins have the ability to transmit their misfolded shape into normal form or variant of the same protein. In a different study, the research group of Würthner has demonstrated conversion of non-luminescent H-type aggregates to luminescent J-type aggregates by following seeded supramolecular polymerization approach.<sup>[28]</sup> The formation of non-fluorescent H-type aggregates was noticed when a solution of PBI derivative (**4**) in methylcyclohexane-toluene (MCH-Tol, 2:1, v/v) cooled from 363 to 283 K at a rate of 5 K/min (**Figure 1.5c**). On the other hand, when the rate of cooling was decreased to 1 K/min, fluorescent J-type aggregates were obtained. Under ambient conditions, the conversion from the non-fluorescent H-type aggregates to fluorescent J-type aggregates was found to take place within a time span of 6 h, which can be accelerated by adding J-type aggregate seeds. Ogi, Yamaguchi and co-workers have observed seeded supramolecular

polymerization in the case of a dipeptide terminal functionalized with pyrene moiety, **5** (**Figure 1.5d**).<sup>[29]</sup> The monomer **5** can adopt an inactive folded form with intramolecular H-bonds, which retarded the spontaneous polymerization process. However, spontaneous supramolecular polymerization through open form (active state) of the diamide was achieved without any lag time when the seed solution (prepared by sonicating the hot monomeric solution for 10 min at 278 K) was added to the trapped monomeric solution of **5**.

The above mentioned examples demonstrate the importance of chromophore-based systems to unravel various aspects of supramolecular polymerization. Due to their intriguing optoelectronic properties, phenyleneethynylene (PE), a repeatable unit for making extended  $\pi$ -systems, is a good candidate for constructing supramolecular polymers. In the coming sections, we have summarized the recent developments in the field of supramolecular polymers by discussing the self-assembly behavior of PEs in the context of their formation mechanism, diversity of morphology, intriguing ground and excited-state properties and applications.

## 1.5. Linear PEs

### 1.5.1. Short PEs (Containing Three Phenyl Rings)

The self-assembly of short linear PE, **6** to nanoparticles, microspheres, and super-structured blue-light emitting organogels have been reported by our research group (**Figure 1.6**).<sup>[30]</sup> The molecule **6** in  $\text{CHCl}_3$  ( $1 \times 10^{-5}$  M) remained as monomers showing a strong  $\pi$ - $\pi^*$  band at 377 nm. In contrast, a red-shifted absorption at 385 nm and an

additional band at 419 nm was observed in *n*-decane, indicating J-type aggregation of **6**. Emission of **6** was red-shifted from 414 to 443 nm when aggregated. Furthermore, a time-dependent gradual decrease in the absorption maximum was noticed, which reached a stable state after 4 h (**Figure 1.6b**), indicating the formation of kinetically controlled aggregates at the initial stage followed by its slow transformation to thermodynamically stable species through first-order kinetics with a rate constant of  $k = 47.41 \text{ min}^{-1}$  (**Figure 1.6b**, inset). Concentration-dependent AFM studies of **6** revealed individually dispersed particles of different sizes. TEM and fluorescence microscopy studies confirmed the vesicular nature of the sphere and their agglomeration and fusion to large blue-emitting microspheres, respectively (**Figure 1.6c**). Moreover, SEM of the gel (**Figure 1.6d,e**) showed micrometer-sized superstructures formed by the fusion of spherical structures above a CGC (**Figure 1.6f**). The formation of various types of supramolecular structures from a single solvent can be explained from the molecular structure of **6**. The H-bonding terminal functional groups and weak molecular interaction of non-planar phenyl rings of **6** were essential for forming nanoparticles at a lower concentration regime. The initially formed aggregates then undergo a slow time-dependent transformation into thermodynamically stable vesicular assemblies. At higher concentration ( $>\text{CGC}$ ),  $\pi$ -stacked lamellar packing of the individual molecules in the self-assembly has been confirmed from the XRD studies, which is essential for stabilizing extended nanostructures that leads to gelation.

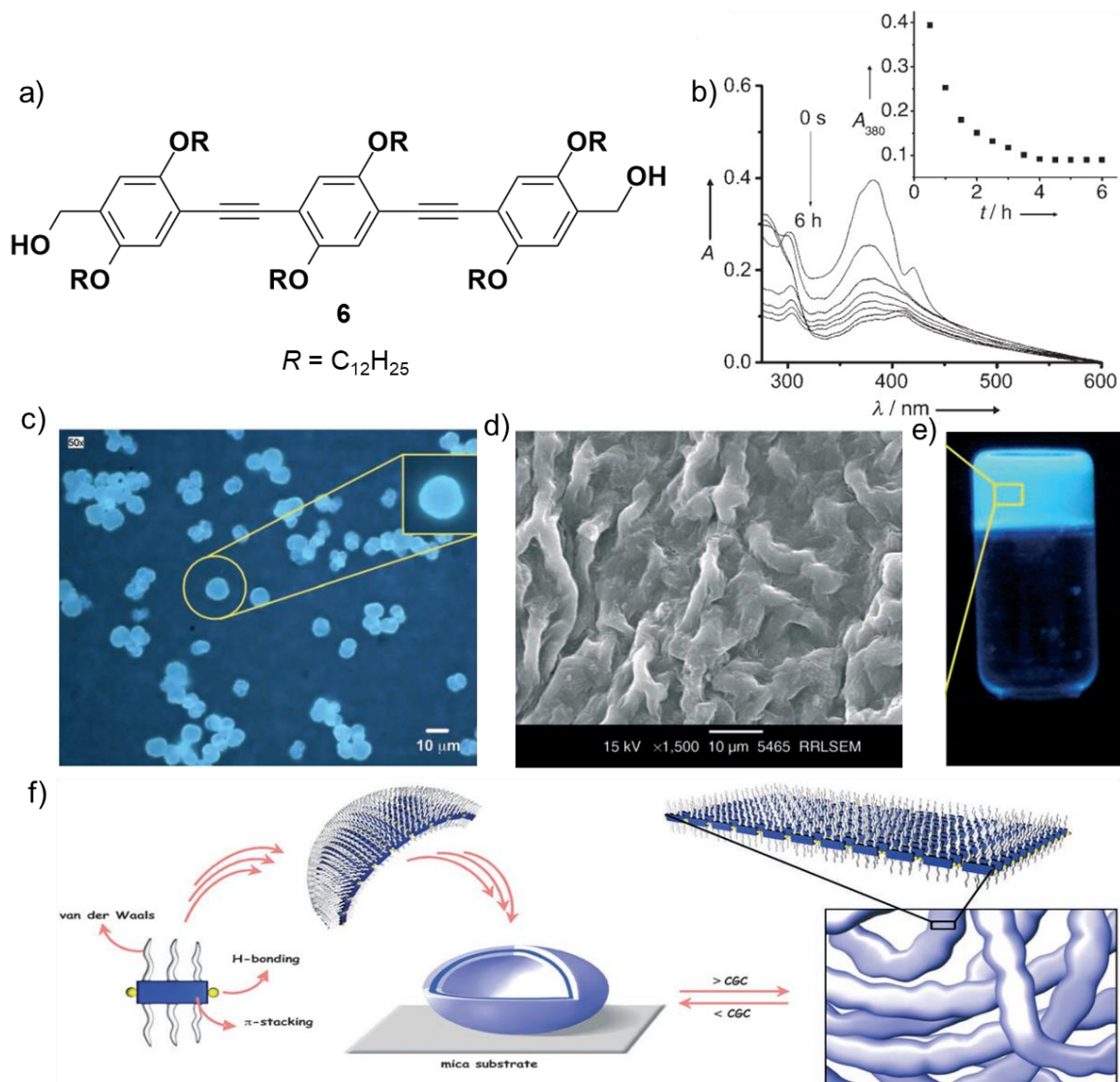


**Figure 1.6.** (a) Molecular structure of **6**. (b) Time-dependent absorption changes of **6** in *n*-decane ( $1.1 \times 10^{-5}$  M), inset shows the time-dependent changes in the absorbance at 380 nm. (c) Fluorescence microscopy image of **6** ( $1 \times 10^{-4}$  M in *n*-decane). (d) SEM image of gel of **6** in *n*-decane ( $3.4 \times 10^{-3}$  M). (e) Photograph of the *n*-decane gel ( $5 \times 10^{-3}$  M) under 365 nm UV light illumination. (f) Schematic representation of the self-assembly processes of **6** in *n*-decane, showing the mode of molecular arrangements in a single layer of the spherical and the extended self-assembly. (Adapted with permission from ref 30).

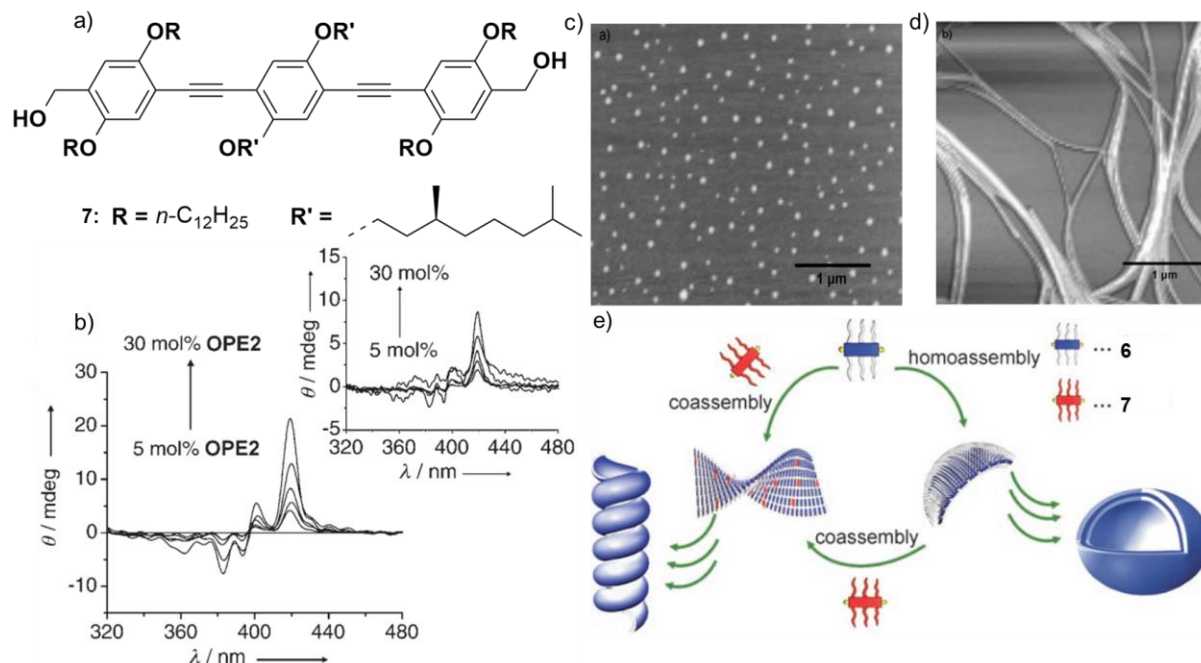


**Figure 1.7.** (a) Molecular structure of the chiral PE, **7**. (b) CD spectra of **6** with different mol% of **7**, obtained after heating followed by cooling. Inset shows the corresponding CD spectra of the solutions upon sonication; without heating and cooling. AFM height image of (c) **6** ( $1 \times 10^{-6}$  M) in *n*-decane and (d) the co-assembly of **6** with 25 mol% of **7** in *n*-decane; having a total concentration of  $1 \times 10^{-5}$  M. (e) Schematic representation showing the transformation of vesicles into helical nanostructures upon the co-assembly between **6** with **7** in *n*-decane. (Adapted with permission from ref 31).

Later, our research group has revealed an unprecedented transition of the vesicles to helical tubes through the co-assembly of the achiral PE **6** and the chiral PE **7** (**Figure 1.7a**).<sup>[31]</sup> As mentioned above, the molecule **6** self-assembled in *n*-decane, whereas **7** failed to aggregate in *n*-decane, as confirmed from its monomer-like absorption and emission features. Both **6** and **7** were found to be CD-silent at  $1 \times 10^{-5}$  M concentration, whereas the addition of **7** (5-30 mol%) to a solution of **6** in *n*-decane followed by heating and cooling resulted in a positive cotton signal followed by a negative signal (**Figure 1.7b**). However, sonication of a simply mixed solution of **6** and **7** resulted in a weak CD signal (**Figure 1.7b**, inset), which shows the importance of the heating/cooling method

in obtaining the co-assembly with enhanced chiro-optical properties. AFM image of **6** revealed the formation of spherical morphology (**Figure 1.7c**). Interestingly, upon mixing 25 mol% of **7** with **6** (total concentration of  $1 \times 10^{-5}$  M) exhibited a complete transformation of the spherical assemblies into helical structures with a uniform pitch of 140 nm (**Figure 1.7d**). **Figure 1.7e** shows a schematic representation of the co-assembly of **6** with **7**, which facilitates the transcription of chirality from the latter to the former following the sergeant-and-soldiers approach,<sup>[5f,31]</sup> thereby leading towards a significant morphological transition. UV-vis absorption spectroscopy studies have confirmed the complete disruption of the vesicular structure of **6** formed in *n*-decane upon the addition of **7** (5-30 mol%), as the intensity of the aggregation band at 420 nm for **6** was significantly decreased and the time-dependent changes were completely arrested. Moreover, the amplification of chirality was noticed when a mixture of **6** and **7** cooled down from high temperature (353 K) to room temperature (293K). During this process, the supramolecular assembly formation is mainly guided by the minimum amount of chiral sergeant molecules present in the mixture, allowing both **6** and **7** to co-assemble in a helical fashion.

Later we reported that hydrophobic PE moiety attached to a hydrophilic group through an amide linkage (**8**) could exhibit a strong fluorescence change upon aggregation in an aqueous medium (**Figure 1.8a**).<sup>[32]</sup> The molecule **8** was soluble in THF, exhibiting an emission maximum at 395 nm, whereas upon aggregation in THF-water (1:9 v/v), the emission maximum was shifted to 488 nm along with a change in emission color from blue to cyan (**Figure 1.8b**). Interestingly, a similar change in

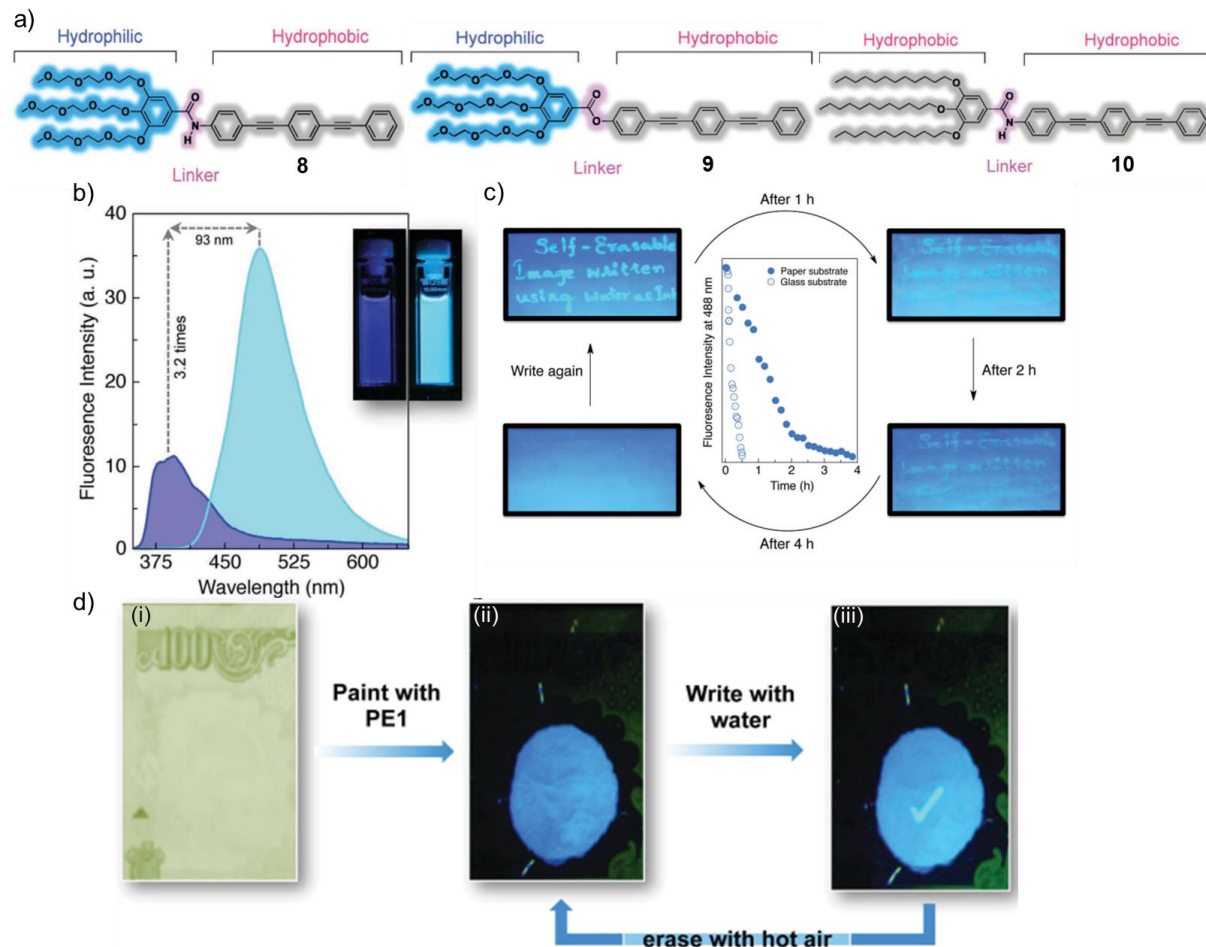


**Figure 1.8.** (a) Chemical structures of the amphiphilic molecules **8**, **9** and lipophilic molecule **10**. (b) Emission spectra ( $\lambda_{\text{ex}} = 340 \text{ nm}$ ) of **8** in THF and THF-water mixture (1:9 v/v),  $1 \times 10^{-5} \text{ M}$ . Inset shows the photographs of **8** in THF (left) and THF-water mixture 1:9 v/v (right) under 365 nm UV light illumination. (c) Photographs of the handwritten images on **8**-coated paper under the illumination of 365 nm UV light over a period of 4 h. A secondary plot shown in the middle exhibits the corresponding changes in the fluorescence to the variation in the nature of the substrate. (d) (i) Photograph showing a part of a currency bill under normal light. (ii) Photograph of **8**-coated currency bill and (iii) tick mark made using water over the coated portion of the currency bill, taken under the illumination of 365 nm UV light. The reversible changes in emission noticed under direct contact with water has been used as a part of self-erasable writing. (Adapted with permission from Ref 32).

emission properties was noticed when a filter paper coated with **8** upon contact with water (**Figure 1.8c**). Furthermore, the initial blue emission can be restored by drying out the water from the filter paper. The reversible change in emission noticed under direct



contact with water has been applied for the self-erasable writing and as a security label for document authentication (**Figure 1.8c,d**). Detailed XRD and FT-IR studies suggested that the presence of amide H-bonding and hydrophilic oxyethylene chains in **8** are crucial for the water-induced change in emission as the molecules **9** and **10** (**Figure 1.8a**) were failed to show similar kind of emission changes.

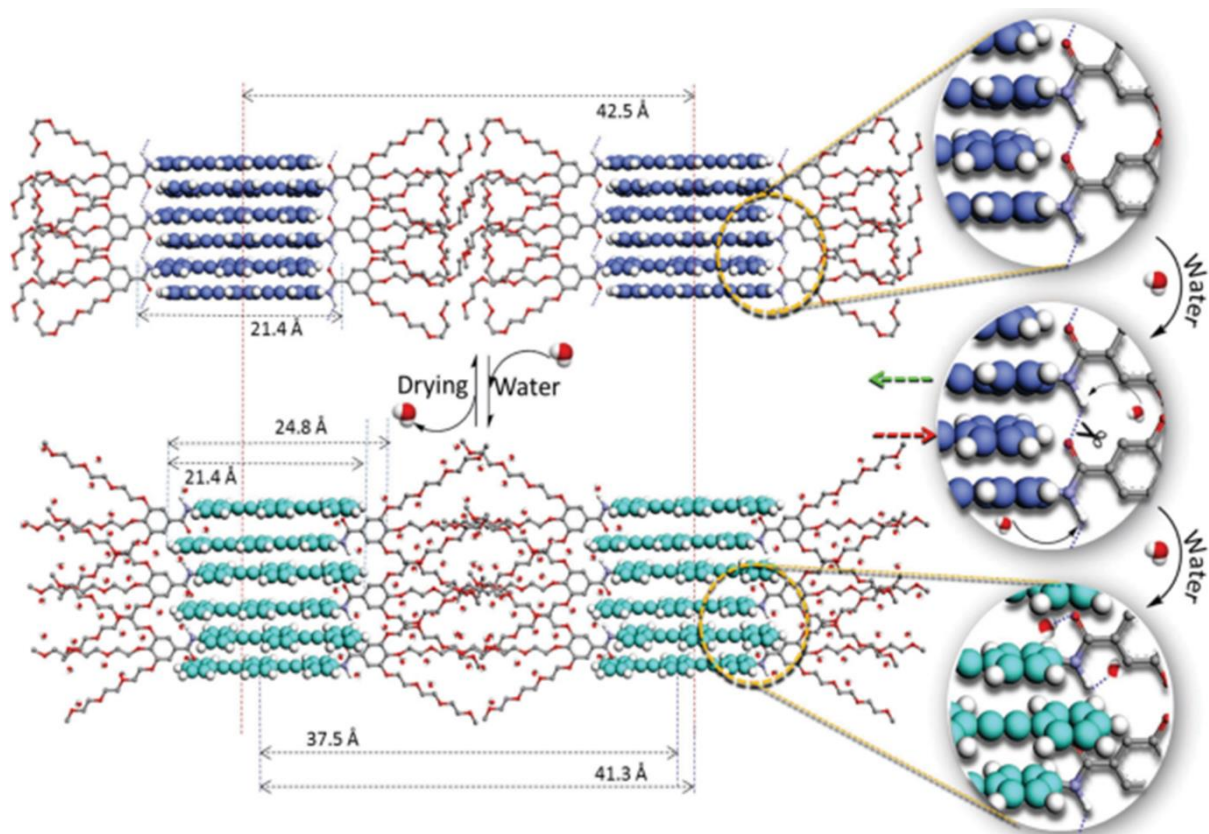


**Figure 1.9.** Schematic illustration demonstrating the sliding mechanism of **8** in the absence and presence of water. The zoomed portion on the right side shows the molecular arrangement illustrating the H-bond breaking and molecular sliding; arrows indicate the direction of sliding. (Adapted with permission from Ref 32).

Based on the above-mentioned results, a probable mechanism for the water-induced emission changes of **8** is depicted in **Figure 1.9**. The presence of water molecules results in the slipping of **8** by breaking the intermolecular H-bonding and



stretching of the oxyethylene chains, which pushes the molecules to the opposite inward directions and thereby changing the chromophore packing from H- to J-type arrangement, resulting in emission change from blue to cyan.

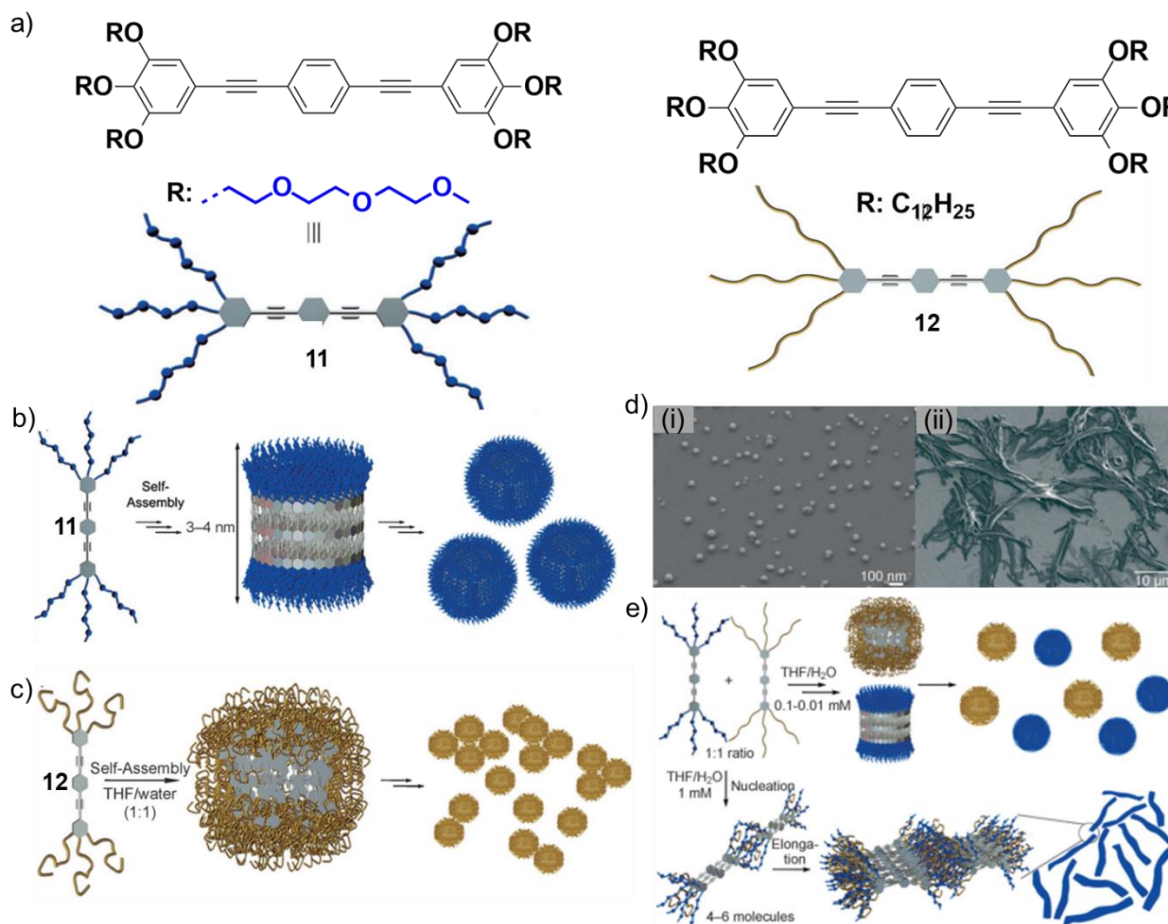


**Figure 1.10.** (a) chemical structures of **11** and **12**. (b) Self-assembly model of **11** in THF/water (1:1) mixtures. (c) Cartoon representation of self-assembly of **12** in THF/water (1:1) mixture. (d) SEM images of 1:1 mixture of **11** and **12** in THF/water (1:1) mixture at (i) 0.1 mM and (ii) 1 mM concentration. (e) Cartoon represents the concentration-dependent self-sorting behavior of a 1:1 mixture of **11** and **12** in THF/water (1:1). Narcissistic and social self-sorting occur at concentrations between 0.01 and 0.1 mM (top) at 1 mM (bottom), respectively. (Adapted with permission from ref 33).

Fernández and co-workers have described the self-assembly of two structurally related PE derivatives functionalized with polar oxyethylene (**11**) and nonpolar dodecyloxy (**12**) chains (**Figure 1.10a**).<sup>[33]</sup> Self-assembly of **11** ( $1 \times 10^{-4}$  M) in

THF/water (1:1) mixture revealed the appearance of discrete globular objects having a size within 3-10 nm, which followed a non-cooperative (isodesmic) pathway. **Figure 1.10b** shows the formation of the spherical structures stabilized via  $\pi$ - $\pi$  stacking and hydrophobic interactions operating between aromatic PE segments, where the peripheral TEG chains are projected towards the aqueous environment by hiding the aromatic core. On the other hand, the achiral derivative **12** ( $1 \times 10^{-5}$  M) self-assembled through hydrophobic effect resulted in spherical objects with diameters in the range of 4-50 nm (**Figure 1.10c**). Interestingly, a 1:1 mixture of **11** and **12** within the concentration range of  $10^{-4}$  to  $10^{-5}$  M in 1:1 THF/water formed independent spherical aggregates with sizes ranging between 5 and 50 nm, confirming the domination of narcissistic self-sorting up to a concentration of 0.1 mM (**Figure 1.10d(i),e**). However, at a higher concentration (1 mM), SEM studies revealed the formation of long ribbon-like aggregates with a width of 2  $\mu\text{m}$  and length of several microns (**Figure 1.10d(ii)**), where the equilibrium has been found shifted towards the formation of a cooperative co-assembly driven by geometrical complementarity and the hydrophobic effect. Polarized optical microscopy was also used to confirm the copolymerization process, which clearly showed the formation of a lyotropic lamellar ( $L_{\alpha}$ ) mesophase through a spherulitic growth process of co-assembled PEs. The schematic diagram shown in **Figure 1.10e** (bottom) represents the intercalation of **12** within the  $\pi$ -stacked aromatic units of **11**, where the lateral interaction between the alternate  $\pi$ -stacks is mainly supported by van der Waals

and solvophobic interactions among the alkyl chains of **12** and thereby yielding larger ribbon-like assemblies.

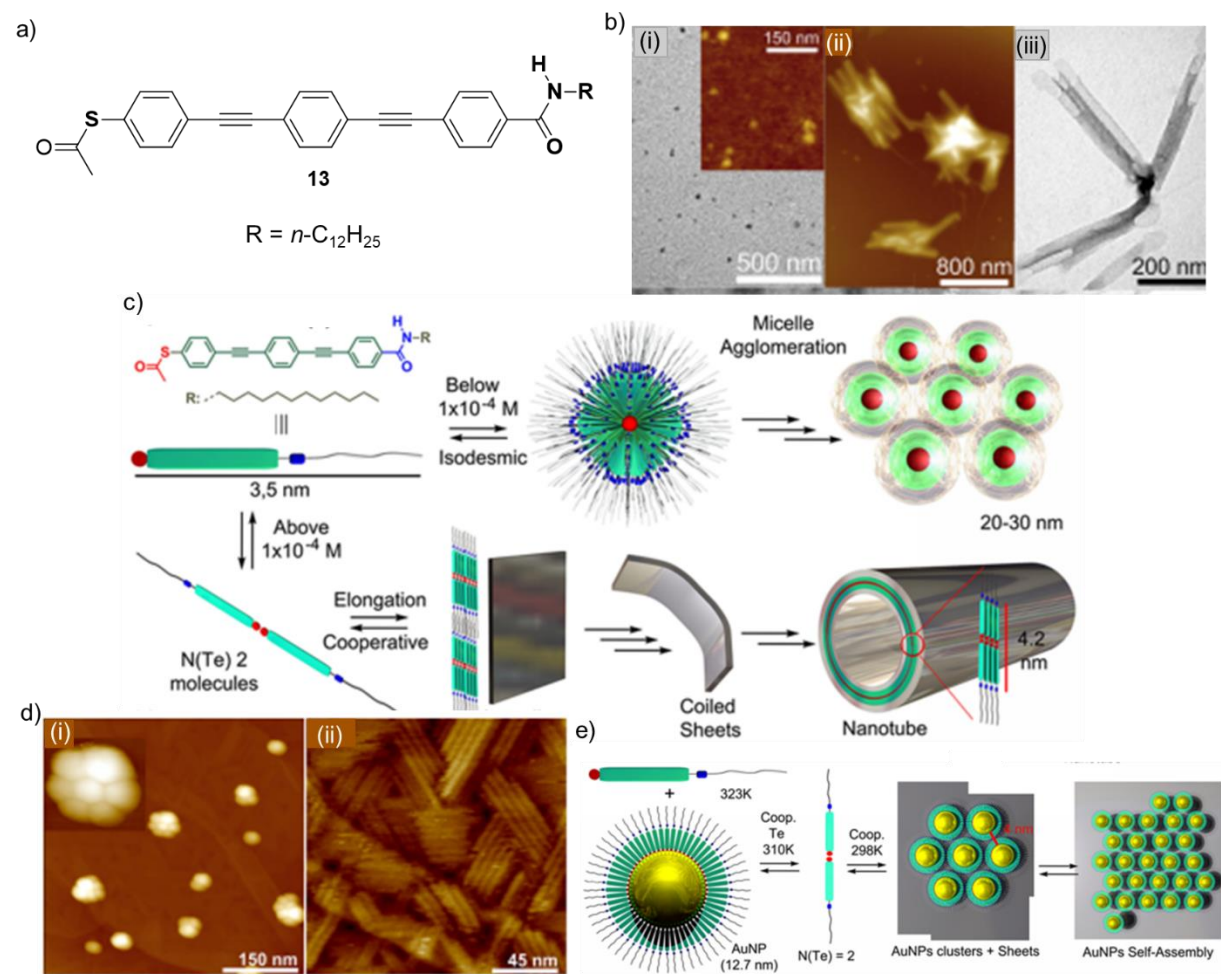


**Figure 1.11.** (a) Chemical structure of unsymmetrically substituted, thiolated PE derivative **13**. (b) (i) TEM and (i, inset) AFM images of **13** in MCH/THF (75:25) at a concentration of  $7 \times 10^{-5}$  M. (ii) AFM and (iii) TEM images of **13** in MCH/THF (75:25) at a concentration of  $1 \times 10^{-4}$  M. (c) Schematic representation for the hierarchical self-assembly of **13** in MCH/THF (75:25) mixture at various concentrations. (d) AFM images of a mixture of **13** ( $1.4 \times 10^{-4}$  M) and PE-AuNPs showing the initial stages of the thiolated PE triggered AuNPs self-assembly, where small AuNPs nuclei are embedded within lamellar structures. (e) Schematic representation showing the impact of cooperative self-assembly of **13** on AuNPs cooperative self-assembly. (Adapted with permission from ref 34).

Transfer of cooperative self-assembly from hierarchical supramolecular polymers of a thiolated  $\pi$ -conjugated PE (**13**) to AuNPs in nonpolar media has been

shown by Fernández, Martínez and co-workers (**Figure 1.11a**).<sup>[34]</sup> The molecule **13** exhibited concentration-dependent distinct self-assembly behavior in a mixture of (75:25) MCH/THF (**Figure 1.11b(i)**). The cooling of a hot monomeric solution of **13** below a critical concentration of  $1 \times 10^{-4}$  M resulted in spherical aggregates in which the polar thioacetate groups are shielded from the nonpolar environment. However, when the concentration of **13** is raised above  $1 \times 10^{-4}$  M, the self-assembly process followed a cooperative pathway, resulting in considerably larger and ordered 1D assemblies, as observed by AFM and TEM analyses (**Figure 1.11b(ii and iii)**). Furthermore, the hollow interior of 1D structures confirms the nanotubular morphology of **13** (**Figure 1.11b**). **Figure 1.11c** shows the difference in the concentration-dependent molecular arrangement of **13**, leading to distinct morphological features. The self-assembled hierarchical structure of **13** could be transferred to the surface of AuNPs having an average diameter of  $12.7 \pm 1.2$  nm through Au-S bonding. The modified AuNPs (PE-AuNPs) were found to have negligible propensity to aggregate in the same MCH/THF 75:25 mixture even at high concentration ( $\sim 1 \times 10^{-7}$  M) and low temperature (273 K). When **13** and PE-AuNPs were mixed to reach a final concentration of  $7 \times 10^{-5}$  and  $1 \times 10^{-9}$  M, the noncooperative self-assembly behavior of **13** did not suffice aggregation of PE-AuNPs and disintegrated the assemblies. However, the behavior of the system turned out to be completely different when the concentration of **13** was increased to  $1.4 \times 10^{-4}$  M and that of PE-AuNPs to  $3.5 \times 10^{-9}$  M. Upon decreasing the temperature of the mixture from 323 to 273 K, a distinct color change from red to purple along with a red-shifted absorption of localized surface plasmon resonance band for AuNPs was noticed,

signifying aggregation of AuNPs while following a cooperative model. Typical AFM images of the co-assembly of **13** and PE-AuNPs reveal small AuNPs clusters formed by the agglomeration of ~3-8 nanocrystals (**Figure 1.11d(i)**). Furthermore, sheet-like lamellar structures were also found to coexist in addition to AuNP clusters (**Figure 1.11d(ii)**), which suggests that the layers of the molecules grow in the presence of AuNPs through a combination of weak H-bonding involving the thioacetate groups, alkyl chain packing involved between the face-to-face molecules present in different layers, simultaneous  $\pi$ - $\pi$  interactions of the aromatic fragments and even by H-bonding operating between the amide bonds within the same layer; leading to a drastic change in the structure from nanotubes to planar sheets (**Figure 1.11e**).

### 1.5.2. Long PEs (Containing Five or More Phenyl Rings)

Our research group has reported the effect of  $\pi$ -repeating units of PE on gelation and morphological properties.<sup>[35]</sup> For this purpose, a series of PE-based gelators with varying repeating units from 3 to 7 (**6**, **14** and **15**) were synthesized and studied their aggregation behavior in nonpolar solvents (**Figure 1.12a**). All the molecules formed fluorescent gels at low critical gelator concentrations (0.6 (**6**), 0.45 (**14**) and 0.34 wt% (**15**)) and exhibited blue, green and greenish-yellow emission, respectively (**Figure 1.12b**). Detailed studies revealed that the conjugation length of the molecules could influence the interactions between the molecules and between the molecule and the substrate. For instance, at lower concentrations in *n*-decane ( $1 \times 10^{-5}$  M), the molecule **6** self-assembled to form vesicles, whereas self-assembly of **14** and **15** led to the formation of micrometer-sized long fibers having an average width of 50 and 30 nm, respectively (**Figure 1.12c**).

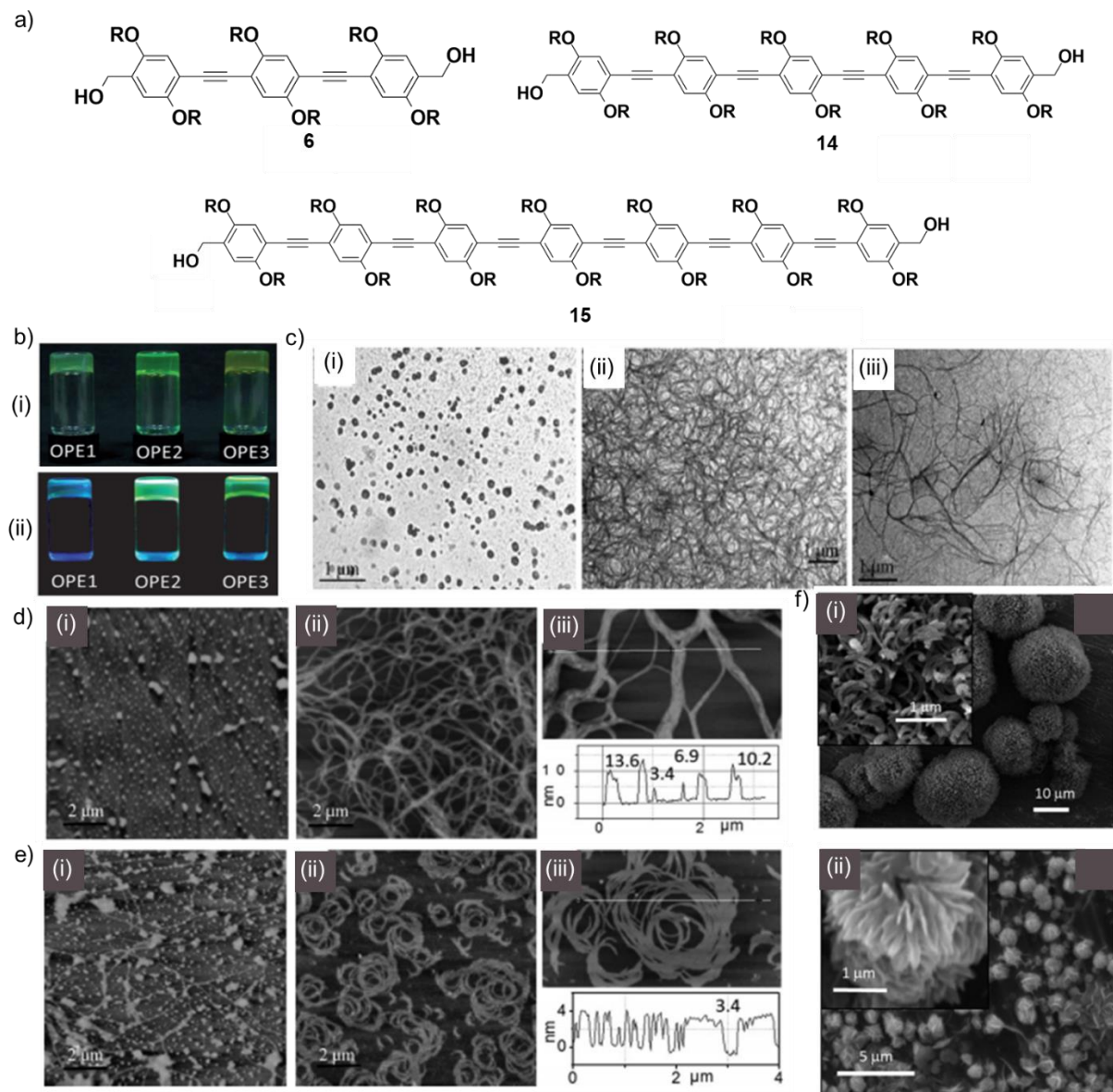


**Figure 1.12.** (a) Chemical structures of the PEs **6**, **14** and **15**. (b) Photographs of the *n*-decane gels under (i) normal light and (ii) UV light. (c) TEM images of (i) **6**, (ii) **14**, and (iii) **15** ( $1 \times 10^{-5}$  M). AFM images of (d) **14** and (e) **15** (*n*-decane,  $1 \times 10^{-5}$  M) on (i) silicon wafer and (ii) mica surface. (iii) Zoomed-in images show the corresponding cross-sectional analysis across the white line drawn. (f) SEM images of (i) **6** and (ii) **14** (at the CGC) on silicon-wafer surfaces under dry conditions ( $< 30\%$  humidity). The fine structures were obtained from the magnified images shown in the insets. (Adapted with permission from ref 35).

Silicon wafer is known to suppress the substrate-molecule interaction, whereas mica surface leads to a more facile interaction with the molecules. The PE molecule **14**

formed smaller nanoparticles over the silicon wafer, whereas entangled fibers were obtained over the mica surface (**Figure 1.12d**). On the other hand, both particles and fiber morphologies were obtained for **15** over the silicon wafer and spiral morphology was obtained over the mica surface (**Figure 1.12e**). The latter observation indicates an epitaxy-driven process that exhibits a strong interaction between **15** and the mica surface. Increasing the concentration of **15** in *n*-decane to  $1 \times 10^{-4}$  M led to the formation of elongated fibers irrespective of the substrates. Furthermore, at higher concentrations, **6** and **14** (or **15**) resulted in the formation of spherical agglomerates of curved super-bundles of fibers and flowerlike short-fiber agglomerates under dry conditions with less than 30% humidity (**Figure 1.12f**). All these results confirm that the increase in the  $\pi$ -conjugation length (from **6**, **14** to **15**) can result in a variety of exotic self-assembled structures and whose formation can be controlled by varying the nature of the substrate, concentration, and humidity.

The helicity of the supramolecular assemblies of azobenzene appended PE derivatives, (*S*)-**16** and (*R*)-**17**, can be reversibly biased to an opposite helicity upon controlled photoisomerization of the azobenzene moiety (**Figure 1.13**).<sup>[36]</sup> Chiral molecules (*S*)-**16** and (*R*)-**17** exhibited absorption features characteristic of monomers in THF ( $1 \times 10^{-5}$  M,  $\lambda_{\text{max}} = 324, 419$  nm). However, the presence of the red-shifted absorption band at 440 nm along with a shoulder band at 480 nm confirms the aggregation behavior of (*S*)-**16** and (*R*)-**17** in MCH. Upon UV light irradiation ( $\lambda = 350 \pm 30$  nm) of an MCH solution at 323 K, *trans* (*S*)-**16** containing azobenzene (*E,E*) isomer



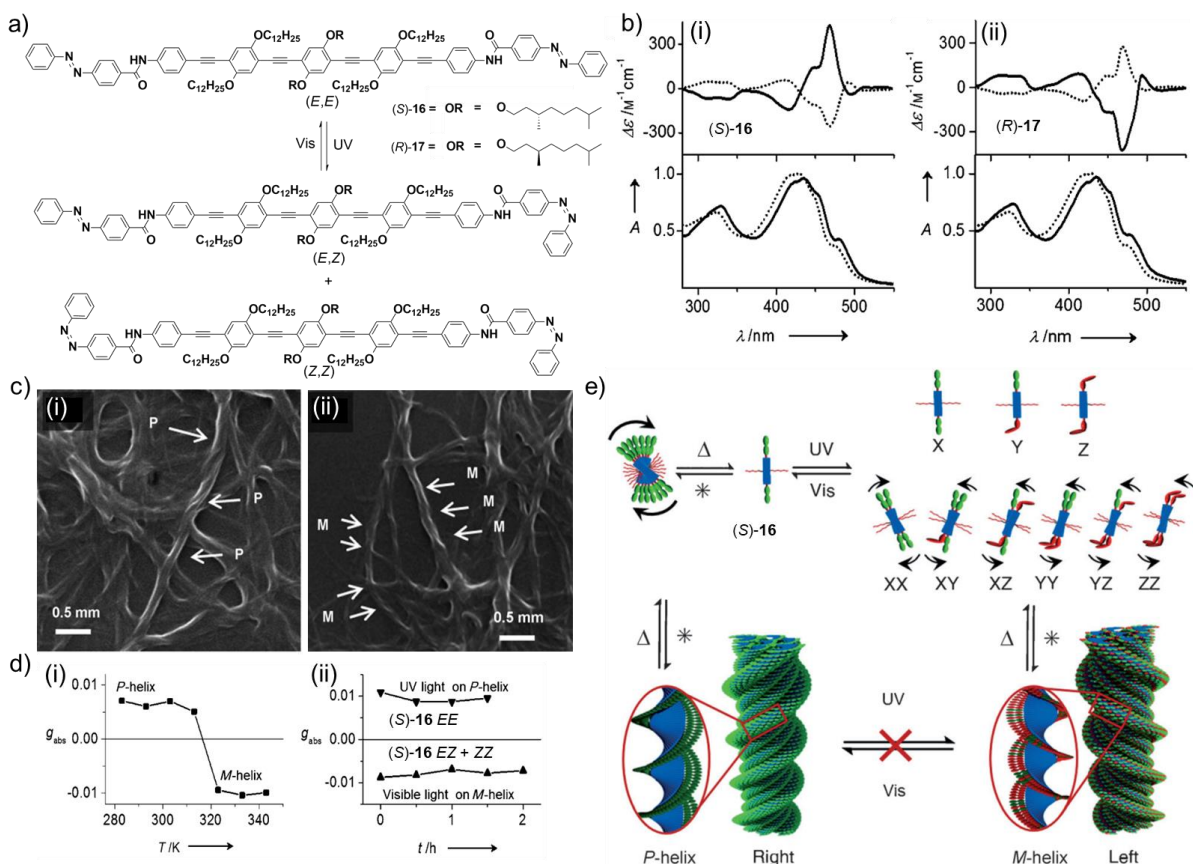


**Figure 1.13.** (a) Photoisomerization of the azobenzene-linked PE derivatives (S)-16 and (R)-17. A mixture of possible isomers (E,E; E,Z and Z,Z) have been shown. (b) CD spectra (top) and the corresponding UV-vis absorption spectra (bottom) for (i) (S)-16 and (ii) (R)-17 before (black) and after (grey) UV irradiation at 273 K. (c) SEM images obtained for (S)-16; (i) before and (ii) after photoisomerization. (d) Evidence for the helicity inversion. (i) Change in  $g_{\text{abs}}$  for (S)-16 as a function of heating, UV irradiation (350 nm), and followed by cooling at a controlled rate. Each point shown in the plot was obtained by irradiating at 350 nm at the specified temperature, followed by cooling. The reversal of the CD signal has been noticed only when UV light irradiation was carried out above 313 K. (ii) Plot of  $g_{\text{abs}}$  versus time for both the P- and M-helices under UV and visible light irradiation, respectively, in the absence of heating. (e) Schematic representation shows the probable helicity inversion mechanism, where direct light-induced conversion of the helix handedness is not possible in the absence of heating ( $\Delta$  = heating;  $*$  = cooling). (Adapted with permission from ref 36).

was converted to the *cis* form; mostly containing (E,Z or Z,Z) isomers (**Figure 1.13a**).

The process was found reversible upon visible light irradiation and even by keeping the system to a relatively higher temperature. The CD spectrum of (S)-16 aggregates



exhibited an intense positive signal at 464 nm along with two negative signals at 407 and 322 nm having a zero cross-over point at 421 nm (**Figure 1.13b(i)**, top), which almost matches with its absorption maximum (**Figure 1.13b**, bottom). Interestingly, UV irradiation at 323 K, followed by cooling the solution to room temperature, showed a complete reversal of the CD spectrum with slightly lower intensity of the bands. On the other hand, an opposite nature in the CD spectrum was noticed for (*R*)-**17** aggregates before and after photoirradiation (**Figure 1.13b(ii)**). SEM analysis of (*S*)-**16** aggregates before photoirradiation showed the formation of micrometer-sized right-handed *P*-type helical ropes having diameters ranging from 50 nm to 1  $\mu$ m (**Figure 1.13c(i)**). Remarkably, UV irradiation of (*S*)-**16** above its  $T_e$  followed by gradual cooling resulted in the formation of left-handed *M*-type helical assemblies as confirmed from the SEM image (**Figure 1.13c(ii)**), which is in accordance with that of the nature of the CD spectrum. **Figure 1.13d(i)** shows that the reversal of helicity is only possible upon photoirradiating MCH solution of (*S*)-**16** around 313 K or above, followed by their subsequent reassembly upon cooling. However, in the absence of heating, helicity inversion did not occur even after prolonged photoirradiation for several hours (**Figure 1.13d(ii)**). This work demonstrates that the handedness of photoresponsive supramolecular helical structures can be biased by simultaneous action of both light and heat (above a critical temperature  $T$ ), while retaining the inherent molecular chirality of the individual building blocks (**Figure 1.13e**).

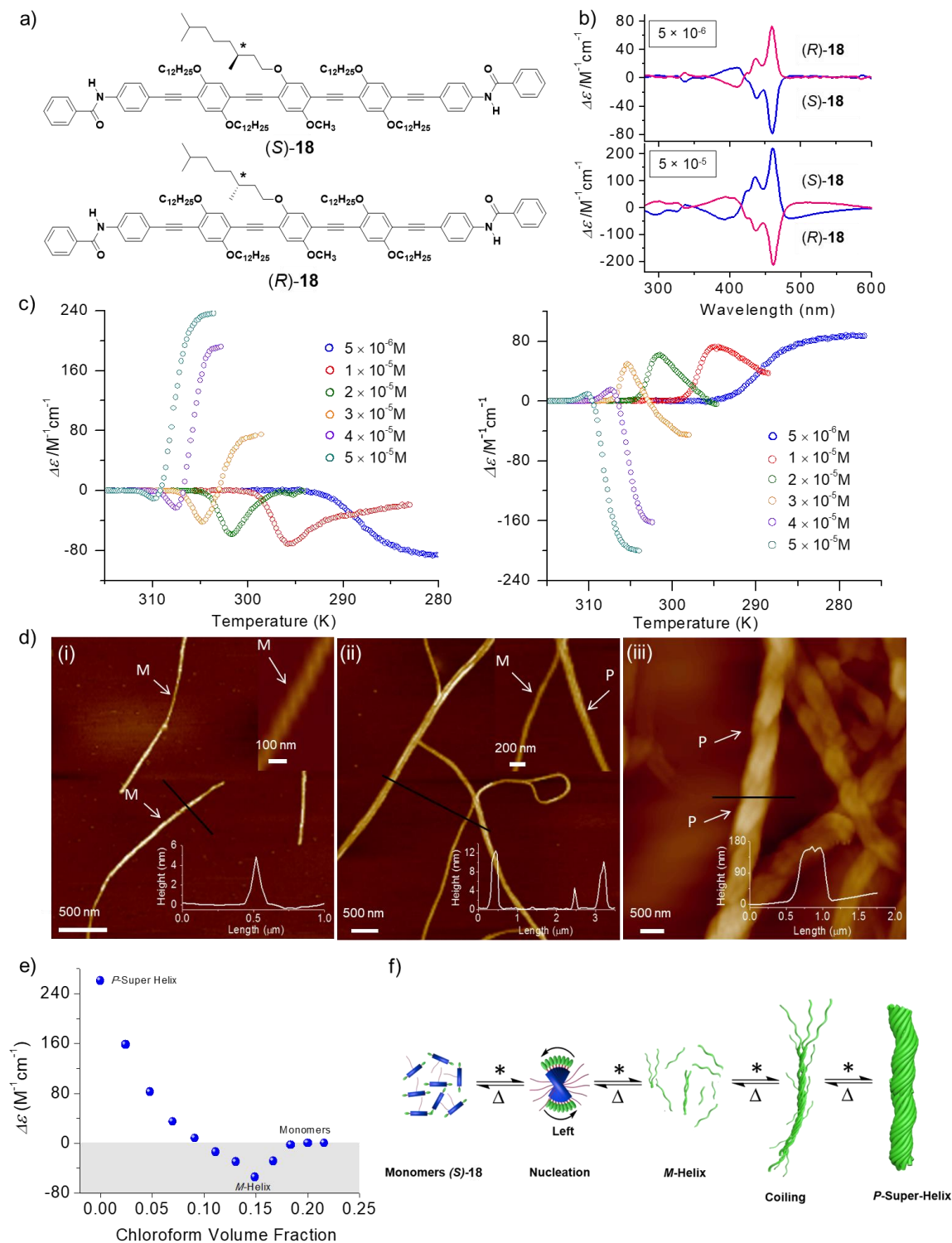


**Figure 1.14.** (a) Molecular structures of (S)-18 and (R)-18. (b) CD Spectra of (S)-18 (blue) and (R)-18 (magenta) at various concentrations in *n*-decane:  $5 \times 10^{-6}$  M (upper panel) and  $5 \times 10^{-5}$  M (lower panel). (c) Variations in CD spectral intensity of (S)-18 and (R)-18 measured at 460 nm upon cooling (1 K/min) *n*-decane solutions at different concentrations. (d) AFM images with height profiles of (S)-18<sub>agg</sub> in *n*-

decane at different concentrations: i)  $5 \times 10^{-6}$  M, ii)  $2 \times 10^{-5}$  M and iii)  $5 \times 10^{-5}$  M, respectively. The insets of i and ii show the zoomed images. The helicity of the fibers has been indicated with arrows in the images. (e) Decoiling of (S)-**18**<sub>agg</sub> ( $5 \times 10^{-5}$  M) formed in *n*-decane by mixing different volume fractions of (S)-**18** in chloroform ( $5 \times 10^{-5}$  M), where the total concentration of the mixture was kept fixed at  $5 \times 10^{-5}$  M. (f) Schematic representation depicting the nucleation-elongation self-assembly pathway leading to the formation of coiled super-helical assemblies of (S)-**18** in *n*-decane. (Adapted with permission from ref 37).

Our research group has unraveled the complex pathway associated with helical to super-helical transformation of a synthetic  $\pi$ -system assembly following a nucleation-elongation mechanism (**Figure 1.14**).<sup>[37]</sup> The aggregation studies of amide functionalized chiral PE derivatives (S)-**18** or (R)-**18** in *n*-decane revealed the concentration-dependent formation of both left- and right-handed helices from the molecule having a specific chiral center. The concentration and temperature-dependent CD analysis of the aggregation pathway showed that the formation of initial helical aggregates (at a lower concentration) is in accordance with the molecular chirality (**Figure 1.14b,c**). Interestingly, an increase in the concentration of (S)-**18** or (R)-**18** leads to coiling of the initially formed helical fibers with an opposite handedness and supersedes the command of the molecular chirality, which is obvious from the concentration-dependent cooling curves (**Figure 1.14b,c**). AFM imaging of (S)-**18** aggregates at different concentrations clearly showed that the initially formed left-handed (*M*-type) helical fibers at lower concentration ( $5 \times 10^{-6}$  M) could undergo coiling ( $2 \times 10^{-5}$  M) followed by the formation of densely coiled helical bundles at higher concentration ( $5 \times 10^{-5}$  M), which confirms the helix to super-helix transition (**Figure 1.14d**). This observation was further confirmed from the solvent-assisted decoiling of the super-helical assemblies, where the *P*-super helix was decoiled to form *M*-fibers and

then to respective monomers through subsequent depolymerization (**Figure 1.14e**). The present system provides a detailed mechanistic insight for a synthetic  $\pi$ -system in explaining the occurrence of both left- and right-handed helical assemblies from the same chiral molecule and can be considered as the reminiscent for the super-helix formation in the case of biopolymers such as proteins (**Figure 1.14f**).

### 1.5.3. Metal Complexes of Linear PEs

Recently, Fernández and co-workers have studied the mechanism for the statistical co-assembly of PE-based dichloro(bis)pyridyl Pd(II) and Pt(II) complexes, **19** and **20** (**Figure 1.15**).<sup>[38]</sup> To enhance the aggregation propensity and ensure the solvent-induced comparable pseudo-parallel arrangement for both the complexes, the self-assembly studies were carried out in *n*-decane, a nonpolar hydrocarbon solvent. A plot of the  $\alpha_{\text{agg}}$  versus temperature revealed non-sigmoidal sharp transitions with  $T_e$  for **19** and **20** ( $5.2 \times 10^{-6}$  M) at 315 and 298 K, respectively (**Figure 1.15c**). However, a 1:1 mixture of **19** and **20** at the same concentration showed a completely different behavior upon cooling from 363 to 273 K with two distinct  $T_e$  values at two different temperature range (308 and 285 K) along with a prominent bathochromic shift in absorption (**Figure 1.15c**, inset), signifying the importance of the presence of Pt(II) monomers in delaying the nucleation event for the Pd(II) complex, characteristic of a co-nucleation event taking place between both the molecules. AFM studies of **19** and **20** revealed the formation of long twisted fibers of several micrometer lengths and discoidal nanostructures, respectively (**Figure 1.15d**(i and ii)). In contrast, the co-assembly of **19** and **20** above

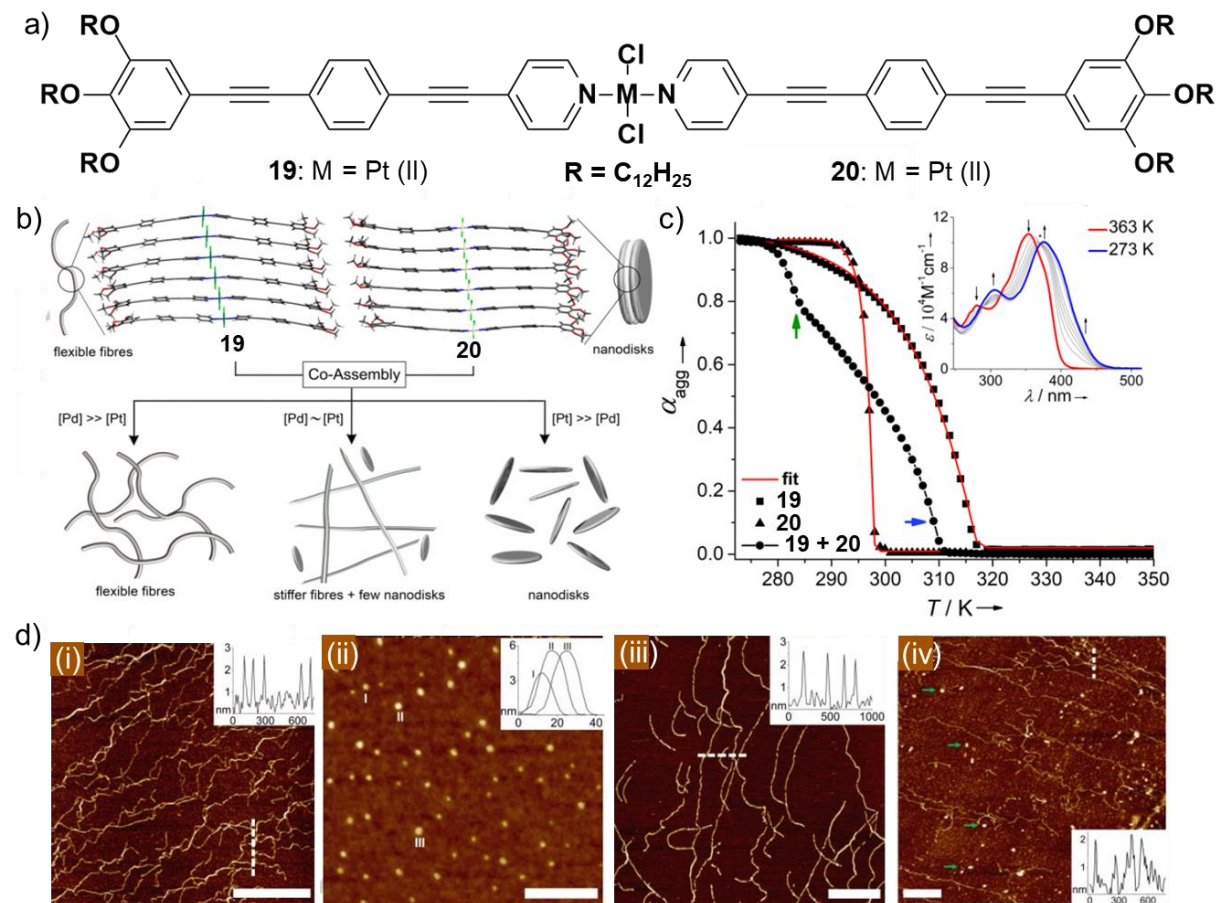


**Figure 1.15.** (a) Molecular structures of PE-based dichloro(bis)pyridyl Pd(II) and Pt(II) complexes **19** and **20**. (b) Schematic representation has been shown for the probable self- and co-assembly processes of **19** and **20** in *n*-decane at different ratios by optimizing their hexameric stacks. (c) Plots of  $\alpha_{agg}$  versus T ( $\lambda = 400$  nm) for **19** (squares), **20** (triangles) and an equimolar mixture of **19** and **20** (circles); the blue and green arrows indicate the  $T_e$  for the mixture of **19** + **20** and the temperature at which the second process begins, respectively. Inset shows the variable temperature UV-vis absorption spectra of the 1:1 mixture of **19** and **20** from 363 to 273 K in *n*-decane (5.2 x 10<sup>-6</sup> M). Black arrows indicate the spectral changes upon cooling and asterisk denotes the isosbestic point. (d) AFM height images of (i) **19**, (ii) **20** at 273 K and (iii) **19** + **20** at 290 K. (iv) AFM image of 4:6 mixture of **19** + **20** showing the coexistence of both fibers and nanodisks at 273 K (nanodisks have been marked with green arrows). Insets show the cross-section analysis corresponding to the white-dashed line shown in the AFM image. (Adapted with permission from ref 38).

second  $T_e$  (285 K) showed the formation of only fibers with no discoidal structures, which indicated a social self-sorting dictated by **19** (Figure 1.15d(iii)).

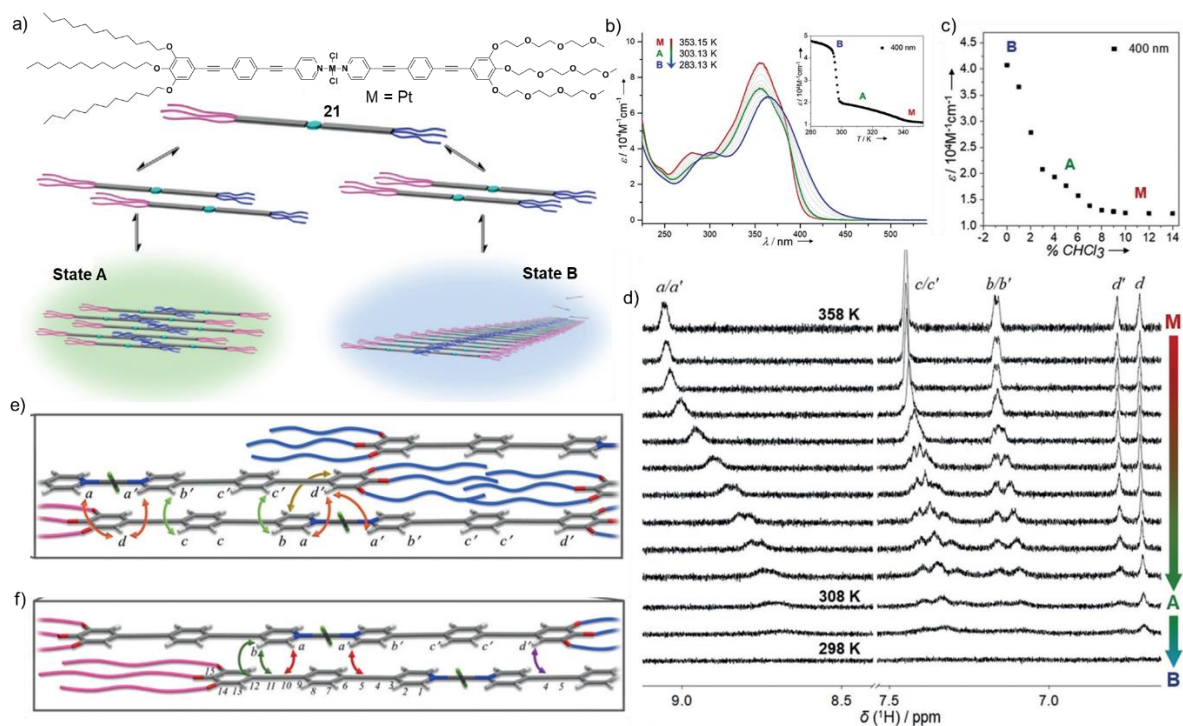


**Figure 1.16.** (a) Chemical structure of **21** and the schematic representation for the self-assembly pathways leading to different aggregate states **A** and **B**. (b) Temperature-dependent (353 to 283 K) UV-vis spectra of **21** at  $3 \times 10^{-4}$  M in MCH at a cooling rate of 0.2 K/min. Inset shows the plot between the extinction coefficient ( $\lambda = 400$  nm) as a function of temperature. (c) The plot of the extinction coefficient ( $\lambda = 400$  nm) as a function of the volume fraction of  $\text{CHCl}_3$  in MCH ( $3 \times 10^{-4}$  M) at 298 K. (d) Temperature-dependent  $^1\text{H}$  NMR spectra of **21** in  $\text{MCH-d}_{14}$  from 358 to 298 K. The double-strand arrangement shows slipped zigzag packing and less pronounced translational displacement between the molecules in forming (e) state **A** and (f) state **B**, respectively. (Adapted with permission from ref 39).

Further lowering in temperature to 273 K resulted in the self-organization of the remaining unassembled Pt(II) monomers rather than forming co-assembly with **19**. This observation was further confirmed from the AFM studies, which revealed a mixture of fibers and nanodisks (**Figure 1.15d(iv)**). When the composition of a particular monomer is 90% within the co-assembly, the resultant co-assembly characteristics were almost identical to that of the individual complexes (**Figure 1.15b**). In sharp contrast, without any significant excess of either component within the co-assembly (having a ratio of 3:7

or 4:6) closely resembled the characteristics of the equimolar mixture, exhibiting a two-step cooling curve along with the coexistence of both types of the aggregates (**Figure 1.15d(iv)**).

Fernández and co-workers have utilized the immiscibility of triethylene glycol (TEG) and alkoxy side chains and their steric effects as a method for controlling the anti-cooperative aggregation pathways to obtain small-sized assemblies selectively (**Figure 1.16**).<sup>[39]</sup> For this purpose, the self-assembly behavior of a linear PE-based amphiphilic Pt(II) complex **21** unsymmetrically substituted with TEG and dodecyloxy side chains was investigated in MCH, which revealed two competing anti-cooperative and cooperative pathways with the distinct molecular arrangement (long- vs. medium-slipped, respectively) and nanoscale morphology (discs vs. fibers, respectively) (**Figure 1.16a**). Aggregate **A** was obtained by the cooling of the hot monomeric solution of **21** from 353 to 303 K, showed a decrease in the intensity of absorption maximum with a concomitant increase in the shoulder band between 390-420 nm as a result of weak coupling between the  $\pi$ -units (**Figure 1.16b**). On the other hand, further reduction in temperature to 283 K led to pronounced broadening in the absorption spectra with 8 nm red-shift in  $\lambda_{\max}$ , suggesting the formation of translationally displaced  $\pi$ -stacks for aggregate **B** (**Figure 1.16b**). Following a controlled cooling process, aggregate **A** can be obtained within a particular temperature range before forming aggregate **B** and hence not stable at room temperature (**Figure 1.16b**, inset). However, aggregate **A** can be obtained selectively upon addition of 4-6% of  $\text{CHCl}_3$  to the aggregate **B** formed in MCH, while maintaining a total concentration of  $3 \times 10^{-4}$  M, which was found stable for several

months without converting to the more stable aggregate **B** or any other form (**Figure 1.16c**). The gradual transformation from the monomer of **21** to aggregate **A** and then to **B** also confirmed from the temperature-dependent  $^1\text{H}$  NMR studies, where a gradual shielding in the aromatic  $^1\text{H}$  signals was noticed (**Figure 1.16d**). The modes of intermolecular interaction for both the aggregates were elucidated with the help of 2D  $^1\text{H}\{^1\text{H}\}$  Rotating-frame Overhauser effect spectroscopy (ROESY), and solid-state NMR spectroscopy experiments as shown in **Figure 1.16e,f**. Furthermore, with the help of mathematical simulations of the UV-vis spectroscopy cooling curves using a coupled, two-pathway equilibrium model, it can be rationalized that the initial buffering of the molecular building blocks leads to anti-cooperative discoidal nanoparticles before the onset of the formation of cooperative 1D supramolecular polymers.

Concomitant packing polymorphism of supramolecular polymers has been unraveled using a  $\pi$ -conjugated Pt(II) complex **22** that self-assembles in MCH into two competing supramolecular polymers with distinct molecular packing such as slipped (**A**) versus pseudoparallel (**B**) arrangement (**Figure 1.17**).<sup>[40]</sup> Precise control over temperature, concentration, and the cooling rate of the self-assembly process enabled understanding the formation of both types of aggregates and their stability selectively (**Figure 1.17a-d**). As inferred from the phase diagram, higher concentration and slow cooling rates favor the pseudoparallel arrangement of the monomers to form the state **B** following an isodesmic mechanism (**Figure 1.17b,c**). In contrast, lower concentrations



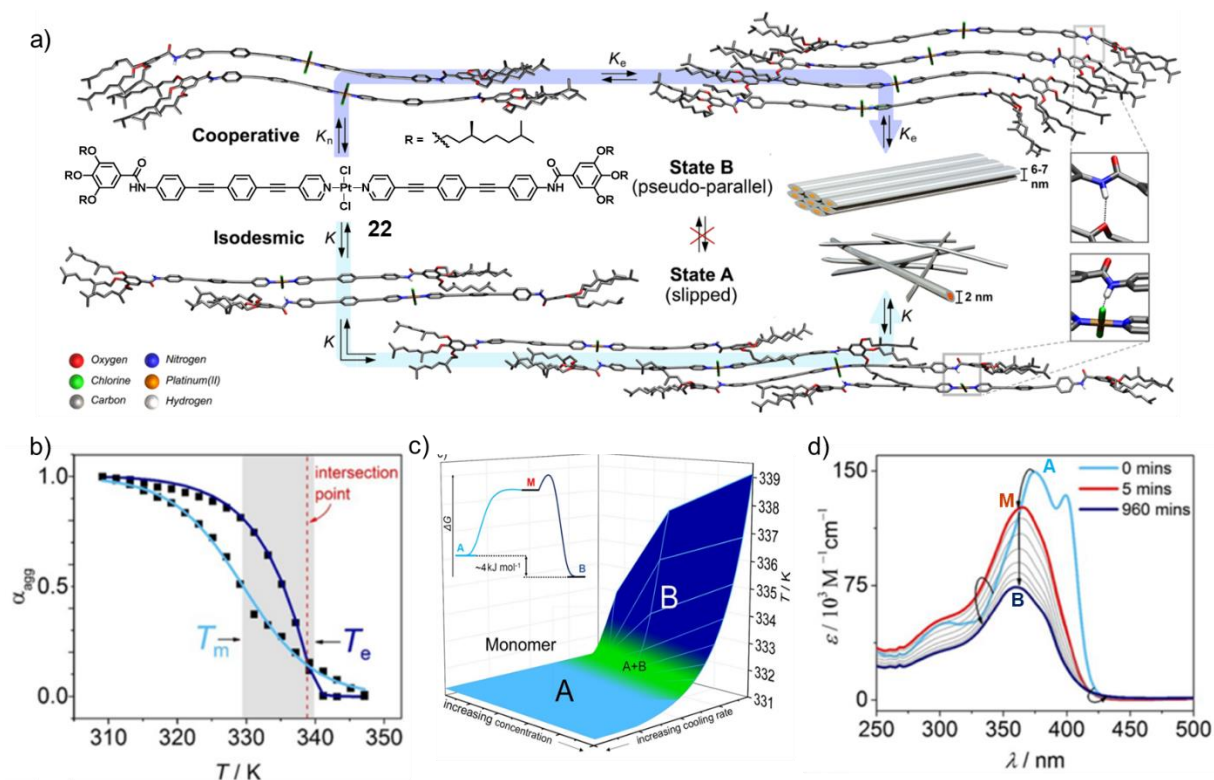


**Figure 1.17.** (a) Chemical structure of **22** and the corresponding theoretical studies depicting the concomitant supramolecular polymerization. (b) Cooling curves of **22** ( $7.5 \times 10^{-6}$  M) obtained by following a controlled rate of 2 K/min (isodesmic fit, cyan color) and 0.1 K/min (cooperative fit, royal blue color) forming aggregate **A** and **B**, respectively. (c) Phase diagram showing the competitive self-assembly behavior of **22** with respect to concentration and cooling rates. Inset shows the corresponding energy landscape diagram for the formation pathways of **A** and **B**. (d) Time-dependent changes in the UV-vis absorption spectra of **22** ( $7.5 \times 10^{-6}$  M) at 337 K showing the transformation from **A** to **B** through formation of monomer **22** (Adapted with permission from ref 40).

and faster cooling rates preferentially favor the slipped arrangement of monomers to form the state **A** via a nucleation-elongation mechanism (Figure 1.17b,c). Based on the spectroscopy studies and theoretical calculations, an unconventional N-H $\cdots$ Cl-Pt and N-H $\cdots$ O alkyl interactions has been found preferable for the stability of the supramolecular polymorphs **A** and **B**, respectively. Kinetic UV-vis studies show that both aggregates are non-interconvertible and stable for a period of at least six months at

room temperature, revealing the narrow energy distribution between the aggregates. However, upon annealing **A** at a temperature between the critical temperatures for the formation pathways of **A** and **B** (337 K, **Figure 1.17b**) for a prolonged time, a slow transformation of **A** into **B** takes place via monomer formation, which is considered to have a close resemblance to concomitant packing polymorphism as seen in the case of the crystals (**Figure 1.17d**). Furthermore, the formation of distinct aggregates has also been confirmed from the AFM studies, which exhibit flexible thin fibers and more rigid, thick bundles of fibers for **A** and **B**, respectively.

## 1.6. Triangular PEs

### 1.6.1. Mechanistic Details and Amplification of Chirality Effect in Supramolecular Polymerization

Cooperative supramolecular polymerization and amplification of chirality effect in the case of  $C_3$ -symmetrical PE-based trisamides **23** and (*S/R*)-**24** have been reported by Sánchez and co-workers (**Figure 1.18**).<sup>[41]</sup> Temperature-dependent UV-vis absorption and  $^1\text{H}$  NMR spectral studies confirmed the supramolecular polymerization of the  $C_3$ -symmetrical PE-monomers in MCH (**Figure 1.18b**) via a triple array of amide H-bonding reinforced  $\pi$ - $\pi$  interaction. These trisamides were found to follow a cooperative self-assembly process as confirmed by fitting the plot of the  $\alpha_{\text{agg}}$  versus temperature (**Figure 1.18b**, inset). The enantiomeric chiral chain appended PEs, (*S*)-**24** and (*R*)-**24** displayed mirror image CD signals corresponding to an assembly having opposite supramolecular helicity (**Figure 1.18c**). Based on the theoretical calculations and

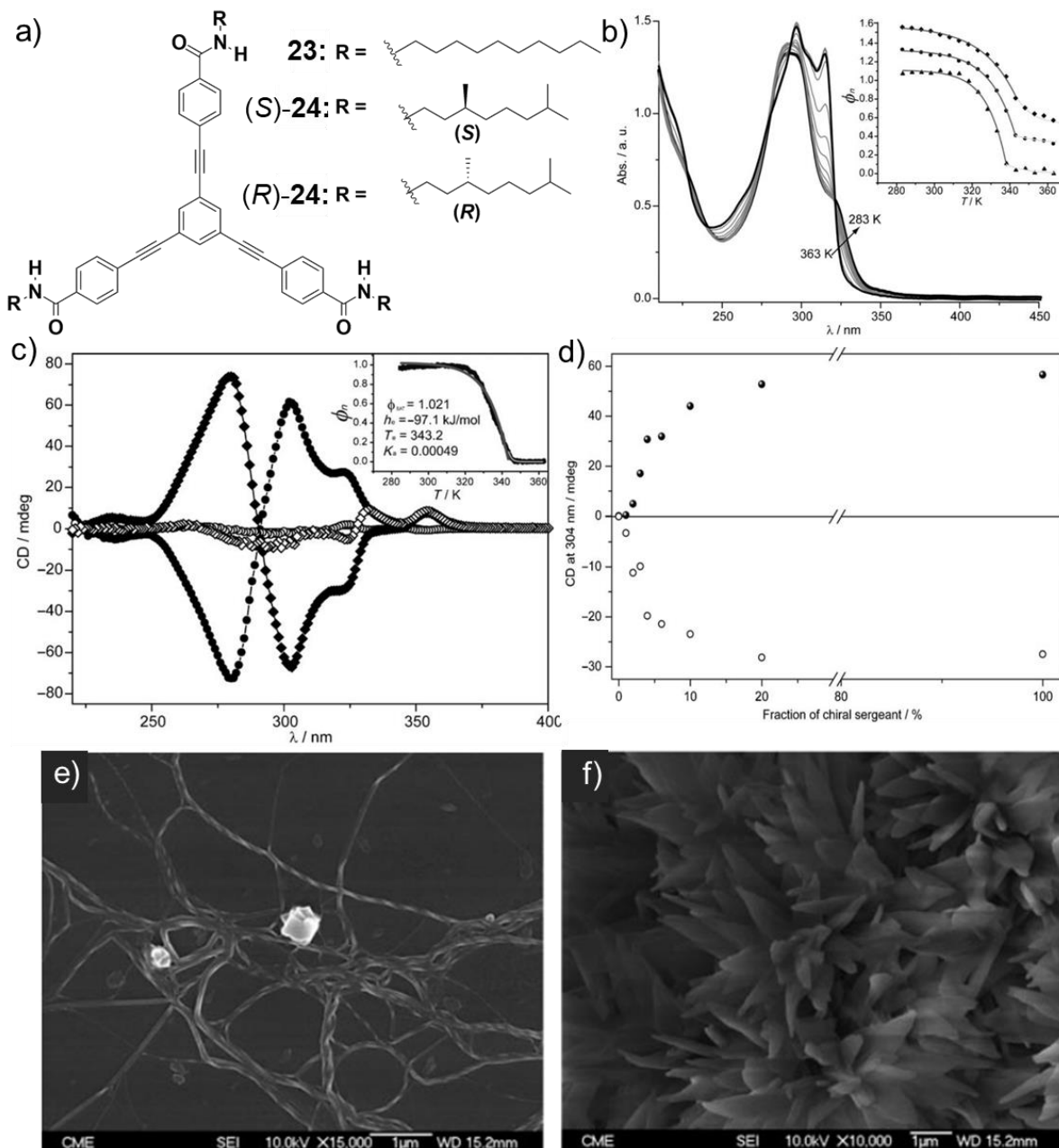


**Figure 1.18.** (a) Molecular structures of  $C_3$ -symmetric PE-based trisamides **23**, **(S)-24** and **(R)-24**. (b) Temperature-dependent UV-vis absorption spectra of **23** in MCH from 363 to 283 K ( $1 \times 10^{-5}$  M). Inset shows the plot between  $\alpha_{agg}$  versus temperature fitted within elongation (dark grey) and nucleation (light grey) regimes. (c) CD spectra of **(S)-24** ( $1 \times 10^{-5}$  M) ( $\blacklozenge$  at 298 K and  $\diamond$  at 363 K), and of **(R)-24** ( $1.5 \times 10^{-5}$  M) ( $\bullet$  at 298 K and  $\circ$  at 363 K) in MCH. Inset shows the melting curve of **(S)-24**. (d) Amplification of CD response for **23** in MCH (298 K,  $1 \times 10^{-5}$  M) upon mixing with **(S)-24** (top) and **(R)-24** (bottom). SEM images of (e) **(S)-24** and (f) **(R)-24**. (Adapted with permission from ref 41).

experimental results, the importance of various structural factors such as the role of chiral substituents in increasing the degree of cooperativity, the extension of the  $\pi$ -framework in favoring the activation step and also the presence of directional non-covalent forces like H-bonding in exhibiting significant cooperativity, has been elucidated. **Figure 1.18d** shows a non-linear relationship between the chiroptical response and the fraction of chiral sergeant (*S* or *R*)-**24**. This observation demonstrates that the homochirality of the monomers of **23** (soldiers) is manifested as strongly amplified CD signals upon co-assembly of the chiral molecules (*S*)-**24** and (*R*)-**24** with **23**. Interestingly, SEM studies revealed that (*S*)-**24** and (*R*)-**24** can exhibit supramolecular polymorphism, forming globular and flower-like structures, respectively (**Figure 1.18e,f**).

Solvent-dependent disassembly of amphiphilic PE-based tricarboxamides has been reported by Sánchez and co-workers (**Figure 1.19**).<sup>[42]</sup> For this purpose, a series of  $C_3$ -symmetric PEs (**25-27**) endowed with many ethylene oxide chains was synthesized, where the amide groups are isolated from the peripheral glycol chains through paraffinic linkers (**Figure 1.19a**). The self-assembly of these molecules in nonpolar solvents like MCH was found to be columnar and mainly driven by the formation of a triple array of N-H $\cdots$ O=C intermolecular H-bonds as confirmed from the NMR studies of **27** (**Figure 1.19b**). However, the gradual addition of water breaks the amide H-bonding, which induces aggregation through the solvophobic effect involving strong  $\pi$ -stacking between the aromatic PE chromophores (**Figure 1.19b**). It is interesting to note that five times

higher amount of water was needed to break the entire amide H-bonds of **27** compared to **25**, indicating a significant enhancement in the stability of the aggregates with more

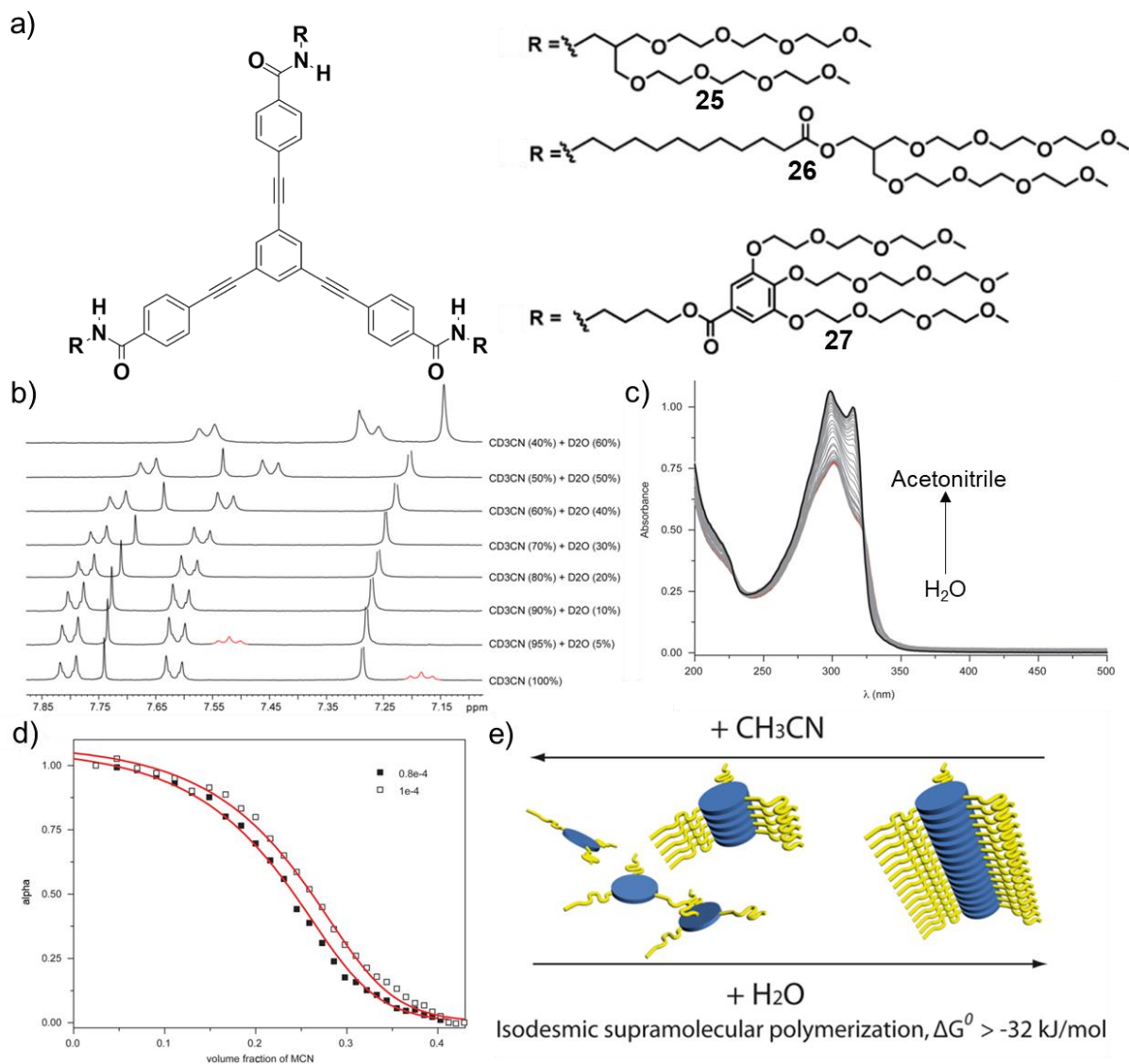


**Figure 1.19.** (a) Molecular structures of the  $C_3$ -symmetric PE-based tricarboxamides **25-27**. (b) Partial  $^1\text{H}$  NMR (300 MHz, 298 K,  $2 \times 10^{-3}$  M) spectra of the compound **27** at various ratios of  $\text{CD}_3\text{CN}/\text{D}_2\text{O}$ . (c) Unfolding of the aggregates of **25** formed in the aqueous medium upon increasing acetonitrile fraction ( $1 \times 10^{-4}$  M). (d) Denaturation curves of **25** fitted to the equilibrium model, which follows an isodesmic supramolecular polymerization. (e) Schematic representation for the solvent-dependent assembly-disassembly process. (Adapted with permission from ref 42).

numbers of glycol chains and larger paraffinic linkage. The stability of the aggregates was then quantified using the folding-unfolding model for the disassembly of supramolecular polymers in mixtures of good (acetonitrile) and poor (water) solvents, which exhibited a gradual change from aggregated to monomeric absorption feature (**Figure 1.19c**). The plot of volume fraction of acetonitrile in water against  $\alpha_{\text{agg}}$  clearly showed that the disassembly of aqueous aggregates follows an isodesmic supramolecular polymerization mechanism with calculated Gibbs free energy of -31.26 and -36.79 kJ/mol for **25** and **27**, respectively (**Figure 1.19d**). On the contrary, calculation of thermodynamic parameters for **26** was not possible because of the presence of a very long paraffinic linkage leading to scarce solubility of **26** in the aqueous medium. The solvent-dependent folding-unfolding mechanism has been schematically represented in **Figure 1.19e**.

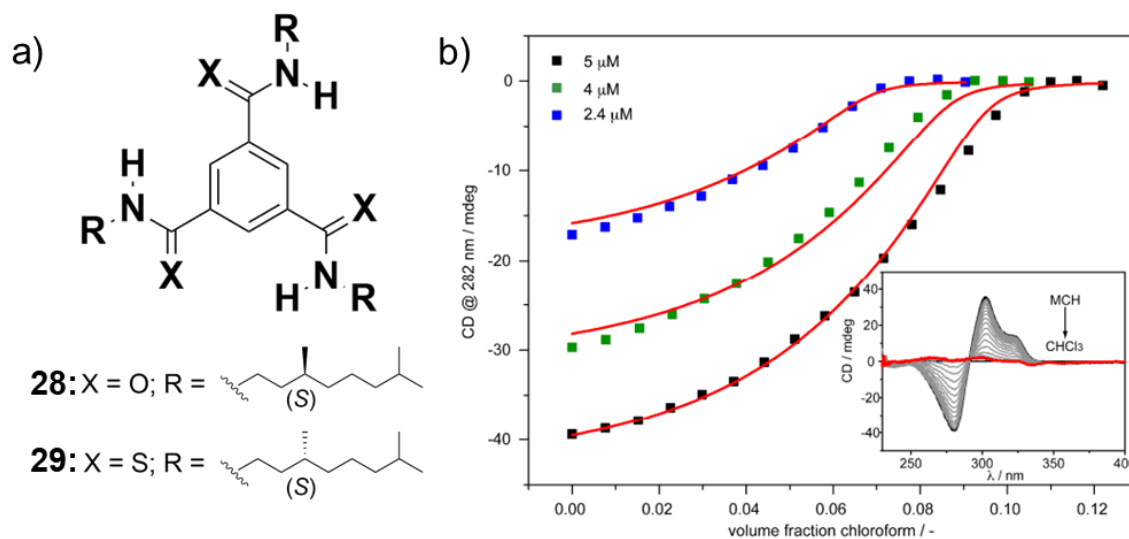


**Figure 1.20.** Chemical structures of the  $C_3$ -symmetric (a) *N*-alkylated benzenetricarboxamides **28,29**. (b) Denaturation curves were obtained for (S)-**24** in MCH/CHCl<sub>3</sub> mixtures at different concentrations. The black lines represent the fitting. Inset shows the CD spectra of the chiral (S)-**24** in MCH/CHCl<sub>3</sub> mixtures ( $5 \times 10^{-6}$  M, 293 K). (Adapted with permission from Ref 43).

Palmans, Sánchez and co-workers have investigated the influence of the extended  $\pi$ -conjugated core over the self-assembly behavior of  $C_3$ -symmetrical systems (**Figure 1.20**).<sup>[43]</sup> For this purpose, various  $C_3$ -symmetric PE tricarboxamides **23**, (*S/R*)-**24** (**OPE-TA**) having an elongated  $\pi$ -core and *N*-alkylated benzenetricarboxamides **28** and **29** (**BTA**) devoid of extended conjugation were synthesized (**Figure 1.20a**). Temperature-dependent cooling experiments related to the formation of supramolecular polymers exhibited almost identical thermodynamic parameter values for both **OPE-TAs** and **BTAs**, signifying their identical stability in nonpolar solvents along with the importance of H-bonding in driving the helical self-assembly process, irrespective of the length of the extended  $\pi$ -core. To further assess the sensitivity of the polymers towards good solvents, the self-assembly behavior of (*S*)-**24** was monitored as a function of the solvent composition, where the ratio of good/poor solvent was varied (**Figure 1.20b**). Titration of small aliquots of monomeric (*S*)-**24** in  $\text{CHCl}_3$  into a solution of (*S*)-**24** in MCH resulted in a gradual decrease in the cotton effect irrespective of concentration, which eventually confirmed the disassembly process of (*S*)-**24** through a cooperative pathway (**Figure 1.20b**). The same depolymerization experiment was not found suitable in the case of **28** because of the overlap of the  $\text{CHCl}_3$  absorption to that of the absorption of **BTA** core. The *m*-parameter (calculated from the equation:  $\Delta G^{0'}(f) = \Delta G^0 + mf$ ; where  $\Delta G^{0'}(f)$  and  $\Delta G^0$  is the Gibbs free energy of monomer association in the mixture of solvents and only in the pure poor solvent, respectively), demonstrates the ability of the good solvent to associate with the monomer for the destabilization of

the supramolecular polymer. The larger value of  $m$  obtained for **OPE-TA** ( $68.2 \pm 4$  kJ/mol) compared to **BTA** ( $29.0 \pm 3$  kJ/mol) clearly demonstrates a larger destabilizing effect on the extended **OPE-TA** core upon addition of the cosolvent  $\text{CHCl}_3$ , which can impart an effective and spontaneous interaction with the larger  $\pi$ -conjugated surface and thereby weakening the self-assembly process.

Sánchez and co-workers have investigated the self-assembly behavior of triangular-shaped PEs peripherally decorated with chiral and linear paraffinic chains in bulk solution and over the surface (**Figure 1.21a**).<sup>[44]</sup> X-ray diffraction studies for chiral systems displayed a broad reflection at a higher  $2\theta$  value. In contrast, several well-resolved reflections were noticed in the case of **32**, signifying higher crystallinity of the

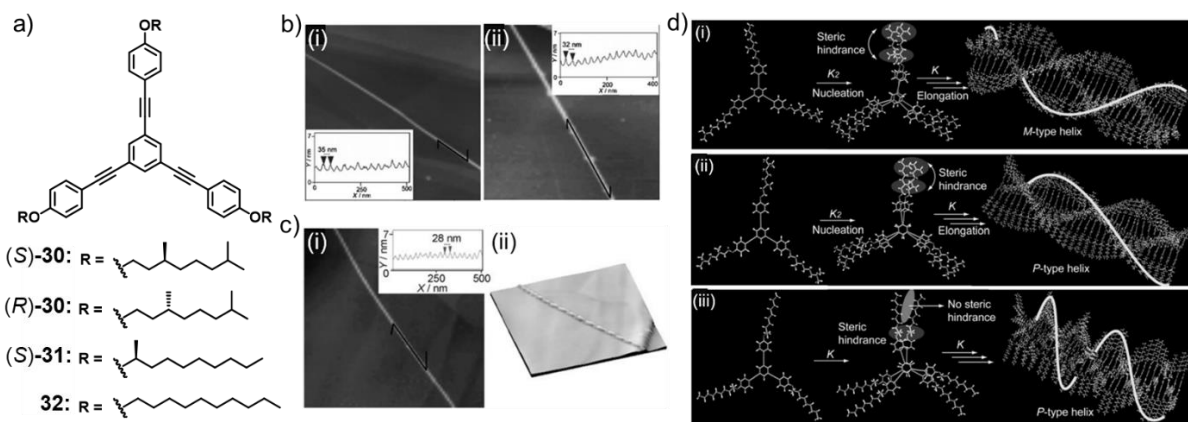


**Figure 1.21.** (a) Molecular structures of triangular OPEs: (S)-30, (R)-30, (S)-31 and 32. (b) AFM images of the aggregates of (i) (S)-30 and (ii) (R)-30 ( $c \sim 10^{-4}$  M) from MCH showing the formation of *M*-type and *P*-type helices, respectively. (c) (i) AFM image and its (ii) 3D view for the aggregates of (S)-31 ( $c \sim 10^{-4}$  M) from MCH, exhibiting *P*-type helix formation. Insets in the figures depict the corresponding height profile and the helical pitch along the black line drawn. (d) Schematic illustration for the self-assembly of (i) (S)-30, (ii) (R)-30 and (iii) (S)-31. The white line shown in the figure depicts the helicity of the aggregates. (Adapted with permission from ref 44).



achiral analog in comparison to that of the chiral systems. (*S*)-**30** and (*R*)-**30** functionalized with (*S*)- and (*R*)-3,7-dimethyloctyloxy chains in MCH were found to transfer their chirality effect to the final supramolecular assemblies, resulting in the formation of *M*-type and *P*-type supramolecular helices, respectively (**Figure 1.21b**). On the other hand, a complete switch in helicity leading to *P*-helix was observed for (*S*)-**2**, decorated with (*S*)-2-methylnonyloxy chains (**Figure 1.21c**). As shown in **Figure 1.21d**, the observed difference in the supramolecular helicity despite identical stereoconfiguration for the stereogenic carbons of (*S/R*)-**30** and (*S*)-**31** can be rationalized. The change in the helicity implies that all the peripheral chiral wedges in (*R*)-**30** (**Figure 1.21d(ii)**) are oppositely rotated with respect to (*S*)-**30** (**Figure 1.21d(i)**) to achieve an optimal  $\pi$ -stacking between the aromatic backbones of the PE and also to avoid the steric constraints exerted by the stereocenter present in the peripheral coiled chains. On the contrary, based on the molecular geometry calculation, monomers of (*S*)-**31** were found to have an opposite rotation when stacking on top of each other in comparison to (*S*)-**30** and thereby attaining stable *P*-helices (**Figure 1.21d(iii)**). Furthermore, temperature-dependent UV-vis studies in MCH have confirmed that the stability of (*S*)-**30** and (*R*)-**30** is comparatively higher than that of (*S*)-**31**, which demonstrates the dependence of the stability of the supramolecular assemblies over the distance between the stereogenic carbon center to the aromatic frameworks. Besides, their self-assembly was also found to follow different polymerization mechanisms; where (*S*)-**30** and (*R*)-**30** self-assembled in a cooperative manner with a low degree of

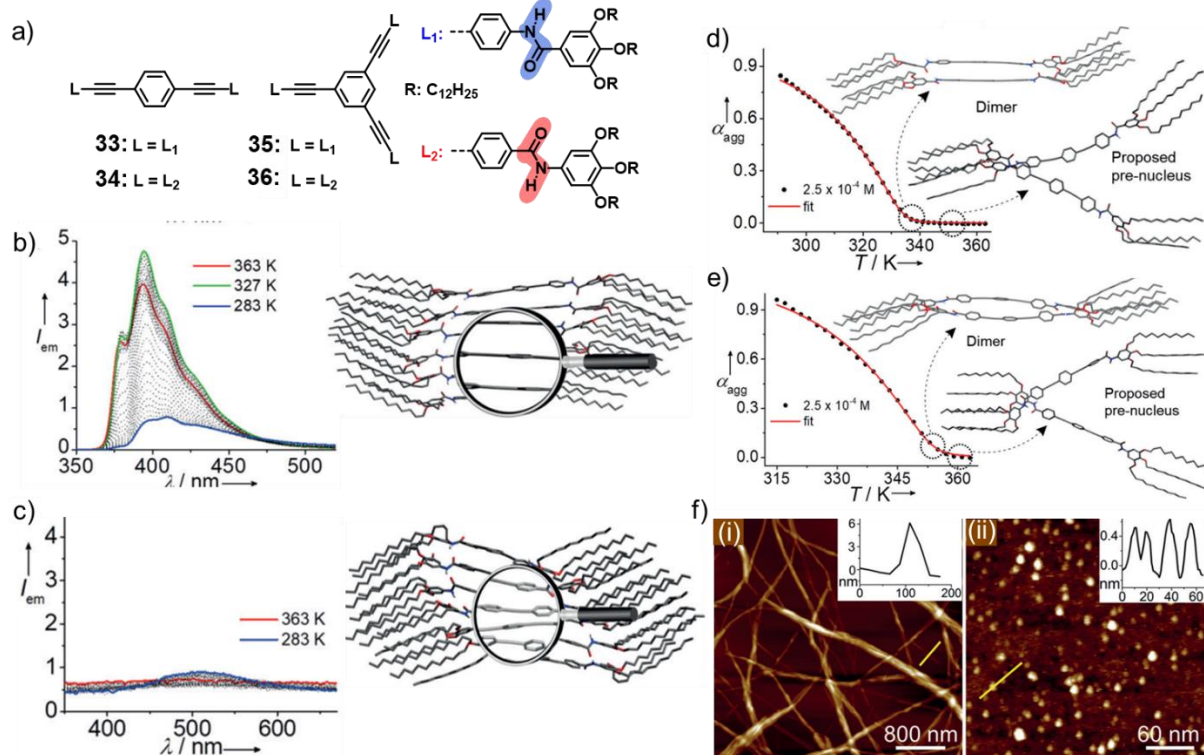


**Figure 1.22.** (a) Chemical structures of PEs **33–36**. Highlighted portions in the figure show the nature of amide connectivity (*N*-centered, blue; *C*-centered, pink). Temperature-dependent emission spectra of (b) **33** and (c) **34** ( $1 \times 10^{-4}$  M, MCH), respectively, with their corresponding side views obtained by PM7-optimization of hexamers. Cooling curves were obtained from Temperature-dependent UV-vis absorbance measurements at  $2.5 \times 10^{-4}$  M for (d) **33** and (e) **34** by monitoring the changes at 385 nm and 380 nm, respectively. The proposed geometries of the corresponding initial prenucleus and the optimized dimer structures are shown. (f) AFM images of the aggregates of (i) **33** and (ii) **34** prepared in MCH ( $c = 5 \times 10^{-5}$  M). The corresponding cross-section analysis is shown in the insets. (Adapted with permission from ref 45).

cooperativity ( $\sigma = 0.2$ ,  $K_n \sim 2.5 \times 10^4 \text{ M}^{-1}$ ,  $K_e \sim 1.5 \times 10^5 \text{ M}^{-1}$ ) and formation of the aggregates for (*S*)-**31** and **32** can be well-described by an isodesmic model. These results demonstrate the importance of minute variations in the molecular structure over the outcome of the supramolecular self-assembly process.

## 1.7. Amides and Retroamides of Linear and Triangular PEs

Fernández and co-workers have demonstrated the importance of the amide topology of PE-based monomers in controlling the self-assembly and photophysical properties (**Figure 1.22**).<sup>[45]</sup> For this purpose, a series of  $C_2$ - and  $C_3$ -symmetric PEs (**33-36**), which differ on the topology ( $N$ - or  $C$ -centered) of their amide units (**Figure 1.22a**), were synthesized and analyzed their self-assembly behavior. From the semi-empirical calculation at the PM7 level, a marked difference in the electron density has been observed upon inverting the amide topology. Furthermore, the  $N$ -centered molecules (**33** and **35**) showed a much stronger overlap between their HOMO and LUMO than that of the  $C$ -centered counterparts (**34** and **36**), indicating more allowed electronic transitions for  $N$ -centered PEs. Temperature-dependent emission studies of **33** initially showed a slight enhancement in fluorescence upon decreasing the temperature from 363 to 327 K, followed by a significant quenching by further reducing the temperature to 283 K (**Figure 1.22b**). The changes indicate restricted molecular rotation of the PE core up to 327 K, which then undergoes planarization-induced preorganization of the molecules upon further reduction in temperature to have an effective aggregation via the interaction between the aromatic PE units. The hexameric stacks of **33**, as optimized from the theoretical calculations, have also confirmed the planar nature of the PE cores within the stacks stabilized with the help of various non-covalent interactions (**Figure 1.22b**, inset). However, **34** was found non-emissive irrespective of the temperature range, which can be attributed to a less compact packing of the PE units due to the slight mismatch between H-bonds and aromatic interactions caused by the inversion in the

amide topology (**Figure 1.22c**). Based on the experimental and theoretical perspectives, the self-assembly process has been divided into three different steps: prenucleation, nucleation and elongation phases. Prenucleation step for **33** and **35** involves the initial association of two monomers via H-bond through the amide groups to form a V-shaped prenucleus dimer, which further rearranges to form a stable, more organized dimer nucleus having a compact parallel arrangement (**Figure 1.22d**) before undergoing the elongation process. **Figure 1.22e** reveals a lower stabilization of the prenucleus for the C-centered monomers (**34** and **36**), which is primarily stabilized through weak, less-efficient H-bonds during the prenucleation stage, and then by forming a more distorted dimer in the nucleation regime. The dissimilar interplay of the non-covalent interactions resulted in distinct morphological features, forming micrometer-sized long fibers for **33** and smaller round-shaped discrete aggregates in the case of **34** (**Figure 1.22f**), which signifies the importance of amide topology over the assembly process.

The cooperative supramolecular polymerization of  $C_3$ -symmetric *N*-centred retroamides (**37** and (*S/R*)-**38**) and *CO*-centred tricarboxamides (**23** and (*S/R*)-**24**) have been demonstrated with the help of both experimental and theoretical studies (**Figure 1.23**).<sup>[46]</sup> Depending upon the absolute configuration (*S* or *R*) of the stereogenic centers located at the peripheral side chains, **37** and (*S/R*)-**38** have been found to yield *P*- or *M*-type helical aggregates; however, the handedness of the final helical supramolecular assemblies was not found to be affected by the connectivity of the amide groups (*N*- or *C*-centered). Molecule (*S*)-**38** (*N*-centered) showed a bisignate Cotton effect with a positive followed by a negative CD signal having maxima at 330 and 290 nm,

respectively, in decalin:CHCl<sub>3</sub> (95:5) solvent mixture (**Figure 1.23b**). The molecule (*R*)-**38** containing the *R*-stereogenic center in the chiral sidechain showed an opposite CD spectrum (**Figure 1.23b**). The change in the amide topology of (*S*)-**38** and (*R*)-**38** (*CO*-centered) resulted in an almost similar dichroic pattern with a slight blue-shift in the maximum, indicating that topology did not affect the helical sense of the columnar assembly (**Figure 1.23b**). Theoretical simulations performed for infinite aggregates

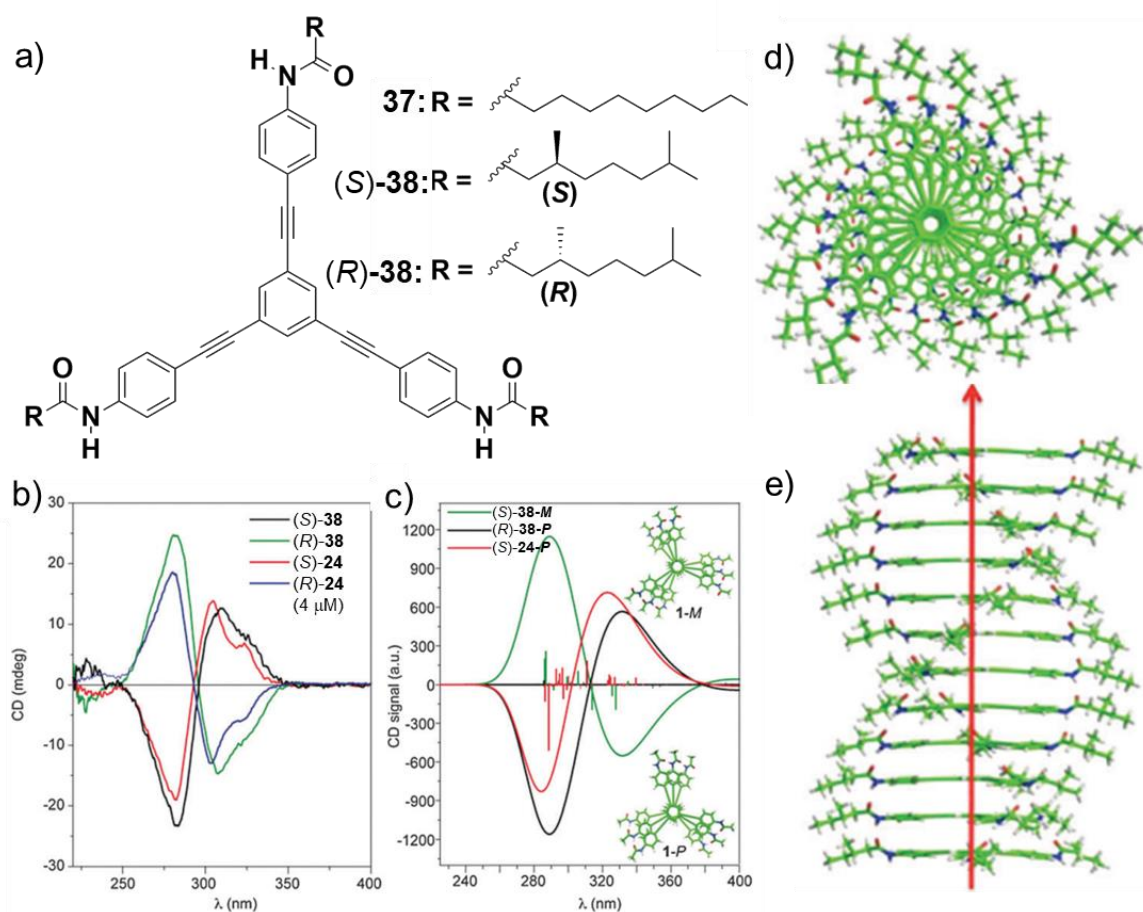


**Figure 1.23.** (a) Chemical structures of the trisamides **37** and (*S*/*R*)-**38**. (b) Experimental CD spectra of (*S*/*R*)-**38** and (*S*/*R*)-**24** in decalin/CHCl<sub>3</sub> (95/5) at 298 K ( $4 \times 10^{-6}$  M). (c) Theoretical simulations of the CD spectra were calculated for the trimers of **38-M**, **38-P** and **24-P**. (d) Top and (e) side views of the right-handed helical columnar arrangement of the ((*S*)-**38**)<sub>12</sub> aggregates substituted with *S*-stereogenic short alkyl chains. Red line shows the direction in which the dipole moment grows within the stack. (Adapted with permission from ref 46).

helped to energetically discriminate between the *P* and *M* arrangements and thus supported the preferential formation of a determined helical handedness depending on the chirality of the stereogenic group, which exactly matches with the experimental results (**Figure 1.23c**). The cooperative character of the supramolecular polymerization is higher for retroamides (**37** or **38**) compared to amides (**23** or **24**), as confirmed from the calculation of dipole moment per monomeric unit that grows exponentially due to the enhancement of the polarization of the H-bonding network during the nucleation process (**Figure 1.23d,e**).

## 1.8. PEs Attached to BODIPY

The PE-BODIPY conjugate functionalized with terminal TEG chains **39** was reported to form flexible fibers in an aqueous medium with the help of  $\pi$ -stacking and hydrophobic interactions (**Figure 1.24**).<sup>[47]</sup> Detailed UV-vis absorption and fluorescence spectroscopy studies revealed that these fibers are composed of H-type aggregates of **39** and can provide a hydrophobic environment for the entrapment of polyaromatic guest molecules. Interestingly, the flexibility of the fibers was found reducing upon encapsulation of tetracene, as a result of the increased  $\pi$ - $\pi$  stacking and hydrophobic interactions operating between **39** and guest molecules (**Figure 1.24b,d,f**). Detailed analysis of UV-vis spectral changes indicated that the co-assembly process occurs through an isodesmic pathway (**Figure 1.24b**, inset). However, the co-assembly process turned out to be significantly different when a slightly smaller aromatic guest molecule

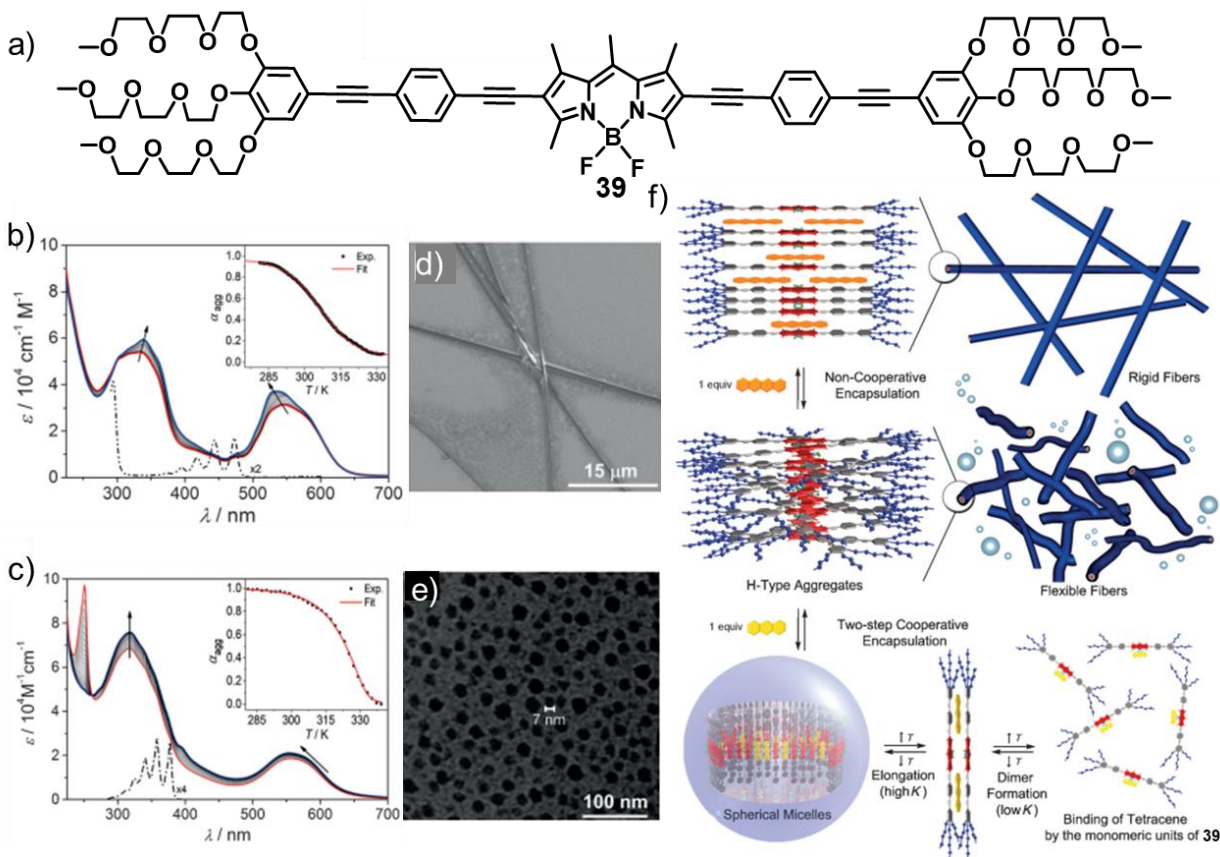


**Figure 1.24.** (a) Molecular structures of PE-BODIPY derivative **39**. (b) Temperature-dependent UV-vis studies of **39** in an aqueous solution containing one equivalent of (b) tetracene and (c) anthracene. Arrows indicate the spectral changes upon a decrease in temperature for both cases. The dash-dotted line corresponds to the UV-vis spectra of (b) tetracene and (c) anthracene in THF. Inset shows the fitting of the spectral changes of **39** to the (b) isodesmic and (c) cooperative model. (d) SEM image of **39** and one equivalent of tetracene in water ( $1 \times 10^{-5}$  M). (e) TEM image of **39** and one equivalent of anthracene in water ( $1 \times 10^{-5}$  M). (f) Schematic representation for the self-assembly of **39** into H-type aggregates and its reversible guest-dependent encapsulation processes. (Adapted with permission from ref 47).

anthracene was utilized, which follows a cooperative pathway as inferred from the UV-vis spectral changes (**Figure 1.24c**). According to titration analysis and temperature-dependent UV-vis studies, at high-temperature, polyaromatic molecules became soluble in water upon binding with monomers of **39**. The 1:1 complex dimerized to form the nucleus upon decreasing the temperature and subsequently elongated to stiff 1D fibers



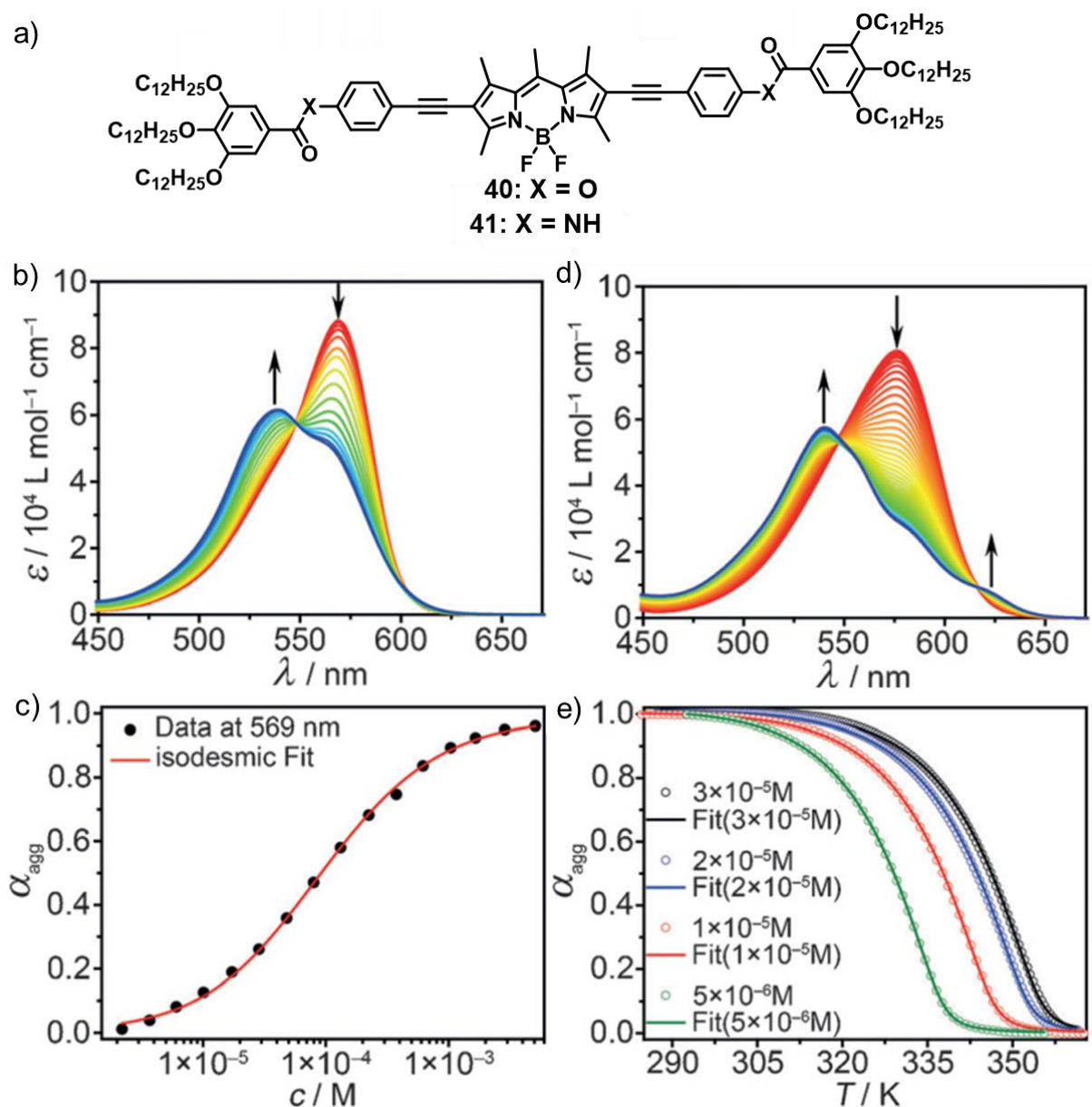


**Figure 1.25.** (a) Molecular structures of ester and amide-linked BODIPY compounds **40** and **41**. (b) Concentration-dependent UV-vis studies of **40** ( $5.09 \times 10^{-3}$  to  $2.20 \times 10^{-6}$  M) in MCH at room temperature. (c) The fit of the data of the absorption experiments of **40** monitored at 569 nm to the isodesmic model. (d) Temperature-dependent UV-vis absorption spectra of **41** ( $c = 1 \times 10^{-5}$  M) in MCH between 365 and 285 K. (e) Cooling curves obtained at different concentrations ( $5 \times 10^{-6}$  to  $3 \times 10^{-5}$  M) by monitoring the changes in absorption of **41** at 576 nm, which fits the nucleation–elongation model. The arrows in (b) and (d) indicate the spectral changes with increase in concentration and decrease in temperature, respectively. (Adapted with permission from ref 48).



and spherical nanoparticles in the case of tetracene and anthracene, respectively (**Figure 1.24d,e**). The change observed in the co-assembly mechanism can be rationalized based on the fact that the molecules of **39** no longer remain in a preferred direction because of the decreased  $\pi$ - $\pi$  interactions between the host and guest molecules in the case of smaller guest molecules (anthracene) leading to a more stable, discrete assemblies (**Figure 1.24f**).

The direct influence of ester and amide linkers on the mechanism of supramolecular polymerization of planar PE-BODIPY conjugates have been discussed by Fernández and co-workers (**Figure 1.25**).<sup>[48]</sup> Though both the molecules were found to self-assemble in H-type fashion in MCH (**Figure 1.25b,c**), **40** found to follow an isodesmic pathway, whereas a nucleation-elongation mechanism prevailed in the case of **41** (**Figure 1.25d,e**). The peak at 520 nm for **41** indicates a face-to-face H-type stacking of the BODIPY chromophores. The shoulder band observed at 620 nm can be correlated with a rotational stacking of the molecules to have a preferred orientation to form intermolecular H-bonds between the amide groups (**Figure 1.25d**). On the other hand, the blue-shifted absorption obtained for **40** without red-shifted shoulder signifies less prominent rotational displacement of the chromophores (**Figure 1.25b**). Variable-temperature  $^1\text{H}$  NMR studies further confirmed the importance of additional intermolecular force assisted by amide H-bonding in switching the packing. Theoretical studies also confirmed a larger helical pitch for **41** than **40**, facilitating an optimal conformation of the amide groups through H-bonding. These results have indicated the

interplay of various types of orthogonal non-covalent interactions to create ordered supramolecular assemblies.

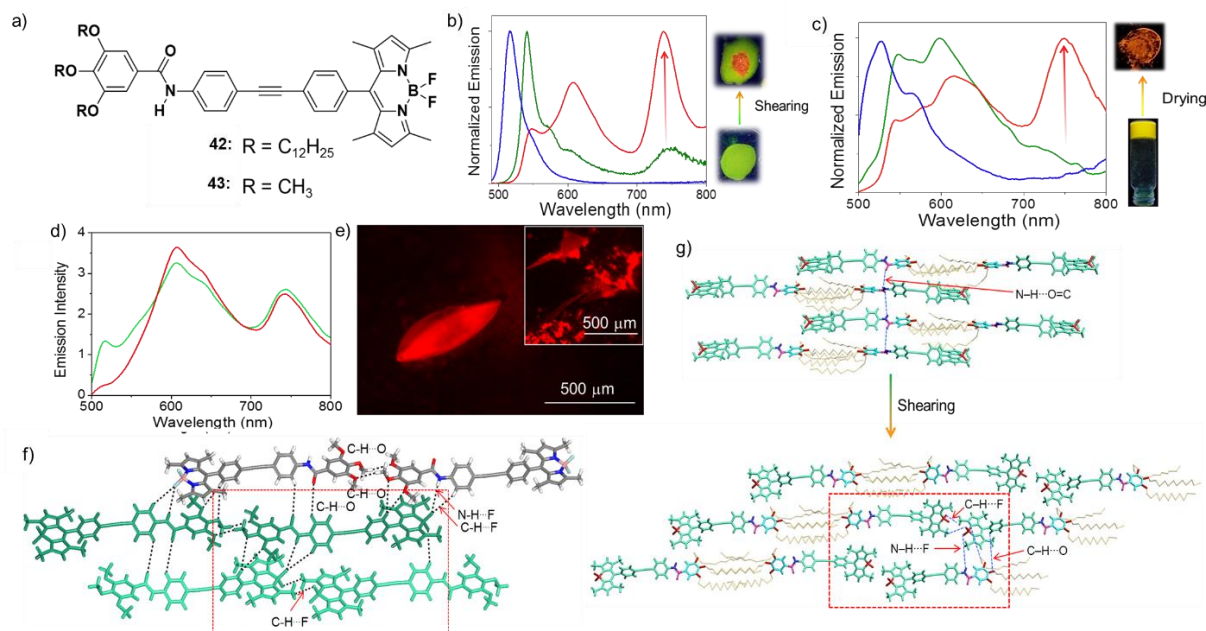


**Figure 1.26.** (a) Molecular structures of BODIPY based *meso*  $\pi$ -extended molecule **42** and **43**. (b) Emission profiles of *n*-decane aggregates of **42** ( $1 \times 10^{-4}$  M, blue); film processed from *n*-decane aggregates (green) and after shearing the film (red). (c) Emission profiles of **42** in DMSO solution ( $1 \times 10^{-4}$  M, blue), DMSO gel (green) and xerogel (red). In all the cases,  $\lambda_{\text{ex}}$  was fixed at 475 nm. The corresponding fluorescence color changes under 365 nm UV light illumination have also been shown. (d) The emission spectrum of single crystal of **43** before (red) and after (green) shearing. (e) Fluorescence microscopy image of single crystal of **43**. Inset shows the fluorescence microscopy image of the sheared crystal. (f) Crystal packing of **43**. The red square shows BODIPY–BODIPY interaction. (g) The schematic representation demonstrating the probable molecular organization of **42** before and after shearing of the film processed from *n*-decane. The red square shows a similar type of BODIPY–BODIPY interaction responsible for NIR emission as seen in the single crystal. (Adapted with permission from ref 49).

We have recently observed an unprecedented amplification of near-infrared (NIR) emission from an amide functionalized Bodipy based *meso*  $\pi$ -extended molecule **42**, which exhibits a weak NIR emission at 738 nm in the film state processed from the self-assembled *n*-decane aggregates (**Figure 1.26a**).<sup>[49]</sup> However, upon mechanical

shearing and xerogel formation, the NIR peak showed 15- and 7-fold enhancement in the emission intensity, respectively (**Figure 1.26b,c**). During the mechanical shearing, the initial greenish-yellow fluorescence of *n*-decane aggregate film was changed to an intense orange-red emission and the yellow-emitting DMSO gel changed to an orange-red emitting xerogel upon complete removal of the solvent (**Figure 1.26b,c**). The hint for the mechanism of the enhancement in NIR emission has been obtained from molecular packing of the model derivative **43** showing NIR emission and intense dark red fluorescence microscopy image in the single crystalline state (**Figure 1.26d,e**). Moreover, the emission spectra and fluorescence microscopy image remained unaltered even after shearing the single crystals of **43** (**Figure 1.26d,e**). Detailed analysis revealed that N-H $\cdots$ F-B bonding-assisted head-to-tail slipped arrangement of the chromophores leading to a strong exciton coupling of Bodipy chromophores and responsible for NIR emission (**Figure 1.26f**). As the emission spectrum of the single crystal of **43** was found similar to that of the sheared *n*-decane film of **42**, they can be considered to have an identical molecular arrangement. Furthermore, the XRD and FT-IR studies have suggested identical molecular arrangement in the case of the sheared *n*-decane aggregate film and DMSO xerogel of **42**. Based on these results, it has been proposed that the intermolecular H-bonds between N-H and C=O, forming an extended molecular organization in *n*-decane aggregate film, which undergo partial breakage upon shearing and thereby changes to a more organized assembly by forming H-bonding between N-H and B-F moiety, which helps in significant fluorescence modulation (**Figure 1.26g**).

The analysis of various reports discussed above clearly reiterates the importance of PE and PE-attached BODIPY based extended  $\pi$ -conjugated systems to the design of self-assembled supramolecular architectures. Their formation mechanism, diversity of morphology, intriguing excited-state properties and applications have been explored to have an overall idea about the structure-property relationships. The insights obtained from these studies have helped chemists to develop new design strategies and self-assembly processes to understand the pathway complexity and properties of supramolecular polymerization.

### **1.9. Origin, Objectives and Approach to the Thesis**

The origin of the work carried out in the thesis has been developed based on the gradual progress in the field of self-assembly of PE and PE-attached BODIPY dyes. Results of all these works have encouraged us to further look into the correlation between the excited state properties and morphological features of various PE and PE-attached BODIPY chromophore assemblies by systematically modifying the structural parameters and self-assembly protocols. At first, we have varied the nature of the substituted alkyl chains (chiral or achiral) on the terminal moieties of PEs and investigated their role over the self-assembly induced emission properties. Subsequently, solvent induced reversible control of the morphology and energy landscape of the supramolecular structures of a Y-shaped PE-BODIPY based chromophoric assembly have been demonstrated. Finally, in the last chapter, we have studied the copolymerization of Y-shaped PE-BODIPY monomers and Y-shaped PE

monomers to understand their morphological and photophysical properties. The overall content of the present thesis is a detailed and systematic presentation of the results obtained by various experimental studies conducted in line with the objectives stated above.

## 1.10. References

- [1] T. Aida, E. W. Meijer, *Isr. J. Chem.* **2020**, *60*, 33-47.
- [2] H. Staudinger, *Ber. Dtsch. Chem. Ges. B* **1920**, *53*, 1073.
- [3] T. Aida, E. W. Meijer, S. I. Stupp, *Science* **2012**, *335*, 813-817.
- [4] N. Roy, B. Bruchmann, J. M. Lehn, *Chem. Soc. Rev.* **2015**, *44*, 3786-3807.
- [5] (a) T. F. A. de Greef, M. M. J. Smulders, M. Wolffs, A. P. H. J. Schenning, R. P. Sijbesma, E. W. Meijer, *Chem. Rev.* **2009**, *109*, 5687-5754. (b) A. Sandeep, V. K. Praveen, K. K. Kartha, V. Karunakaran, A. Ajayaghosh, *Chem. Sci.* **2016**, *7*, 4460-4467. (c) M. Yamasaki, W. Li, D. J. D. Johnson, J. A. Huntington, *Nature* **2008**, *455*, 1255-1259. (d) G. Rivas, A. Lopez, J. Mingorance, M. J. Ferrandiz, S. Zorrilla, A. P. Minton, M. Vicente, J. M. Andreu, *J. Biol. Chem.* **2000**, *275*, 11740-11749. (e) F. Oosawa, M. Kasai, *J. Mol. Biol.* **1962**, *4*, 10. (f) M. M. J. Smulders, A. P. H. J. Schenning, E. W. Meijer, *J. Am. Chem. Soc.* **2008**, *130*, 606-611.
- [6] L. Brunsveld, B. J. B. Folmer, E. W. Meijer, R. P. Sijbesma, *Chem. Rev.* **2001**, *101*, 4071-4098.
- [7] T. F. A. de Greef, E. W. Meijer, *Nature* **2008**, *453*, 171-173.
- [8] R. P. Sijbesma, F. H. Beijer, L. Brunsveld, B. J. B. Folmer, J. H. K. K. Hirschberg, R. F. M. Lange, J. K. L. Lowe, E. W. Meijer, *Science* **1997**, *278*, 1601-1604.
- [9] C. Rest, R. Kandanelli, G. Fernández, *Chem. Soc. Rev.* **2015**, *44*, 2543-2572.
- [10] P. A. Korevaar, S. J. George, A. J. Markvoort, M. M. J. Smulders, P. A. J. Hilbers, A. P. H. J. Schenning, T. F. A. De Greef, E. W. Meijer, *Nature* **2012**, *481*, 492-496.

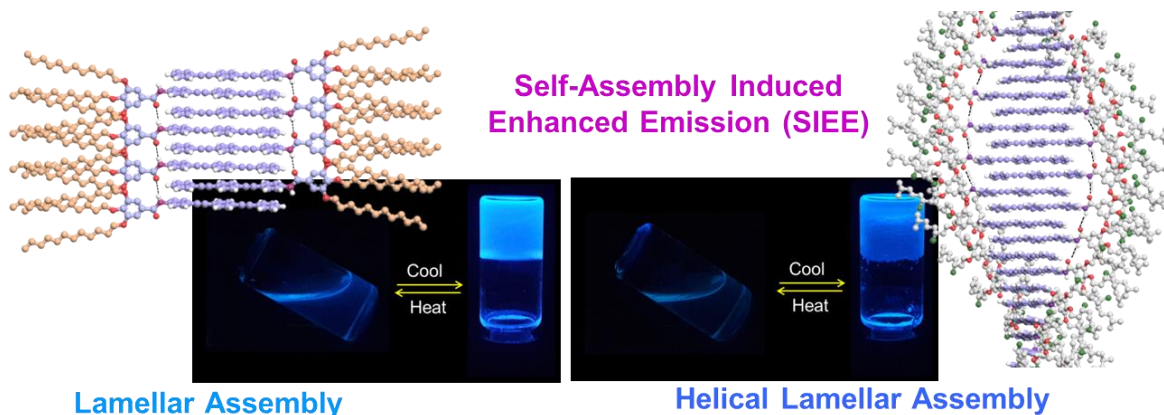
- [11] M. M. J. Smulders, M. M. L. Nieuwenhuizen, T. F. A. de Greef, P. Van Der Schoot, A. P. H. J. Schenning, E. W. Meijer, *Chem. Eur. J.* **2010**, *16*, 362-367.
- [12] M. M. J. Smulders, I. A. W. Filot, J. M. A. Leenders, P. Van Der Schoot, A. R. A. Palmans, A. P. H. J. Schenning, E. W. Meijer, *J. Am. Chem. Soc.* **2010**, *132*, 611-619.
- [13] P. Jonkheijm, P. Van Der Schoot, A. P. H. J. Schenning, E. W. Meijer, *Science* **2006**, *313*, 80-83.
- [14] S. Dhiman, S. J. George, *Bull. Chem. Soc. Jpn.* **2018**, *91*, 687-699.
- [15] J. Matern, Y. Dorca, L. Sánchez, G. Fernández, *Angew. Chem. Int. Ed.* **2019**, *58*, 16730-16740.
- [16] A. Sorrenti, J. Leira-Iglesias, A. J. Markvoort, T. F. A. de Greef, T. M. Hermans, *Chem. Soc. Rev.* **2017**, *46*, 5476-5490.
- [17] P. A. Korevaar, C. J. Newcomb, E. W. Meijer, S. I. Stupp, *J. Am. Chem. Soc.* **2014**, *136*, 8540-8548.
- [18] S. Ogi, V. Stepanenko, J. Thein, F. Würthner, *J. Am. Chem. Soc.* **2016**, *138*, 670-678.
- [19] T. Fukui, S. Kawai, S. Fujinuma, Y. Matsushita, T. Yasuda, T. Sakurai, S. Seki, M. Takeuchi, K. Sugiyasu, *Nat. Chem.* **2017**, *9*, 493-499.
- [20] E. Mattia, S. Otto, *Nat. Nanotechnol.* **2015**, *10*, 111-119.
- [21] S. Sevim, A. Sorrenti, C. Franco, S. Furukawa, S. Pané, A. J. Demello, J. Puigmartí-Luis, *Chem. Soc. Rev.* **2018**, *47*, 3788-3803.
- [22] F. della Sala, S. Neri, S. Maiti, J. L. Y. Chen, L. J. Prins, *Curr. Opin. Biotechnol.* **2017**, *46*, 27-33.
- [23] A. T. Haedler, S. C. J. Meskers, R. H. Zha, M. Kivala, H. W. Schmidt, E. W. Meijer, *J. Am. Chem. Soc.* **2016**, *138*, 10539-10545.
- [24] D. Van Der Zwaag, P. A. Pieters, P. A. Korevaar, A. J. Markvoort, A. J. H. Spiering, T. F. A. De Greef, E. W. Meijer, *J. Am. Chem. Soc.* **2015**, *137*, 12677-12688.

- [25] J. Kang, D. Miyajima, T. Mori, Y. Inoue, Y. Itoh, T. Aida, *Science* **2015**, *347*, 646-651.
- [26] S. Ogi, K. Sugiyasu, S. Manna, S. Samitsu, M. Takeuchi, *Nat. Chem.* **2014**, *6*, 188-195.
- [27] I. V. Baskakov, G. Legname, M. A. Baldwin, S. B. Prusiner, F. E. Cohen, *J. Biol. Chem.* **2002**, *277*, 21140-21148.
- [28] W. Wagner, M. Wehner, V. Stepanenko, S. Ogi, F. Würthner, *Angew. Chem. Int. Ed.* **2017**, *56*, 16008-16012.
- [29] S. Ogi, K. Matsumoto, S. Yamaguchi, *Angew. Chem. Int. Ed.* **2018**, *57*, 2339-2343.
- [30] A. Ajayaghosh, R. Varghese, S. Mahesh, V. K. Praveen, *Angew. Chem. Int. Ed.* **2006**, *45*, 7729-7732.
- [31] (a) A. Ajayaghosh, R. Varghese, V. K. Praveen, S. Mahesh, *Angew. Chem. Int. Ed.* **2006**, *45*, 3261-3264. (b) A. Ajayaghosh, R. Varghese, S. J. George, C. Vijayakumar, *Angew. Chem. Int. Ed.* **2006**, *45*, 1141-1144. (c) M. M. Green, M. P. Reidy, R. D. Johnson, G. Darling, D. J. O'Leary, G. Willson, *J. Am. Chem. Soc.* **1989**, *111*, 6452-6454. (d) A. J. Wilson, M. Masuda, R. P. Sijbesma, E.W. Meijer, *Angew. Chem. Int. Ed.* **2005**, *44*, 2275-2279
- [32] R. Thirumalai, R. D. Mukhopadhyay, V. K. Praveen, A. Ajayaghosh, *Sci. Rep.* **2015**, *5*, 9842.
- [33] M. J. Mayoral, C. Rest, J. Schellheimer, V. Stepanenko, G. Fernández, *Chem. Eur. J.* **2012**, *18*, 15607-15611.
- [34] J. P. Coelho, G. Tardajos, V. Stepanenko, A. Rödle, G. Fernández, A. Guerrero-Martínez, *ACS Nano* **2015**, *9*, 11241-11248.
- [35] A. Gopal, R. Varghese, A. Ajayaghosh, *Chem. Asian J.* **2012**, *7*, 2061-2067.
- [36] A. Gopal, M. Hifudheen, S. Furumi, M. Takeuchi, A. Ajayaghosh, *Angew. Chem. Int. Ed.* **2012**, *51*, 10505-10509.
- [37] M. Hifudheen, R. K. Mishra, B. Vedhanarayanan, V. K. Praveen, A. Ajayaghosh,

- Angew. Chem. Int. Ed.* **2017**, *56*, 12634-12638.
- [38] J. P. Coelho, J. Matern, R. Q. Albuquerque, G. Fernández, *Chem. Eur. J.* **2019**, *25*, 8960-8964.
- [39] L. Herkert, J. Droste, K. K. Kartha, P. A. Korevaar, T. F. A. de Greef, M. R. Hansen, G. Fernández, *Angew. Chem. Int. Ed.* **2019**, *58*, 11344-11349.
- [40] A. Langenstroer, K. K. Kartha, Y. Dorca, J. Droste, V. Stepanenko, R. Q. Albuquerque, M. R. Hansen, L. Sánchez, G. Fernández, *J. Am. Chem. Soc.* **2019**, *141*, 5192-5200.
- [41] F. García, P. M. Viruela, E. Matesanz, E. Ortí, L. Sánchez, *Chem. Eur. J.* **2011**, *17*, 7755-7759.
- [42] J. Buendía, L. Sánchez, *Org. Lett.* **2013**, *15*, 5746-5749.
- [43] F. García, P. A. Korevaar, A. Verlee, E. W. Meijer, A. R. A. Palmans, L. Sánchez, *Chem. Commun.* **2013**, *49*, 8674-8676.
- [44] F. Aparicio, F. García, G. Fernández, E. Matesanz, L. Sánchez, *Chem. Eur. J.* **2011**, *17*, 2769-2776.
- [45] D. S. Philips, K. K. Kartha, A. T. Politi, T. Krüger, R. Q. Albuquerque, G. Fernández, *Angew. Chem. Int. Ed.* **2019**, *58*, 4732-4736.
- [46] J. Buendía, J. Calbo, F. García, J. Aragón, P. M. Viruela, E. Ortí, L. Sánchez, *Chem. Commun.* **2016**, *52*, 6907-6910.
- [47] N. K. Allampally, A. Florian, M. J. Mayoral, C. Rest, V. Stepanenko, G. Fernández, *Chem. Eur. J.* **2014**, *20*, 10669-10678.
- [48] A. Rödle, B. Ritschel, C. Mück-Lichtenfeld, V. Stepanenko, G. Fernández, *Chem. Eur. J.* **2016**, *22*, 15772-15777.
- [49] S. Cherumukkil, S. Ghosh, V. K. Praveen, A. Ajayaghosh, *Chem. Sci.* **2017**, *8*, 5644-5649.



## Self-Assembly Induced Enhanced Emission in Phenyleneethynylene Derived $\pi$ -Gelators



### 2.1. Abstract

Optical properties of  $\pi$ -systems are of great significance for a wide range of applications in materials and biology. Aggregation and self-assembly induced emission are one of such phenomena. Herein, we report the self-assembly induced modulation of the emission of *p*-phenyleneethynylene chromophores bearing linear achiral (**1**) or branched chiral (**2**) alkoxy chains. Self-assembled structures of both **1** and **2** from *n*-decane exhibited enhanced emission with  $\Phi_F$  values of 0.34 and 0.25, respectively, whereas these molecules were less-emissive in chloroform ( $\Phi_F = 0.02$ ). TEM and fluorescence microscopy studies revealed the formation of entangled blue-emissive fibers for **1** and supercoiled helical blue-emissive fiber bundles for **2**. At higher concentrations (8.8 mM for **1** and 23.6 mM for **2**) in *n*-decane, intense blue-

*emitting gels were formed. Significant shift in the emission towards longer wavelength can be seen from solution state to aggregates to the gel state. The WAXS and fluorescence data indicate interdigitated lamellar assembly with weaker  $\pi$ -stacking and the resultant restricted rotation of the PE chromophores are responsible for the enhanced emission of the self-assembled gel state.*

## 2.2. Introduction

Fluorescence is one of the most sensitive optical properties of  $\pi$ -systems. Since fluorescence strongly depends upon the structural features, intermolecular interaction, and several external factors, fluorescent molecules are used for wide-ranging applications.<sup>[1-5]</sup> For example, fluorescent  $\pi$ -systems are used for sensing of analytes,<sup>[6-8]</sup> imaging,<sup>[9,10]</sup> and lighting applications.<sup>[11,12]</sup> However, in aggregated and solid states, most of the  $\pi$ -systems exhibit reduced quantum yield for emission due to self-quenching phenomenon associated with strong  $\pi$ - $\pi$  interaction.<sup>[13]</sup> Therefore, it is necessary to prevent the fluorescence quenching by incorporating bulky terminal groups<sup>[14,15]</sup> or by modulating the viscosity of the medium<sup>[16]</sup> for any practical applications. Interestingly, in some cases, fluorescence is found to increase upon aggregation or self-assembly.<sup>[13,16,17]</sup> Though this phenomenon has been extensively studied in recent times as AIE, it is actually a manifestation of the previously known restricted rotation of chromophores in the solid and crystalline states.

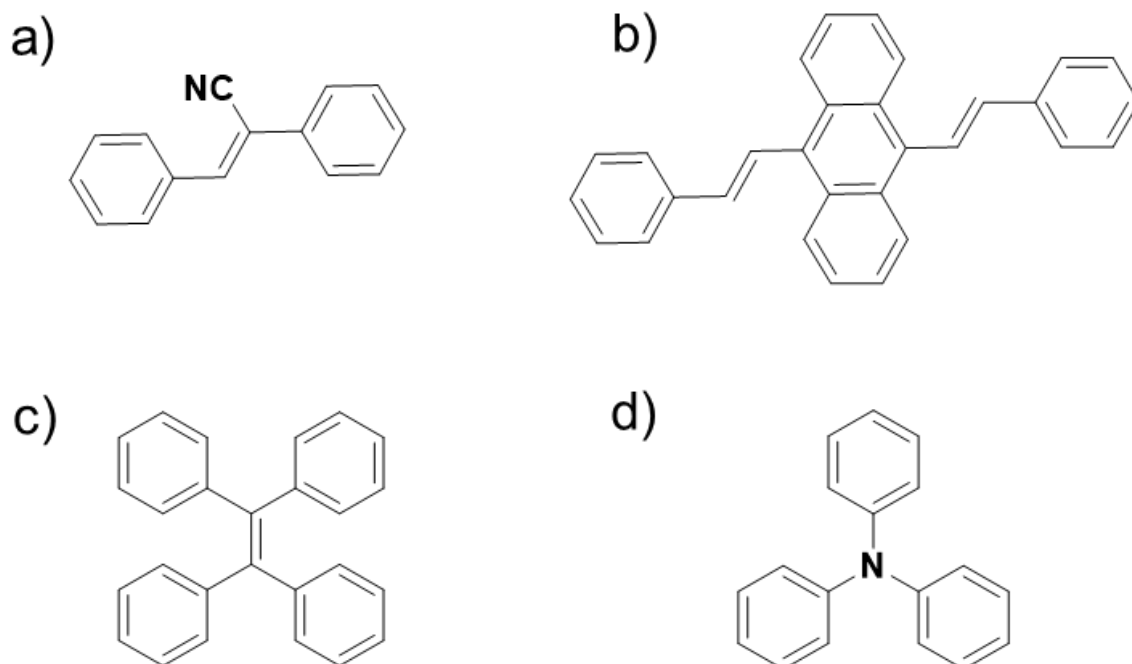


**Figure 2.1.** Various chromophores exhibiting AIEE phenomenon: (a) cyanostilbene, (b) distyrylanthracene, (c) tetraphenylethylene and (d) triphenylamine.

Though several  $\pi$ -systems are known to exhibit AIEE, chromophores such as heteroatom-containing molecules,<sup>[18]</sup> cyano stilbenes,<sup>[19-21]</sup> distyrylanthracene,<sup>[22]</sup> tetraphenylethylenes,<sup>[23]</sup> excited state intramolecular proton transfer systems<sup>[24]</sup> and so on are the best-studied systems (**Figure 2.1**).<sup>[6,16,17]</sup> In the case of AIEE-inactive chromophores, the energy provided to excite the molecules is utilized for the rotational and vibrational motion of the molecules and thus non-radiative decay paths are found to be more effective to form less or non-emissive states. However, in the case of AIEE-active molecules, upon aggregation, intramolecular rotation and vibrational motion gets restricted and the radiative decay channels are activated to exhibit enhanced emission.<sup>[13,16]</sup> Another interesting  $\pi$ -system that display SIEE is PEs.<sup>[25-29]</sup> Due to the

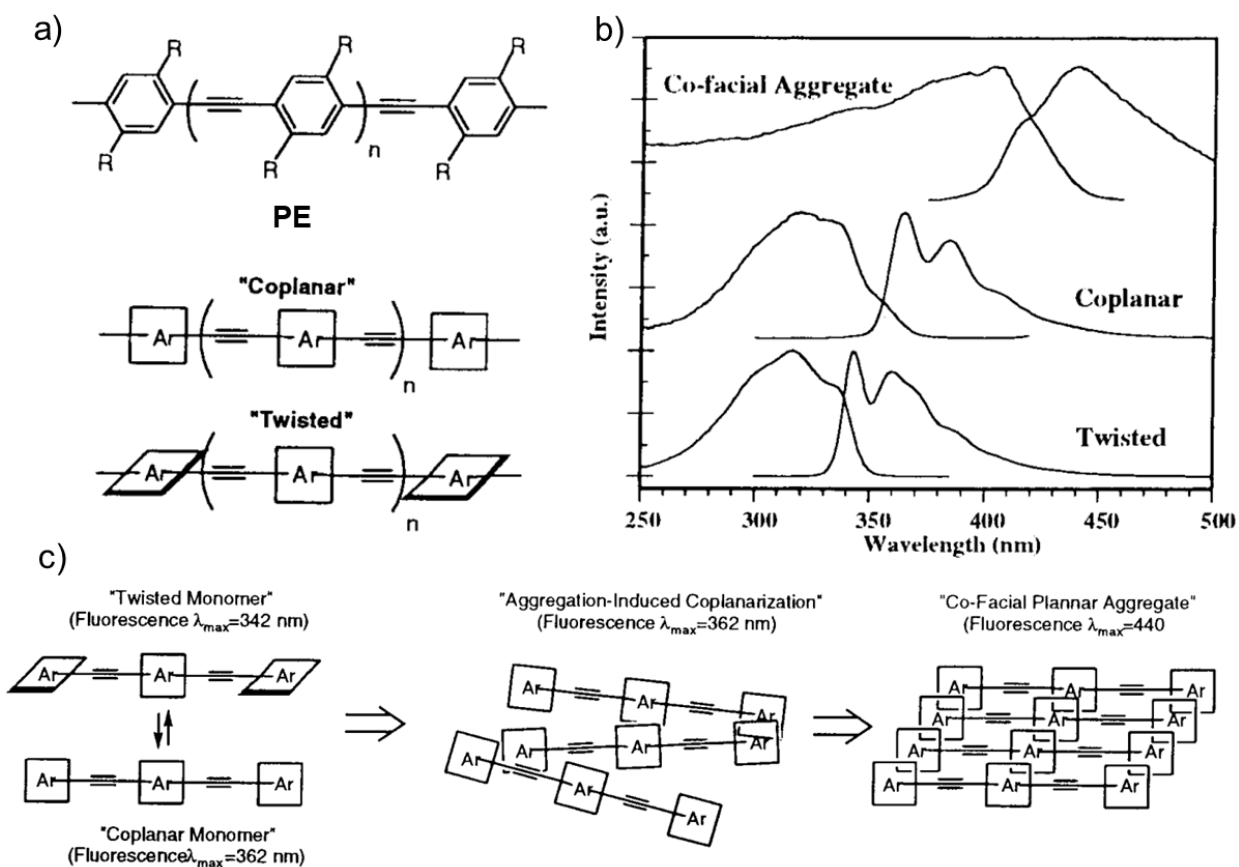


**Figure 2.2.** (a) Molecular structures of PE in its coplanar and twisted forms. (b) Excitation (left) and emission (right) spectra and (c) schematic representation of structural arrangements of PE in its twisted, coplanar and co-facial planar forms. (Adapted with permission from ref 25).

freedom of rotation of the phenyl rings around the triple bonds, they are less emissive in solution-state. However, properly functionalized PEs show strong fluorescence upon self-assembly. Bunz, Garcia-Garibay and co-workers have demonstrated that variable optoelectronic properties of PEs can be achieved by controlling the extent of phenyl group rotation (**Figure 2.2**).<sup>[25,26]</sup> Furthermore, they have also showed that the equilibration process of PEs in solution do not undergo any significant changes in the ground state, but upon electronic excitation, the rotation of alkyne-aryl single bonds lead to the changes in

the bond order of the coplanar and twisted forms, which results in emission spectral shifts. The emission spectrum of PE remains structured when the phenyl rings are in the twisted conformation or in the case of self-assembly induced planarization of the phenyl rings. However, the emission spectrum of PEs can be broadened and red-shifted upon the formation of co-facial planar PE assemblies (**Figure 2.2b**). For example, the excitation and emission spectra of the crystalline aggregates of PE was found red-shifted by 70-80 nm when compared to the emission spectra obtained in dilute solutions. According to these optical studies, it can be interpreted that the relatively disordered aggregates may facilitate planarization of the PE moieties before co-facial interaction, which leads to red-shift and broadening of the spectrum (**Figure 2.2b,c**).

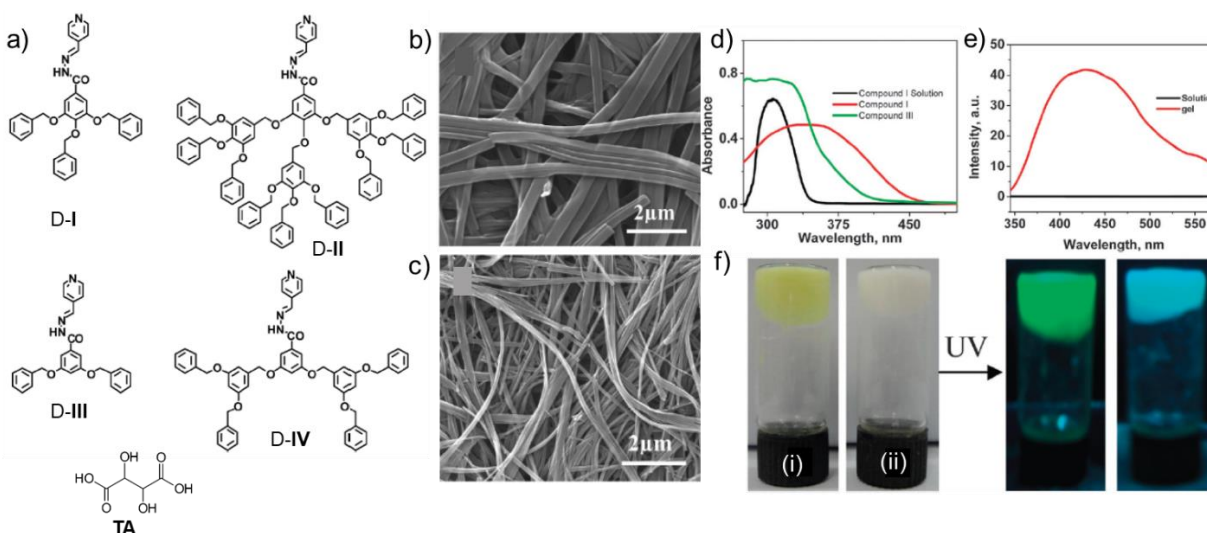


**Figure 2.3.** (a) Molecular structures of pyridine group attached dendrons (D-I to D-IV) and tartaric acid (TA). SEM images of the xerogels in THF–water (1:1) mixture for (b) D-I/TA (2:1) and (c) D-III/TA (2:1). (d) UV-vis absorption spectra of the dendron (solution phase, black) and dendron/TA gels at room temperature (red and green for D-I and D-II in the gel phase, respectively). (e) Emission spectra of D-II/TA in THF–water and gel phase ( $\lambda_{\text{ex}} = 340$  nm). (f) Photographs of the gels: (i) D-I/TA and (ii) D-II/TA in THF–water (1:1) under ambient light (left) and 365 nm UV light illumination (right). (Adapted with permission from ref 30).

Prasad and co-workers have reported the in-situ formation of two-component hydrogel exhibiting AIE in the visible region (**Figure 2.3**).<sup>[30]</sup> For this purpose, they designed pyridine attached AB<sub>3</sub> type (D-I and D-II) and AB<sub>2</sub> type (D-III and D-IV) poly(aryl ether) dendrons having the propensity to interact with aliphatic acids through H-bonding (**Figure 2.3a**). These molecules were found soluble in THF and formed aggregates in THF-water mixture (1:1). Interestingly, upon adding an equimolar amount of TA in water to a 0.25 wt% solution of D-I in THF, the aggregates immediately turned into a gel. The Job plot analysis showed that the dendrons and TA require a 2:1 ratio to form a stable complex leading to gelation. The gelation ability was found to follow the order D-I>D-II>D-III>D-IV, indicating the importance of a delicate balance between the H-bonding and  $\pi$ -stacking interactions for efficient gelation. SEM images shown in **Figure 2.3b** and **2.3c** revealed that the gels of D-I/TA (2:1) and D-III/TA (2:1) form an entangled network of fibers. The photophysical properties indicate significant modulation of the TA induced gelation of dendrons (**Figure 2.3d,e**). UV-vis spectral studies showed a red-shifted absorption for both D-I and D-II after gelation, signifying J-type aggregate formation (**Figure 2.3d**). The non-emissive solution of dendron aggregates (D-II) showed a broad emission in the visible region upon interacting with TA (**Figure 2.3e**), confirming AIE behavior in the gel state. **Figure 2.3f** shows the photographs of D-I/TA and D-III/TA gels (under normal and UV light), which exhibit green and blue emission, respectively, despite the absence of a conventional fluorophore unit.

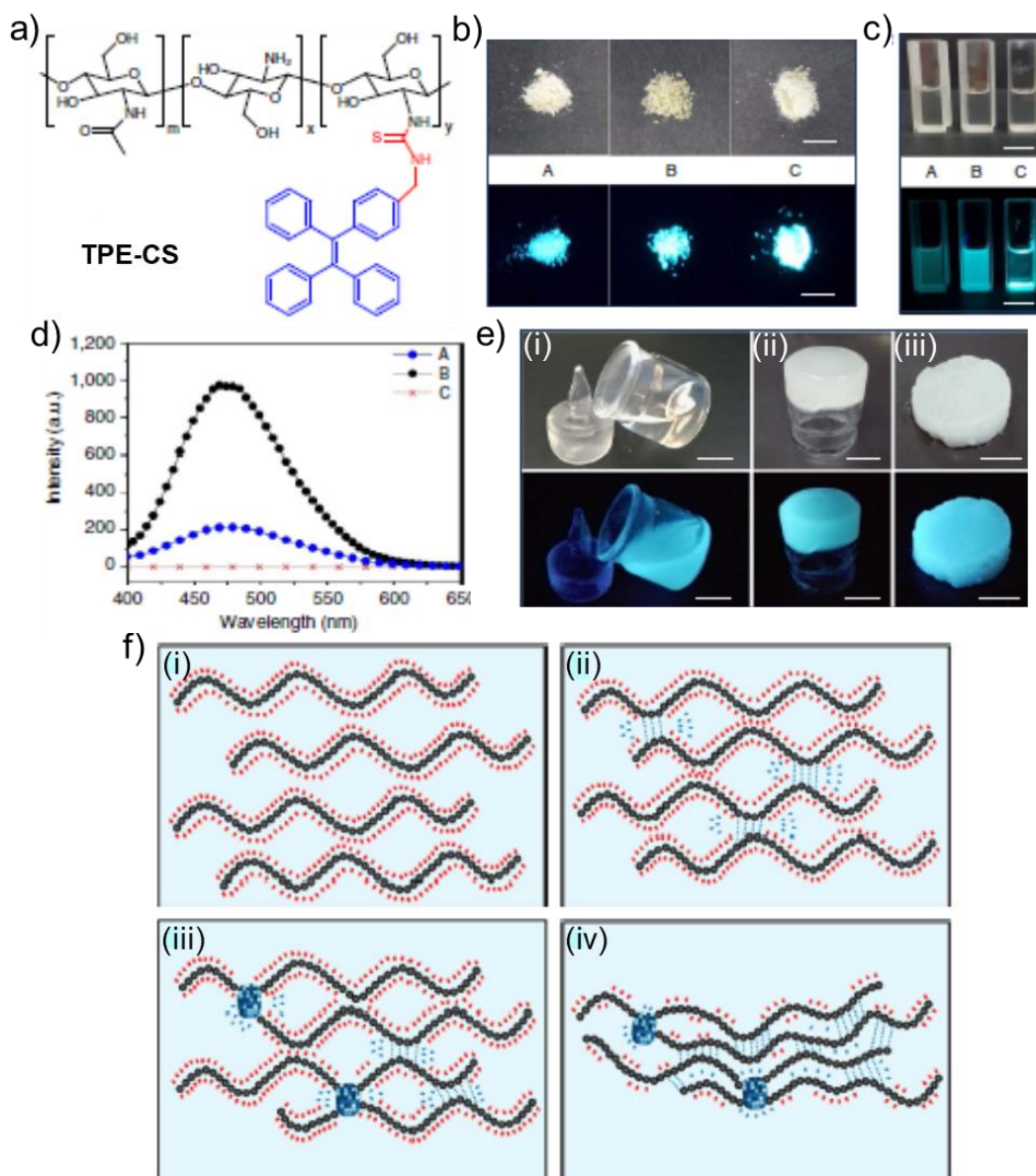


**Figure 2.4.** (a) Molecular structure of **TPE-CS**. (b) Photographs of the powder samples of **TPE-CS** under normal light and illumination with 365 nm UV light (scale bar, 1.0 cm). (c) Normal light and UV light images of **TPE-CS** samples obtained after treating with freeze-thaw dissolving procedure in LiOH-urea aqueous solution (scale bar, 1.0 cm). (d) Emission spectra of various **TPE-CS** solution, where the intensity of the sample C was considered as zero, since sample C cannot be dissolved in the LiOH-urea solvent. (e) Photographs for the stepwise formation of hydrogel with **TPE-CS**: (i) solution of **TPE-CS**, (ii) **TPE-CS** gel after gelation, and (iii) **TPE-CS** hydrogel after complete removal of LiOH and urea (scale bar, 5.0 mm). (f) The schematic illustration for the mechanism associated with the formation of the junction points of **CS** hydrogel in LiOH-urea solution: (i) well-dissolved solution of **TPE-CS**; (ii) formation of various inter/intramolecular hydrogen bonds of **CS**, induced by heating; (iii) formation of crystalline (physical

junctions) within **CS** gel; and (iv) formation of H-bonds of **CS**, induced by the removal of LiOH and urea. (Adapted with permission from ref 31).

Visualization of gelation process by AIE fluorogens has been reported by Wang, Hu, Tang and co-workers (**Figure 2.4**).<sup>[31]</sup> These authors have proposed the mechanism for the gelation of chitosan LiOH-urea aqueous system by focusing on the formation of several junction points including H-bonded and crystalline (physical junctions). **Figure 2.4a** shows the molecular structures of different tetraphenylethene-labelled chitosan (**TPE-CS**). The degree of labelling of three different **CS** samples was gradually increased from 0.93 to 1.54 followed by 3.56 mol% and were designated as sample A, B and C, respectively. The powder samples were found to be light yellow in appearance under normal light, however, exhibited a strong blue luminescence under illumination of 365 nm UV light (**Figure 2.4b**). Sample A and B were found to be soluble in LiOH-urea aqueous solvent, whereas C was found to be least soluble (**Figure 2.4c**), owing to the strong hydrophobic interaction between tetraphenylethene chromophores. However, based on the emission spectra as shown in **Figure 2.4d**, sample **B** has been considered as optimum condition to understand the mechanism for AIE. The precreation method of **TPE-CS** hydrogels in LiOH-urea solvent is shown in **Figure 2.4e**, which includes thermal gelation followed by a rinse procedure. The stepwise mechanistic pathway leading to gelation has been shown in **Figure 2.4f**. At the initial stage, a dynamic intermolecular interaction occurs between LiOH, urea and polysaccharide in the alkaline medium, where a molecular level interaction takes place through H-bonding between OH<sup>-</sup> (hydroxyl) anions with the -NH<sub>2</sub> and -OH



present on the **CS** chain and hence **CS** becomes highly soluble in aqueous medium (**Figure 2.4f** (i)). Thereafter, the gelation mechanism is mainly guided by two competitive reactions, where the first reaction describes the formation of H-bonds between  $\text{OH}^-$  and **CS** and the second one deals with the formation of inter/intramolecular H-bonds among **CS**. It has been observed that rise in the temperature of the system cannot significantly affect the second reaction with respect to the first one and hence the equilibrium completely shifts to the direction, where a large number of inter/intramolecular H-bonds can be formed among **CS** units along with the formation of crystalline (**Figure 2.4f** (ii,iii)). At the final rinse stage, which is mainly driven by the changes of the components present within the system, the equilibrium is further shifted towards the formation of more numbers of inter/intramolecular H-bonds among **CS** and thereby forming a very stable and tough gel (**Figure 2.4f** (iv)). Essentially, both the stages during gelation have a common phenomenon, dealing with the reduction in the interactions between solvent and molecules so that the inter/intramolecular interactions among **CS** can be increased.

We have previously exploited PEs to design fluorescent assemblies and organogels that respond to various stimuli.<sup>[8,32-37]</sup> For example, the weak blue fluorescence of a PE attached with hydrophilic terminal groups has been shown to enhance upon contact with water, resulting in intense cyan emission.<sup>[35]</sup> In view of this observation, we thought of investigating the role of the nature of the side chains<sup>[38-41]</sup> on the terminal moiety of PEs on their emission behavior. For this purpose, we have designed PEs **1** and **2**, in which the PE core is connected to a benzamide moiety bearing linear achiral or branched chiral alkoxy

chains, respectively (**Chart 2.1**). It is envisaged that the presence of solubilizing achiral and chiral side chains could modulate the amide H-bond directed assembly of PE molecules and allow to explore their SIEE behavior in terms of small structural difference.

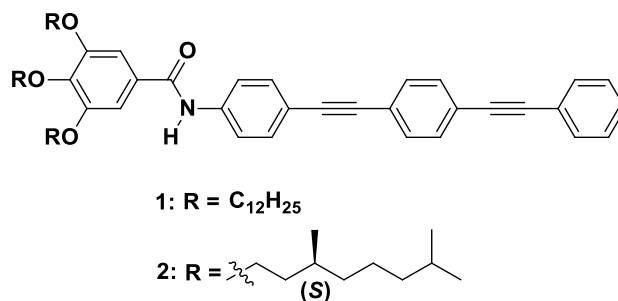
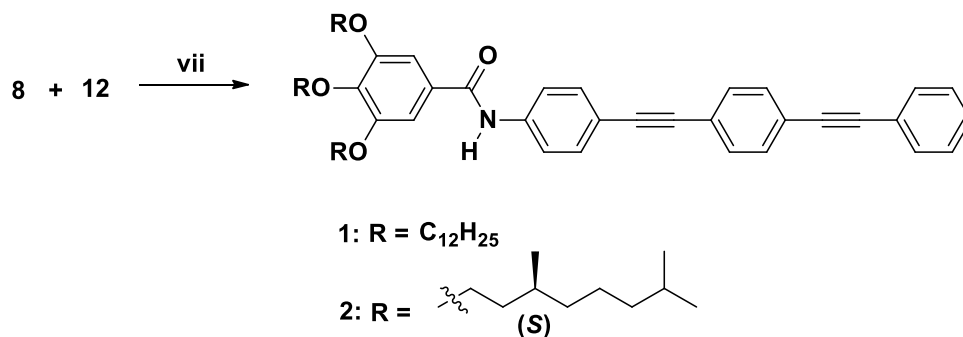
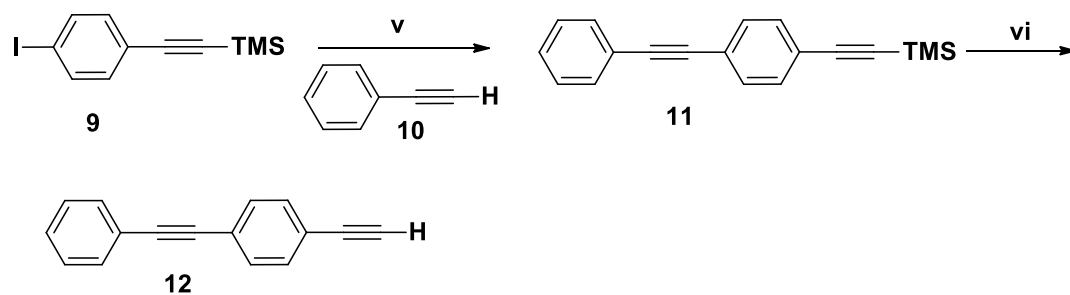
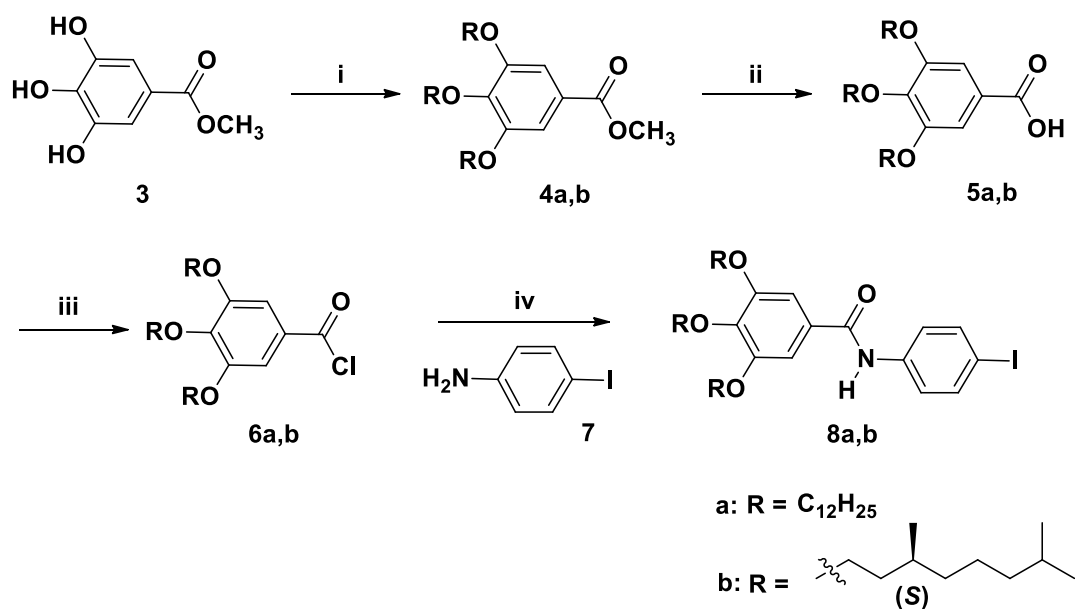


**Chart 2.1.** Molecular structures of the PE-based achiral (**1**) and chiral (**2**) gelators.

## 2.3. Results and Discussion

### 2.3.1. Synthesis of PE Derivatives

The PE derivatives **1** and **2** were synthesized using multistep palladium-catalyzed Sonogashira-Hagihara cross coupling reactions between 3,4,5-trialkoxy-*N*-(4-iodophenyl)benzamide (**8**) and 1-ethynyl-4-(phenylethynyl)benzene (**12**), as shown in **Scheme 2.1**. At first, methyl-3,4,5-trihydroxybenzoate (**3**) on reaction with linear-achiral and branched-chiral alkyl bromides in dry DMF in the presence of anhydrous K<sub>2</sub>CO<sub>3</sub> afforded different alkyl chain substituted methyl-3,4,5-trialkoxybenzoate derivatives **4a** in 80% and **4b** in 70% yields, respectively. Thereafter, ester hydrolysis of **4** in the presence of KOH provided 3,4,5-trialkoxybenzoic acid (**5**) in 90% yield. Subsequently, **5** was converted to 3,4,5-trialkoxybenzoyl chloride (**6**) in the presence of SOCl<sub>2</sub>, which was further allowed to immediately interact with 4-iodoaniline (**7**), providing 3,4,5-trialkoxy-*N*-(4-iodophenyl)benzamide in 70 and 60% yield for **8a** and **8b**, respectively.



**Scheme 2.1.** Reagents and conditions: (i) C<sub>12</sub>H<sub>25</sub>Br/(S)-C<sub>10</sub>H<sub>21</sub>Br, K<sub>2</sub>CO<sub>3</sub>, DMF, 80 °C, 24 h; (ii) KOH, EtOH, 80 °C, 12 h; (iii) SOCl<sub>2</sub>, CH<sub>2</sub>Cl<sub>2</sub>, r.t., 5 h; (iv) toluene, Et<sub>3</sub>N, r.t., 12 h; (v) PdCl<sub>2</sub>(PPh<sub>3</sub>)<sub>2</sub>, CuI, THF, Et<sub>3</sub>N, r.t., 12 h; (vi) KF, CH<sub>2</sub>Cl<sub>2</sub>, MeOH, r.t., 6 h; (vii) PdCl<sub>2</sub>(PPh<sub>3</sub>)<sub>2</sub>, CuI, THF, Et<sub>3</sub>N, r.t., 18 h.

In parallel, Sonogashira-Hagihara coupling reaction between ((4-Iodophenyl)ethynyl)trimethylsilane (**9**) with ethynylbenzene (**10**) provided trimethyl((4-(phenylethynyl)phenyl)ethynyl)silane (**11**) with 69% yield. Deprotection of trimethylsilyl group in presence of KF gave 1-ethynyl-4-(phenylethynyl)benzene (**12**) in 94% yield. At last, Sonogashira-Hagihara cross coupling reaction of the molecule **8a** or **8b** with **12** provided **1** and **2** with 48 and 60% yield, respectively. All intermediates and final products have been characterized by  $^1\text{H}$  and  $^{13}\text{C}$  NMR spectroscopy and high-resolution mass spectrometry. The detailed procedure of synthesis and characterization data are provided in the experimental section 2.5.3.-2.5.9.

### 2.3.2. Photophysical Studies

In order to understand the aggregation properties, UV-vis absorption studies of **1** and **2** in chloroform and *n*-decane ( $5 \times 10^{-4}$  M) have been carried out. At 298 K in chloroform, **1** exists as monomers which showed a strong  $\pi$ - $\pi^*$  absorption band with a maximum ( $\lambda_{\text{max}}$ ) at 333 nm (**Figure 2.5a**). In *n*-decane at 363 K, the absorption spectrum of **1** was almost similar to that in chloroform with  $\lambda_{\text{max}}$  at 332 nm, whereas at 283 K, the  $\lambda_{\text{max}}$  was found blue-shifted to 307 nm with the formation of a new shoulder band at 372 nm (**Figure 2.5a**). Similarly, in chloroform at 298 K, **2** showed a strong  $\pi$ - $\pi^*$  absorption band with  $\lambda_{\text{max}}$  at 334 nm, whereas in *n*-decane at 283 K, a decrease in the intensity with no shift of  $\lambda_{\text{max}}$  was observed (**Figure 2.5c**). Temperature-dependent absorption spectral changes of **1** in *n*-decane confirmed transition from the monomers at a higher

temperature (363K) to the aggregates at 283 K (**Figure 2.5a**). While gradually decreasing the temperature, a gradual decrease in the intensity of  $\lambda_{\max}$  at 332 nm accompanied by a concomitant increase in the intensity of the shoulder band at 372 nm with an isosbestic point at 364 nm was noticed. Similarly, the temperature-dependent absorption spectra of **2** displayed a gradual decrease in the intensity of  $\lambda_{\max}$  at 334 nm

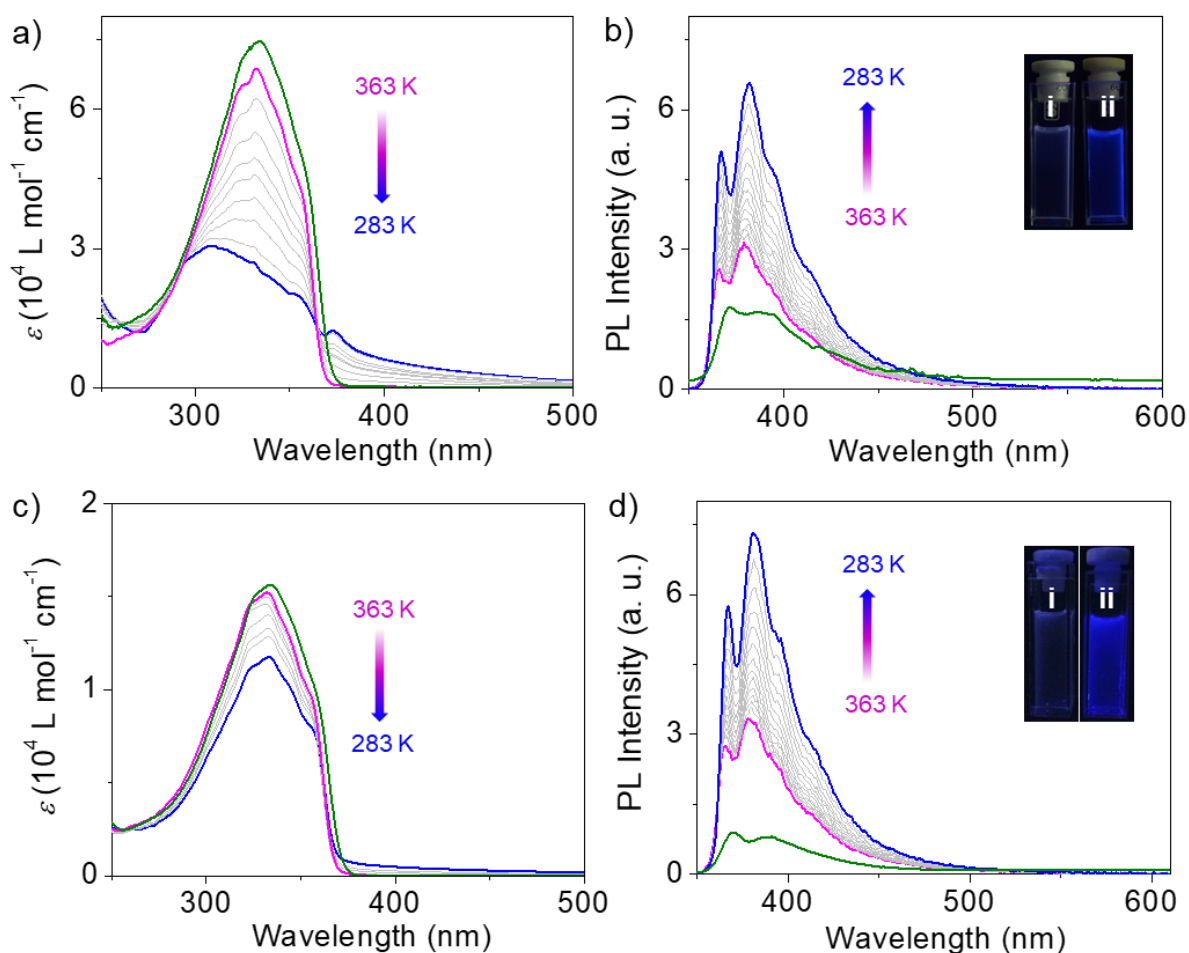


**Figure 2.5.** Absorption and emission ( $\lambda_{\text{ex}} = 340 \text{ nm}$ ) spectra of (a,b) **1** and (c,d) **2** in chloroform (— at 298 K) and *n*-decane ( $5 \times 10^{-4} \text{ M}$ ). Temperature-dependent absorption and emission spectra of (a,b) **1**<sub>agg</sub> and (c,d) **2**<sub>agg</sub> in *n*-decane (— at 283 K and - - at 363 K). Inset shows the photographs of (i) monomers and (ii) aggregates emission of **1** and **2** under 365 nm UV light illumination.

with a concomitant increase in the intensity of the band at 385 nm with an isosbestic point at 365 nm (**Figure 2.5c**).

The emission studies of **1** and **2** have also been carried out in chloroform and *n*-decane ( $5 \times 10^{-4}$  M). In the case of **1** in chloroform (298 K), a very weak emission with maxima centered at 372 and 385 nm ( $\Phi_F = 0.02$ ) was observed (**Figure 2.5b**). However, in *n*-decane, aggregates of **1** (**1<sub>agg</sub>**) exhibited structured and enhanced emission with maxima at 367 and 382 nm ( $\Phi_F = 0.34$ ) in comparison to the chloroform solution, where the molecules exist in the monomeric state.

Similarly, **2** in the monomeric state also showed a weak emission in chloroform with maxima at 367 and 381 nm ( $\Phi_F = 0.02$ ), whereas in *n*-decane, **2<sub>agg</sub>** exhibited enhanced emission ( $\Phi_F = 0.25$ ) (**Figure 2.5d**). These observations indicate that both the molecules are SIEE active in their aggregated state. To further confirm the SIEE behavior, we have carried out temperature-dependent emission studies of **1<sub>agg</sub>** and **2<sub>agg</sub>**. Both **1** and **2** showed a gradual increase in the emission intensity while decreasing the temperature from 363 to 283 K. Around a 2-fold enhancement in emission was noticed upon comparing the emission intensities of *n*-decane solutions at 363 and 283 K (**Figure 2.5b,d**). Encouraged by these observations, we have carried out detailed studies on the effect of hierarchical self-assembly of **1** and **2** on their emission behavior.

Self-assembly pathway of both **1** and **2** in *n*-decane was probed by monitoring the changes in UV-vis absorption spectra as a function of temperature by maintaining a fixed cooling rate of  $1 \text{ Kmin}^{-1}$ . The plot of  $\alpha_{\text{agg}}$  with respect to the gradual decrease in

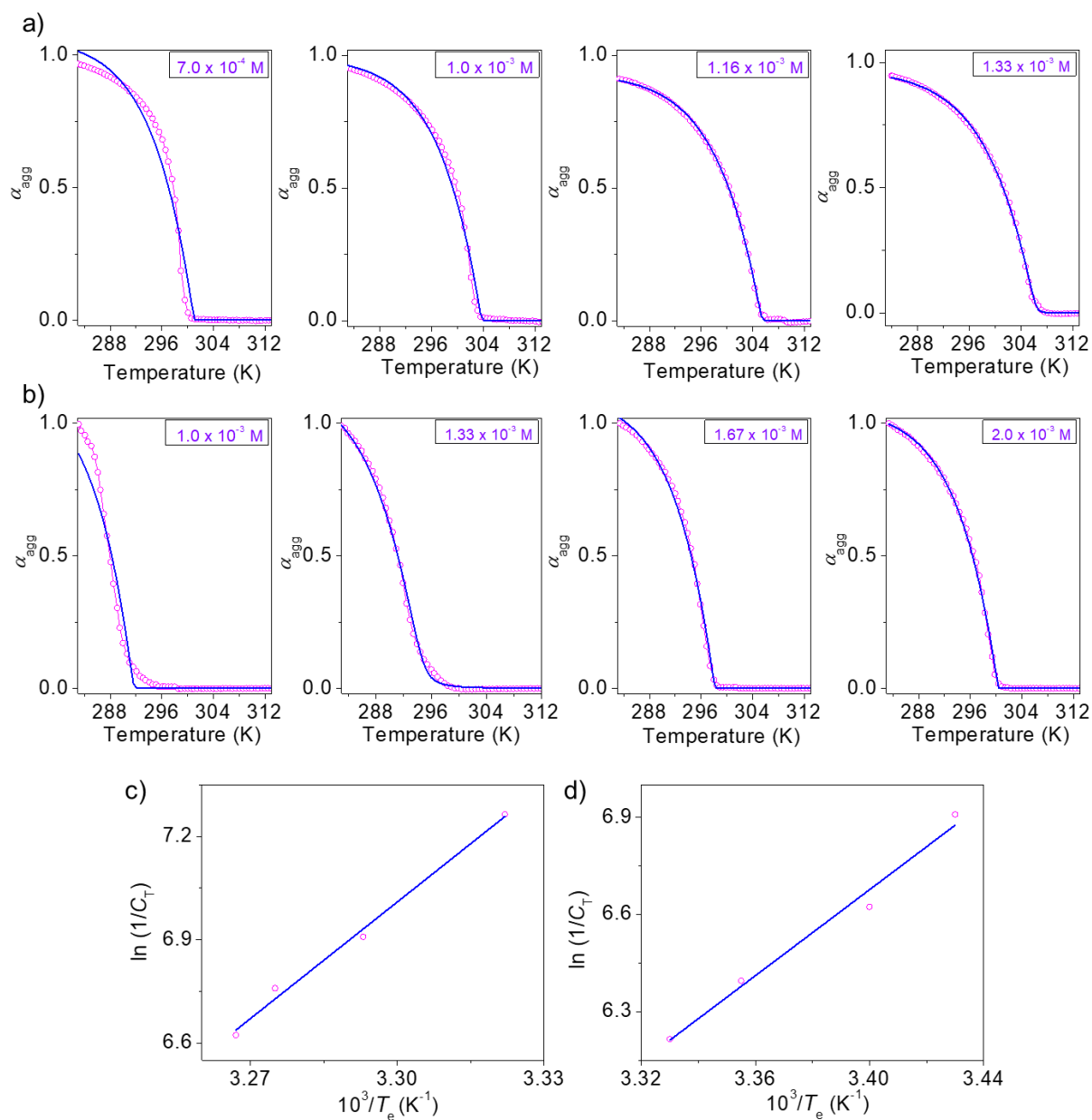


**Figure 2.6.** Plot of fraction of aggregates ( $\alpha_{agg}$ ) versus temperature (cooling rate of 1 Kmin $^{-1}$ ) at different concentrations of (a)  $\mathbf{1}_{agg}$  and (b)  $\mathbf{2}_{agg}$  in *n*-decane. The cooperative supramolecular polymerization can be described using the individual EQ model fitting.<sup>[42,43]</sup> Deviations in the fitting was observed for  $7 \times 10^{-4}$  M for  $\mathbf{1}_{agg}$  and  $1 \times 10^{-3}$  M for  $\mathbf{2}_{agg}$ . van 't Hoff plot showing the relationship between natural logarithm of the reciprocal concentration and reciprocal  $T_e$ , obtained through the cooling experiments in *n*-decane for (c)  $\mathbf{1}_{agg}$  and (d)  $\mathbf{2}_{agg}$ .

**Table 2.1.** Concentration dependent changes in the  $T_e$  of **1**<sub>agg</sub> in *n*-decane.  $T_e$  is obtained from the individual EQ model fitting of the temperature dependent  $\alpha_{agg}$ , **Figure 2.6a**.<sup>[42,43]</sup>

$C$ (M)	$T_e$	$T_e$ (STD)
$7.0 \times 10^{-4}$	300.989479	0.326989
$1.0 \times 10^{-3}$	303.718176	0.209710
$1.16 \times 10^{-3}$	305.332795	0.064197
$1.33 \times 10^{-3}$	306.133435	0.079472

STD = standard deviation (deviation from the actual value)

**Table 2.2.** Concentration dependent changes in the  $T_e$  of **2**<sub>agg</sub> in *n*-decane.  $T_e$  is obtained from the individual EQ model fitting of the temperature dependent  $\alpha_{agg}$ , **Figure 2.6b**.<sup>[42,43]</sup>

$C$ (M)	$T_e$	$T_e$ (STD)
$1.0 \times 10^{-3}$	291.572029	0.540577
$1.33 \times 10^{-3}$	294.108150	0.221531
$1.67 \times 10^{-3}$	298.092400	0.130002
$2.0 \times 10^{-3}$	300.304367	0.071274

temperature revealed non-sigmoidal nature of the cooling curves for a wide range of concentrations for **1** ( $7 \times 10^{-4}$  to  $1.33 \times 10^{-3}$  M) and **2** ( $1 \times 10^{-3}$  to  $2 \times 10^{-3}$  M). For all the concentrations under study, the cooling curves could be fitted with an equilibrium model<sup>[42-44]</sup> characteristic of a co-operative self-assembly process (**Figure 2.6a,b**).<sup>[37,41-48]</sup> A gradual shift in the  $T_e$  to higher temperatures was observed upon increasing the concentration



(Table 2.1 and 2.2). The plot between the natural logarithm of the reciprocal concentration of **1** against reciprocal of  $T_e$  exhibited a linear relationship (Figure 2.6c).

From the van 't Hoff plot (Figure 2.6c), we have estimated the  $\Delta H^\circ$  and  $\Delta S^\circ$  values as  $-93.74 \text{ kJmol}^{-1}$  and  $-251.07 \text{ Jmol}^{-1}\text{K}^{-1}$ , respectively. With the help of  $\Delta H^\circ$  and  $\Delta S^\circ$ , the  $\Delta G^\circ$  at 298 K for **1**<sub>agg</sub> has been determined to be  $-18.92 \text{ kJmol}^{-1}$ . Similar to this, the van 't Hoff plot for **2**<sub>agg</sub> in *n*-decane also exhibited a linear relationship (Figure 2.6d), from where the thermodynamic parameters such as  $\Delta H^\circ = -55.13 \text{ kJmol}^{-1}$ ,  $\Delta S^\circ = -131.94 \text{ Jmol}^{-1}\text{K}^{-1}$ ,  $\Delta G^\circ = -15.81 \text{ kJmol}^{-1}$  have been determined. The standard thermodynamic parameters obtained for both **1**<sub>agg</sub> and **2**<sub>agg</sub> in *n*-decane indicate the involvement of nucleation-elongation process as found in the case of H-bonded supramolecular polymers.<sup>[37,43,46,47]</sup>

### 2.3.3. Morphological Characterization

To gain visual insight about the morphology of **1**<sub>agg</sub> and **2**<sub>agg</sub> in *n*-decane, samples were dropcast over carbon-coated copper grid and imaged using TEM. Images of **1**<sub>agg</sub> showed micrometer long entangled fibers, whereas **2**<sub>agg</sub> displayed the formation of right-handed micrometer long twisted helical fibers (Figure 2.7a,b). In both the cases, the width of the fibers is found within 50-200 nm. TEM image of **1**<sub>agg</sub> reveals that the elongated fibers are formed by lateral bundling of thin fibrils of a few nanometers in width. In the case of **2**<sub>agg</sub>, helical bundling of such thin helices resulted in super-helical fiber bundles.<sup>[37, 49-51]</sup>

In order to further establish the formation of helical fibers of **2**, chiroptical properties were studied in comparison with **1** in chloroform and *n*-decane at 298 K (Figure 2.8). As

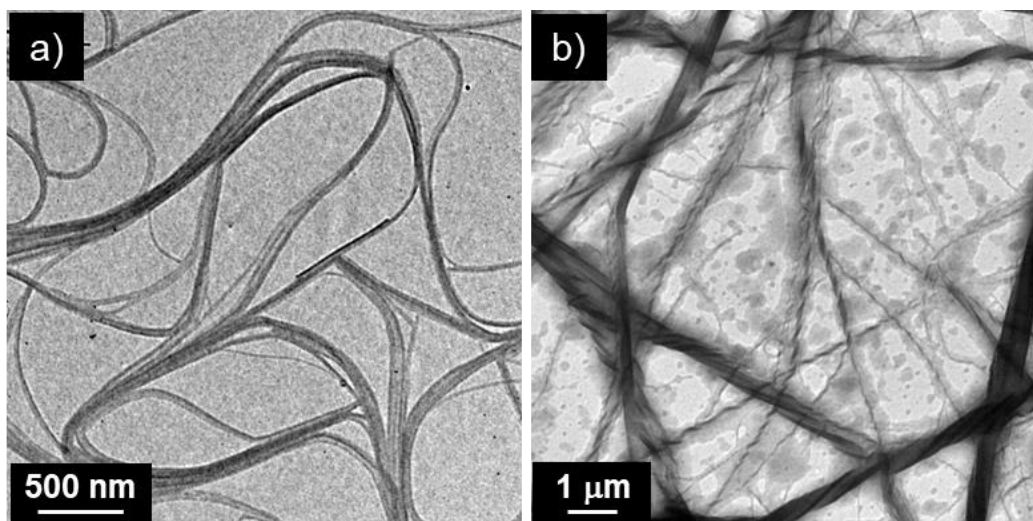


Figure 2.7. TEM images of (a)  $1_{agg}$  and (b)  $2_{agg}$  in *n*-decane ( $5 \times 10^{-4}$  M).

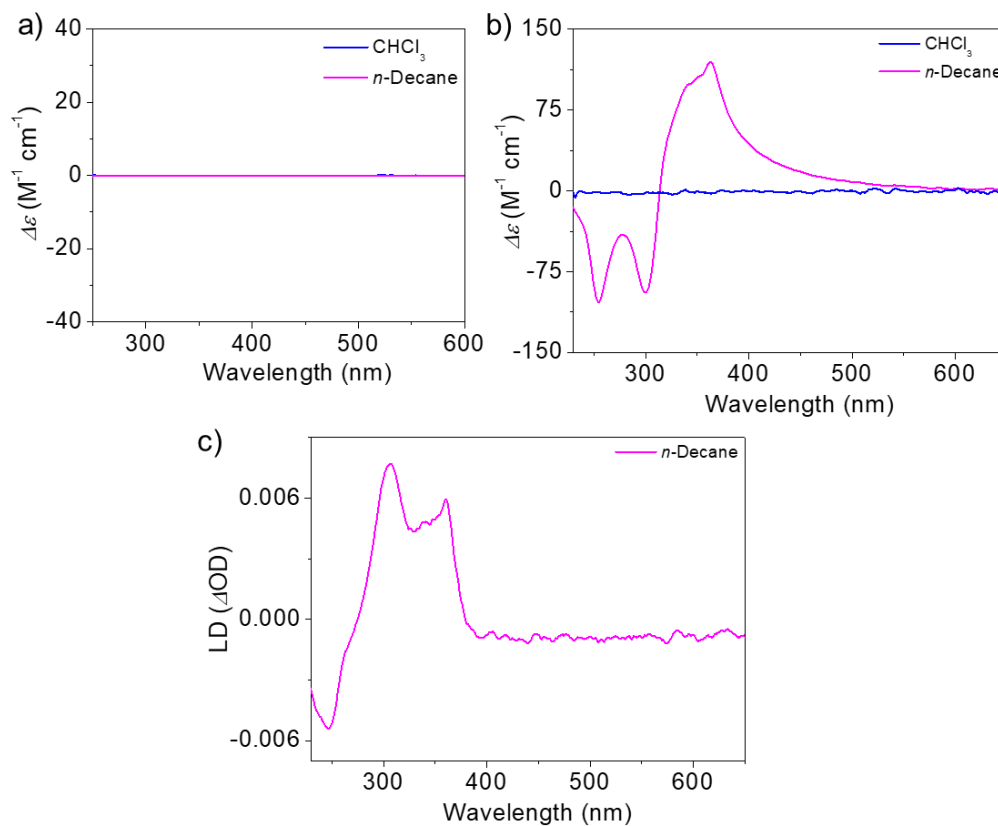


Figure 2.8. CD spectra of (a)  $1_{agg}$  and (b)  $2_{agg}$  in chloroform and *n*-decane ( $5 \times 10^{-4}$  M) at 298 K. (c) LD spectrum of  $2_{agg}$  in *n*-decane ( $5 \times 10^{-4}$  M) at 298 K.

anticipated, both the compounds were CD-silent in chloroform ( $5 \times 10^{-4}$  M), indicating their existence as monomers. In addition, **1**<sub>agg</sub> in *n*-decane ( $5 \times 10^{-4}$  M) did not show any CD activity since molecule is achiral (**Figure 2.8a**). However, CD measurements of **2**<sub>agg</sub> in *n*-decane ( $5 \times 10^{-4}$  M) exhibited a bisignate Cotton effect (**Figure 2.8b**). In this case, an intense positive signal at 363 nm followed by two negative signals at 300 and 255 nm were noticed. The observed CD spectrum might include contribution from the LD effect associated with the fiber bundling (**Figure 2.8c**).<sup>[44]</sup>

### 2.3.4. Gelation Studies

Interestingly, both **1** and **2** formed gels in *n*-decane above a critical concentration. Hence, gelation abilities of these molecules were examined in various hydrocarbon solvents and the results are summarized in **Table 2.3**. In all the solvents tested, the CGC values of **1** have been found to be lower than that of **2**. For instance, in *n*-decane, CGC of **1** is 8.8 mM and that of **2** is 23.6 mM, which implies that **1** having achiral dodecyloxy side chains is a better gelator in comparison to that of **2** containing branched chiral decyloxy side chains. This gelation ability has been further confirmed by studying the viscoelastic nature of the gels in *n*-decane (**Figure 2.9**). Dynamic frequency sweep experiments revealed that the  $G'$  and  $G''$  values are independent of the oscillation frequency within the range of 1-100 rad s<sup>-1</sup>, where the  $\gamma$  has been kept fixed at 0.01 (**Figure 2.9a,b**). In both cases, the  $G'$  value is obtained to be an order of magnitude higher than  $G''$ , a characteristic feature of supramolecular gels.<sup>[52-54]</sup> Furthermore, the individual values of  $G'$  and  $G''$  of **1**<sub>gel</sub> was found higher than that of the **2**<sub>gel</sub>, which shows the ability of **1** to form a stronger gel in *n*-decane.

Quantitative analysis of rheological studies showed that  $\mathbf{1}_{\text{gel}}$  is 2.6 times stronger with respect to  $\mathbf{2}_{\text{gel}}$  formed in *n*-decane, which almost matches the ratio ( $\sim 2.68$ ) of CGC values of **2** and **1** in *n*-decane. This behavior was found to remain unaltered when the nature of the nonpolar solvents was varied to other linear or cyclic solvents (**Table 2.3**).

**Table 2.3.** CGC (in mM)<sup>a</sup> of **1** and **2** in different solvents.

Compound	<i>n</i> -Decane	MCH	Cyclohexane	<i>n</i> -Hexane	Toluene
<b>1</b>	8.8 (G)	12.5 (G)	16.6 (G)	10.1 (G)	(S)
<b>2</b>	23.6 (G)	29.0 (G)	39.2 (G)	14.7 (G)	(S)

<sup>a</sup>CGC = is the minimum concentration required for the formation of a stable gel at room temperature. In parenthesis, G = gel and S = solution at room temperature.

SEM image of the dried  $\mathbf{1}_{\text{gel}}$  revealed the formation of entangled fibers having a length of several micrometers (**Figure 2.9c**), which is found to be almost similar to that of the morphologies obtained by TEM at lower concentration (**Figure 2.7a**). On the contrary, SEM images of  $\mathbf{2}_{\text{gel}}$  exhibited coiling of individual fibers to form right-handed supercoiled fibers (**Figure 2.9d**) having similarity with that of the TEM images obtained at lower concentration (**Figure 2.7b**). The observed morphologies of the gels are found to have correlation with the texture of the gel (insets of **Figure 2.9c** and **2.9d**).  $\mathbf{1}_{\text{gel}}$  and  $\mathbf{2}_{\text{gel}}$  in *n*-decane under normal light are translucent and opaque in nature, respectively. The translucent nature of  $\mathbf{1}_{\text{gel}}$  indicates less scattering of light as a result

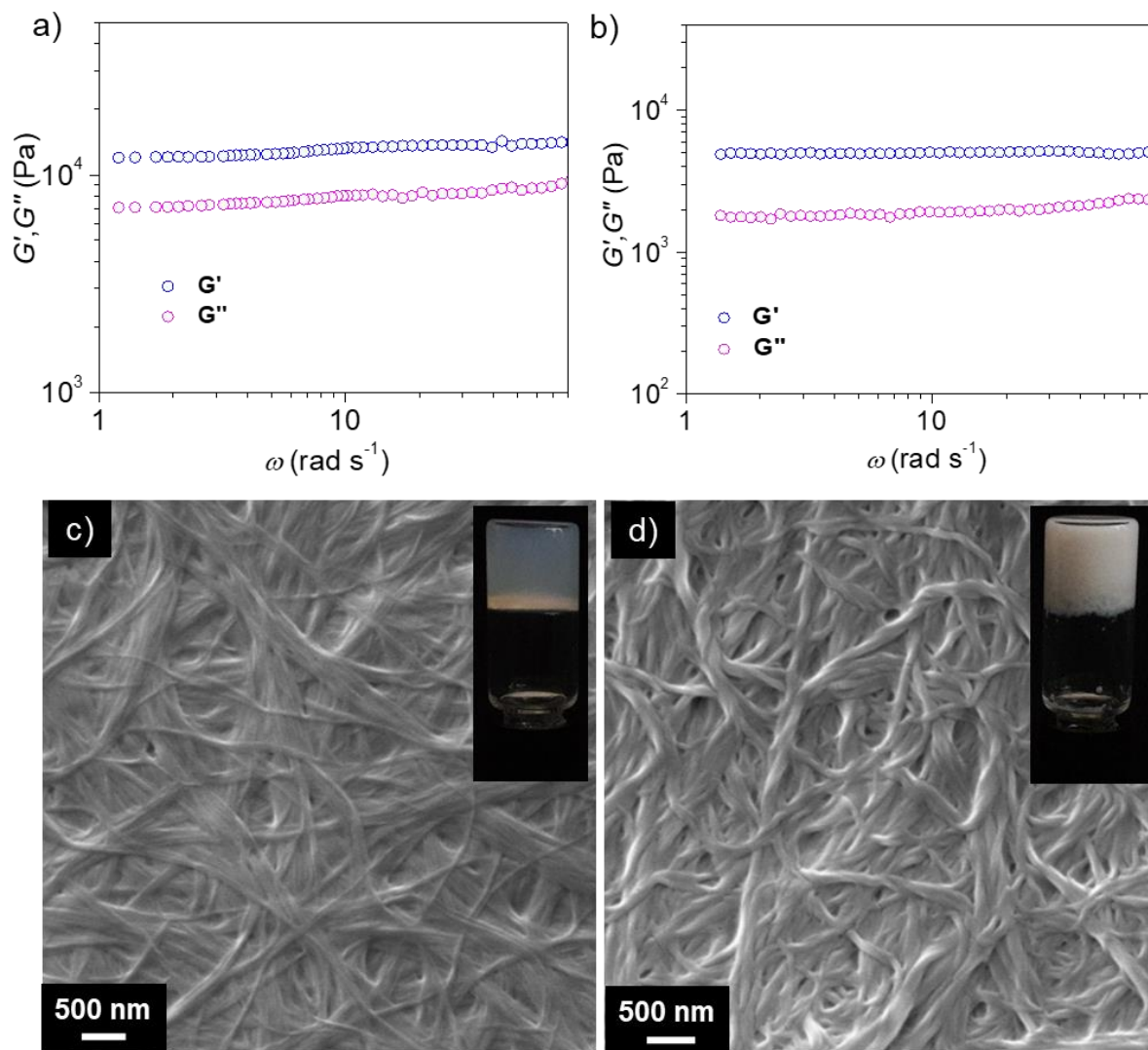


**Figure 2.9.** Plot of dynamic storage modulus ( $G'$ , blue) and loss modulus ( $G''$ , magenta) against angular frequency ( $\omega$ ) for (a) **1** (8.8 mM) and (b) **2** (23.6 mM) *n*-decane gels at 293 K, at a strain amplitude ( $\gamma$ ) of 0.01. SEM images of (c) **1** and (d) **2** *n*-decane gels. Inset shows the photographs of the corresponding *n*-decane gels under normal light.

of bundling of thin fibers. On the other hand, coiling of helical fibrils forming thick supercoiled fibers in  $\mathbf{2}_{\text{gel}}$  scatter light in a greater extent and thus makes the gel opaque.

## 2.3.5. FT-IR Studies

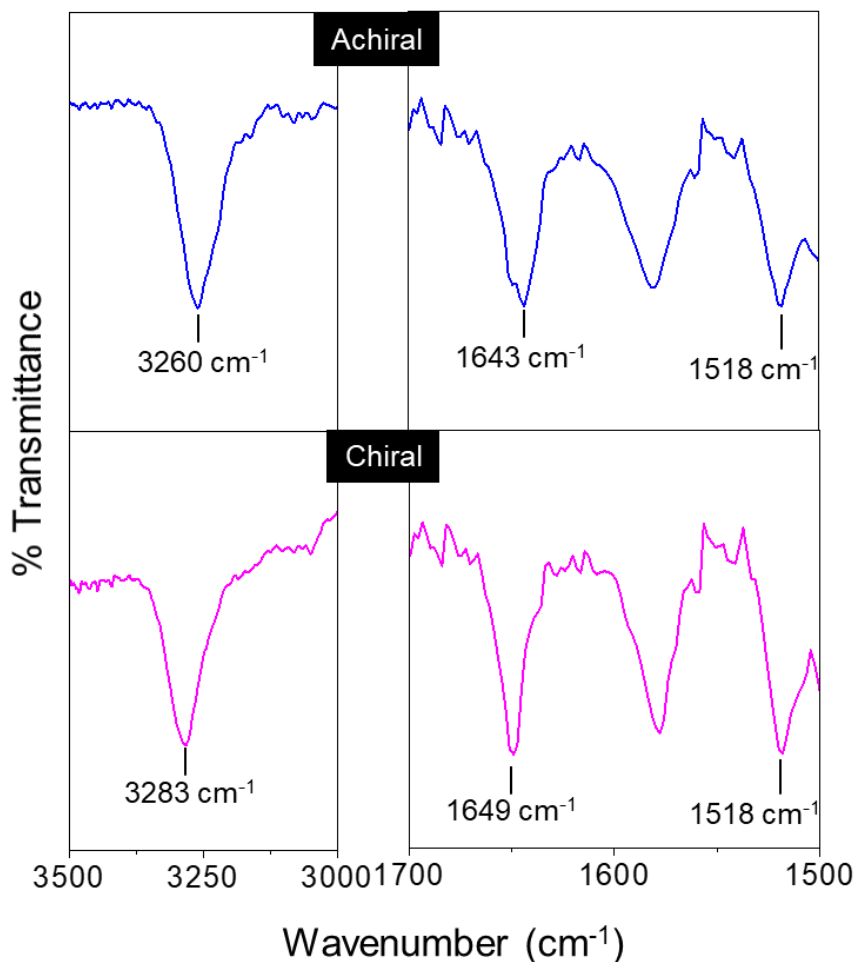


**Figure 2.10.** Film state FT-IR spectra of **1** (achiral) and **2** (chiral) *n*-decane xerogels.

Formation of non-helical and helical 1D assemblies by **1** and **2** in *n*-decane, respectively, can be considered as a result of cooperative involvement of various non-covalent motifs including alkoxy side chains, amide functional group and  $\pi$ -conjugated units.

FT-IR spectrum of **1** revealed H-bonded N-H stretching frequency at 3260 cm<sup>-1</sup>, the amide I band at 1643 cm<sup>-1</sup> and the amide II band at 1518 cm<sup>-1</sup>, indicating the involvement of intermolecular H-bonding in the assembly process (**Figure 2.10** upper panel).<sup>[38,55]</sup>

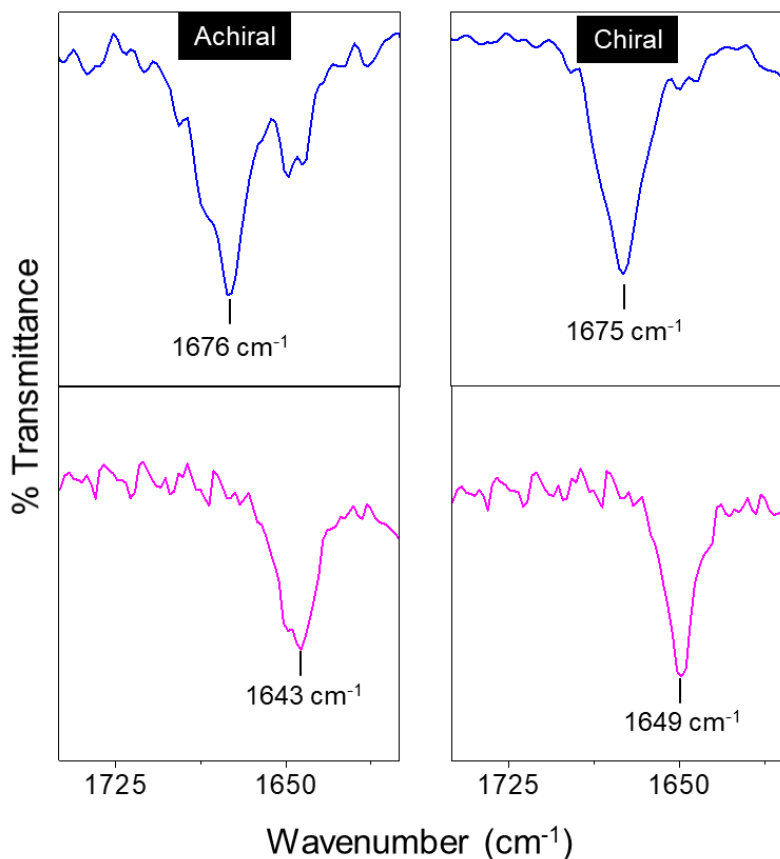


**Figure 2.11.** Comparison between the FT-IR spectra of **1** (achiral) and **2** (chiral) in their monomeric solution (blue) and *n*-decane xerogel film state (magenta) showing the changes in the Amide I band.

However, the same peaks were shifted to 3283, 1649 and 1518 cm<sup>-1</sup>, respectively, for **2** (**Figure 2.10** lower panel), which clearly signifies weakening of the amide H-bonding. Moreover, a significant shift in the amide I band was observed for xerogel films of **1** and **2** in comparison to their monomers in CDCl<sub>3</sub>, corroborating to the intermolecular amide H-bonding in the gel state (**Figure 2.11**). This observation was further supported by comparing the shift of symmetric and asymmetric –CH<sub>2</sub> vibrations of both **1** and **2** xerogel films (**Figure 2.12**). FT-IR spectrum of **1** displayed symmetric and asymmetric –CH<sub>2</sub> vibrations around 2848 and 2918 cm<sup>-1</sup>, respectively. On the other hand, a shift in the symmetric and asymmetric –CH<sub>2</sub> vibrations to 2870 and 2924 cm<sup>-1</sup>, respectively, was

noticed in the case of **2**. These results indicate that linear alkoxy chains of **1** are in all *trans* configuration and interdigitated, whereas the branched chiral alkoxy chains of **2** remain non-interdigitated.<sup>[55]</sup>

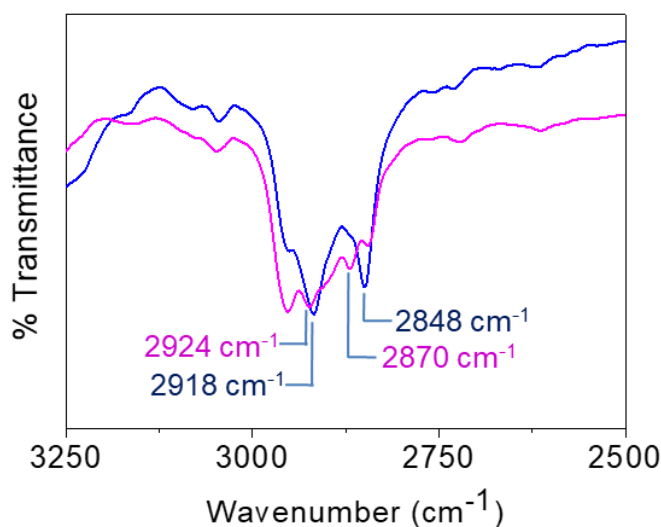


**Figure 2.12.** FT-IR spectra of the xerogel film of **1** (blue) and **2** (magenta) showing the asymmetric and symmetric methylene stretching.

### 2.3.6. WAXS Studies

To understand the role of molecular packing on morphological properties and gel strength of **1** and **2**, we have carried out WAXS analysis. **Figure 2.13a** shows the WAXS pattern of **1** xerogel exhibiting two well-resolved peaks with a reciprocal *d*-spacing ratio of 1:2. The two intense sharp diffraction bands observed at 50.7 Å (001) and 25.4 Å (002) indicate a long-range lamellar type arrangement of the molecules.<sup>[55-58]</sup> The intense sharp peak at 50.7 Å corresponds to the width of a single 1D layer of the molecules, when two molecules of **1** are oriented from the opposite direction as shown in **Figure 2.13b**. In addition, the H-bonded intermolecular distance between the secondary amides is found to be ~ 4.3



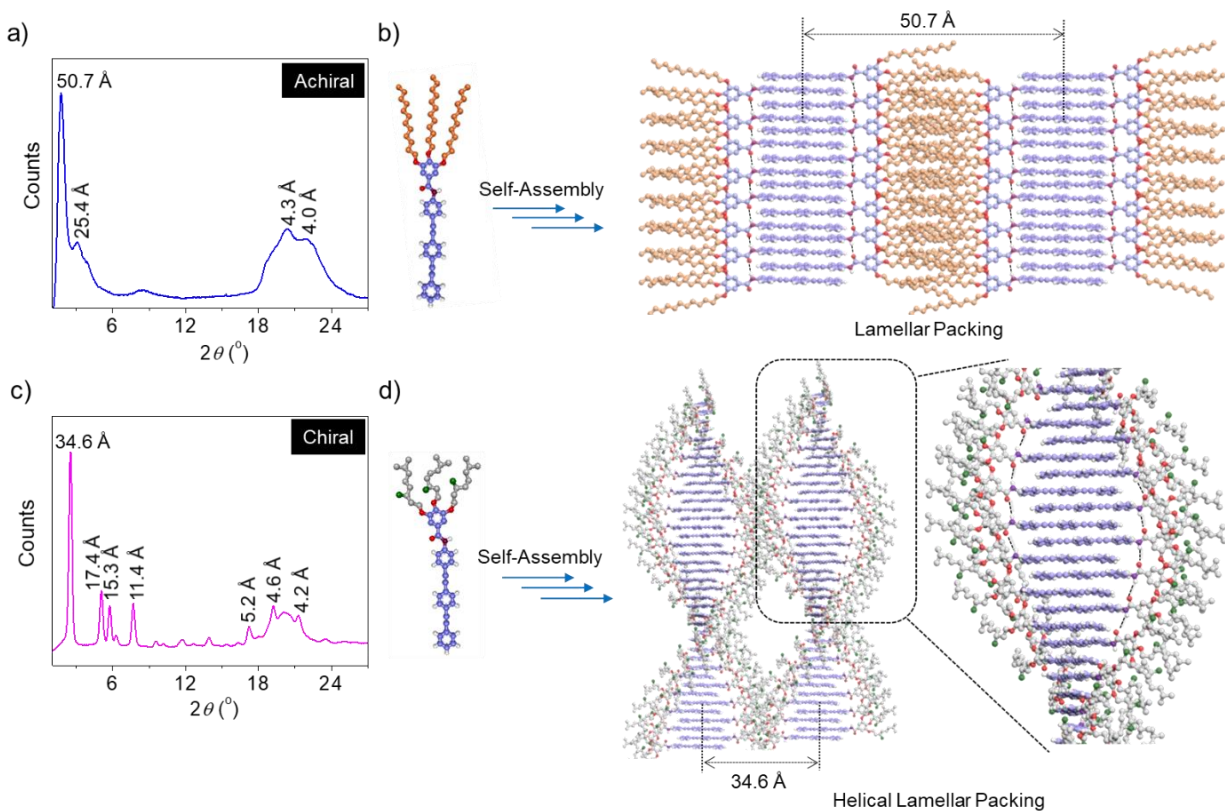


**Figure 2.13.** WAXS pattern of (a)  $1_{agg}$  and (c)  $2_{agg}$  in the xerogel state. Schematic representation of the *n*-decane assemblies of (b)  $1_{agg}$  and (d)  $2_{agg}$ .

Å.<sup>[55,59,60]</sup> As seen in **Figure 2.13c**, the xerogel film of **2** shows a significant difference along with a larger set of reflections at 34.6, 17.4, 15.3, 11.4, 5.2, 4.6, 4.2 Å. The intense reflection at 34.6 Å (001) followed by a weak reflection at 17.4 Å (002) with a *d*-spacing ratio of 1:1/2 confirms lamellar arrangement of **2**. However, the first peak at 34.6 Å corresponds to the inter-columnar period as shown in **Figure 2.13d**<sup>[58]</sup> and the 4.6 Å peak to the H-bonded distance between the secondary amides. Furthermore, the lamellar arrangement of the molecules in **2** changes to a tilted fashion to allow for the  $\pi$ -stacking interaction and thereby leading to the formation of a long-range helical lamellar assembly.

Comparison between the H-bonding distance between **1** and **2** clearly shows that the assembly of **1** is much stronger than that of **2**.

### 2.3.7. SIEE Studies

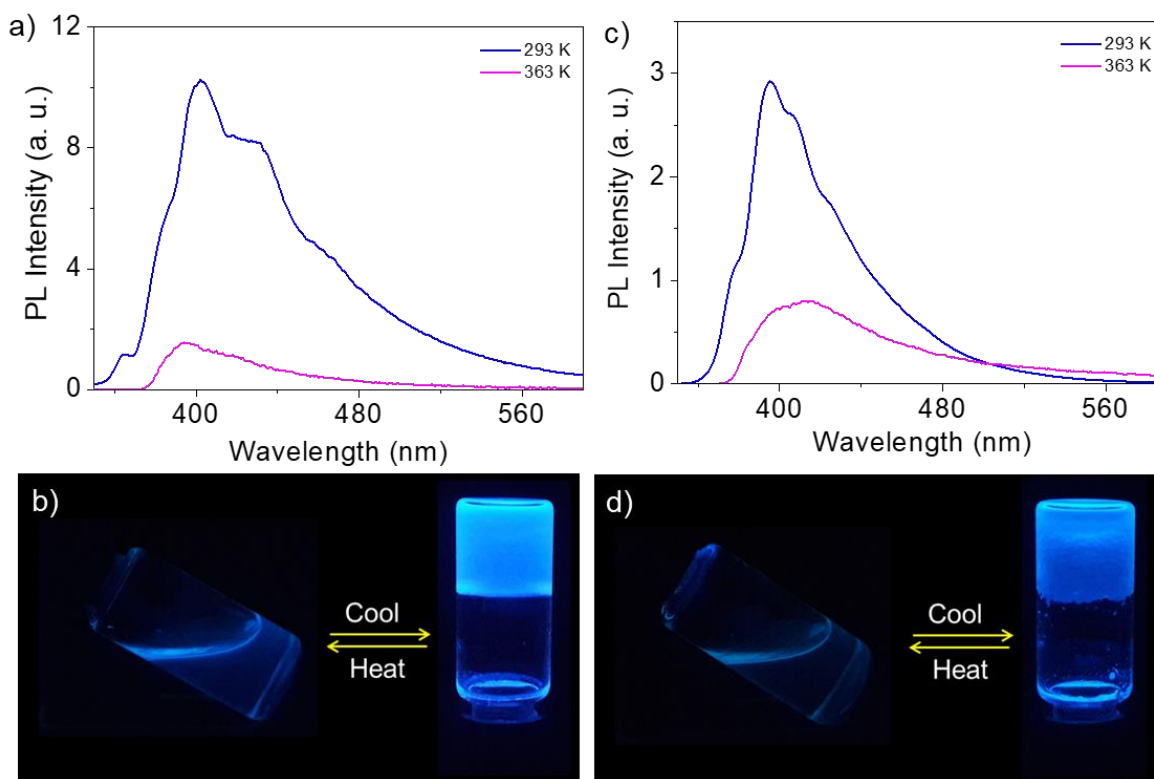


**Figure 2.14.** Emission spectra ( $\lambda_{\text{ex}} = 340 \text{ nm}$ ) of *n*-decane gels (293 K) and the corresponding sols (363 K) of (a) **1** and (c) **2**. Photographs of the corresponding *n*-decane gels and sols under the illumination of 365 nm UV light (b) **1** and (d) **2**.

Interestingly, the gels formed by both **1** and **2** are found to be emissive in the blue region (**Figure 2.14**). In comparison to the *n*-decane gel of **2** ( $\lambda_{\text{max}} = 395 \text{ nm}$ ), the emission maximum of **1**<sub>gel</sub> was found to be slightly red-shifted ( $\lambda_{\text{max}} = 402 \text{ nm}$ ), which points towards the stronger aggregation between the PE chromophores of the latter in presence of linear achiral alkoxy chains. However, in the case of **2**, the presence of asymmetric carbon centers

reduces the interaction between the chromophores leading to the formation of a weak gel with a blue-shifted emission maximum. Furthermore, the solutions formed by heating the corresponding gels at higher temperature (363 K) were found to be less emissive (**Figure 2.14b** and **2.14d**). In fact, the self-assembly induced sol to gel transition resulted in nearly 6.6 and 3.7 times enhancement in the emission intensity of **1** and **2**, respectively, which indicate that the SIEE behavior of these molecules in the gel state<sup>[30,31,61]</sup> by preventing rotation of PE chromophore.<sup>[25-28]</sup> This has been further confirmed with the help of fluorescence microscopy studies, which revealed the strong solid-state emission of **1**<sub>gel</sub> and **2**<sub>gel</sub> (**Figure 2.15a,b**). Fluorescence microscopy images display the presence of blue emissive entangled fibers and densely coiled helical fibers for **1**<sub>gel</sub> and **2**<sub>gel</sub>, respectively.

The SIEE behavior of both **1** and **2** was further studied by measuring the fluorescence decay profiles of monomeric species in chloroform and self-assembled aggregates in *n*-decane (**Figure 2.16**). **1**<sub>agg</sub> in *n*-decane exhibited a bi-exponential decay (emission monitored at  $\lambda_{em} = 382$  nm) having lifetimes of 0.15 (98.22%) and 1.10 ns (1.78%), whereas monomers of **1** in chloroform ( $\lambda_{em} = 372$  nm) exhibited a mono-exponential decay with lifetime of 0.075 ns (**Figure 2.16a**). The increase in the lifetime values of **1**<sub>agg</sub> can be correlated to the formation of H-type aggregates in *n*-decane, which has also been confirmed from the blue shift in the absorption maximum from 333 to 307 nm (**Figure 2.5a**). As in the case of **1**<sub>agg</sub> in *n*-decane, the fluorescence decay profile of **2**<sub>agg</sub> in *n*-decane ( $\lambda_{em} = 381$  nm) was found to follow a bi-exponential decay with

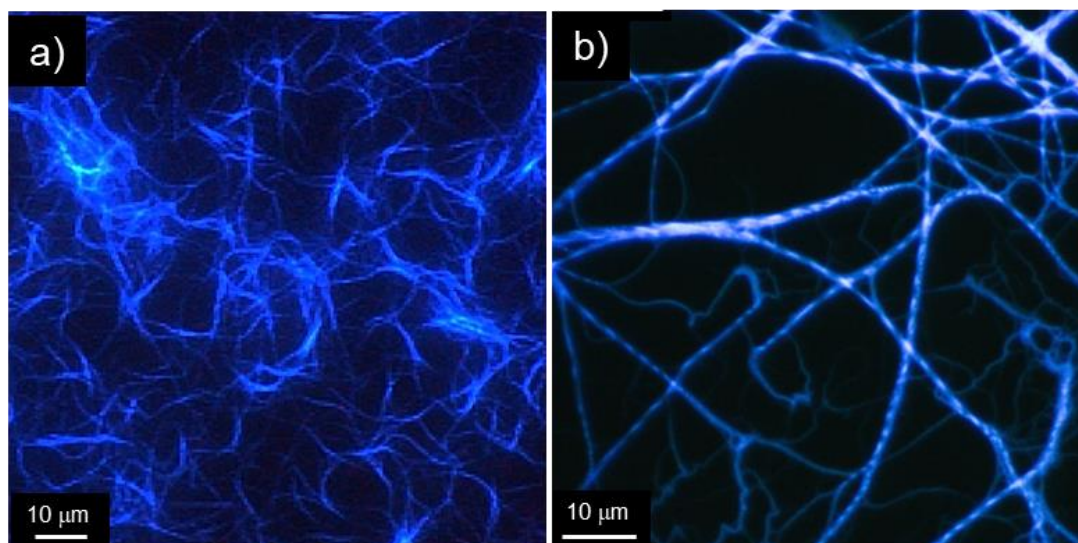


**Figure 2.15.** Fluorescence microscopy images of (a) **1** and (b) **2** *n*-decane xerogels.

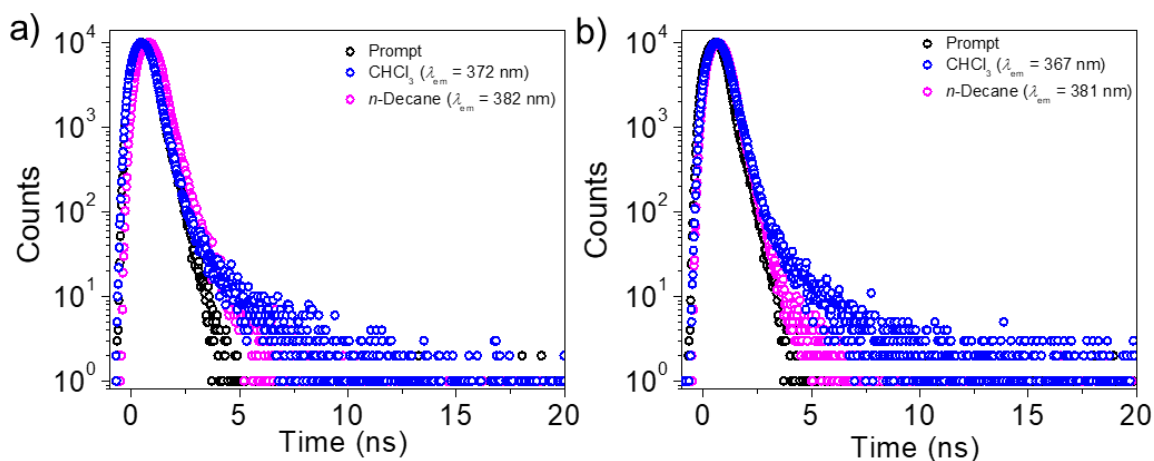


**Figure 2.16.** Lifetime decay profiles of (a) **1** and (b) **2** in chloroform and *n*-decane,  $\lambda_{em}$  monitored has been shown in the figure. In all the cases 331 nm excitation source has been used.

lifetime values 0.06 (81.76%) and 0.18 ns (18.24%) and a mono-exponential decay with lifetime value of 0.15 ns in the monomeric state ( $\lambda_{em} = 367$  nm) (**Figure 2.16b**). The decrease in lifetime value of the major emitting component of **2**<sub>agg</sub> in *n*-decane when compared to that of the monomer in chloroform indicate an assembly different from **1**<sub>agg</sub>

in *n*-decane. The photophysical parameters of **1** and **2** in their monomeric and self-assembled states have been summarized in **Table 2.4**. These data reveal that the *n*-decane aggregates of both **1** and **2** exhibit higher  $k_r/k_{nr}$  values of 0.52, 0.33, respectively than that of the monomeric state in  $\text{CHCl}_3$  ( $k_r/k_{nr}$  values of 0.02, for both **1** and **2**), confirming the SIEE behavior.

**Table 2.4.** Photophysical parameters of **1** and **2** in different conditions.

Compound	$\Phi_F$	$\tau$ (ns)	$k_r$ ( $\text{s}^{-1}$ ) <sup>b</sup>	$k_{nr}$ ( $\text{s}^{-1}$ ) <sup>c</sup>	$k_r/k_{nr}$
<b>1</b> in $\text{CHCl}_3$	0.02	0.08	$2.67 \times 10^8$	$1.31 \times 10^{10}$	0.02
<b>1</b> <sub>agg</sub> in <i>n</i> -Decane	0.34	0.15 <sup>a</sup>	$2.24 \times 10^9$	$4.34 \times 10^9$	0.52
<b>2</b> in $\text{CHCl}_3$	0.02	0.15	$1.38 \times 10^8$	$6.76 \times 10^9$	0.02
<b>2</b> <sub>agg</sub> in <i>n</i> -Decane	0.25	0.06 <sup>a</sup>	$3.91 \times 10^9$	$1.17 \times 10^{10}$	0.33

<sup>a</sup>average fluorescence lifetime ( $\tau_{av}$ ); <sup>b</sup> $k_r$  is radiative decay rate; <sup>c</sup> $k_{nr}$  is non-radiative decay rate.

## 2.4. Conclusions

In summary, we have established that the self-assembly of the amide functionalized PE derivatives substituted with linear achiral (**1**) and branched chiral (**2**) alkoxy side chains result in highly luminescent gels comprising of 1D fibers. Absorption and emission spectroscopy studies have revealed that both the molecules undergo aggregation in *n*-decane at lower concentrations resulting in enhanced blue fluorescence. Above a critical concentration, self-assembly of both **1** and **2** led to gelation of linear and cyclic nonpolar solvents. The observed SIEE phenomenon in compounds **1** and **2** is attributed to the

restriction of rotation of the PE chromophores in the gel state. Comparison of the optical properties between the gels of **1** and **2** revealed relatively stronger emission with the former having achiral side chains.

## 2.5. Experimental Section: Synthesis

### 2.5.1. General Procedure

Unless otherwise stated, all starting materials and reagents were purchased from commercial suppliers and used without further purification. All solvents used were purified and dried by standard methods. Triethylamine was distilled in presence of KOH and stored over KOH for further use. The reactions were monitored using thin layer chromatography on silica gel 60 F<sub>254</sub> (0.2 mm; Merck). Visualization was accomplished using UV light (254 and 365 nm). Preparative column chromatography was performed on glass columns of different sizes hand packed with 100-200 mesh silica gel (Merck). Molecules **1** and **2** were synthesized according to Scheme 2.1 based on standard protocols.

### 2.5.2. Characterization Techniques

Melting points were determined using a calibrated digital melting point apparatus (Stuart melting point apparatus SMP30). Infrared spectra were recorded on a Shimadzu IR Prestige-21 FT-IR spectrophotometer using KBr pellets and only intense peaks were reported. <sup>1</sup>H and <sup>13</sup>C NMR spectra were obtained with Bruker Avance DPX spectrometer using TMS (0 ppm for <sup>1</sup>H NMR) or CDCl<sub>3</sub> (77 ppm for <sup>13</sup>C NMR) as an internal reference. Mass spectra were recorded on a Thermo Scientific Q Exactive Hybrid Quadrupole-Orbitrap ESI-MS.

**2.5.3. Synthesis of methyl-3,4,5-trialkoxybenzoate (4):** Compound **3** (6.5 mmol, 1 equiv.) and  $K_2CO_3$  (39 mmol, 6 equiv.) were dissolved in dry DMF (50 mL) in a 250 mL round bottom flask under inert atmosphere upon stirring at 50 °C for 30 min. The reaction medium was cooled to room temperature and the required alkyl bromide (22.7 mmol, 3.5 equiv.) was added dropwise. The reaction mixture became turbid within 1 h and was stirred at 80 °C for 24 h under inert condition. After cooling to room temperature, the reaction mixture was poured into water and extracted with chloroform. The combined organic layer was washed with brine and water for several times, dried over anhydrous  $Na_2SO_4$ . After removal of the solvent under reduced pressure, the residue was subjected to column chromatography (5% ethyl acetate/*n*-hexane) over silica gel afforded the pure product as a colorless solid (**4a**) and liquid (**4b**).

**4a:** Yield: 80%;  $^1H$  NMR (500 MHz,  $CDCl_3$ , TMS):  $\delta$  = 7.25 (s, 2H, Ar-*H*), 4.03–3.99 (m, 6H,  $-OCH_2$ ), 3.89 (s, 3H,  $-OCH_3$ ), 1.83–1.73 (m, 6H,  $-CH_2$ ), 1.49–1.44 (m, 6H,  $-CH_2$ ), 1.30–1.25 (m, 48H,  $-CH_2$ ), 0.88 (t,  $J$  = 7.0 Hz, 9H,  $-CH_3$ ) ppm;  $^{13}C$  NMR (125 MHz,  $CDCl_3$ ):  $\delta$  = 167.0, 152.8 (2C), 142.5, 124.7, 108.1 (2C), 73.5, 69.2 (2C), 52.1, 31.9 (3C), 29.7 (9C), 29.6 (3C), 29.4 (6C), 29.3 (3C), 26.1 (3C), 22.7 (3C), 14.1 (3C) ppm; HRMS-ESI calculated for  $C_{44}H_{80}O_5$   $[M+H]^+$ , 689.6006; found 689.6088.

**4b:** Yield: 70%;  $^1H$  NMR (500 MHz,  $CDCl_3$ , TMS):  $\delta$  = 7.19 (s, 2H, Ar-*H*), 4.04–3.81 (m, 6H,  $-OCH_2$ ), 3.81 (s, 3H,  $-OCH_3$ ), 1.82–1.73 (m, 3H,  $-CH(CH_3)_2$ ), 1.63 (br, 3H,  $-CH(CH_3)_2$ ), 1.57–1.43 (m, 6H,  $-CH_2$ ), 1.26–1.18 (m, 10H,  $-CH_2$ ), 1.10–1.08 (m, 8H,  $-CH_2$ ), 0.88–0.84 (m, 9H,  $-CH_3$ ), 0.79 (d,  $J$  = 6.5 Hz, 18H,  $-CH(CH_3)_2$ ) ppm;  $^{13}C$  NMR (125 MHz,  $CDCl_3$ ):  $\delta$  = 165.9, 151.8 (2C), 141.3, 123.7, 106.9 (2C), 70.8, 66.4 (2C), 51.1, 38.3, 38.2

(2C), 36.5, 36.3 (2C), 35.3 (3C), 28.8 (2C), 28.6, 27.0 (3C), 23.7 (3C), 21.6 (6C), 18.5 (3C) ppm; HRMS-ESI calculated for  $C_{38}H_{68}O_5$   $[M+H]^+$ , 605.5067; found, 605.5856.

**2.5.4. Synthesis of 3,4,5-trialkoxybenzoic acid (5):** In a general procedure, compound **4** (4.35 mmol, 1 equiv.) and solid KOH (9.16 mmol, 2.2 equiv.) were dissolved in distilled ethanol (60 mL) and was refluxed at 80 °C inside a 250 mL round bottom flask for 12 h. The reaction medium was cooled to room temperature and ethanol was completely removed from the reaction mixture under reduced pressure. Then, the reaction mixture was acidified (pH = 2) with cold dilute HCl with continuous stirring and was extracted using chloroform. The organic layer was washed with brine thrice, dried over anhydrous  $Na_2SO_4$ , filtered, and the filtrate was concentrated under reduced pressure. The products **5a** (colorless solid) and **5b** (viscous liquid) formed were used for the next step without further purification.

**5a:** Yield: 90%;  $^1H$  NMR (500 MHz,  $CDCl_3$ , TMS):  $\delta$  = 7.31 (s, 2H, Ar-H), 4.10–3.91 (m, 6H,  $-OCH_2$ ), 1.86–1.71 (m, 8H,  $-CH_2$ ), 1.51–1.44 (m, 6H,  $-CH_2$ ), 1.32–1.24 (m, 46H,  $-CH_2$ ), 0.88 (t,  $J$  = 7.0 Hz, 9H,  $-CH_3$ ) ppm;  $^{13}C$  NMR (125 MHz,  $CDCl_3$ )  $\delta$  = 170.2, 152.9 (2C), 143.1, 123.5, 108.5 (2C), 73.6, 69.2 (2C), 32.8, 31.9 (2C), 29.8–29.3 (21C), 26.1 (2C), 25.7, 22.7 (3C), 14.1 (3C) ppm; HRMS-ESI calculated for  $C_{43}H_{78}O_5$   $[M+H]^+$ , 675.5849; found, 675.6787.

**5b:** Yield: 90%;  $^1H$  NMR (500 MHz,  $CDCl_3$ , TMS):  $\delta$  = 7.25 (s, 2H, Ar-H), 4.02–3.94 (m, 6H,  $-OCH_2$ ), 1.82–1.75 (m, 3H,  $-CH(CH_3)_2$ ), 1.64 (br, 3H,  $-CH(CH_3)_2$ ), 1.55–1.44 (m, 6H,  $-CH_2$ ), 1.26–1.19 (m, 12H,  $-CH_2$ ), 1.09 (br, 6H,  $-CH_2$ ), 0.88–0.84 (m, 9H,  $-CH_3$ ), 0.80 (d,



$J = 6.5$  Hz, 18H,  $-\text{CH}(\text{CH}_3)_2$  ppm;  $^{13}\text{C}$  NMR (125 MHz,  $\text{CDCl}_3$ ):  $\delta = 165.8, 152.9$  (2C), 142.9, 124.7, 108.4 (2C), 71.8, 67.5 (2C), 39.4, 39.3 (2C), 37.5, 37.3 (2C), 36.3 (3C), 29.7 (2C), 29.6, 28.0 (3C), 24.7 (3C), 22.7 (6C), 19.6 (3C) ppm; HRMS-ESI calculated for  $\text{C}_{37}\text{H}_{66}\text{O}_5$   $[\text{M}+\text{H}]^+$ , 591.4910; found, 591.5004.

**2.5.5. Synthesis of 3,4,5-trialkoxybenzoyl chloride (6):** Compound **5** (2.22 mmol, 1 equiv.) was dissolved in dry dichloromethane (5 mL) in a round bottom flask.  $\text{SOCl}_2$  (6.72 mmol, 3 equiv.) was added dropwise into the reaction mixture and stirred at room temperature for 5 h under nitrogen atmosphere. Unreacted  $\text{SOCl}_2$  and the solvent were removed upon purging argon. The residue obtained **6** was then used for the next step without further purification and characterization.

**2.5.6. Synthesis of 3,4,5-trialkoxy-*N*-(4-iodophenyl)benzamide (8):** 4-Iodoaniline, **7** (3.35 mmol, 1.5 equiv) was dissolved in dry toluene (20 mL) in a two neck round bottom flask. Dry trimethylamine (2 mL) was added into the mixture and stirred under inert atmosphere for 15 minutes. Compound **6** dissolved in dry toluene (10 mL) was added dropwise into the medium and the reaction mixture was stirred at room temperature for 12 h, maintaining the same condition. The progress of the reaction was monitored using TLC. On completion of the reaction, the mixture of solvents was removed under reduced pressure and the residue was extracted using chloroform. The organic layer was washed with brine thrice, dried over anhydrous  $\text{Na}_2\text{SO}_4$ , filtered, and the filtrate was concentrated under reduced pressure. The obtained crude product was then purified by column chromatography over silica gel (5% ethyl acetate/*n*-hexane) to yield compound **8a** and **8b** as colorless solids.

**8a:** Yield: 70%; m.p.: 91-93 °C; FT-IR (KBr):  $\nu_{\max} = 3277$  (s;  $\nu_{\text{str}}(\text{N-H})$ ), 2918 (s;  $\nu_{\text{as}}(-\text{CH}_2)$ ), 2849 (s;  $\nu_{\text{s}}(-\text{CH}_2)$ ), 1649 (s;  $\nu_{\text{str}}(\text{C=O})$ ), 1517 (s;  $\nu_{\text{def}}(\text{N-H}) + \nu_{\text{str}}(\text{C-N})$ )  $\text{cm}^{-1}$ ;  $^1\text{H}$  NMR (500 MHz,  $\text{CDCl}_3$ , TMS):  $\delta = 7.68$  (s, 1H,  $-\text{CONH}$ ), 7.59 (d,  $J = 8.5$  Hz, 2H, Ar- $H$ ), 7.35 (d,  $J = 8.5$  Hz, 2H, Ar- $H$ ), 6.94 (s, 2H, Ar- $H$ ), 3.94 (t,  $J = 5.5$  Hz, 6H,  $-\text{OCH}_2$ ), 1.76 – 1.66 (m, 6H,  $-\text{CH}_2$ ), 1.40 (s, 6H,  $-\text{CH}_2$ ), 1.19 (s, 48H,  $-\text{CH}_2$ ), 0.81 (t,  $J = 6.5$  Hz, 9H,  $-\text{CH}_3$ ) ppm;  $^{13}\text{C}$  NMR (125 MHz,  $\text{CDCl}_3$ ):  $\delta = 165.6$ , 153.3 (2C), 141.7, 138.0 (2C), 137.8, 129.5, 121.9 (2C), 105.8 (2C), 87.6, 73.6, 69.5 (2C), 31.9 (2C), 30.3, 29.7 (18C), 29.4 (3C), 26.1 (3C), 22.7 (3C), 14.1 (3C) ppm; HRMS-ESI calculated for  $\text{C}_{49}\text{H}_{82}\text{INO}_4$   $[\text{M}]^+$ , 875.5289; found, 875.7909.

**8b:** Yield: 60%; m.p.: 92-94 °C; FT-IR (KBr):  $\nu_{\max} = 3289$  (s;  $\nu_{\text{str}}(\text{N-H})$ ), 2954 (s;  $\nu_{\text{as}}(-\text{CH}_2)$ ), 2868 (s;  $\nu_{\text{s}}(-\text{CH}_2)$ ), 1647 (s;  $\nu_{\text{str}}(\text{C=O})$ ), 1510 (s;  $\nu_{\text{def}}(\text{N-H}) + \nu_{\text{str}}(\text{C-N})$ )  $\text{cm}^{-1}$ ;  $^1\text{H}$  NMR (500 MHz,  $\text{CDCl}_3$ , TMS):  $\delta = 7.66$  (s, 1H,  $-\text{CONH}$ ), 7.60 (d,  $J = 8.5$  Hz, 2H, Ar- $H$ ), 7.35 (d,  $J = 8.5$  Hz, 2H, Ar- $H$ ), 6.96 (s, 2H, Ar- $H$ ), 3.99–3.94 (m, 6H,  $-\text{OCH}_2$ ), 1.82–1.74 (m, 3H,  $-\text{CH}(\text{CH}_3)_2$ ), 1.63 (br, 3H,  $-\text{CH}(\text{CH}_3)_2$ ), 1.56–1.43 (m, 6H,  $-\text{CH}_2$ ), 1.26–1.18 (m, 10H,  $-\text{CH}_2$ ), 1.10–1.08 (m, 8H,  $-\text{CH}_2$ ), 0.88–0.85 (m, 9H,  $-\text{CH}_3$ ), 0.80 (d,  $J = 6.5$  Hz, 18H,  $-\text{CH}(\text{CH}_3)_2$ ) ppm;  $^{13}\text{C}$  NMR (125 MHz,  $\text{CDCl}_3$ ):  $\delta = 165.63$ , 153.3 (2C), 141.7, 138.0 (2C), 137.8, 129.6, 122.0 (2C), 105.8 (2C), 87.7, 71.8, 67.8 (2C), 39.4, 39.3 (2C), 37.5, 37.4 (2C), 36.4 (3C), 29.8 (2C), 29.7, 28.0 (3C), 24.7 (3C), 22.7 (6C), 19.6 (3C) ppm; HRMS-ESI calculated for  $\text{C}_{43}\text{H}_{70}\text{INO}_4$   $[\text{M}+\text{H}]^+$ , 792.4350; found, 792.4603.

### 2.5.7. Synthesis of trimethyl((4-(phenylethynyl)phenyl)ethynyl)silane (11):

((4-iodophenyl) ethynyl)trimethylsilane **9** (0.7 g, 2.33 mmol, 1 equiv.),  $\text{PdCl}_2(\text{PPh}_3)_2$  (0.08

g, 5 mol%) and CuI (0.02 g, 5 mol%) were dissolved in a degassed mixture (1:1) of triethylamine and THF (20 mL) in a two-neck round bottom flask under argon atmosphere. Phenylacetylene **10** (0.31 mL, 2.80 mmol, 1.2 equiv.) was added to the reaction mixture and was stirred at room temperature for 12 h. The progress of the coupling reaction was monitored using TLC. On completion of the reaction, the mixture of solvents was evaporated under reduced pressure and the residue was washed with 10% HCl solution to neutralize the remaining amount of triethylamine present in the medium. The residue was extracted using chloroform, and the organic layer washed thrice with brine, dried over anhydrous Na<sub>2</sub>SO<sub>4</sub>, filtered and the filtrate was concentrated under reduced pressure. The obtained crude product was then purified by column chromatography over silica gel (2% ethyl acetate/*n*-hexane) to yield compound **11**.

Yield: 69%; <sup>1</sup>H NMR (500 MHz, CDCl<sub>3</sub>, TMS):  $\delta$  = 7.53–7.51 (m, 2H, Ar-*H*), 7.47–7.42 (m, 4H, Ar-*H*), 7.36–7.34 (m, 3H, Ar-*H*), 0.26 (s, 9H,  $\equiv$ C-Si(CH<sub>3</sub>)<sub>3</sub>) ppm; <sup>13</sup>C NMR (125 MHz, CDCl<sub>3</sub>):  $\delta$  = 132.0 (2C), 131.7 (2C), 131.5 (2C), 128.6, 128.5 (2C), 123.4, 123.1, 123.0, 104.7, 96.3, 91.4, 89.1, 0.0 (3C) ppm; HRMS-ESI calculated for C<sub>19</sub>H<sub>18</sub>Si [M+H]<sup>+</sup>, 275.1178; found 275.6302.

**2.5.8. Synthesis of 1-ethynyl-4-(phenylethynyl)benzene (12):** To a solution of **11** (0.42 g, 1.7 mmol, 1 equiv.) in dichloromethane (5 mL), KF (1.0 g, 17.8 mmol, 10.5 equiv.) in methanol (15 mL) was added and stirred at room temperature for 6 h. The progress of the reaction was monitored using TLC. On completion of the reaction, the mixture of solvents was evaporated under reduced pressure and the residue was extracted using chloroform. The organic layer was washed thrice with brine, dried over anhydrous Na<sub>2</sub>SO<sub>4</sub>,

filtered and the filtrate was concentrated under reduced pressure. The obtained residue **12** (0.29 g, 93.7%) was used for the next step without further purification.

Yield: 94%; m.p.: 82-84 °C; <sup>1</sup>H NMR (500 MHz, CDCl<sub>3</sub>, TMS): δ = 7.48–7.45 (m, 2H, Ar-H), 7.43–7.39 (m, 4H, Ar-H), 7.30–7.27 (m, 3H, Ar-H), 3.10 (s, 1H, ≡C-H) ppm; <sup>13</sup>C NMR (125 MHz, CDCl<sub>3</sub>): δ = 132.1 (2C), 131.7 (2C), 131.5 (2C), 128.6, 128.4 (2C), 123.8, 122.9, 121.9, 88.8, 83.3, 78.9 (2C) ppm; HRMS-ESI calculated for C<sub>16</sub>H<sub>10</sub> [M]<sup>+</sup>, 202.0783; found 202.0784.

**2.5.9. Synthesis of 1 and 2:** Compound **8** (0.70 mmol, 1 equiv.), Pd(PPh<sub>3</sub>)<sub>2</sub>Cl<sub>2</sub> (10 mol%) and CuI (10 mol%) were dissolved in a mixture (1:1) of degassed triethylamine and THF (20 mL) in a 100 mL two-neck round bottom flask under inert atmosphere. Compound **12** (0.80 mmol, 1.15 equiv.) dissolved in a degassed (1:1) mixture of triethylamine and THF (10 mL) was added into the reaction mixture and stirred at room temperature for 18 h. The progress of the reaction was monitored by TLC. On completion of the reaction, the mixture of solvents was evaporated under reduced pressure and the residue was washed with 10% HCl solution to neutralize the remaining triethylamine present in the medium. The residue was extracted using chloroform and the organic layer washed thrice with brine, dried over anhydrous Na<sub>2</sub>SO<sub>4</sub>, filtered and the filtrate was concentrated under reduced pressure. The obtained crude product was then purified by column chromatography over silica gel using 5 and 6% ethyl acetate/*n*-hexane as an eluent to yield compound **1** and **2**, respectively as colorless solids.

**1:** Yield, 48%; m.p.: 114-116 °C; FT-IR (KBr):  $\nu = 3260$  (s;  $\nu_{\text{str}}(\text{N-H})$ ), 2918 (s;  $\nu_{\text{as}}(-\text{CH}_2)$ ), 2849 (s;  $\nu_{\text{s}}(-\text{CH}_2)$ ), 2212 (w;  $\nu_{\text{str}}(\text{C}\equiv\text{C})$ ), 1647 (s;  $\nu_{\text{str}}(\text{C}=\text{O})$ ), 1518 (s;  $\nu_{\text{def}}(\text{N-H}) + \nu_{\text{str}}(\text{C-N})$ )  $\text{cm}^{-1}$ ;  $^1\text{H}$  NMR (500 MHz,  $\text{CDCl}_3$ , TMS):  $\delta = 7.69$  (s, 1H, -CONH), 7.58 (d,  $J = 10.0$  Hz, 2H, Ar-H), 7.47-7.44 (m, 8H, Ar-H), 7.29-7.28 (m, 3H, Ar-H), 6.97 (s, 2H, Ar-H), 3.98-3.94 (m, 6H, -OCH<sub>2</sub>), 1.78-1.66 (m, 6H, -CH<sub>2</sub>), 1.44-1.38 (m, 6H, -CH<sub>2</sub>), 1.29-1.24 (m, 48H, -CH<sub>2</sub>), 0.82-0.80 (t,  $J = 9.0$  Hz, 9H, -CH<sub>3</sub>) ppm;  $^{13}\text{C}$  NMR (125 MHz,  $\text{CDCl}_3$ ):  $\delta = 165.6$ , 153.3 (2C), 141.8, 138.3, 132.5 (2C), 131.6 (4C), 131.5 (2C), 129.6, 128.5, 128.4 (2C), 123.2, 123.1, 123.0, 119.8 (2C), 118.8, 106.0 (2C), 91.2, 91.1, 89.1, 89.0, 73.8, 69.6 (2C), 31.9 (3C), 29.7 (9C), 29.6 (3C), 29.4 (9C), 25.1 (3C), 22.7 (3C), 14.1 (3C) ppm; HRMS-ESI calculated for  $\text{C}_{65}\text{H}_{91}\text{NO}_4$   $[\text{M}+\text{H}]^+$ , 950.6948; found, 950.7018.

**2:** Yield: 60%; m.p.: 143-145 °C; FT-IR (KBr):  $\nu = 3285$  (s;  $\nu_{\text{str}}(\text{N-H})$ ), 2953 (s;  $\nu_{\text{as}}(-\text{CH}_2)$ ), 2924 (s;  $\nu_{\text{s}}(-\text{CH}_2)$ ), 2216 (w;  $\nu_{\text{str}}(\text{C}\equiv\text{C})$ ), 1651 (s;  $\nu_{\text{str}}(\text{C}=\text{O})$ ), 1518 (s;  $\nu_{\text{def}}(\text{N-H}) + \nu_{\text{str}}(\text{C-N})$ )  $\text{cm}^{-1}$ ;  $^1\text{H}$  NMR (500 MHz,  $\text{CDCl}_3$ , TMS):  $\delta = 7.78$  (s, 1H, -CONH), 7.65 (d,  $J = 10.0$  Hz, 2H, Ar-H), 7.55-7.50 (m, 8H, Ar-H), 7.36-7.35 (m, 3H, Ar-H), 7.05 (s, 2H, Ar-H), 4.11-4.00 (m, 6H, -OCH<sub>2</sub>), 1.85-1.71 (m, 3H, -CH(CH<sub>3</sub>)<sub>2</sub>), 1.62 (br, 3H, -CH(CH<sub>3</sub>)<sub>2</sub>), 1.57-1.44 (m, 6H, -CH<sub>2</sub>), 1.35-1.32 (m, 10H, -CH<sub>2</sub>), 1.20-1.14 (m, 8H, -CH<sub>2</sub>), 0.96-0.92 (m, 9H, -CH<sub>3</sub>), 0.87 (d,  $J = 5.0$  Hz, 18H, -CH(CH<sub>3</sub>)<sub>2</sub>) ppm;  $^{13}\text{C}$  NMR (125 MHz,  $\text{CDCl}_3$ ):  $\delta = 165.7$ , 153.5 (2C), 141.5, 138.2, 132.7 (2C), 131.5 (4C), 131.4 (2C), 129.7, 128.6, 128.5 (2C), 123.0, 119.7 (2C), 118.7, 106.0 (2C), 103.8, 100.0, 91.4, 91.3, 89.3, 89.2, 72.0, 67.8 (2C), 39.3 (3C), 37.5 (3C), 36.3 (3C), 30.0 (3C), 28.1 (3C), 24.8 (3C), 22.8 (3C), 22.7 (3C), 19.6 (3C) ppm; HRMS-ESI calculated for  $\text{C}_{59}\text{H}_{79}\text{NO}_4$   $[\text{M}+\text{H}]^+$ , 866.6009; found, 866.6090.

## 2.6. Description on Experimental Techniques

### 2.6.1. Optical Measurements

The electronic absorption spectra were recorded on a Shimadzu UV-2600 UV-vis scanning spectrophotometer equipped with peltier thermostatic cell holder and the fluorescence spectra were recorded on a SPEX-Fluorolog-3 FL3-221 spectrofluorimeter. Optical studies in solution-state were performed either in a 1 cm or 1 mm quartz cuvette. Temperature-dependent studies were carried out with a thermostat directly attached to the wall of the cuvette holder. Temperature-dependent emission spectra were recorded on a FluoroMax-4 spectrofluorometer (Model: Fluoromax-4c). Fluorescence lifetime measurements were carried out using Horiba (model DeltaFlex) time-correlated single photon counting system. The lifetime values ( $\tau$ ), relative amplitude ( $a$ ) and average lifetime ( $\tau_{av}$ ) were determined using EzTime decay analysis software. The equation used for the calculation of  $\tau_{av}$  of biexponential decay is  $a_1\tau_1+a_2\tau_2$ , where  $a$  is normalized pre-exponential value. The quality of the fit has been judged by the fitting parameters such as  $\chi^2$  (<1.1) as well as the visual inspection of the residuals.  $k_r$  and  $k_{nr}$  values are calculated based on the following equations.<sup>[62]</sup>

$$k_r = \Phi_F / \tau \dots\dots\dots (1)$$

$$k_{nr} = (1 - \Phi_F) / \tau \dots\dots\dots (2)$$

CD measurements were performed on JASCO 810 spectrometer equipped with Peltier thermostatic cell holders. Sensitivity, response time and scanning speed were chosen appropriately. CD spectra were recorded as  $\theta$  in millidegree using a quartz cuvette of 1 mm

path length at 298 K, and then converted into  $\Delta\varepsilon$  using the equation  $\Delta\varepsilon = \theta / (33982cl)$ , where  $\Delta\varepsilon$  is the difference in the molar absorptivity for oppositely polarized light in  $M^{-1}cm^{-1}$ ,  $c$  is the concentration in M and  $l$  is the path length in cm.

### 2.6.2. Morphological Studies

TEM experiments were performed on a JEOL-JEM 0310 microscope with an accelerating voltage of 100 kV. Samples for electron microscopy were prepared by dropcasting **1**<sub>agg</sub> and **2**<sub>agg</sub> *n*-decane solutions on carbon-coated copper grids and then dried under air overnight. TEM images were obtained without staining. SEM images were obtained using a Zeiss EVO 18cryo SEM Special Edn. with an accelerating voltage of 20 kV after sputtering with gold. Samples were prepared by dropcasting **1**<sub>agg</sub> and **2**<sub>agg</sub> *n*-decane solutions over a smooth aluminum foil and dried under air overnight. Fluorescence microscopy images were recorded on a Leica-DMIR2 Optical Microscope using UV light (340-380 nm) as the excitation source. Samples were prepared by dropcasting **1**<sub>agg</sub> and **2**<sub>agg</sub> over coverslip slides followed by slow evaporation.

### 2.6.3. Gelation Studies

Gelation studies for both **1** and **2** have been carried out according to the following procedure: A definite amount of the compound in an appropriate solvent was initially placed inside a glass vial. The glass vial was then sealed, heated until the compound was dissolved and the hot solution was then allowed to cool immediately to room temperature. Gel formation was confirmed by the failure of the solvent to flow while inverting the vial. Furthermore, thermo-reversible nature of the gels was confirmed by repeated heating and cooling processes.

In order to compare and understand the gel strength of **1** and **2**, rheological measurements were conducted on an Anton Paar modular compact (MCR 150) stress controlled rheometer (Physica) equipped with a parallel plate geometry (20 mm diameter), striated cone and a rough plate to minimize the errors due to sliding of the gel layers. Hot solution of compounds in *n*-decane was poured on to the Peltier kept at 20 °C and was allowed to form a uniform layer. In order to avoid the solvent evaporation, the plate was properly covered. The gap between the cone and the plate was kept fixed between 0.25 mm.

#### **2.6.4. WAXS Analysis**

WAXS measurements were carried out on XEUSS SAXS/WAXS system using a Genix microsource from Xenocs. The generator was operated at 50 kV and 0.6 mA. The Cu  $K_{\alpha}$  radiation ( $\lambda = 1.54 \text{ \AA}$ ) was collimated with FOX2D mirror and two pairs of scatterless slits from Xenocs. The 2D-patterns were recorded on a Mar345 image plate and processed using the Fit2D software. The sample to detector distance was calibrated with silver behenate standard. All the measurements were made in the transmission mode. The 2D WAXS images were azimuthally averaged to obtain 1D scattering intensity profiles as a function of  $2d \sin\theta = n\lambda$ , where  $\theta$  is the scattering angle,  $d$  is the interplanar distance between the lattice planes and  $\lambda$  is the wavelength of X-ray radiation. Samples for WAXS analysis were prepared by complete removal of the solvents from the organogels under high vacuum, resulting in xerogels of **1** and **2**.



## 2.7. References

- [1] L. Maggini, D. Bonifazi, *Chem. Soc. Rev.* **2012**, *41*, 211-241.
- [2] S. Varughese, *J. Mater. Chem. C* **2014**, *2*, 3499-3516.
- [3] S. S. Babu, V. K. Praveen, A. Ajayaghosh, *Chem. Rev.* **2014**, *114*, 1973-2129.
- [4] Y. Sagara, S. Yamane, M. Mitani, C. Weder, T. Kato, *Adv. Mater.* **2016**, *28*, 1073-1095.
- [5] P. Data, Y. Takeda, *Chem. Asian J.* **2019**, *14*, 1613-1636.
- [6] M. Gao, B. Z. Tang, *ACS Sensors* **2017**, *2*, 1382-1399.
- [7] *Self-Assembly in Sensor Nanotechnology*, P. Anees, V. K. Praveen, K. K. Kartha, A. Ajayaghosh, in *Comprehensive Supramolecular Chemistry II*, Vol. 9 (Ed. C. Raston), Elsevier Ltd., **2017**.
- [8] V. K. Praveen, B. Vedhanarayanan, A. Mal, R. K. Mishra, A. Ajayaghosh, *Acc. Chem. Res.* **2020**, *53*, 496-507.
- [9] L. D. Lavis, R. T. Raines, *ACS Chem. Biol.* **2014**, *9*, 855-866.
- [10] J. Schill, A. P. H. J. Schenning, L. Brunsveld, *Macromol. Rapid Commun.* **2015**, *36*, 1306-1321.
- [11] G. Feng, R. T. K. Kwok, B. Z. Tang, B. Liu, *Appl. Phys. Rev.* **2017**, *4*, 021307.
- [12] *Photoluminescent Materials and Electroluminescent Devices* (Eds: N. Armaroli, H. J. Bolink), *Topics in Current Chemistry*, Springer International Publishing, Switzerland **2017**.
- [13] Y. Chen, J. W. Y. Lam, R. T. K. Kwok, B. Liu, B. Z. Tang, *Mater. Horiz.* **2019**, *6*, 428-433.

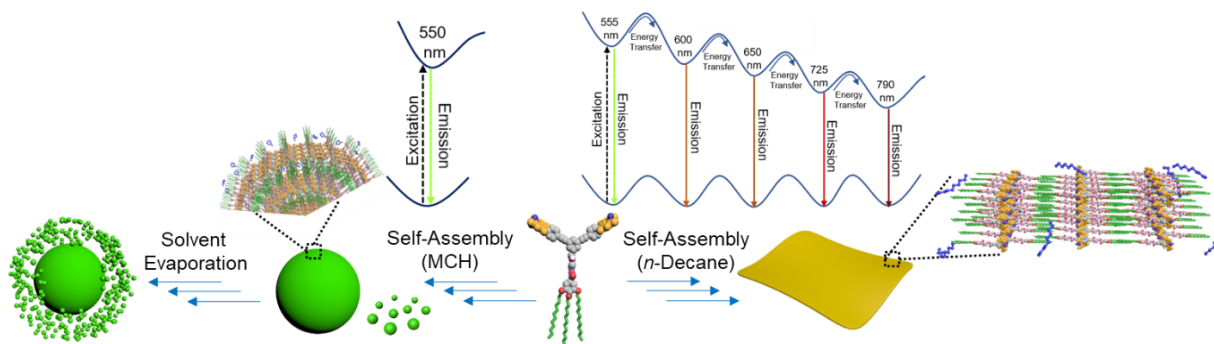
- [14] S. S. Babu, V. K. Praveen, K. K. Kartha, S. Mahesh, A. Ajayaghosh, *Chem. Asian J.* **2014**, *9*, 1830-1840.
- [15] F. Lu, T. Nakanishi, *Adv. Opt. Mater.* **2019**, *7*, 1900176.
- [16] J. Mei, N. L. C. Leung, R. T. K. Kwok, J. W. Y. Lam, B. Z. Tang, *Chem. Rev.* **2015**, *115*, 11718-11940.
- [17] J. Li, J. Wang, H. Li, N. Song, D. Wang, B. Z. Tang, *Chem. Soc. Rev.* **2020**, *49*, 1144-1172.
- [18] P. Shen, Z. Zhuang, Z. Zhao, B. Z. Tang, *J. Mater. Chem. C* **2018**, *6*, 11835-11852.
- [19] B. K. An, J. Gierschner, S. Y. Park, *Acc. Chem. Res.* **2012**, *45*, 544-554.
- [20] F. Aparicio, S. Cherumukkil, A. Ajayaghosh, L. Sánchez, *Langmuir* **2016**, *32*, 284-289.
- [21] M. Martínez-Abadía, R. Giménez, M. B. Ros, *Adv. Mater.* **2018**, *30*, 1704161.
- [22] J. Zhao, Z. Chi, Z. Yang, Z. Mao, Y. Zhang, E. Ubba, Z. Chi, *Mater. Chem. Front.* **2018**, *2*, 1595-1608.
- [23] D. D. La, S. V. Bhosale, L. A. Jones, S. V. Bhosale, *ACS Appl. Mater. Interfaces* **2018**, *10*, 12189-12216.
- [24] V. S. Padalkar, S. Seki, *Chem. Soc. Rev.* **2016**, *45*, 169-202.
- [25] M. Levitus, K. Schmieder, H. Ricks, K. D. Shimizu, U. H. F. Bunz, M. A. Garcia-Garibay, *J. Am. Chem. Soc.* **2001**, *123*, 4259-4265.
- [26] M. Levitus, G. Zepeda, H. Dang, C. Godinez, T. A. V. Khuong, K. Schmieder, M. A. Garcia-Garibay, *J. Org. Chem.* **2001**, *66*, 3188-3195.
- [27] S. K. Albert, H. V. P. Thelu, M. Golla, N. Krishnan, S. Chaudhary, R. Varghese, *Angew.*

- Chem. Int. Ed.* **2014**, *53*, 8352-8357.
- [28] S. Roy, D. Samanta, P. Kumar, T. K. Maji, *Chem. Commun.* **2018**, *54*, 275-278.
- [29] D. S. Philips, K. K. Kartha, A. T. Politi, T. Krüger, R. Q. Albuquerque, G. Fernández, *Angew. Chem. Int. Ed.* **2019**, *58*, 4732-4736.
- [30] P. Rajamalli, S. Atta, S. Maity, E. Prasad, *Chem. Commun.* **2013**, *49*, 1744.
- [31] Z. Wang, J. Nie, W. Qin, Q. Hu, B. Z. Tang, *Nat. Commun.* **2016**, *7*, 12033.
- [32] A. Ajayaghosh, R. Varghese, V. K. Praveen, S. Mahesh, *Angew. Chem. Int. Ed.* **2006**, *45*, 3261-3264.
- [33] A. Gopal, R. Varghese, A. Ajayaghosh, *Chem. Asian J.* **2012**, *7*, 2061-2067.
- [34] A. Gopal, M. Hifsudheen, S. Furumi, M. Takeuchi, A. Ajayaghosh, *Angew. Chem. Int. Ed.* **2012**, *51*, 10505-10509.
- [35] R. Thirumalai, R. D. Mukhopadhyay, V. K. Praveen, A. Ajayaghosh, *Sci. Rep.* **2015**, *5*, 09842.
- [36] S. Cherumukkil, S. Ghosh, V. K. Praveen, A. Ajayaghosh, *Chem. Sci.* **2017**, *8*, 5644-5649.
- [37] M. Hifsudheen, R. K. Mishra, B. Vedhanarayanan, V. K. Praveen, A. Ajayaghosh, *Angew. Chem. Int. Ed.* **2017**, *56*, 12634-12638.
- [38] F. García, L. Sánchez, *J. Am. Chem. Soc.* **2012**, *134*, 734-742.
- [39] A. Sandeep, V. K. Praveen, D. S. Shankar Rao, S. Krishna Prasad, A. Ajayaghosh, *ACS Omega* **2018**, *3*, 4392-4399.
- [40] K. K. Kartha, V. S. Nair, V. K. Praveen, M. Takeuchi, A. Ajayaghosh, *J. Mater. Chem. C* **2019**, *7*, 1292-1297.

- [41] R. van der Weegen, A. J. P. Teunissen, E. W. Meijer, *Chem. Eur. J.* **2017**, *23*, 3773-3783.
- [42] H. M. M. ten Eikelder, A. J. Markvoort, T. F. A. de Greef, P. A. J. Hilbers, *J. Phys. Chem. B* **2012**, *116*, 5291-5301.
- [43] B. Adelizzi, I. A. W. Filot, A. R. A. Palmans, E. W. Meijer, *Chem. Eur. J.* **2017**, *23*, 6103-6110.
- [44] A. Langenstroer, K. K. Kartha, Y. Dorca, J. Droste, V. Stepanenko, R. Q. Albuquerque, M. R. Hansen, L. Sánchez, G. Fernández, *J. Am. Chem. Soc.* **2019**, *141*, 5192-5200.
- [45] A. Sandeep, V. K. Praveen, K. K. Kartha, V. Karunakaran, A. Ajayaghosh, *Chem. Sci.* **2016**, *7*, 4460-4467.
- [46] S. Ogi, V. Stepanenko, K. Sugiyasu, M. Takeuchi, F. Würthner, *J. Am. Chem. Soc.* **2015**, *137*, 3300-3307.
- [47] M. Endo, T. Fukui, S. H. Jung, S. Yagai, M. Takeuchi, K. Sugiyasu, *J. Am. Chem. Soc.* **2016**, *138*, 14347-14353.
- [48] D. D. Prabhu, K. Aratsu, Y. Kitamoto, H. Ouchi, T. Ohba, M. J. Hollamby, N. Shimizu, H. Takagi, R. Haruki, S.-i. Adachi, S. Yagai, *Sci. Adv.* **2018**, *4*, eaat8466.
- [49] E. E. Greciano, B. Matarranz, L. Sánchez, *Angew. Chem. Int. Ed.* **2018**, *57*, 4697-4701.
- [50] F. Li, X. Li, Y. Wang, X. Zhang, *Angew. Chem. Int. Ed.* **2019**, *58*, 17994-18002.
- [51] A. Osypenko, E. Moulin, O. Gavot, G. Fuks, M. Maaloum, M. A. J. Koenis, W. J. Buma, N. Giuseppone, *Chem. Eur. J.* **2019**, *25*, 13008-13016.

- [52] S. Srinivasan, S. S. Babu, V. K. Praveen, A. Ajayaghosh, *Angew. Chem. Int. Ed.* **2008**, *47*, 5746-5749.
- [53] K. V. Rao, K. K. R. Datta, M. Eswaramoorthy, S. J. George, *Adv. Mater.* **2013**, *25*, 1713-1718.
- [54] R. D. Mukhopadhyay, G. Das, A. Ajayaghosh, *Nat. Commun.* **2018**, *9*, 1987.
- [55] J. M. Malicka, A. Sandeep, F. Monti, E. Bandini, M. Gazzano, C. Ranjith, V. K. Praveen, A. Ajayaghosh, N. Armaroli, *Chem. Eur. J.* **2013**, *19*, 12991-13001.
- [56] J. H. Ryu, E. Lee, Y. B. Lim, M. Lee, *J. Am. Chem. Soc.* **2007**, *129*, 4808-4813.
- [57] H. Cao, Q. Yuan, X. Zhu, Y. P. Zhao, M. Liu, *Langmuir* **2012**, *28*, 15410-15417.
- [58] A. Sarbu, L. Biniek, J.-M. Guenet, P. J. Mésini, M. Brinkmann, *J. Mater. Chem. C* **2015**, *3*, 1235-1242.
- [59] F. D. Lewis, J.-S. Yang, C. L. Stern, *J. Am. Chem. Soc.* **1996**, *118*, 2772-2773.
- [60] R. Abbel, R. van Der Weegen, W. Pisula, M. Surin, P. Leclère, R. Lazzaroni, E. W. Meijer, A. P. H. J. Schenning, *Chem. Eur. J.* **2009**, *15*, 9737-9746.
- [61] M. K. Nayak, B.-H. Kim, J. E. Kwon, S. Park, J. Seo, J. W. Chung, S. Y. Park, *Chem. Eur. J.* **2010**, *16*, 7437-7447.
- [62] J. R. Lakowicz, *Principles of Fluorescence Spectroscopy*, 3<sup>rd</sup> ed., Springer, New York, **2006**.

## Distinct Morphology and Optical Properties of a Y-Shaped BODIPY Self-Assembly



### 3.1. Abstract

*Excited state properties such as emission, exciton transport, electron transfer, etc., are strongly dependent on the shape, size and molecular arrangement of chromophore based supramolecular architectures. Herein, we demonstrate creation and control of distinct supramolecular architectures and their energy landscapes for the reversible control of the excited-state emission processes through cascade energy transfer, facilitated by an unprecedented solvent effect. In MCH, a tailor-made Y-shaped BODIPY derivative self-assembles to form an unusual spherical architecture of 400-1200 nm size, which exhibits a single emission at 540 nm upon 475 nm excitation through a normal excitation deactivation process. However, in *n*-decane, the same BODIPY derivative forms two-dimensional supramolecular sheets, exhibiting multiple emission peaks at 540, 610, 650, 725 and 790 nm with 475 nm excitation due to cascade*

*energy transfer. Further control on the morphology and excitation energy transfer is possible with variable solvent composition and ultrasound stimulation, resulting in enhanced near-infrared emission with an overall pseudo Stokes shift of 7105 cm<sup>-1</sup>.*

## **3.2. Introduction**

Creation of supramolecular architectures of different shapes, sizes and properties is the fundamental step to realize next generation complex multi-component systems with specific functions and applications.<sup>[1]</sup> In this context, chromophore based supramolecular systems have been at the center stage due to their reversible optoelectronic properties that can be modulated through the molecular assembly.<sup>[2]</sup> In recent times, several approaches have been introduced for the controlled assembly of  $\pi$ -conjugated molecules.<sup>[3-5]</sup> Living supramolecular polymerization,<sup>[3,5a]</sup> crystallization-driven self-assembly<sup>[6]</sup> and seeded supramolecular polymerization<sup>[7]</sup> are examples that control the length and dimension of supramolecular structures through kinetic and thermodynamic control of self-assembly. While living supramolecular polymerization is undoubtedly a powerful tool for the precise control of molecular self-assembly, it cannot be applied as a general strategy. Therefore, different kinds of external stimuli such as light,<sup>[8]</sup> pH,<sup>[9]</sup> redox,<sup>[10]</sup> enzyme,<sup>[11]</sup> ultrasound,<sup>[12]</sup> and solvents,<sup>[13]</sup> have been exploited for controlled supramolecular polymerization of functional  $\pi$ -systems.<sup>[14]</sup>

The Y-shaped wedge-coil molecule (**Amphi-PP**) has been reported to form self-assembled nanofibers with tunable stiffness (**Figure 3.1**).<sup>[15]</sup> The **Amphi-PP** consists of

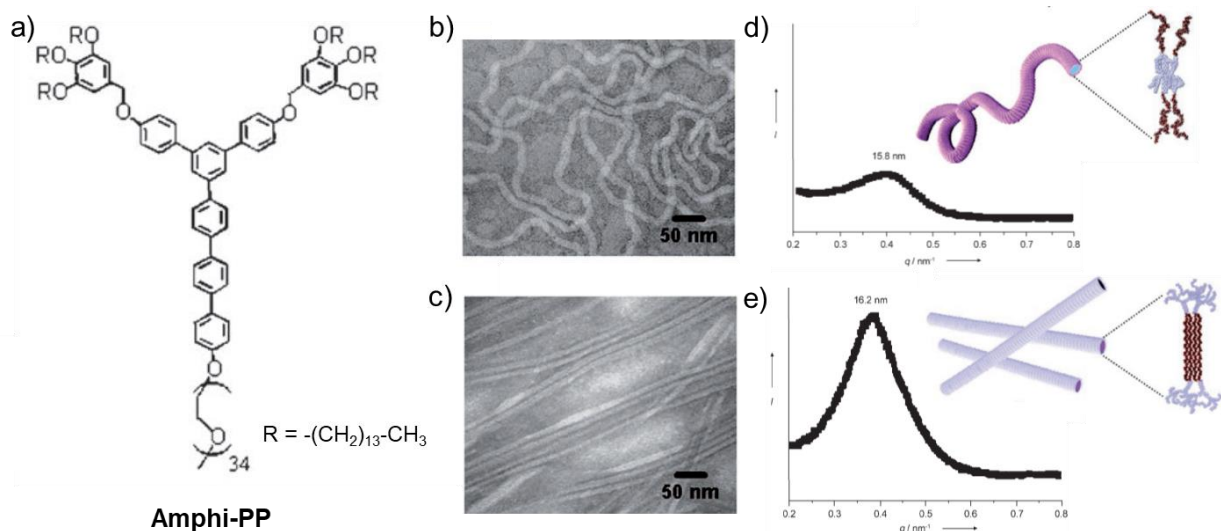


**Figure 3.1.** (a) Molecular structure of Y-shaped wedge-coil molecule, **Amphi-PP**. (b,c) TEM and (d,e) SAXS pattern and schematic representation (inset) for flexible coil-like and stiff-rod like nanofibers of **Amphi-PP** in water and *n*-hexane, respectively. (Adapted with permission from Ref 15).

linear hydrophobic chains on two of its arms and polar poly(ethylene oxide) chains on the linear end (**Figure 3.1a**). **Amphi-PP** in water self-assembled to form flexible coil-like fibers with a uniform diameter (**Figure 3.1b,d**), whereas rigid rod-like fibers were obtained in a non-polar solvent like *n*-hexane (**Figure 3.1c,e**). The stiffness of the nanostructures obtained in different mediums was analyzed with the help of the SAXS technique. These studies revealed that in an aqueous medium, the non-crystalline packing of alkyl chains of **Amphi-PP** led to nanofibers with amorphous core showing weak reflection in the SAXS pattern (**Figure 3.1d**). On the other hand, the SAXS pattern of the aggregates formed in *n*-hexane showed a strong reflection corresponding to an ordered *d*-spacing arrangement of 16.2 nm (**Figure 3.1e**). In this case, the core of the fibers is densely packed, containing crystalline poly(ethylene oxide) chains surrounded by hydrophobic wedge segments (**Figure 3.1e**).



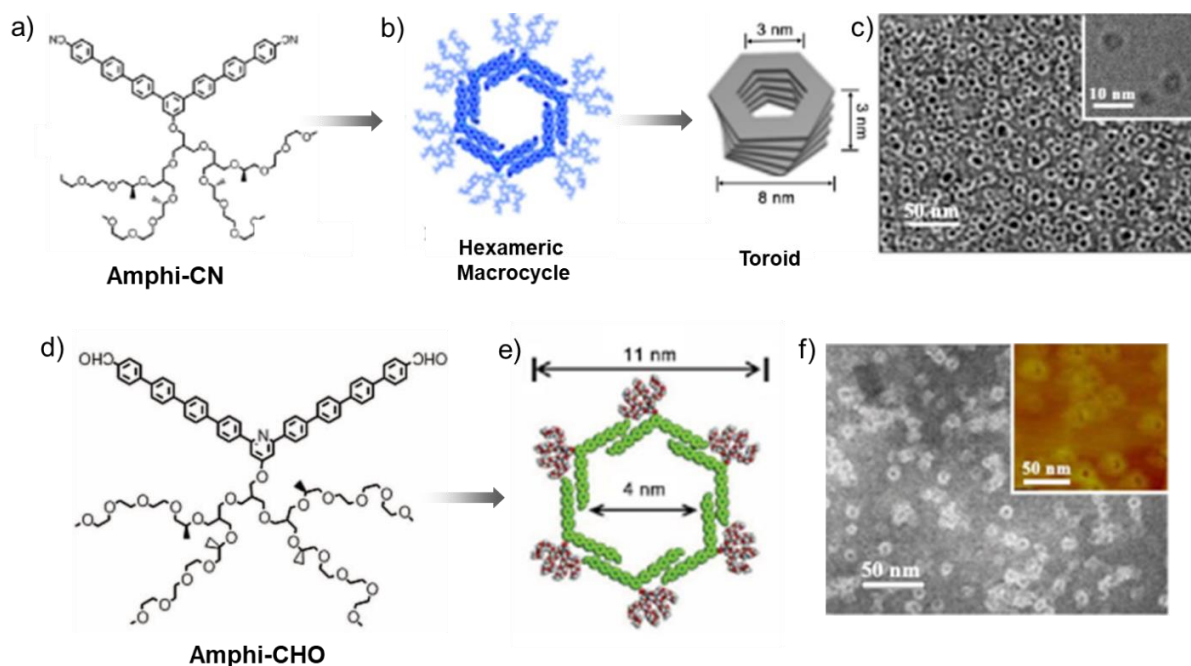


**Figure 3.2.** Molecular structure of bent-shaped (a) **Amphi-CN** and (d) **Amphi-CHO**. Schematic representation for the helical stacking of hexameric toroidal macrocycles and negatively stained TEM images for (b,c) **Amphi-CN** and (e,f) **Amphi-CHO**, respectively. A cryo-TEM image has been shown in the inset of **Figure 3.2c**. The inset in **Figure 3.2f** shows the AFM image of **Amphi-CHO**. (Adapted with permission from Ref 16).

Lee and co-workers have demonstrated the self-assembled toroid formation through the stacking of the macrocycles from bent-shaped amphiphilic molecules, **Amphi-CN** and **Amphi-CHO** (**Figure 3.2**).<sup>[16]</sup> These molecular structures have similarities, such as an internal angle of  $120^\circ$  from a meta-linked aromatic segment and the presence of an oligoether dendron side group on one of the sides (**Figure 3.2a,d**). Self-assembly of **Amphi-CN** in water initially formed the hexameric macrocycles (**Figure 3.2b**), followed by the stacking of the macrocycles to toroid-shaped nanostructures (**Figure 3.2c**). The cryogenic TEM image shown in the inset of **Figure 3.2c** has revealed that the toroids are almost uniform in size with an internal and external diameter of approximately 3 and 8 nm,

respectively. Similar type of stacking of the macrocycles was confirmed from the self-assembly of **Amphi-CHO** substituted with formyl group, which contains a larger volume of hydrophilic dendron moiety and an increased length for the pyridine-linked aromatic segment (**Figure 3.2d**).<sup>[16b]</sup> The self-assembly of **Amphi-CHO** was found to be highly affected by the weak dipole interaction of the formyl group and the steric repulsion created by the water cluster at the pyridine center, resulting in inducing a slippery motion of the adjacent aromatic segments to form hexameric macrocycles by preferring the *p*-phenylene chromophores to orient in a J-type fashion (**Figure 3.2e**). Moreover, TEM and AFM studies have confirmed that the toroids formed upon the self-assembly of **Amphi-CHO** in an aqueous medium are relatively larger with an internal and external diameter of 4 and 11 nm, respectively (**Figure 3.2f**). The aforementioned examples demonstrate the importance of designing bent-shaped monomers to achieve toroidal nanostructures with controlled structural parameters.

A novel strategy to obtain white-light emitting organogel through the partial excitation energy transfer from blue-light emitting donor **BC-OPV** and a red-light-emitting acceptor **PYPV** has been reported (**Figure 3.3a**).<sup>[17]</sup> **BC-OPV** formed pseudo-H-type aggregates and twisted helical tapes in *n*-decane.<sup>[17b]</sup> **Figure 3.3b** shows the TRES analysis for **BC-OPV**, by which the excited state property particularly the excitation energy migration in the gel state can be explained. Upon exciting with 375 nm UV light, the emission spectrum was found to be red-shifted from 494 to 528 nm with an increase in time after excitation. The spectrum obtained after 1.46 ns was found to be almost similar

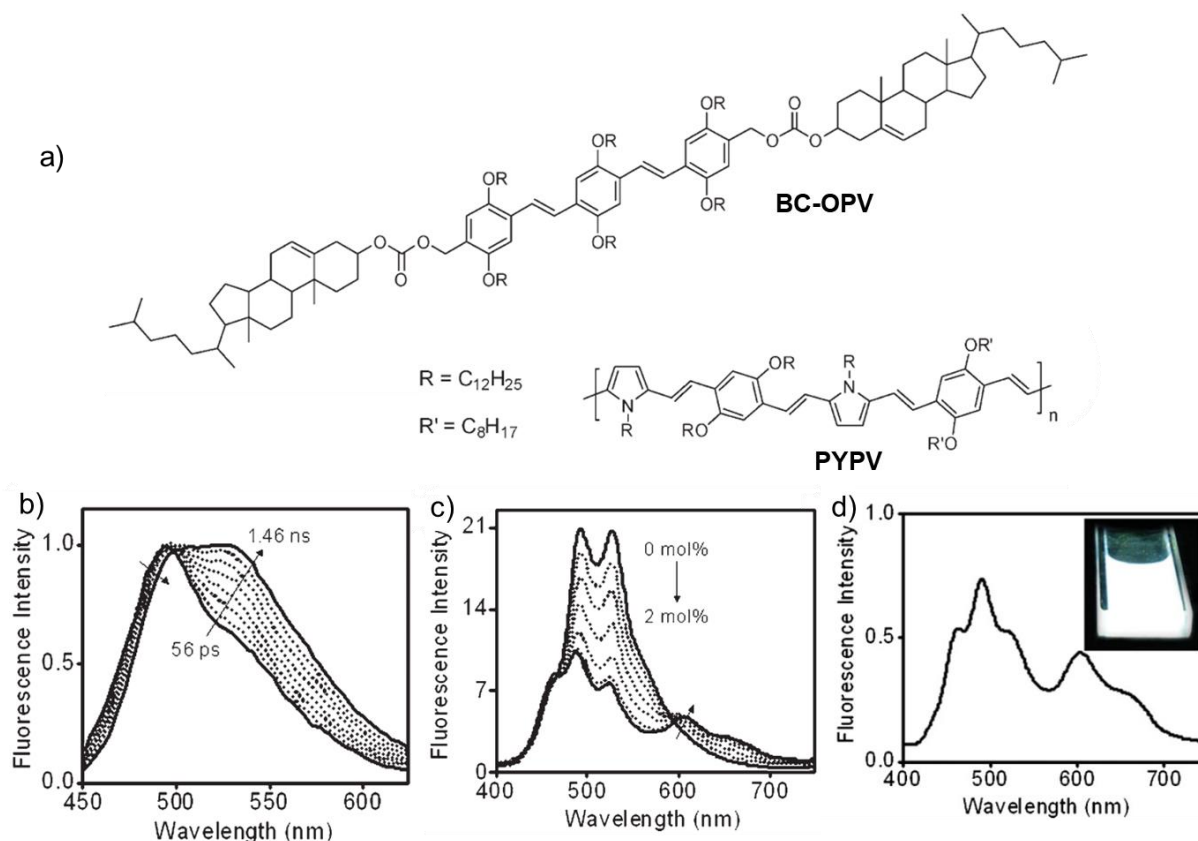


**Figure 3.3.** Molecular structures of cholesterol appended **BC-OPV** energy donor and **PYPV** energy acceptor. (b) Time-resolved emission spectra of **BC-OPV** in *n*-decane at room temperature ( $\lambda_{\text{ex}} = 375$  nm), indicating excitation energy migration. (c) Changes in the fluorescence emission ( $\lambda_{\text{ex}} = 380$  nm) of **BC-OPV** on the addition of increasing amounts of **PYPV** in *n*-decane at room temperature. (d) Emission spectrum of *n*-decane gel of **BC-OPV** donor in the presence of 2.1 mol% of **PYPV** acceptor ( $\lambda_{\text{ex}} = 380$  nm). Inset shows the white-light emission of the gel under the illumination of 365 nm UV light. (Adapted with permission from Ref 17).

to that of the steady-state emission of the *n*-decane gel (**Figure 3.3b**). Because of the weak gelation and slow exciton diffusion in **BC-OPV**, the probability of partial energy transfer has been further tested by doping with a red-emitting acceptor **PYPV**. Upon gradual increase in the acceptor percentage, the emission maxima for **BC-OPV** obtained at 492 and 528 nm was quenched by 63%, with concomitant formation of a new peak at 607 nm corresponding to the acceptor emission (**Figure 3.3c**). Besides, the fluorescence lifetime decay of **BC-OPV** in the presence of **PYPV** was found fast compared to that of **BC-OPV**

and a profound growth component was observed at the initial time scale. Both these factors confirm the energy transfer from the donor to acceptor. Furthermore, the *n*-decane gel of **BC-OPV** exhibited white light emission covering a broad region of 400-750 nm in the presence of 2.0 mol% of **PYPV** with CIE coordinates of (0.28, 0.34). The purity of the white-light emission (0.31, 0.35) in the gel state has been further improved by optimizing the concentration of **BC-OPV** ( $3.2 \times 10^{-4}$  M) and 2.1 mol% **PYPV** (**Figure 3.3d**).

Recently, a BODIPY dye substituted with a phenyl group at 2-position (**2-BODIPY**) exhibiting multi-emission across red and near-infrared (NIR) region in the solid-state has been reported (**Figure 3.4a**).<sup>[18]</sup> In THF, **2-BODIPY** showed an intense green emission ( $\lambda_{\text{max}} = 552$  nm) corresponding to monomers (**Figure 3.4b**). However, this dye showed a multiple emission at 605, 768, 868 and 976 nm across the red and NIR region in the powder and microcrystalline states (**Figure 3.4b**). Detailed TRES studies revealed that the origin of multi-emission feature is a result of successive energy transfer from high to lower energy levels in a stepwise fashion. Quantum chemical calculations further verified this result. Based on computational studies, a probable mechanism for the energy transfer between the multiple excitation states of BODIPY dyes have been proposed (**Figure 3.4c**). Accordingly, the peak at 605 nm assigned as monomeric emission and the origin of the peaks at 768, 868, and 976 nm attributed to the formation of dimer, trimer, and multimers, respectively.

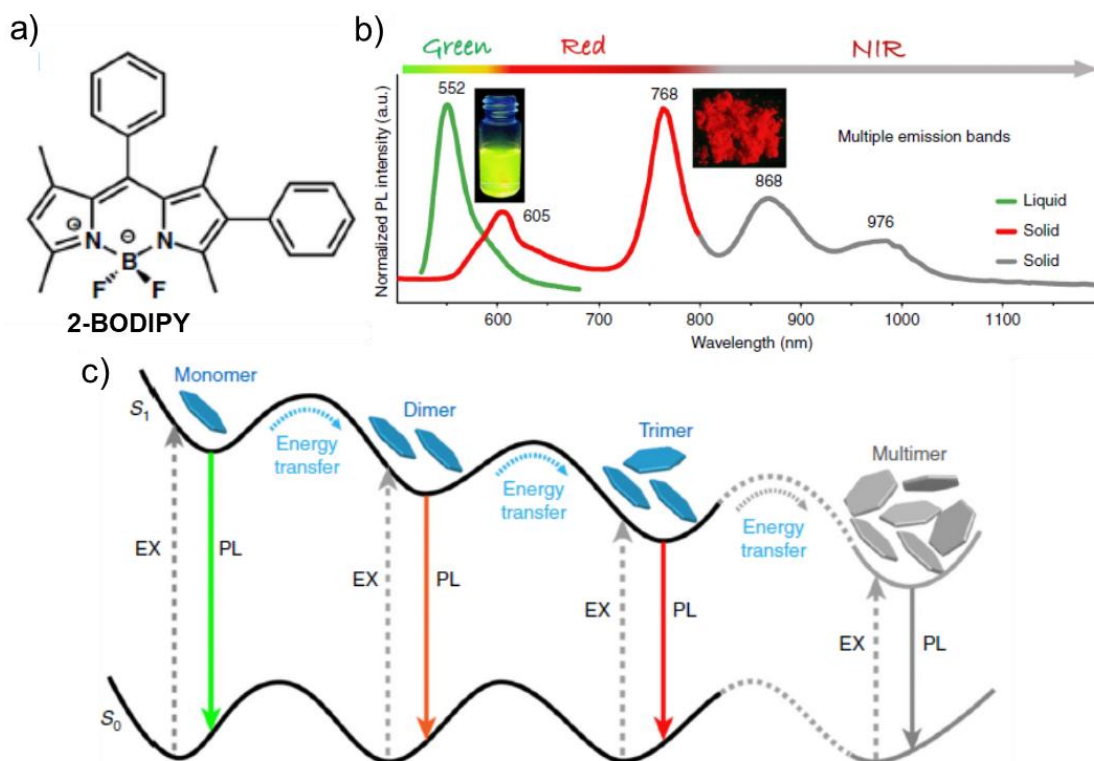


**Figure 3.4.** (a) Molecular structure of **2-BODIPY**. (b) Emission spectra of **2-BODIPY** in solution (green line) and microcrystalline powder state (red and grey line). (c) Schematic diagram showing the successive energy transfer and multiple emissions in the solid-state. (Adapted with permission from Ref 18).

Cascade energy transfer in supramolecular architectures is a fundamentally important process applicable to the biological and materials world.<sup>[19]</sup> For example, the phycobilisomes, which is the major light-harvesting complex in cyanobacteria and red algae, is considered one of the most efficient light-harvesting systems with more than 95% efficiency due to the cascade energy transfer.<sup>[19a,e]</sup> Though inferior to natural light-harvesting systems, the artificial supramolecular systems, due to the presence of aggregates of varying energy levels with large anisotropy, provides ample opportunities to simulate the natural light-harvesting processes. In this context, molecular assemblies of certain chromophores having the mixture of aggregates with different levels of electronic coupling have been shown to facilitate cascade energy transfer leading to red-shifted emission.<sup>[17,20]</sup>

This red-shift can lead either to a broad emission, if aggregates of closely matching energy levels are involved or to multiple emission if aggregates of discrete energy levels are present in the hierarchical self-assembly. However, the latter type of molecular assembly resulting in multiple emission covering the entire visible-NIR region upon a single excitation remains a challenge.

Among different chromophores, BODIPY is an excellent choice for creating supramolecular optoelectronic materials due to their photostability, high molar absorptivity and sensitive fluorescence features.<sup>[21-24]</sup> Here, we demonstrate how distinct energy landscapes can be obtained by creating different morphological features that facilitate reversible modulation of emission behavior. This is possible by tweaking the self-assembly of *meso*  $\pi$ -extended BODIPY dyes **1-3** (**Chart 3.1**) with solvents as established in this work. The high ground state dipole moment ( $\mu_g = 7.53$  D) of the Y-shaped molecules **1** and **2**, drives the self-assembly in cyclic nonpolar solvents such as MCH or *trans*-decalin, initially resulting in 10-20 nm spheres, which transform into large spheres of 600-800 nm with time as confirmed by DLS experiments. Evaporation of the MCH solution of **1** or **2** on a substrate resulted in an assembly of spherical structures, wherein each large sphere is surrounded by a layer of self-assembled nanospheres, appearing like a core-shell structure with an average size of 400-1200 nm. The spherical particles exhibited a normal emission spectrum with a single maximum at 540 nm. On the other hand, in linear nonpolar solvents such as *n*-heptane or *n*-decane, 2D supramolecular sheets having broad emission comprising of 540, 610, 650, 725 and 790 nm bands are formed. Interestingly, the single

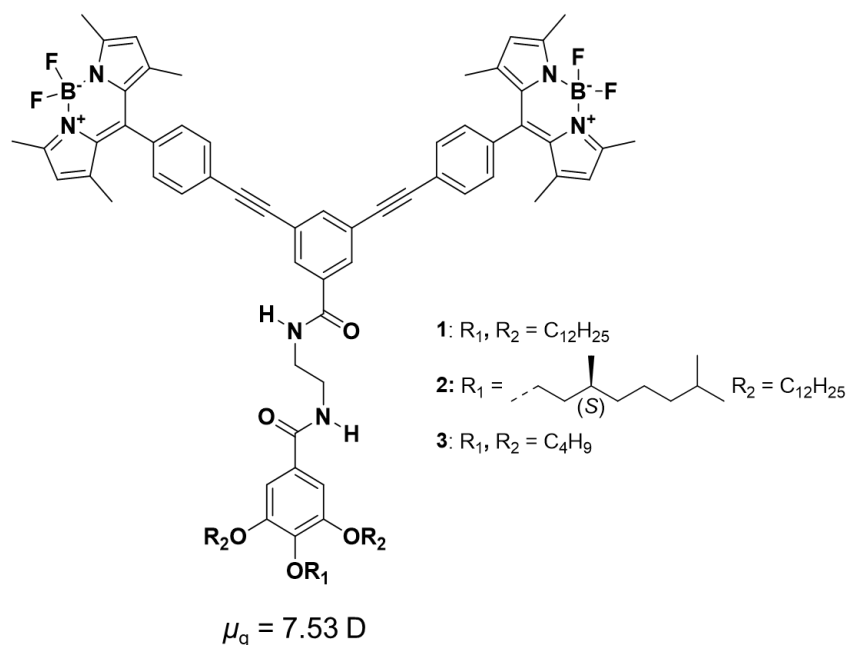


**Chart 3.1.** Molecular structures of Y-shaped BODIPY derivatives **1–3**.

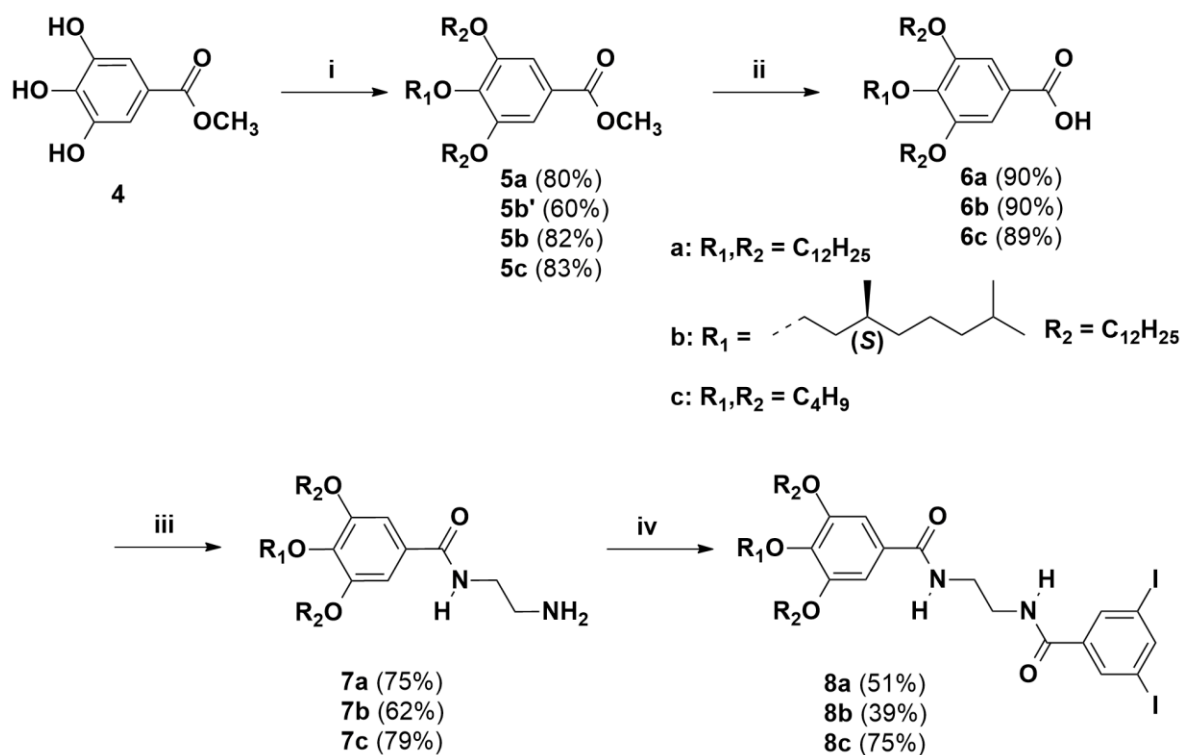
and multiple emission could be reversibly controlled by tweaking the morphology between the spherical and 2D assemblies by changing the solvent composition. Molecule **3** having short alkyl chains failed to form either the spherical morphology or 2D sheets, revealing the importance of the alkyl chains in the self-assembly process. Ultrasound stimulation of the 2D sheets exhibited better efficiency for the successive energy transfer as evident by a 2.2-fold increase in the intensity of the NIR bands at 725 and 790 nm. The morphological features and the associated emission behavior described here are unprecedented and the origin of multiple emission ascribed is the manifestation of a cascade effect of the excitation energy as established by time-resolved emission and anisotropy studies.

### 3.3. Results and Discussion

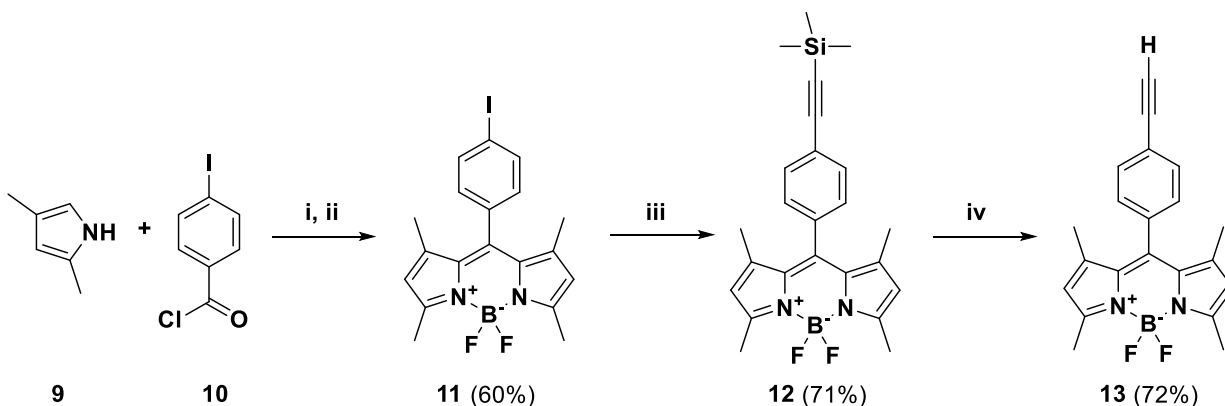
#### 3.3.1. Synthesis of BODIPY Derivatives

The BODIPY derivatives **1-3** were synthesized using multistep palladium-catalyzed Sonogashira-Hagihara cross coupling reactions between *N*-(2-(3,5-diiodobenzamido)ethyl)-3,4,5-trialkoxybenzamide (**8**) and 4,4-difluoro-1,3,5,7-tetramethyl-8-(4-ethynyl)-4-bora-3a,4a-diaza-*s*-indacene (**13**), as mentioned in **Scheme 3.3**. At first, methyl-3,4,5-trihydroxybenzoate (**4**) on reaction with different types of linear and branched alkyl halides in dry DMF in the presence of anhydrous K<sub>2</sub>CO<sub>3</sub> afforded various methyl-3,4,5-trialkoxybenzoate (**5**) derivatives with different (**5a**: 80%; **5b**: 83%; **5c**: 82%) yield. Subsequent ester hydrolysis of **5** in presence of KOH provided 3,4,5-trialkoxybenzoic acid (**6**) having yield around 90%. In presence of BOP reagent, compound **6** and ethylenediamine underwent amide coupling reaction to provide *N*-(2-aminoethyl)-3,4,5-trialkoxybenzamide (**7**) with various ranges of yield (**7a**: 75%; **7b**: 79%; **7c**: 22%). Compound **7** was then allowed to undergo another amide coupling with 3,5-diiodobenzoic acid in presence of BOP reagent following an identical method, resulting in *N*-(2-(3,5-diiodobenzamido)ethyl)-3,4,5-trialkoxybenzamide (**8**), having different yields with respect to the nature of the substituted alkyl chains (**8a**: 51%; **8b**: 75%; **8c**: 39%). The reaction conditions related to all of these reactions have been represented in **Scheme 3.1**. Subsequently, 4-Iodobenzoylchloride (**9**) was allowed to react with 2,4-dimethylpyrrole (**10**) in dry DCM under refluxing condition to provide 4,4-difluoro-

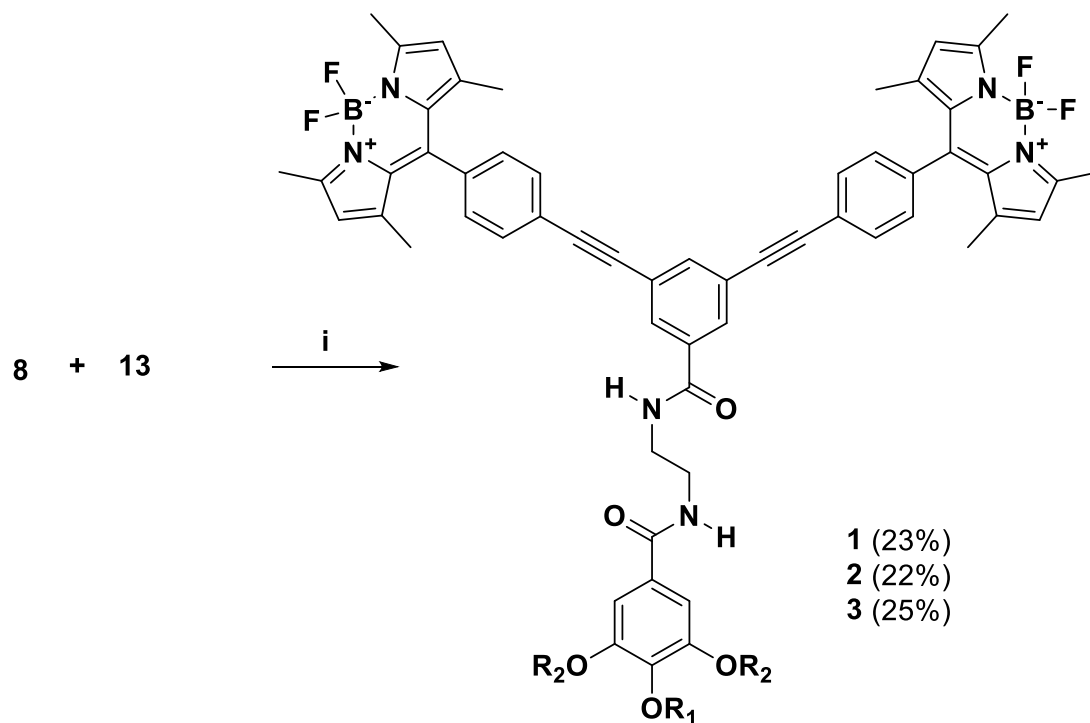




**Scheme 3.1.** Reagents and conditions: (i)  $C_{12}H_{25}Br/(S)\text{-}C_{10}H_{21}Br:C_{12}H_{25}Br$  (1:2)/ $C_4H_9Br$ ,  $K_2CO_3$ , DMF, 80 °C, 24 h; (ii) KOH, ethanol, 80 °C, 12 h; (iii) BOP reagent, ethylenediamine, DCM, r.t., 3 h; (iv) 3,5-diiodobenzoic acid, BOP reagent, DCM,  $Et_3N$ , r.t., 5 h.



**Scheme 3.2.** Reagents and conditions: (i) DCM, 35 °C, 3 h; (ii)  $Et_3N$ ,  $BF_3 \cdot Et_2O$ , 35 °C, 30 min; (iii) Ethynyltrimethylsilane,  $PdCl_2(PPh_3)_2$ , CuI, THF- $Et_3N$  (v:v 1:1), r.t., 12 h; (iv)  $K_2CO_3$ , THF-MeOH, r.t., 1 h.



**Scheme 3.3.** Reagents and conditions: (i)  $PdCl_2(PPh_3)_2$ ,  $CuI$ , THF- $Et_3N$  (v:v 1:1), 70 °C, 18 h.

1,3,5,7-tetramethyl-8-(4-iodo)-4-bora-3a,4a-diaza-*s*-indacene (**11**) with a yield of 60% (**Scheme 3.2**). Compound **11** was obtained as *meso* iodo-substituted BODIPY core. Upon reacting **11** with ethynyltrimethylsilane following Sonogashira-Hagihara coupling reaction resulted in the formation of 4,4-difluoro-1,3,5,7-tetramethyl-8-(4-(trimethylsilyl)ethynyl)-4-bora-3a,4a-diaza-*s*-indacene (**12**) in 71% yield. Furthermore, deprotection of trimethylsilyl group of **12** with the help of  $K_2CO_3$ , resulted in the formation of 4,4-difluoro-1,3,5,7-tetramethyl-8-(4-ethynyl)-4-bora-3a,4a-diaza-*s*-indacene (**13**) with 72% yield. Finally, the key step was accomplished using Sonogashira-Hagihara cross coupling reactions between **8** and **13** yielding the final compounds **1**, **2** and **3** around 25% yield (**Scheme 3.3**).

### 3.3.2. Photophysical Properties and Self-Assembly

After synthesizing **1–3** (Chart 3.1), we have studied their optical behavior and self-assembly processes (Figure 3.5). In CHCl<sub>3</sub> ( $1 \times 10^{-4}$  M) at 295 K, the UV-vis absorption spectrum of **1** exhibited two maxima at 290 and 504 nm with a shoulder band around 475 nm (Figure 3.5a). The broad absorption observed at 290 nm ( $\varepsilon = 5.6 \times 10^4$  M<sup>-1</sup> cm<sup>-1</sup>) corresponds to the phenyleneethynylene moiety, whereas the narrow absorption feature at 504 nm ( $\varepsilon = 1.3 \times 10^5$  M<sup>-1</sup> cm<sup>-1</sup>) implies the strong S<sub>0</sub> → S<sub>1</sub> electronic transition involving (0 → 0) vibrational states of the BODIPY chromophore. The band at 475 nm can be considered as the vibronic shoulder of S<sub>0</sub>-S<sub>1</sub> transition.<sup>[24]</sup> On the other hand, the absorption spectrum of **1** ( $3 \times 10^{-4}$  M) in MCH or *trans*-decalin, when heated to 363 K followed by cooling to 283 K at a rate of 1 K/min, exhibited an absorption maximum at 288 nm ( $\varepsilon = 6.75 \times 10^4$  M<sup>-1</sup> cm<sup>-1</sup>), with a broad band ( $\lambda_{\max} = 504$  nm,  $\varepsilon = 1.04 \times 10^5$  M<sup>-1</sup> cm<sup>-1</sup>) between 420-550 nm (Figure 3.5a). Furthermore, **1** exhibited an emission maximum at 520 nm ( $\Phi_F = 0.39$ ) in CHCl<sub>3</sub>, whereas in MCH a red shifted maximum at 540 nm ( $\Phi_F = 0.20$ ) (Figure 3.5b). Variable temperature <sup>1</sup>H NMR experiment carried out in cyclohexane-d<sub>12</sub> revealed the presence of well-resolved peaks of **1** at 343 K, whereas a decrease of temperature to ambient condition (298 K) exhibited complete disappearance of the NMR peaks (Figure 3.6). This process was found to be reversible with respect to temperature and hence confirms the aggregation of **1** in cyclic nonpolar solvents.

Upon gradual reduction in temperature from 363 to 283 K, the intensity of the absorption maximum was reduced and the absorption spectrum corresponding to both

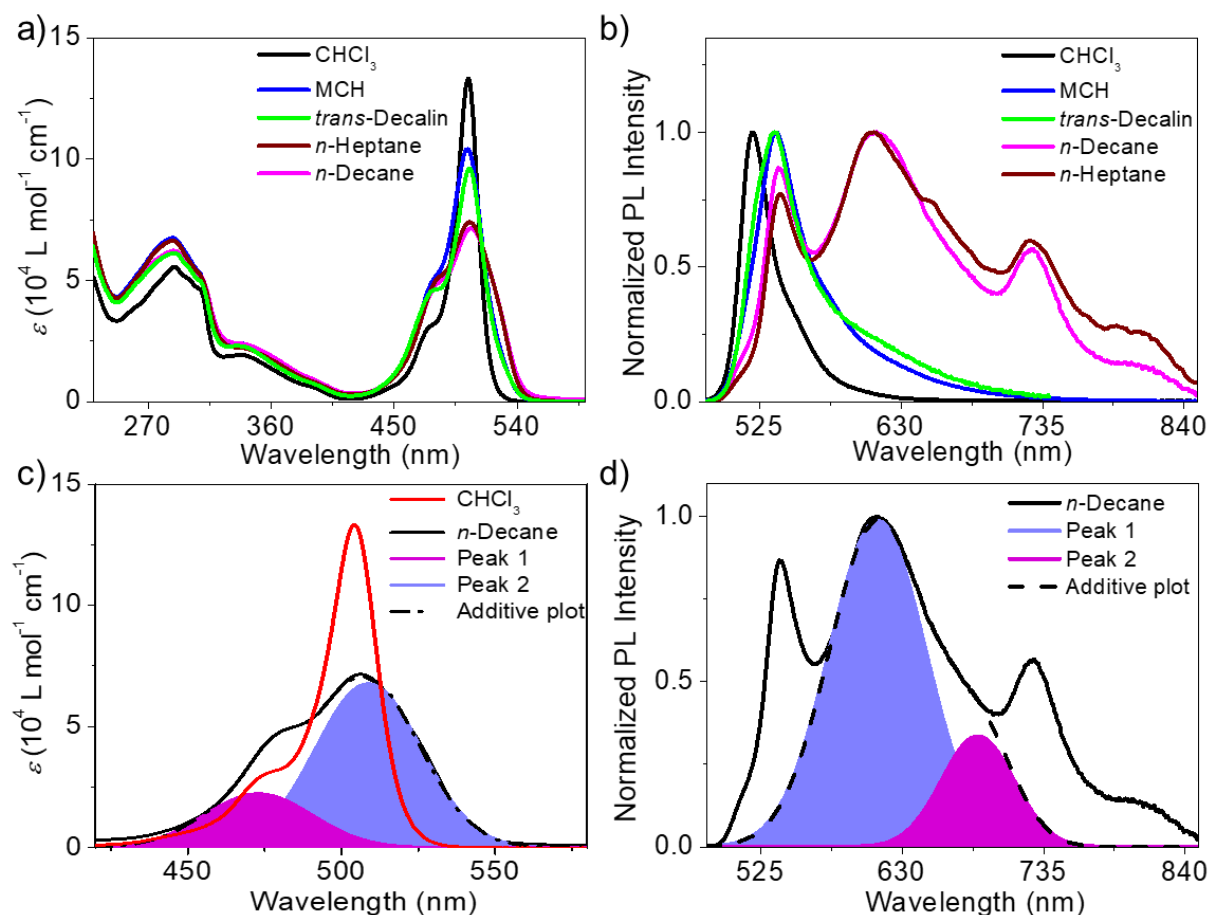


**Figure 3.5.** (a) Absorption and (b) normalized emission spectra ( $\lambda_{\text{ex}} = 475 \text{ nm}$ ) of **1** in chloroform ( $1 \times 10^{-4} \text{ M}$ ), MCH, *trans*-decalin ( $3 \times 10^{-4} \text{ M}$ ) and *n*-decane, *n*-heptane ( $3 \times 10^{-4} \text{ M}$ ). Deconvoluted (c) absorption and (d) emission spectra of **1** in *n*-decane at 506 and 610 nm, respectively.

BODIPY and PE part became broad (**Figure 3.7a**). In contrast, the temperature-dependent emission studies showed a gradual increase in the intensity when **1** in MCH was cooled from 363 to 283 K, indicating AIEE behavior (**Figure 3.7b**).<sup>[2a,25a]</sup> Since the phenyl ring attached at the *meso* position of BODIPY chromophore **1** is unsubstituted, rotational and vibrational motions are facilitated at higher temperature, leading to non-radiative deactivation of the excited state and less emission.<sup>[24a]</sup> However, upon gradual reduction in temperature, aggregation of **1** restricts the rotation and vibrational motion and activates

radiative excited state decay to display enhanced emission. Aggregation of **1** in MCH at a concentration of  $3 \times 10^{-4}$  M was further confirmed from the plot of  $\alpha_{\text{agg}}$  of **1** with respect to temperature, revealing a non-sigmoidal cooling curve, which is characteristic of a cooperative self-assembly process (**Figure 3.7c** and **Table 3.1**).<sup>[25]</sup>

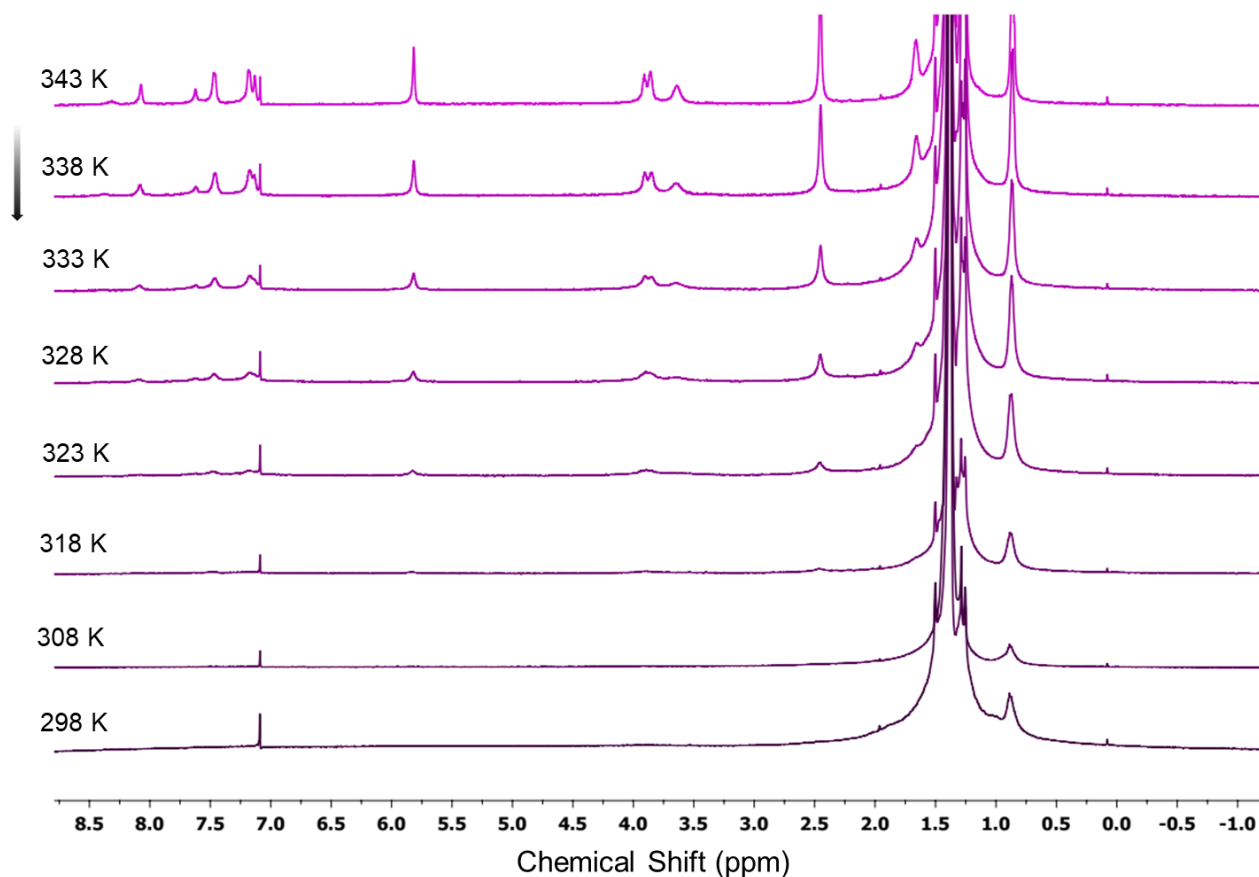


**Figure 3.6.** Variable temperature-<sup>1</sup>H NMR (500 MHz) spectra of **1** in cyclohexane-d<sub>12</sub> ( $1 \times 10^{-3}$  M).

In *n*-decane or *n*-heptane ( $3 \times 10^{-4}$  M), the absorption spectra of **1** within 230-420 nm was almost similar to those in CHCl<sub>3</sub> and MCH (**Figure 3.5a**), however, the absorption corresponding to the BODIPY chromophore appeared much broader ( $\lambda_{\text{max}} = 506$  nm,  $\epsilon =$

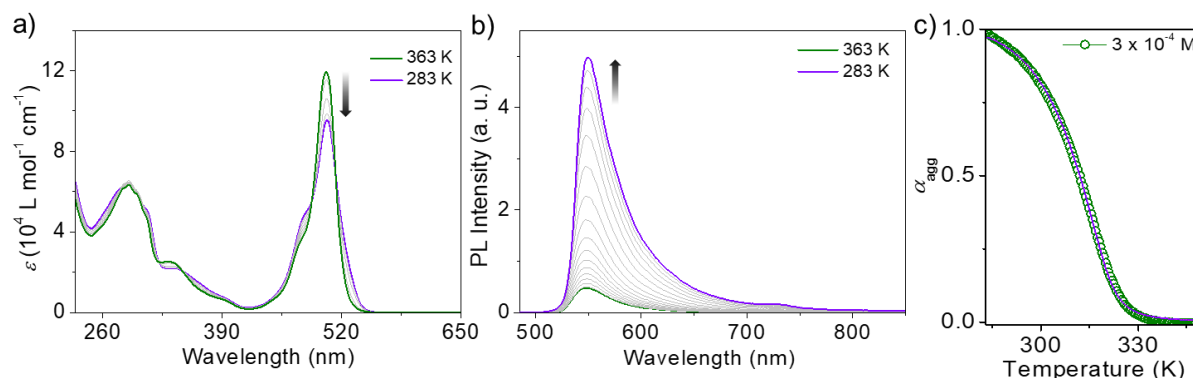


**Figure 3.7.** Temperature-dependent (a) absorption and (b) emission spectra ( $\lambda_{\text{ex}} = 475 \text{ nm}$ ) of **1** in MCH ( $3 \times 10^{-4} \text{ M}$ ). (c) The plot of  $\alpha_{\text{agg}}$  versus temperature at a concentration of  $3 \times 10^{-4} \text{ M}$  of **1** in MCH;  $\alpha_{\text{agg}}$  was calculated by monitoring the absorbance changes at 533 nm.

**Table 3.1.** Different thermodynamic parameters obtained by fitting temperature-dependent  $\alpha_{\text{agg}}$  of **1** in MCH to the equilibrium model.<sup>[25]</sup>

Conc. (M)	$\Delta H^\circ$ (kJmol <sup>-1</sup> )	$\Delta H^\circ$ (STD) (kJmol <sup>-1</sup> )	$\Delta S^\circ$ (kJmol <sup>-1</sup> K <sup>-1</sup> )	$\Delta S^\circ$ (STD) (kJmol <sup>-1</sup> K <sup>-1</sup> )	$\Delta H^\circ_{\text{nucl}}$ (kJmol <sup>-1</sup> )	$\Delta H^\circ_{\text{nucl}}$ (STD) (kJmol <sup>-1</sup> )	$T_e$ (K)	$T_e$ (STD)
$3 \times 10^{-4}$	-54.76	0.77	-0.103339	0.002461	-13.70	0.23	320.63	0.13

$\Delta H^\circ$ : Enthalpy of elongation (kJ/mol);  $\Delta S^\circ$ : Entropy difference (kJ/mol K);  $\Delta H^\circ_{\text{nucl}}$ : Nucleation penalty (kJ/mol);  $T_e$ : Elongation temperature.

$7.2 \times 10^4 \text{ M}^{-1} \text{ cm}^{-1}$ ), with predominant shoulder bands in the lower and higher wavelength region (470 and 570 nm), indicating the formation of multiple aggregates (**Figures 3.5a** and **3.8a**). Surprisingly, the emission spectrum of **1** ( $3 \times 10^{-4} \text{ M}$ ) in *n*-decane or *n*-heptane exhibited an unusually broad band with multiple maxima at 540, 610, 650, 725 and 790 nm ( $\Phi_F = 0.14$ ). The peak at 650 nm is more resolved in *n*-heptane (**Figure 3.5b**). Deconvolution of the broad absorption peak (506 nm) obtained in *n*-decane shows two peaks at 473 and 509 nm, confirming the formation of aggregates (possibly mixture of both H- and J-type aggregates) (**Figure 3.5c**).<sup>[26]</sup> Deconvolution of the broad emission band at 610 nm in *n*-decane revealed two peaks at 612 and 686 nm (**Figure 3.5d**).

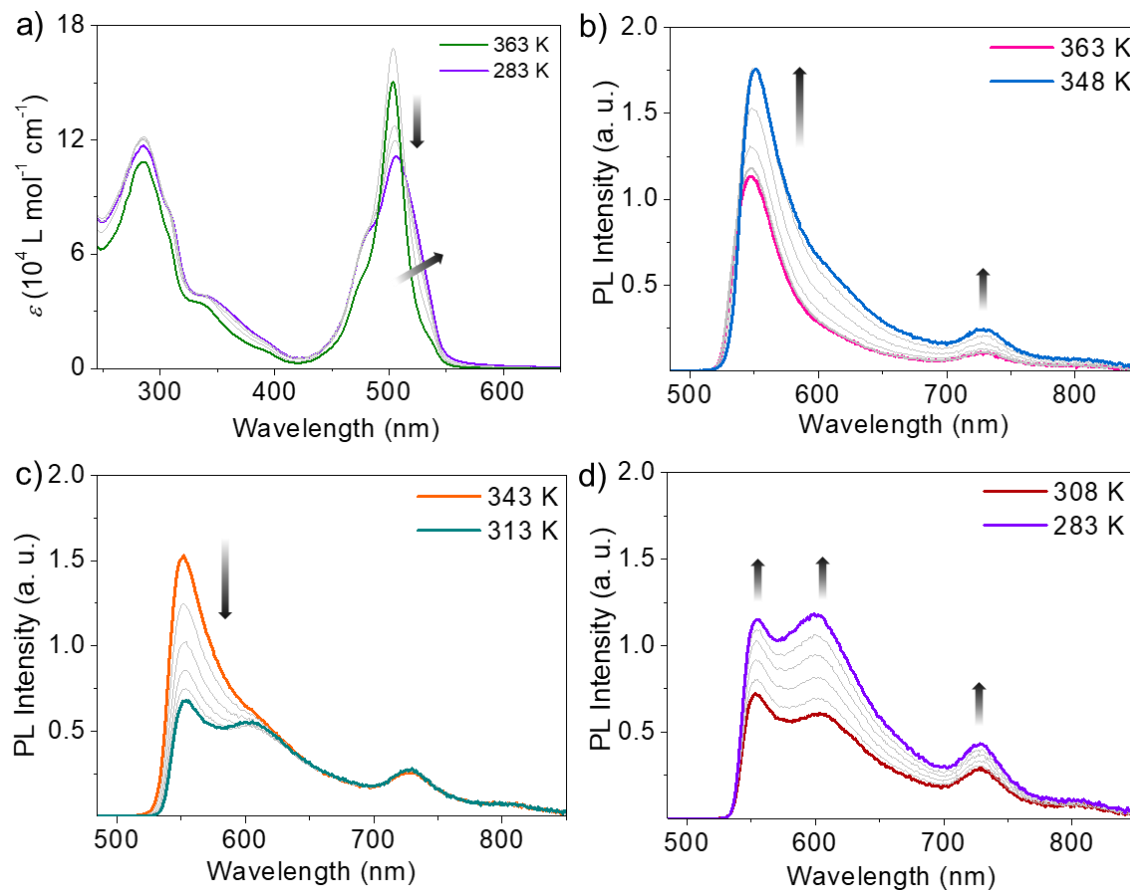


**Figure 3.8.** (a) Temperature-dependent absorption spectra of **1** in *n*-decane ( $3 \times 10^{-4}$  M). Variable temperature emission spectra of **1** in *n*-decane ( $3 \times 10^{-4}$  M),  $\lambda_{\text{ex}} = 475$  nm; at different temperature ranges: (b) 363 to 348 K, (c) 343 to 313 K and (d) 308 to 283 K.

These observations were further confirmed from the temperature-dependent absorption and emission studies of **1** in *n*-decane (**Figure 3.8**). At 363 K, **1** in *n*-decane displayed a sharp absorption band at 504 nm, which gradually reduced its intensity and became broad at 283 K (**Figure 3.8a**). The intensity of the emission spectrum of **1** in *n*-decane was initially found to increase with an appearance of a new peak at 725 nm upon reducing the temperature 363 to 348 K (**Figure 3.8b**). Between 343 to 313 K, the emission intensity of the peak at 552 nm was found to gradually decrease with the

appearance of a new peak at 600 nm (**Figure 3.8c**). Further reduction in temperature to 283 K resulted in an overall enhancement in the intensity of emission profile with three distinct maxima at 552, 600 and 725 nm (**Figure 3.8d**). BODIPY derivatives are known to exhibit such broad multiple emission in solid/semicrystalline powder form, however not in any solvents.<sup>[18,23f,24d]</sup> While MCH and *n*-decane have more or less identical polarity, except their difference in structure and shape (cyclic and linear), the observed difference in the emission behavior in these solvents could be associated with the hierarchical assembly of the BODIPYs.

Plots of  $\alpha_{\text{agg}}$  of **1** with respect to temperature revealed non-sigmoidal cooling curves for a wide range of concentrations ( $1 \times 10^{-4}$  to  $3 \times 10^{-4}$  M) (**Figure 3.9a**). The cooling curves thus obtained were fitted to an equilibrium model, characteristics of a co-operative self-assembly process.<sup>[25]</sup> Details of the thermodynamic parameters related to the fitting are summarized in **Table 3.2**. The plot of the natural logarithm of the reciprocal concentration of **1** against reciprocal of  $T_e$  exhibited a linear relationship (van 't Hoff plot, **Figure 3.9b**).

**Table 3.2.** Different thermodynamic parameters obtained by fitting temperature-dependent  $\alpha_{\text{agg}}$  of **1** in *n*-decane to the equilibrium model.<sup>[25]</sup>

Conc. (M)	$\Delta H^\circ$ (kJmol <sup>-1</sup> )	$\Delta H^\circ$ (STD) (kJmol <sup>-1</sup> )	$\Delta S^\circ$ (kJmol <sup>-1</sup> K <sup>-1</sup> )	$\Delta S^\circ$ (STD) (kJmol <sup>-1</sup> K <sup>-1</sup> )	$\Delta H^\circ_{\text{nucl}}$ (kJmol <sup>-1</sup> )	$\Delta H^\circ_{\text{nucl}}$ (STD) (kJmol <sup>-1</sup> )	$T_e$ (K)	$T_e$ (STD)
$1 \times 10^{-4}$	-44.97	0.76	-0.053618	0.002278	-27.84	2.11	345.43	0.23
$1.5 \times 10^{-4}$	-45.22	0.65	-0.057055	0.001942	-33.64	4.28	347.15	0.19
$2 \times 10^{-4}$	-49.93	0.76	-0.071111	0.002226	-26.34	1.68	351.83	0.22
$3 \times 10^{-4}$	-54.12	0.63	-0.083861	0.001833	-29.98	2.32	357.69	0.17

$\Delta H^\circ$ : Enthalpy of elongation (kJ/mol);  $\Delta S^\circ$ : Entropy difference (kJ/mol K);  $\Delta H^\circ_{\text{nucl}}$ : Nucleation penalty (kJ/mol);  $T_e$ : Elongation temperature.



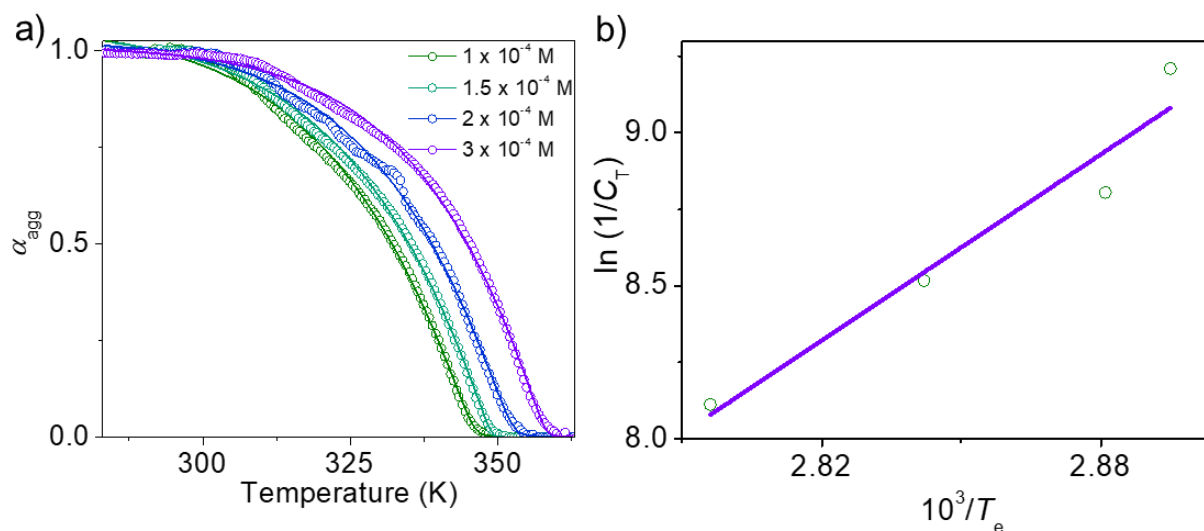


**Figure 3.9.** (a) The plot of  $\alpha_{agg}$  versus temperature at different concentrations of **1** in *n*-decane;  $\alpha_{agg}$  has been calculated by monitoring the changes in absorbance at 530 nm. (b) van 't Hoff plot obtained through the controlled cooling experiments of **1** in *n*-decane.

The thermodynamic parameters of **1** in *n*-decane were  $\Delta H^\circ = -84.26$  kJ/mol,  $\Delta S^\circ = -168.43$  J/mol K and  $\Delta G^\circ = -34.07$  kJ/mol, indicating that the self-assembly takes place through an enthalpically driven co-operative process. DLS experiments of **1** in MCH ( $3 \times 10^{-4}$  M) under fast cooling revealed the existence of two different bands with size distributions of 10-20 nm (80-90%) and 200-300 nm (10-20%) (**Figure 3.10a**). After aging for 24 h, the size of the aggregates increased to 600-800 nm (70%) while the population of the 10-20 nm size aggregates decreased to 30% (**Figure 3.10b**), indicating a consecutive process taking place, where the initially formed smaller spherical aggregates were directly transformed into bigger size assemblies without converting into the monomers (**Figure 3.10b**).<sup>[5b]</sup> However, a slow cooled (1 K/min) solution exhibited almost similar size of the assemblies as obtained by aging (**Figure 3.10c**). No time-dependent changes were noticed in the case of aggregates of **1** in *n*-decane, implying that

these aggregates have reached equilibrium when cooled at a controlled rate (**Figure 3.11**).

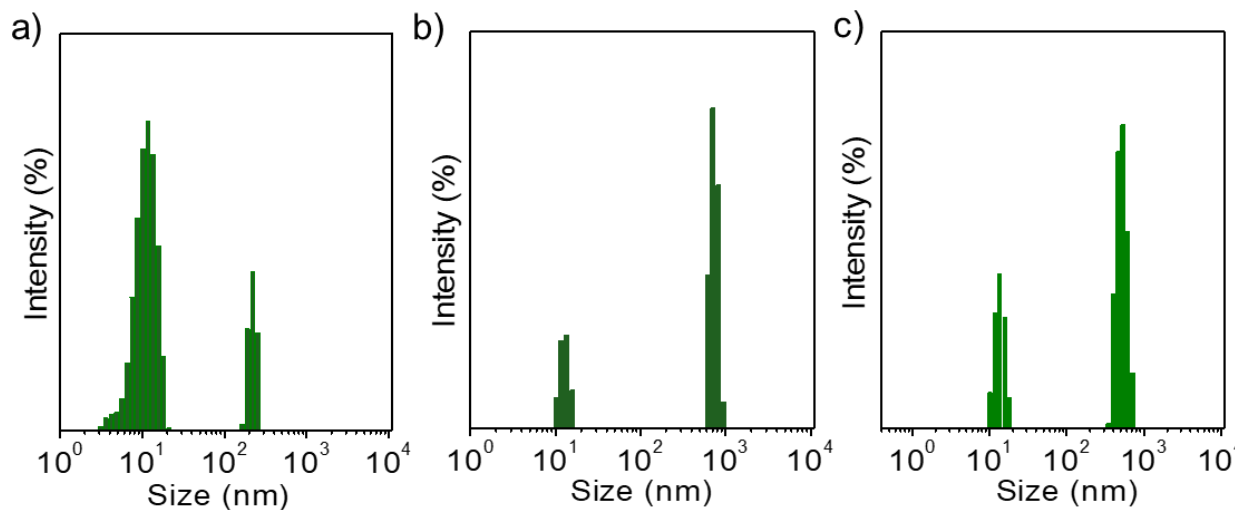


**Figure 3.10.** DLS size distribution of **1** in MCH ( $3 \times 10^{-4}$  M): (a) immediately after fast cooling, (b) after aging the sample for 24 h, and (c) after cooling at a controlled rate of 1 K/min.

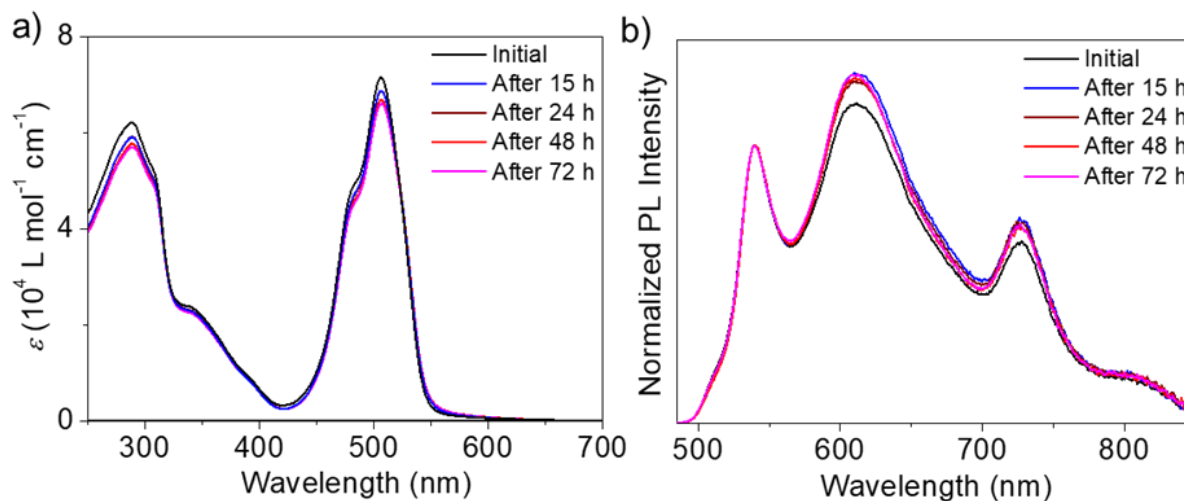


**Figure 3.11.** Time-dependent (a) absorption and (b) emission spectra of *n*-decane aggregates of **1** ( $3 \times 10^{-4}$  M).

### 3.3.3. Morphological Characterization

TEM images of the self-assembly in MCH ( $3 \times 10^{-4}$  M) exhibited an unusual ‘spherical’ morphology akin to a core-shell type structure<sup>[27]</sup> having broad size distributions of 400–1200 nm. The spheres from the fast-cooled solution of **1** in MCH have diameters between 400 and 600 nm (**Figure 3.12a,b**), which upon aging for 24 h showed a size increase of

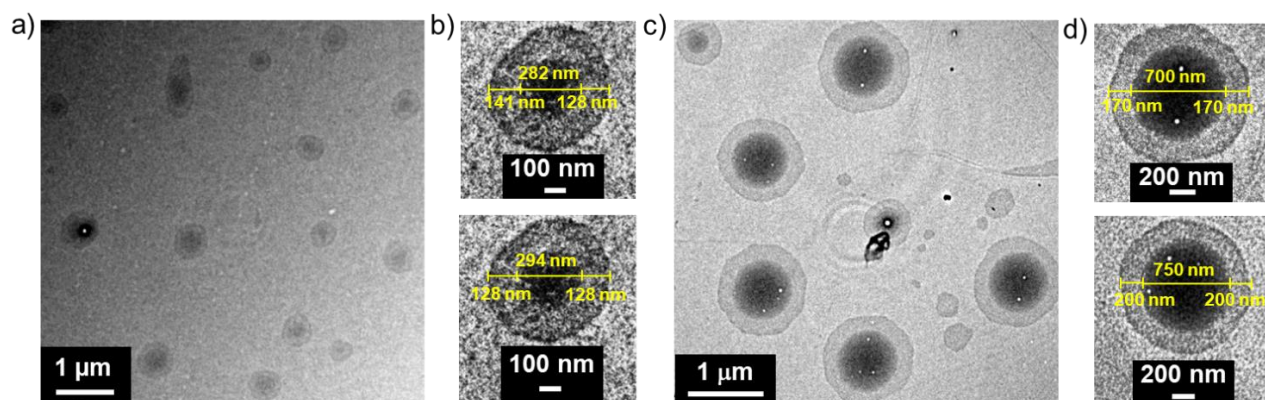


**Figure 3.12.** TEM images of **1** in MCH ( $3 \times 10^{-4}$  M), (a) immediately after fast cooling and (c) after aging the sample for 24 h. (b,d) Magnified images corresponding to **Figure 3.12a** and **3.12c**, respectively.

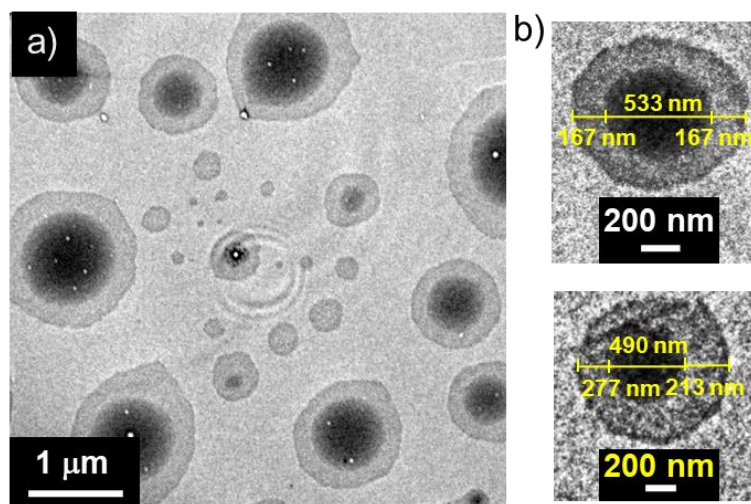


**Figure 3.13.** (a) TEM images of **1** in MCH ( $3 \times 10^{-4}$  M) after controlled cooling (1 K/min). (b) Magnified TEM images of a few spherical aggregates prepared by controlled cooling (1 K/min).

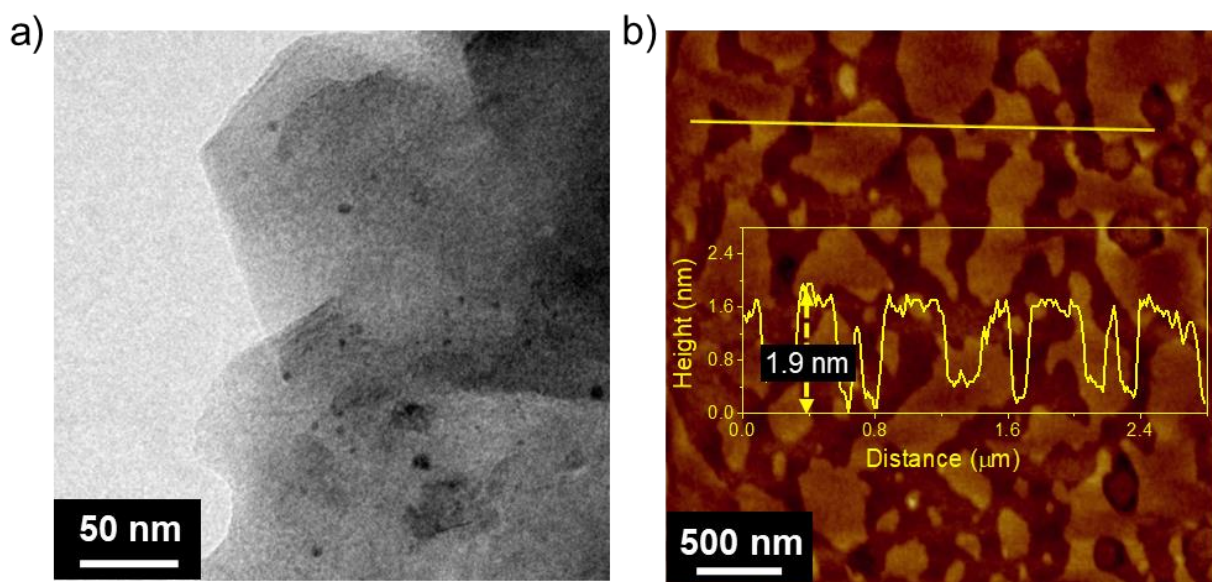


**Figure 3.14.** (a) TEM and (b) AFM images of **1** in *n*-decane ( $3 \times 10^{-4}$  M). The height profile along the yellow line is shown in the inset of **Figure 3.14b**.

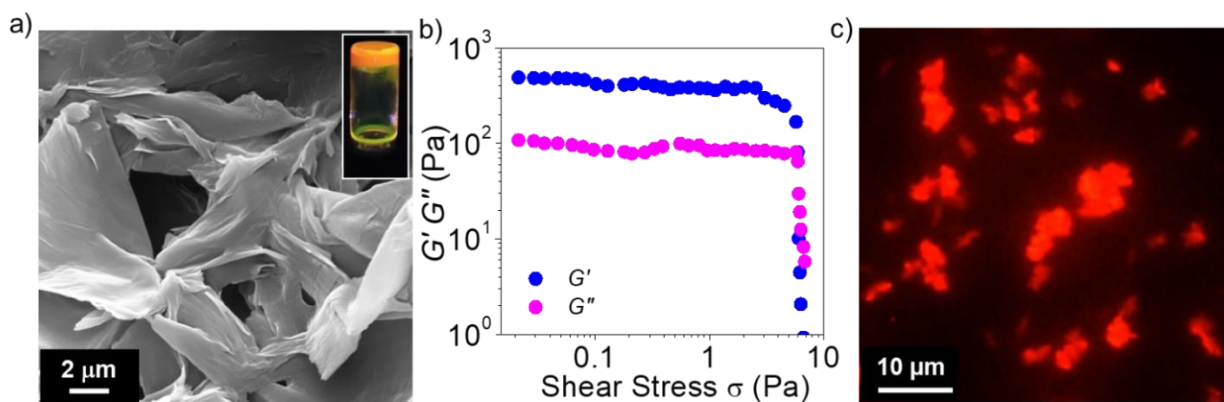


**Figure 3.15.** (a) SEM image of the *n*-decane gel ( $8 \times 10^{-3}$  M). Inset shows the photograph of the corresponding gel under illumination of 365 nm UV light. (b) The plot of dynamic storage modulus ( $G'$ , blue) and loss modulus ( $G''$ , magenta) against shear stress ( $\sigma$ ) for *n*-decane gel ( $8 \times 10^{-3}$  M) at 298 K. Frequency ( $\nu$ ) was kept fixed at 1 rad/s. (c) Fluorescence microscopy image of diluted *n*-decane gel.

600-1200 nm (**Figure 3.12c,d**). However, a slowly cooled solution (1 K/min) resulted in spherical assemblies of 400-1000 nm (**Figure 3.13**). Magnified images of the spherical

structures revealed a hyperdense core region having an average diameter of 200-900 nm and a less dense shell region of about 100-300 nm width (**Figure 3.12b,d** and **Figure 3.13b**).

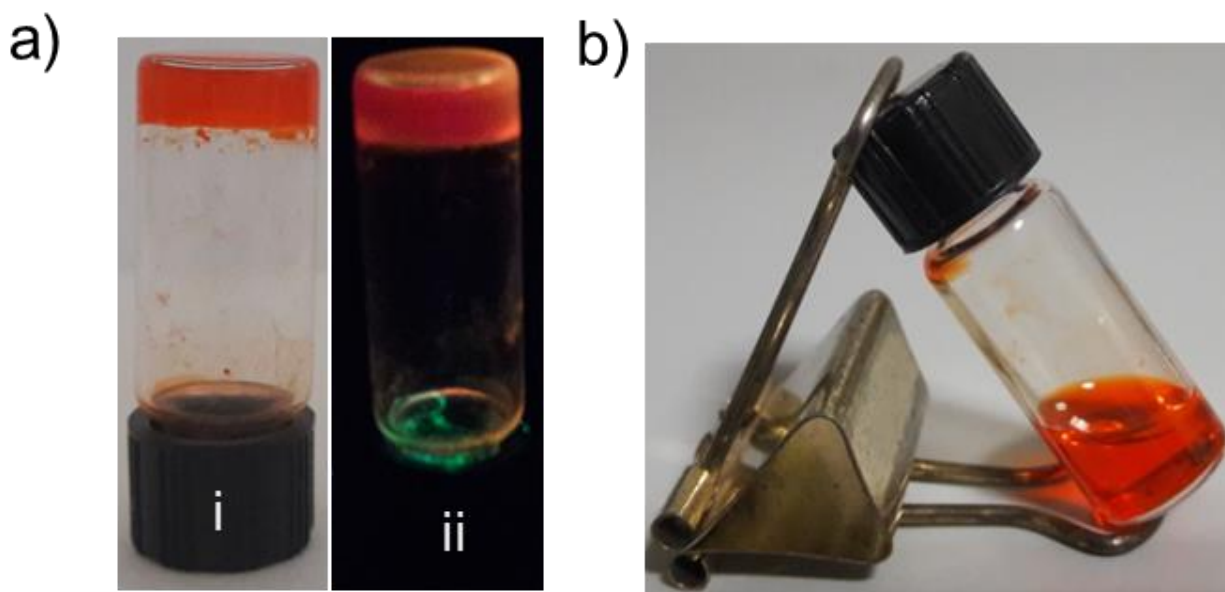


**Figure 3.16.** Gelation studies of **1** in *n*-heptane and MCH. (a) Photographs of *n*-heptane gel ( $8 \times 10^{-3}$  M) under (i) normal and (ii) illumination of 365 nm UV light. (b) Photograph taken in normal light exhibiting the inability of **1** to form gel in MCH at the same concentration.

While these types of structures are common in the case of inorganic semiconductors, such structures are rare in the case of organic single molecular self-assembly. The solvent evaporation on TEM grid may result in a thick core, around which excess nanospheres present in the mixture self-assemble to form a shell. On the other hand, from *n*-decane solution ( $3 \times 10^{-4}$  M), 2D sheet-like structures were obtained (**Figure 3.14** and **Figure 3.15**). AFM cross-sectional analysis indicates an average height of  $1.9 \pm 0.1$  nm with marginal surface roughness (**Figure 3.14b**). Upon increasing the concentration of **1** in *n*-decane ( $8 \times 10^{-3}$  M), the nanosheets were grown into large interconnected structures leading to an orange-red emitting gel (**Figure 3.15**). The viscoelastic nature of the *n*-decane gel is



evident from the stress sweep experiments, which revealed the dependencies of  $G'$  and  $G''$  on the applied shear stress. Both the  $G'$  and  $G''$  were independent of applied stress up to 5.75 Pa, indicating the substantial elastic nature of the gel (**Figure 3.15b**).<sup>[28]</sup> These observations underpin the ability of **1** to undergo 2D supramolecular polymerization in *n*-decane and *n*-heptane (**Figure 3.16a**).<sup>[4,29,30]</sup> However, the molecule **1** failed to form gel in MCH (**Figure 3.16b**), indicating that the spherical assembly is not able to arrest the solvent mobility in contrast to the 2D polymers obtained from *n*-decane.

#### **3.3.4. Self-Assembly of Chiral BODIPY Derivative**

After having an idea on the unique optical and morphological features of **1**, we looked into the properties of the chiral BODIPY derivative **2** to know whether the chiral side chains have any effect on the self-assembly. We anticipated that **2** in MCH and *n*-decane may result in the helical assembly due to the presence of chiral side chains. However, to our surprise, we observed that **2** resulted in spherical assemblies in MCH and 2D-sheets in *n*-decane (**Figure 3.17a-d**), similar to the morphologies of the achiral BODIPY derivative **1**. However, the 2D sheets obtained for **2** were rather crumbled (**Figure 3.17c,d**). The absence of helical structures points to the fact that **2** is reluctant to pack through a preferred handedness, despite having chiral handles. To confirm the absence of helical packing, we have recorded the circular dichroism (CD) spectra of **2** both in MCH and *n*-decane at various concentrations. In both the cases, no considerable CD signals could be seen (**Figure**

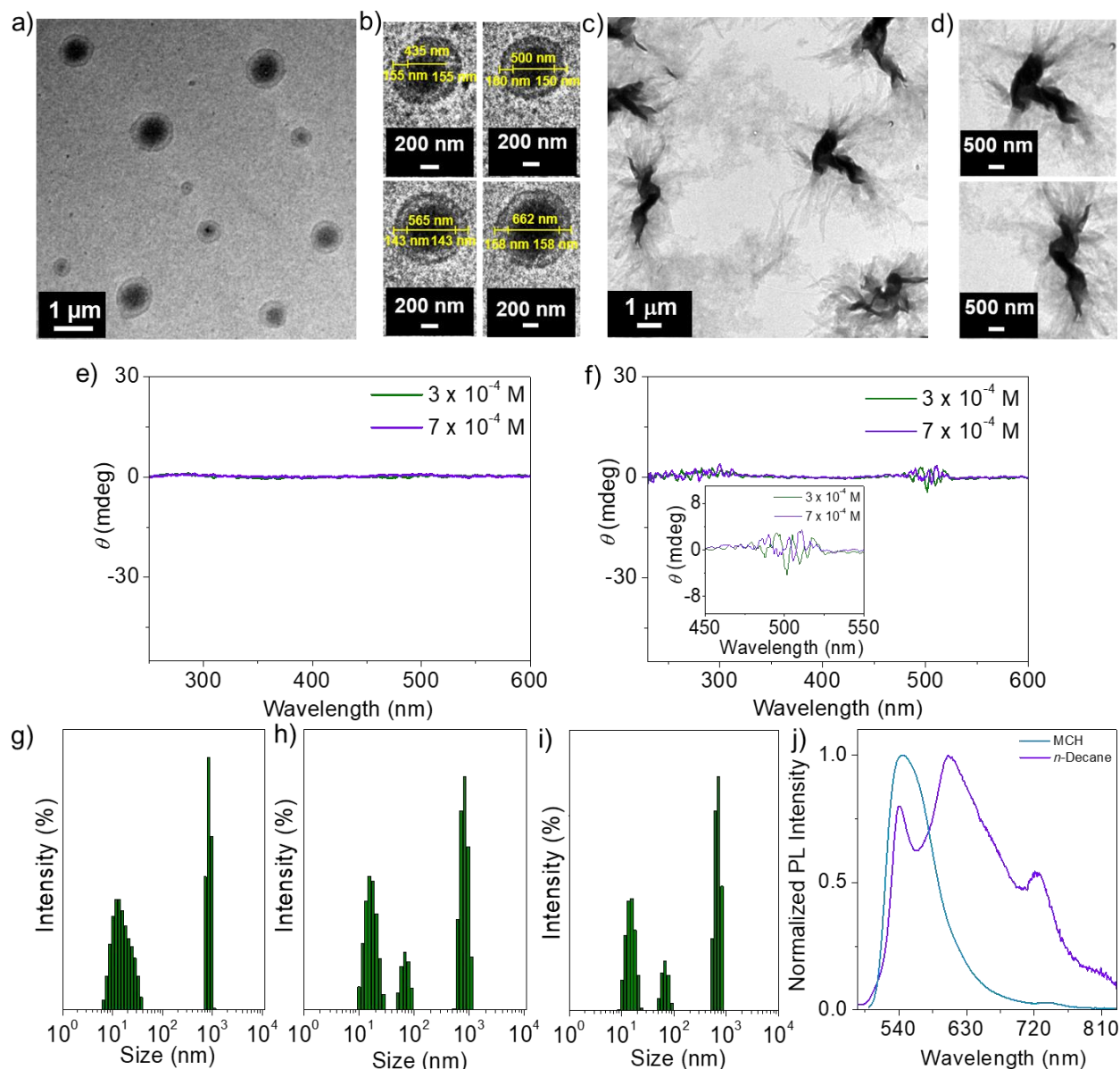


**Figure 3.17.** Self-assembly of the chiral BODIPY **2**. TEM images in (a) MCH ( $3 \times 10^{-4}$  M) and (c) *n*-decane ( $3 \times 10^{-4}$  M). (b,d) Magnified TEM images of a few spherical aggregates (size of the core within the range of 400-700 nm and that of the shell is within 100-200 nm) and crumbled 2D sheets, respectively. CD spectra in (e) MCH and (f) *n*-decane at two different concentrations ( $T = 298$  K). Inset in **Figure 3.17f** shows the zoomed portion of the CD spectral intensity between 450-550 nm corresponding to the BODIPY chromophore region. DLS size distribution in MCH ( $3 \times 10^{-4}$  M): (g) immediately after fast cooling, (h) after aging the sample for 24 h and (i) after cooling at a controlled rate (1 K/min). (j) Normalized emission spectra ( $\lambda_{\text{ex}} = 475$  nm) in MCH ( $3 \times 10^{-4}$  M) and *n*-decane ( $3 \times 10^{-4}$  M).

**3.17e,f**). These observations imply that the molecular structure of **2** does not facilitate helical arrangement of the chromophore. As a result, the exciton coupling between chromophores is extremely weak to reflect in the form of a measurable CD signal. The observed self-assembly and chiroptical properties of chiral BODIPY **2** are in contrast to the helical assembly exhibited by chromophores attached with chiral handles.<sup>[4a,31]</sup> The DLS analysis revealed a mixture of spherical particles of varying hydrodynamic volume in MCH, showing similar trends in the self-assembly behavior to that of **1** (**Figure 3.17g-i**). Furthermore, the emission spectra of the spherical structures exhibited a maximum at 540 nm, whereas that in *n*-decane showed multiple emission maxima at 540, 606, 725 and 790 nm (**Figure 3.17j**), similar to that of **1**.

### 3.3.5. The Origin of Multiple Emission: Energy Migration Studies

We hypothesized that, if the emission behavior is associated with morphological features, tweaking the spherical assembly to the 2D sheets may change the single emissive state to multi-emissive one. Addition of different volume fractions ( $f = v/v$ ) of *n*-decane to **1** in MCH ( $3 \times 10^{-4}$  M), induced a slow change of the spherical structures to elongated sheets and then to large 2D sheets (**Figure 3.18**). Upon increasing  $f$ , the intensity of the absorption of the BODIPY moiety ( $\lambda_{\text{max}} = 504$  nm) gradually decreased with the appearance of a shoulder band at higher wavelength. Interestingly, we could see multiple emission peaks at 600 and 725 nm in addition to the peak at 540 nm (**Figure 3.19a**). Similarly, upon addition of MCH to **1** in *n*-decane, the multiple emission changed to a single emission



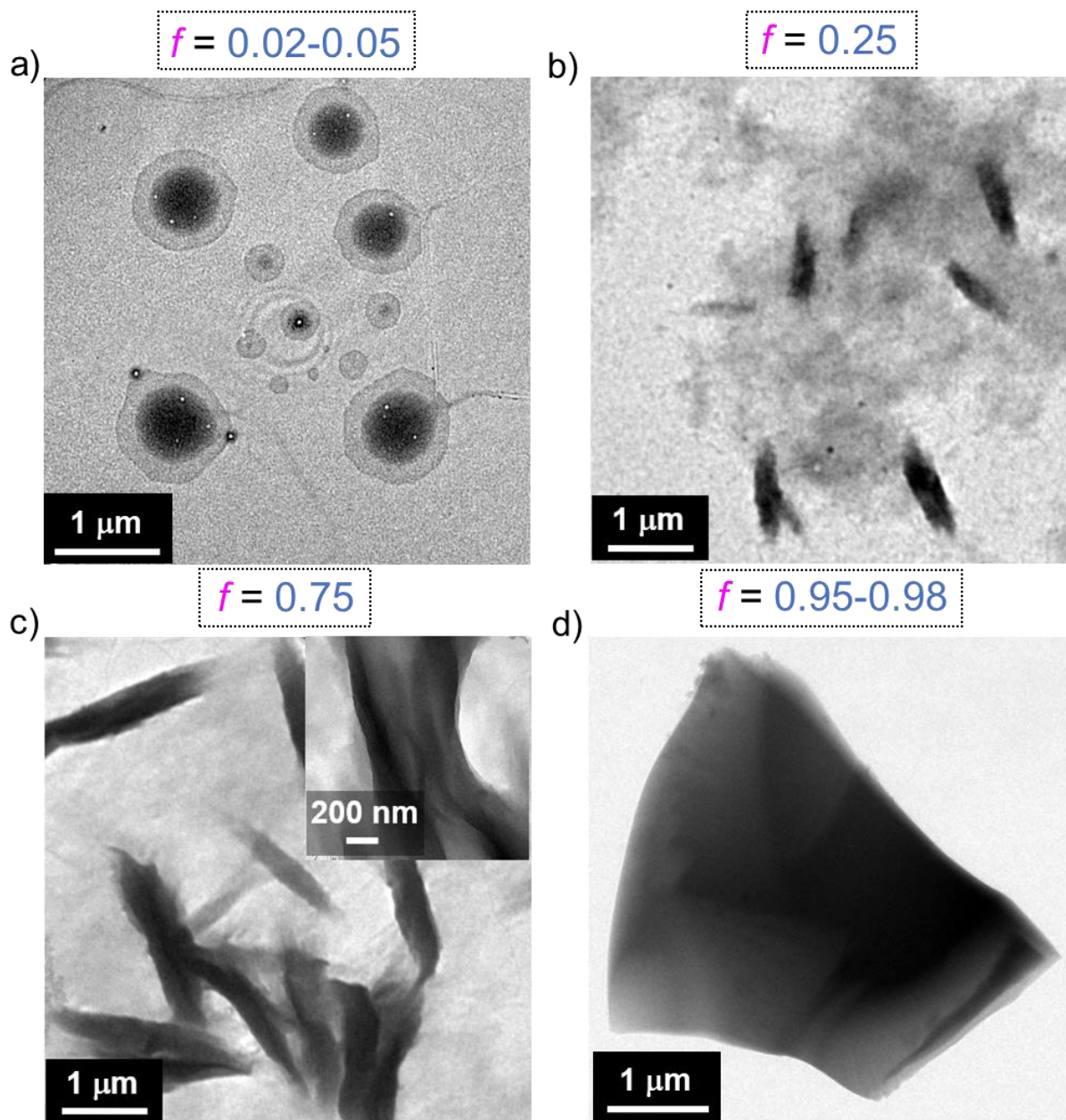


**Figure 3.18.** TEM images of aggregates of **1** upon increasing the volume fractions of *n*-decane in MCH ( $f$ ): (a)  $f = 0.02-0.05$ , (b)  $f = 0.25$ , (c)  $f = 0.75$  and (d)  $f = 0.95-0.98$ . **Figure 3.18c** inset shows the zoomed image.

(**Figure 3.19b**). The reversibility in the emission feature along with the change in morphology underpin the role of the solvent induced self-assembly<sup>[32]</sup> in perturbing the

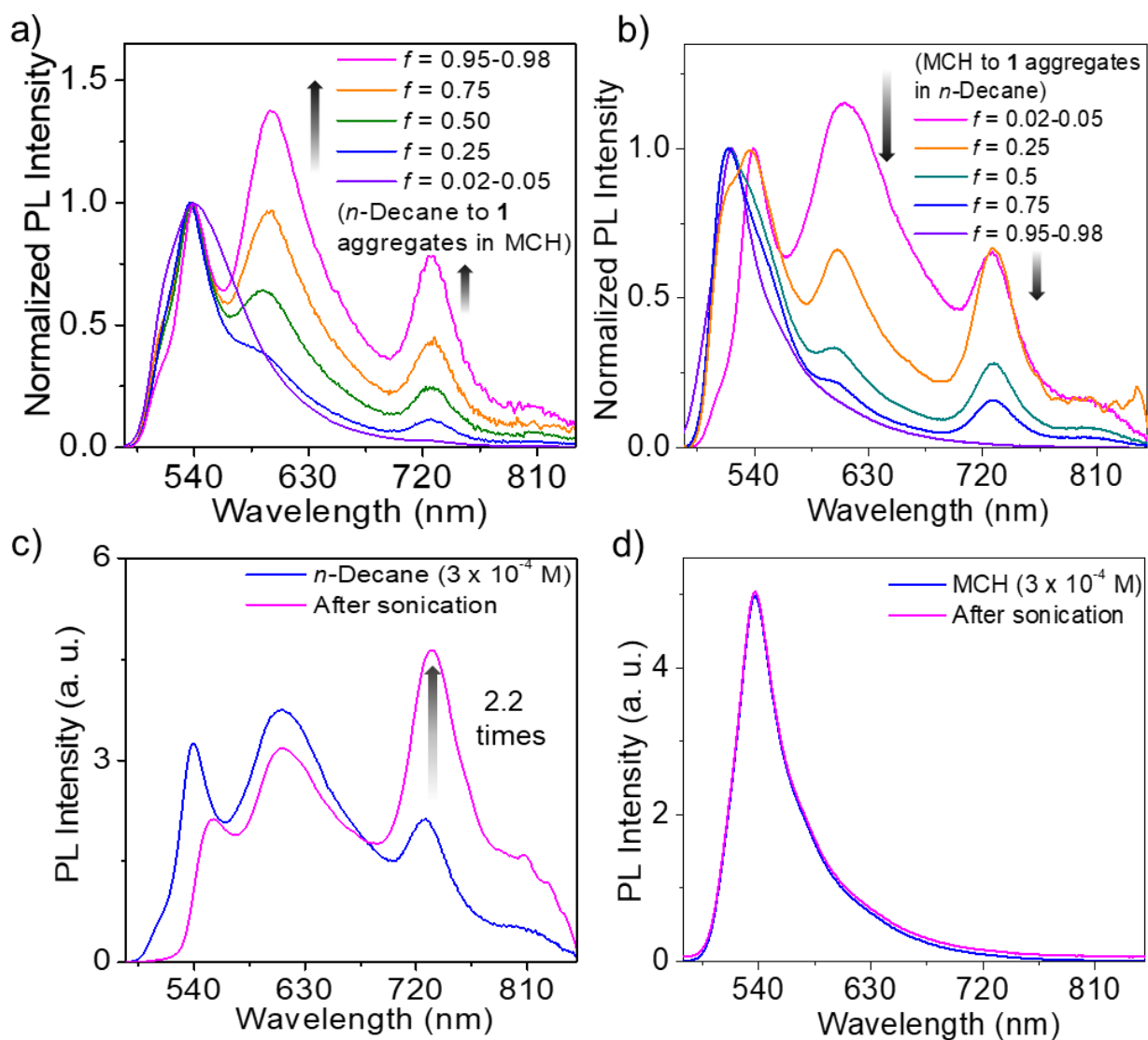


**Figure 3.19.** Changes in emission ( $\lambda_{\text{ex}} = 475$  nm) upon varying the solvent compositions: (a) addition of various fractions of *n*-decane to aggregates of **1** in MCH and (b) addition of various fractions of MCH to aggregates of **1** in *n*-decane ( $3 \times 10^{-4}$  M). Emission spectra of **1** ( $\lambda_{\text{ex}} = 475$  nm) in (c) *n*-decane and (d) MCH ( $3 \times 10^{-4}$  M), before (blue) and after (magenta) sonication.

excited state properties.<sup>[33]</sup> Surprisingly, the intensities of the 540 and 600 nm bands were decreased while the intensity of the NIR emission band at 725 and 790 nm exhibited a 2.2 times enhancement upon sonication<sup>[12,28a,34]</sup> of **1** in *n*-decane (**Figure 3.19c**). Similarly, the enhancement in NIR emission was also noticed when *n*-decane aggregates

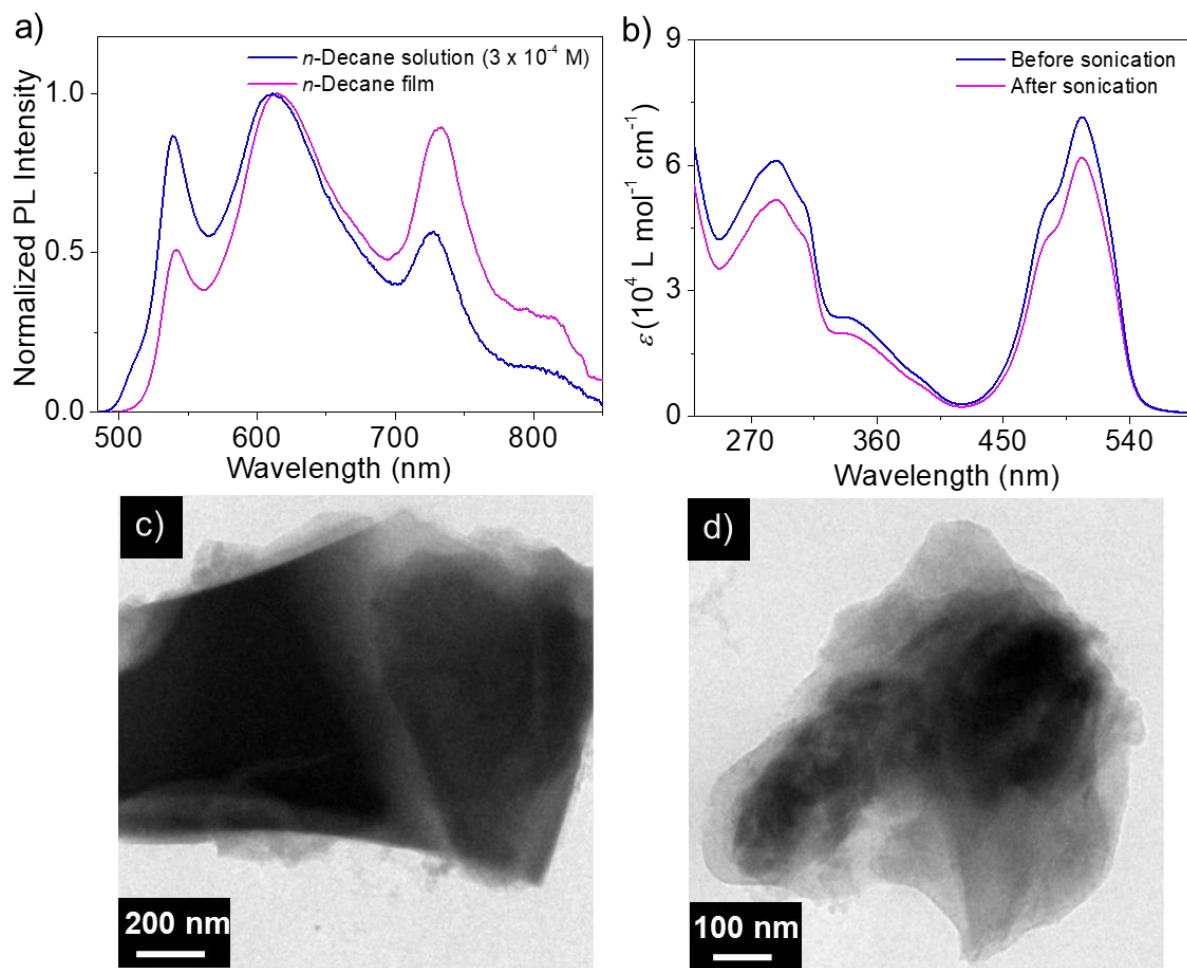


**Figure 3.20.** (a) Emission spectra ( $\lambda_{\text{ex}} = 475$  nm) of **1** aggregate in *n*-decane ( $3 \times 10^{-4}$  M) (blue) and after casting as a film (magenta). (b) Absorption spectra of **1** aggregate in *n*-decane ( $3 \times 10^{-4}$  M) before (blue) and after (magenta) sonication. (c,d) TEM images of the *n*-decane aggregates of **1** after sonication.

of **1** were cast as a film (**Figure 3.20a**). Upon sonication, the absorption intensity was slightly reduced (**Figure 3.20b**) and the formation of multilayered 2D structures was observed by TEM analysis (**Figure 3.20c,d**). In contrast, when sonication was applied to **1** aggregates in MCH, the emission profile remained almost unaltered (**Figure 3.19d**). The results of these studies indicate that sonication and film formation favor multilayered 2D assemblies of **1**, which enhance the NIR emission.

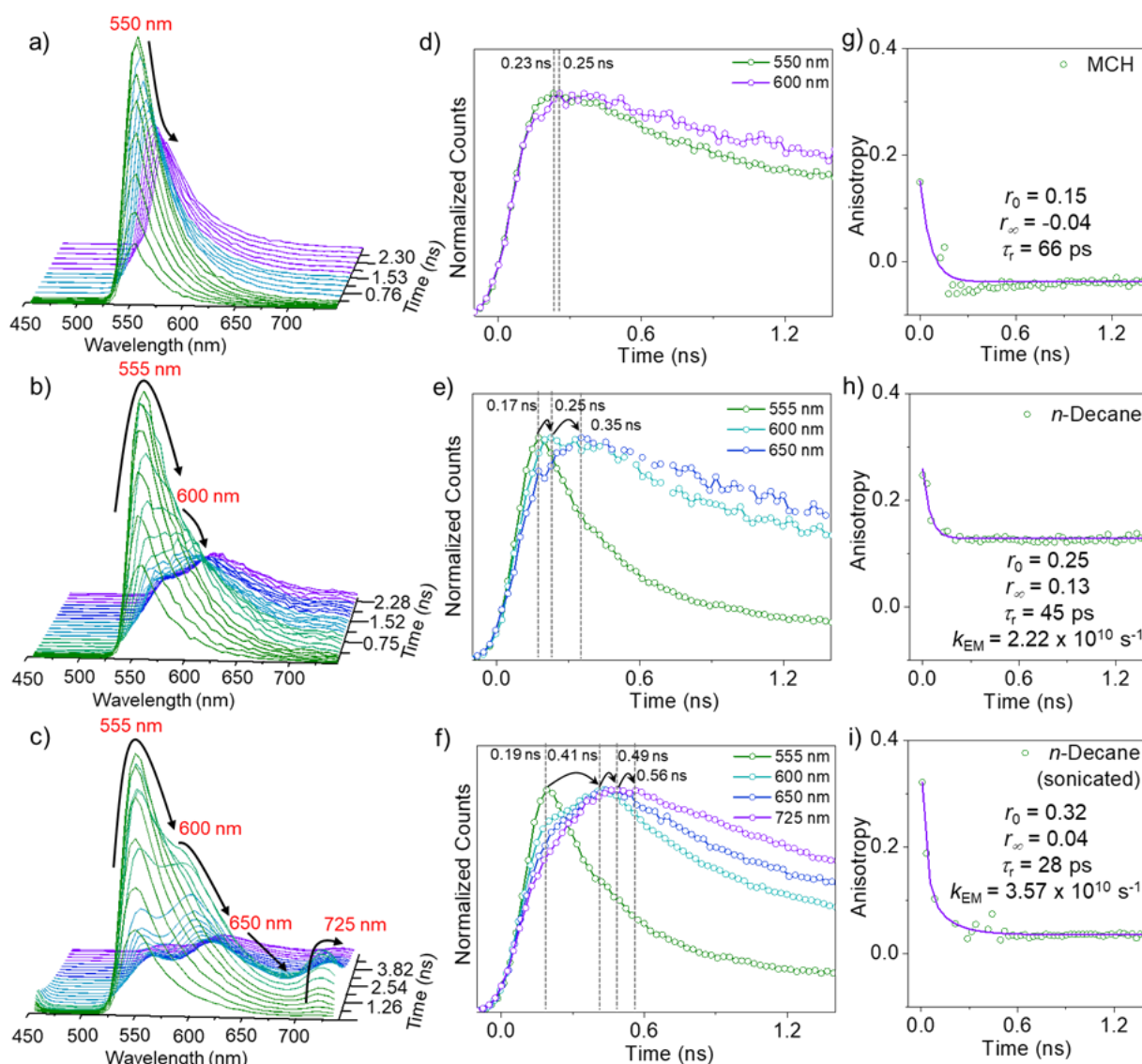


**Figure 3.21.** TRES of **1** in (a) MCH, (b) *n*-decane before sonication and (c) after sonication. The normalized fluorescence decay curves in (d) MCH, (e) *n*-decane before sonication and (f) after sonication; monitored at different emission wavelengths ( $3 \times 10^{-4}$  M,  $\lambda_{ex} = 375$  nm). Time-resolved fluorescence anisotropy decay in (g) MCH ( $\lambda_{em} = 550$  nm), (h) *n*-decane ( $\lambda_{em} = 555$  nm) before sonication and (i) after sonication ( $3 \times 10^{-4}$  M,  $\lambda_{ex} = 375$  nm).

A deeper understanding of the origin of multi-emission feature was possible with TRES studies of **1** in MCH and *n*-decane ( $3 \times 10^{-4}$  M) (**Figure 3.21a-f**). The emission spectra at different time scales in MCH ( $\lambda_{ex} = 375$  nm) showed an increase in the intensity

at 550 nm up to 280 ps followed by a gradual decrease in the intensity while retaining the nature of the emission profile up to 2.80 ns (**Figure 3.21a**). This observation indicates a normal excitation-deactivation process (**Figure 3.21d**). However, upon excitation in *n*-decane at 375 nm, a growth profile at 555 nm was observed within 32–210 ps (**Figure 3.21b**). With further increase in timescale up to 520 ps, the intensity of the 555 nm emission gradually decayed with a red shift of the emission peak to 600 nm within the time scale of 950 ps. Thereafter, the emission peak at 600 nm showed a time-dependent decay up to a timescale of 2.40 ns. The time-dependent decay of the emission at lower wavelength and the growth at the higher wavelength with dynamic red-shift of the emission are characteristic of energy migration from the excited states of lower order aggregates (higher excited state energy) to the higher order aggregates (lower excited state energy) leading to the multiple emission.<sup>[17,20]</sup> **Figure 3.21e** reveals that within 0.17 ns, the peak intensity at 555 nm reaches maximum and then undergoes a rapid tri-exponential decay with time constants of 1.49 ns (44.76%), 5.82 ns (35.63%) and 0.25 ns (19.61%). The emission at 600 nm reaches the maximum at 0.25 ns with a negative pre-exponential. The fitted rise time value of 0.34 ns at 600 nm is found to correlate with the 0.25 ns decay component observed at 555 nm emission, thus validating the energy migration process. In a similar manner, the 650 nm emission peak also reached the maximum at 0.35 ns followed by a successive decay.

Since the multi-emissive nature is found to be strongly influenced by ultrasound, TRES analysis of the sonicated samples in *n*-decane was performed (**Figure 3.21c**). The initial increase in the emission profile at 555 nm within 30–160 ps exhibited a subsequent

decrease in the intensity within a time scale of 390 ps, with the formation of a new red-shifted peak at 600 nm. The peak at 600 nm exhibited an increase in the emission intensity within 260–590 ps followed by a successive time-dependent decay. Within 650 ps, another peak at 725 nm (NIR region) was formed, which reached its maximum and then gradually decayed, showing a perfect correlation between 600 and 725 nm peaks, indicating energy transfer from the 600 nm emitting species. Plots of the normalized emission counts at different emission peaks and the time scale of the successive energy transfer is clear from **Figure 3.21f**. The peak intensity at 555 nm reached maximum within 0.19 ns followed by decay, whereas the 600 nm emission reached its maximum at 0.41 ns. The rise time value (0.97 ns) obtained at 600 nm can be correlated with the decay component (0.81 ns) observed at 555 nm. In a similar fashion, 650 and 725 nm peak reached its maximum within 0.49 and 0.56 ns, respectively and then decayed. A negative pre-exponential factor observed at 650 and 725 nm emission decays confirms the step-wise energy transfer from 555 to 600 nm, 600 to 650 nm, 650 to 725 nm and then a weak energy transfer from the 725 to 790 nm, suggesting multiple long-range energy migration. <sup>[6a,17,18,20b,24d]</sup>

Further insights on the energy migration could be obtained from time-resolved anisotropy studies (**Figure 3.21g-i**). In general, the loss of anisotropy of organized donors within an assembly occurs either through rotational motion or by energy migration.<sup>[20,35]</sup> In *n*-decane, depolarization through rotational motion is less favored as spontaneous nucleation assists the formation of 2D assemblies and hence energy migration can be the possible pathway for depolarization.<sup>[20,35]</sup> At  $3 \times 10^{-4}$  M, **1** in *n*-decane exhibited an initial

anisotropy value ( $r_0$ ) of 0.25 and reached the plateau region ( $r_\infty$ ) at 0.13 by losing the anisotropy with a decay time,  $\tau_r = 45$  ps (**Figure 3.21h**). The  $r_0$  value of 0.25 at around zero time indicates that the initial orientation of the transition dipole moments has an angle of  $30^\circ$ .<sup>[36]</sup> On the other hand, at similar concentration in MCH,  $r_0$  was found to be 0.15, which reached the final anisotropy ( $r_\infty$ ) value of -0.04 (**Figure 3.21g**). The difference in the initial anisotropy value indicates the random independent orientation of the chromophores in MCH, where a large angle ( $40^\circ$ ) exists between the excitation and emission dipole moments. Interestingly, studies carried out in *n*-decane after sonication showed a higher  $r_0$  value of 0.32, where the angle ( $21^\circ$ ) between the excitation and emission transition dipole moments was found to be much smaller in comparison to the other cases (**Figure 3.21i**). In addition,  $r_\infty$  value of 0.04 was reached within a very short decay time ( $\tau_r$ ) of 28 ps. The anisotropy decay time  $\tau_r$ , which gives an estimation of the rate of energy migration ( $k_{EM}$ ) from the higher to the lower energy state,<sup>[17,20b]</sup> was found to be  $3.57 \times 10^{10}$  and  $2.22 \times 10^{10}$  s<sup>-1</sup> for sonicated and non-sonicated samples, respectively. The fast fluorescence depolarization and rate of energy migration obtained in sonicated *n*-decane sample signifies a fast interchromophore energy migration of a singlet exciton,<sup>[17,20,35]</sup> facilitating successive and partial energy transfer process within the aggregates having different HOMO-LUMO energy levels.

### 3.3.6. Effect of Noncovalent Interactions

The solvent dependent origin of the distinct morphological features and the associated excited state property could be rationalized on the basis of the difference in molecular



packing (**Figure 3.22**) as evident from various experimental results. The anti-parallel arrangement of the dipoles can lead to the initial formation of a centrosymmetric dimer structure,<sup>[37]</sup> which can further involve in the nucleation process dictated by the nature of the solvent molecules (**Figure 3.22**).<sup>[32]</sup> In the case of MCH, the nucleation process was sluggish ( $T_e = 321$  K) in comparison to that in *n*-decane ( $T_e = 358$  K) due to the difference

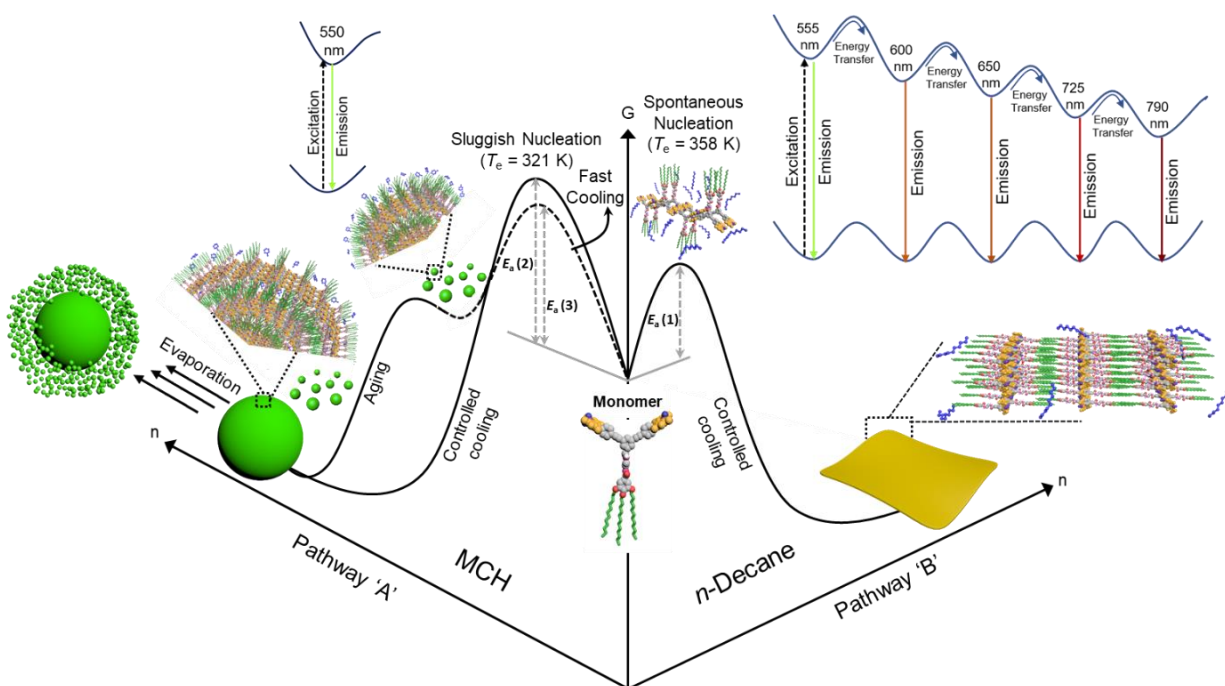


**Figure 3.22.** Schematic diagram for the self-assembly pathways and the morphology dependent exciton deactivation in BODIPY assemblies. Self-assembly in MCH (left panel, pathway A) and *n*-decane (right panel, pathway B), forming spherical supramolecular structures and 2D sheets, leading to normal (single emission) and cascade energy transfer (multiple emission), respectively.

in the activation energy barriers (**Figure 3.22**). The fast nucleation-elongation process in *n*-decane resulted in 2D sheets stabilized by intermolecular H-bonding and interdigitated alkyl chains. FT-IR studies have shown that the 2D sheets formed in *n*-decane are stabilized by various noncovalent interactions (**Figure 3.23**). Film state FT-IR spectrum of **1** obtained



from *n*-decane exhibited bands at 3288, 1640 and 1545 cm<sup>-1</sup>, suggesting intermolecular H-bonding.<sup>[12b,25a]</sup> On the other hand, the BODIPY **1** in CDCl<sub>3</sub> displayed two bands at 3450 and 3348 cm<sup>-1</sup>, assigned as amide A bands. The amide I and II bands appeared at 1654 and 1543 cm<sup>-1</sup>, respectively. Intramolecular H-bonding was overruled based on the negligible hysteresis observed between cooling and heating curves for the *n*-decane aggregates and also from the identical cooling curves obtained when the cooling rate was varied from 1 to 5 K/min (**Figure 3.24**). In addition, the symmetric and asymmetric -CH<sub>2</sub> vibrations of **1** in the xerogel state were noticed at 2852 and 2922 cm<sup>-1</sup>, respectively and shifted towards the lower frequency region with respect to **1** in CDCl<sub>3</sub> (**Figure 3.25a**), indicating that the dodecyl chains of **1** remain in all *trans* configuration and interdigitated in the 2D assembly forming aggregates.<sup>[12b]</sup> These 2D sheets possess anisotropically organized aggregates of BODIPY chromophores having different energy bandgaps leading to multi-emissive feature. In addition, the sluggish nucleation-elongation of **1** in MCH resulted in small particles (upon fast cooling) and their subsequent coalescence to large spheres with time, forming isotopically organized assembly of the BODIPY chromophores leading to a single emission peak. In this case, amide A, I and II bands were observed at 3289, 1637 and 1506 cm<sup>-1</sup>, respectively, suggesting the formation of intermolecular H-bonding between the molecules (**Figure 3.23** and **3.24**).

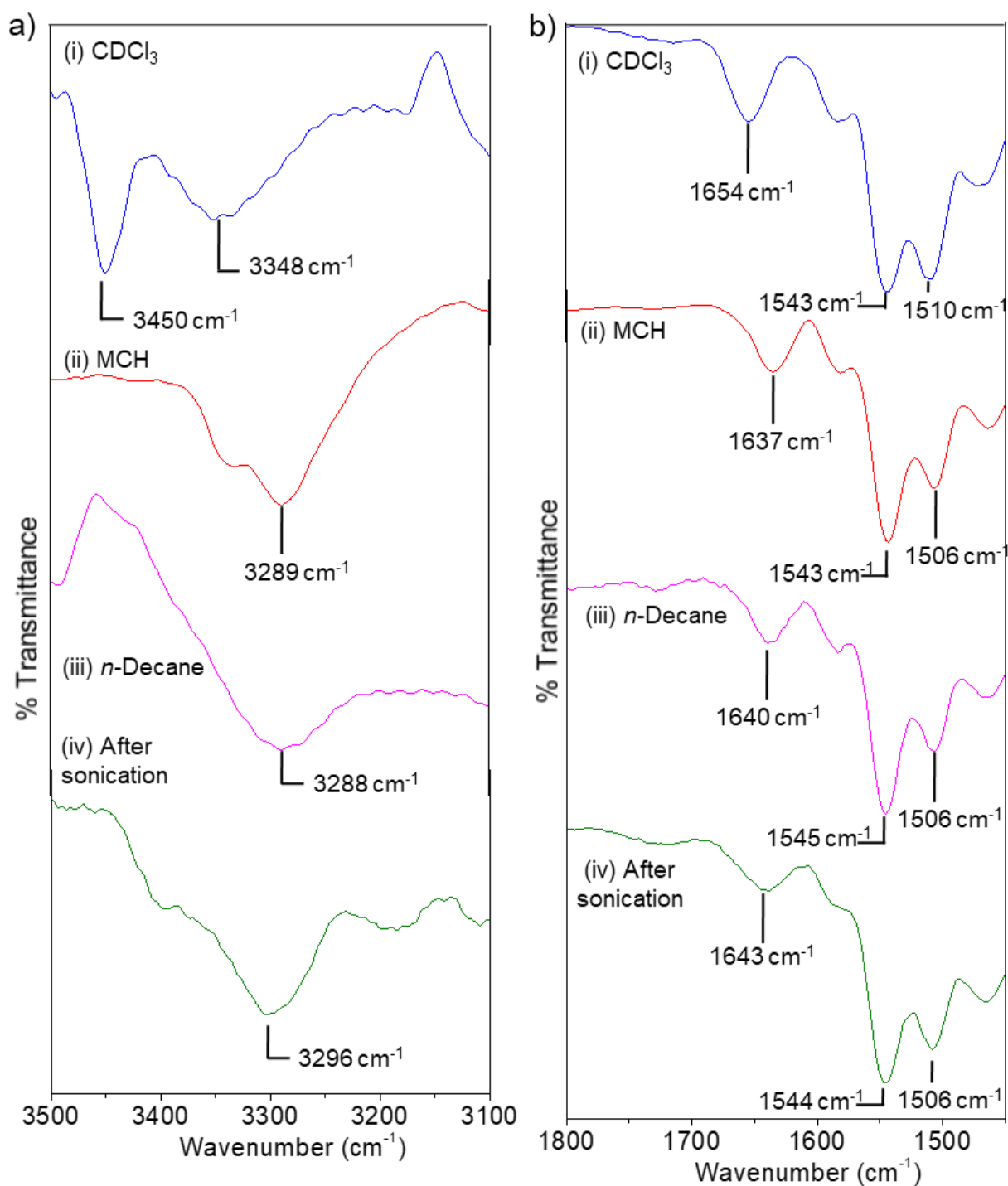


**Figure 3.23.** FT-IR spectra corresponding to (a) amide A band and (b) amide I and II bands of **1** at different conditions. (i) **1** in monomeric state in  $\text{CDCl}_3$  ( $1 \times 10^{-3}$  M) (blue), (ii) **1** aggregate in MCH (red), (iii) **1** aggregate in *n*-decane (magenta) and (iv) **1** aggregate in decane after sonication (green). The FT-IR spectra in solution state were recorded in a KBr liquid cell and aggregates were recorded as a cast film on a KBr plate.

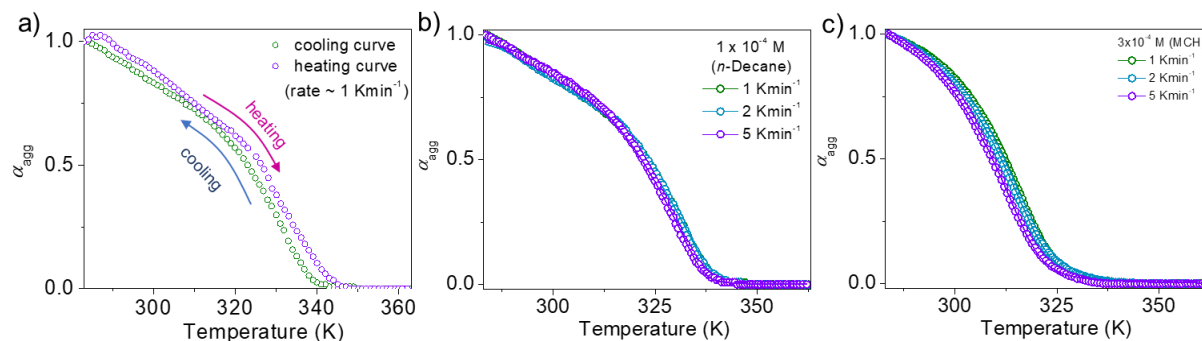


**Figure 3.24.** (a) Effect of cooling and heating (rate  $\sim 1$  K/min) on the aggregation (green) and dissociation (violet) processes of **1** in *n*-decane. Effect of different cooling rates over  $\alpha_{agg}$  of **1**,  $\alpha_{agg}$  was calculated by monitoring the absorbance changes at 530 nm and 533 nm for (b) *n*-decane and (c) MCH, respectively.

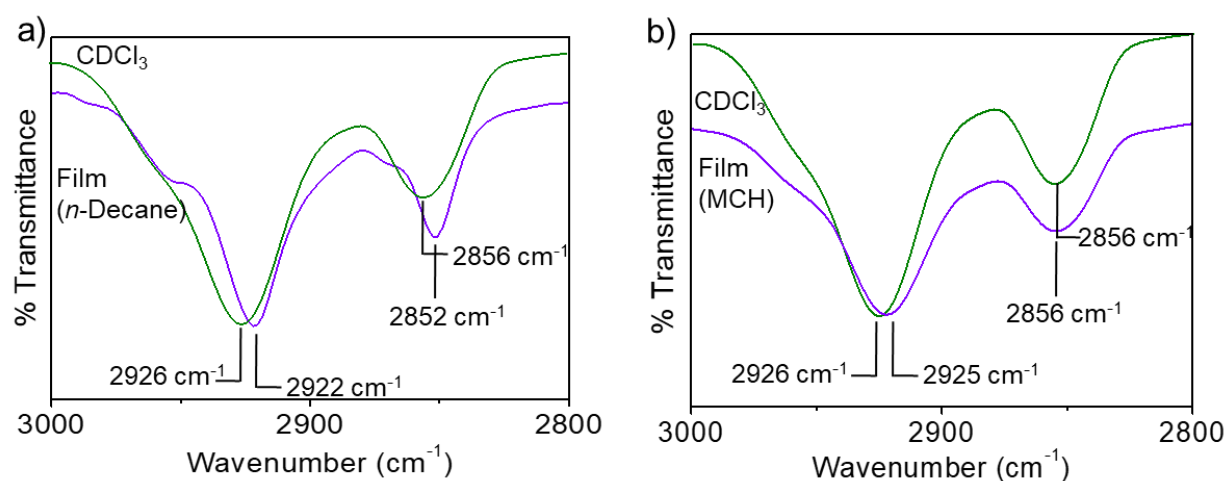


**Figure 3.25.** Comparison of the FT-IR spectra of **1** in CDCl<sub>3</sub> ( $1 \times 10^{-3}$  M) and the film cast from (a) *n*-decane and (b) MCH; showing asymmetric and symmetric methylene stretching vibrations.

However, FT-IR bands corresponds to symmetric and asymmetric -CH<sub>2</sub> vibrations were almost indistinguishable in the case of **1** in MCH to that of CDCl<sub>3</sub>, indicating randomly arranged dodecyl chains and thus unable to form gels (**Figure 3.25b**). Molecular arrangement of **1** was further confirmed from WAXS (**Figure 3.26**). WAXS pattern of *n*-decane xerogel of **1** exhibited several well-resolved peaks, characteristic of long-range crystalline ordering of **1** (**Figure 3.26a**). The peaks obtained at  $2\theta = 1.57, 3.15,$  and  $4.7^\circ$

corresponding to the  $d$ -spacing values of 56.2 (001), 28.0 (002) and 18.8 Å (003), respectively; imply a lamellar structure<sup>[12b,25a,38]</sup> with an interlayer distance of 56.2 Å, matching with the centrosymmetric dimer structure (**Figure 3.26c** and d).<sup>[25a,38]</sup> The reflections obtained between  $2\theta$  of 21.6 to 24.0° ( $d$ -spacing values of 4.1, 3.9 and 3.7 Å) can be ascribed to the intermolecular interactions assisted stacking of aromatic units and the crystalline packing of the interdigitated alkyl chains.<sup>[12b,25a]</sup>

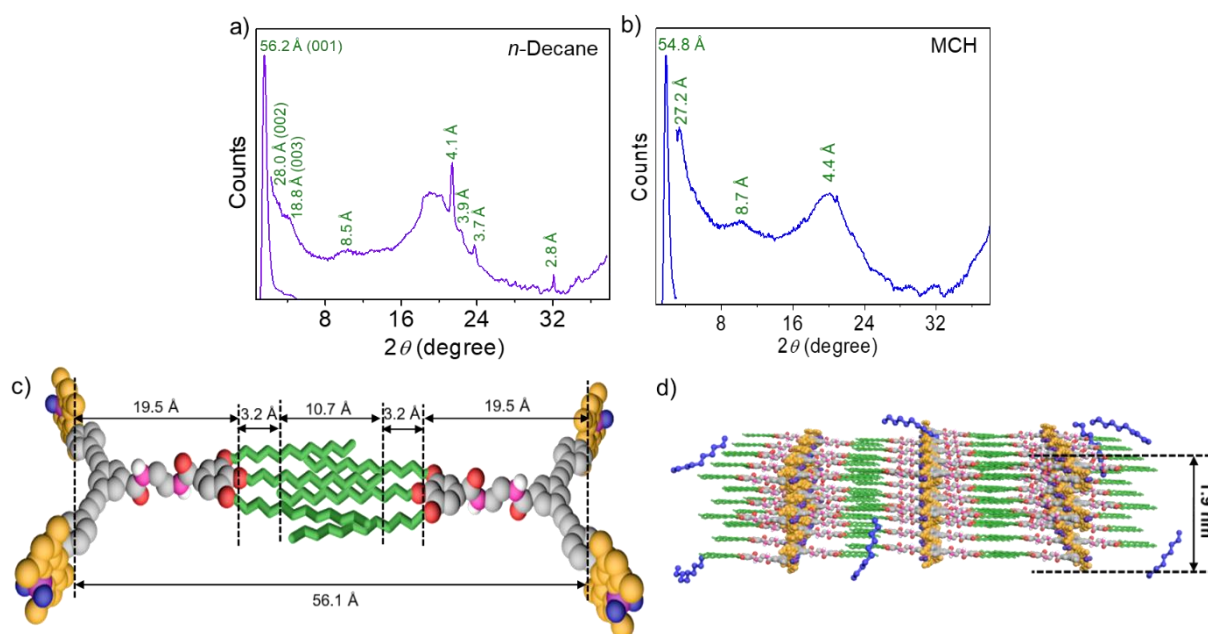


**Figure 3.26.** WAXS pattern of **1** aggregates in (a) *n*-decane and (b) MCH. In both cases, the concentration was fixed at  $8 \times 10^{-3}$  M (CGC of **1** in *n*-decane). (c) Schematic representation demonstrating the periodic distance and (d) probable lamellar assembly of **1** in *n*-decane; the distance 1.9 nm corresponding to the average height of the 2D sheets observed in the AFM image (**Figure 3.14**).

On the other hand, a lamellar type arrangement with an interlayer distance of 54.8 Å was noticed in the case of aggregates of **1** in MCH (**Figure 3.26b**). However, long-range crystalline ordering of the molecules was not observed in the case of assembly of **1** in MCH

as confirmed from the WAXS pattern between  $2\theta$  value of 16-28°, implying the probable presence of randomly arranged alkyl chains. It is interesting to note that the self-assembly of BODIPY derivative **3** having short butyl chains in *n*-decane ( $3 \times 10^{-4}$  M) resulted in a single emission maximum at 527 nm upon excitation at 475 nm (**Figure 3.27a**). Furthermore, failure of **3** to form a gel in *n*-decane ( $8 \times 10^{-3}$  M) and the formation of spherical particle-like precipitates (**Figure 3.27b**) underpin the role of long hydrocarbon side chains of **1** and **2** in *n*-decane in the observed 2D morphology.

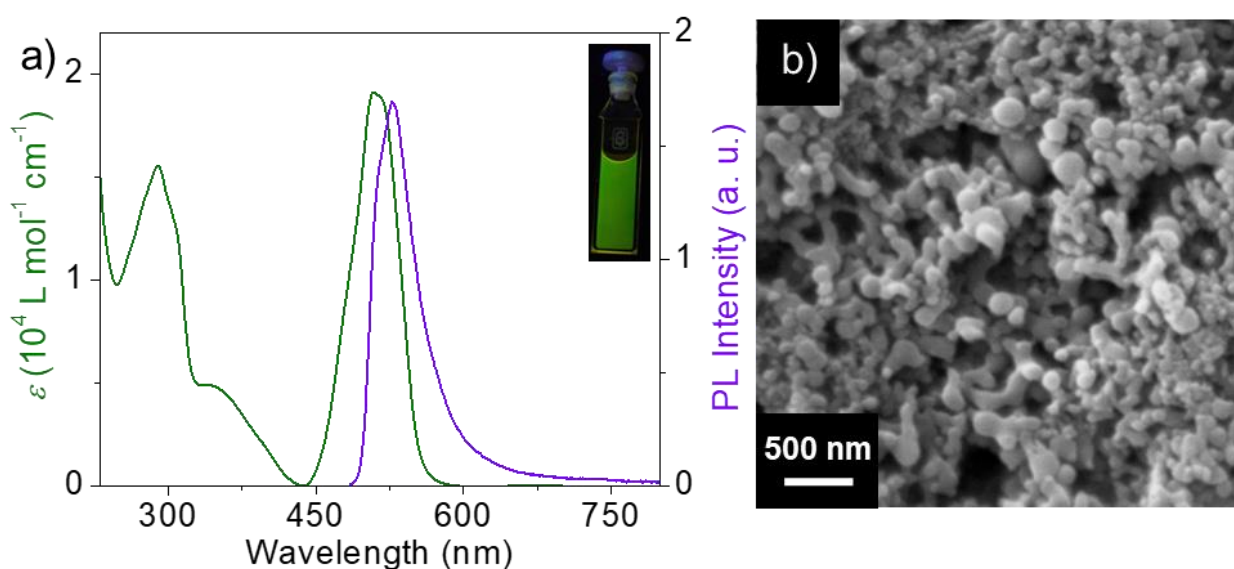


**Figure 3.27.** Photophysical and morphological properties of **3**. (a) Absorption (green) and emission (violet,  $\lambda_{\text{ex}} = 475$  nm) spectra in *n*-decane ( $3 \times 10^{-4}$  M). Inset shows the photograph of **3** in *n*-decane under illumination of 365 nm UV light. (b) SEM image of the precipitates formed in *n*-decane ( $8 \times 10^{-3}$  M).

### 3.4. Conclusions

The spherical morphology formed through multistep assembly of the BODIPY **1** in MCH behaves like a normal chromophore assembly in terms of the excited state behavior, however, the 2D sheets formed in *n*-decane exhibits an unusual multi-emission associated

with successive energy transfer within the energetically anisotropic chromophore assembly landscape. The presence of the long hydrocarbon chains in **1** and **2** is essential to form 2D sheets as illustrated with the inability of **3** to form such assembly in linear non-polar solvents. The transformation between the spherical assembly in MCH and 2D sheets in *n*-decane along with the changes from single to multiple emission underpin an assembly dependent excited state behavior. Our results show that it is possible to reversibly control the excited state properties with two different stimuli such as solvent composition and ultrasound. Moreover, the effect of ultrasound stimulation of the 2D sheets on successive energy transfer with one of the largest observed pseudo Stokes-shift of 7105 cm<sup>-1</sup> may be useful for designing self-assembly based light harvesting and photonic devices. Though there are many reports on cascade energy transfer, the present system is the only example available on intentionally modulated cascade exciton transfer in a chromophore based supramolecular system, which can be reversibly controlled with solvents as a consequence of morphological change.

### **3.5. Experimental Section: Synthesis**

#### **3.5.1. General Procedure**

The details of solvent purification, compound purification techniques, etc. have been provided in the Section 2.5.1 of Chapter 2. 3,4,5-Trihydroxymethyl benzoate, 1-bromododecane, (*S*)-1-bromo-3,7-dimethyloctane, Pd(PPh<sub>3</sub>)<sub>2</sub>Cl<sub>2</sub> and CuI were purchased from Sigma-Aldrich. Ethylenediamine, (benzotriazol-1-yloxy)tris (dimethylamino)

phosphonium hexafluorophosphate (BOP reagent), 2,4-dimethylpyrrole and ethynyltrimethylsilane were purchased from TCI Chemicals (India). Boron trifluoride diethyl etherate and 1-bromobutane were purchased from Spectrochem Pvt. Ltd (India). Size exclusion chromatography was carried out using styrene divinylbenzene beads with 1% cross-linkage and 40-80  $\mu\text{m}$  beads size (Bio-Rad Bio-Beads S-X1 Support).

### **3.5.2. Characterization Techniques**

The details of various characterization techniques have been provided in Section 2.5.2 of Chapter 2. MALDI-TOF mass spectrometry was performed in the reflector mode using a Bruker model autoflex TM speed spectrometer using  $\alpha$ -cyano-4-hydroxycinnamic acid as the matrix.

**3.5.3. Synthesis of methyl-3,4,5-trialkoxybenzoate (5):** Compound 4 (6.5 mmol, 1 equiv.) and  $\text{K}_2\text{CO}_3$  (39 mmol, 6 equiv. for compound 5a and 5c; 6.5 mmol, 1 equiv. for compound 5b' and 13.51 mmol, 2.07 equiv. for 5b) were dissolved in dry DMF (50 mL) in a 250 mL round bottom flask under inert atmosphere upon stirring at 50  $^\circ\text{C}$  for 30 min. The reaction medium was cooled to room temperature and the required alkyl bromide (22.7 mmol, 3.5 equiv. for a and c; 6.5 mmol, 1 equiv. for b' and 13.51 mmol, 2.07 equiv. for b) was added drop wise. The reaction mixture became turbid within 1 h and was stirred at 80  $^\circ\text{C}$  for 24 h under inert condition. The progress of the reaction was monitored using TLC. On completion of the reaction, the mixture of solvents was evaporated under reduced pressure and the residue was extracted using ethyl acetate. The organic layer was washed with brine thrice, dried over anhydrous  $\text{Na}_2\text{SO}_4$ , filtered, and the filtrate was concentrated under reduced pressure. The obtained crude product was then purified by column

chromatography over silica gel to obtain **5a** (5% ethyl acetate/*n*-hexane) and **5c** (2% ethyl acetate/*n*-hexane) as colorless solids. **5b'** and **5b** (eluted in chloroform) was obtained as a light brown oil.

**5a:** Detailed characterization data have been provided in Section 2.5.3. of Chapter 2.

**5b':** Yield: 60%; <sup>1</sup>H NMR (500 MHz, CDCl<sub>3</sub>, TMS):  $\delta$  = 7.23 (s, 2H, Ar-*H*), 5.84 (s, 2H, Ar-OH), 4.20–4.14 (m, 2H, -OCH<sub>2</sub>), 3.88 (s, 3H, -OCH<sub>3</sub>), 1.66–1.48 (m, 4H, -CH<sub>2</sub>), 1.35–1.26 (m, 4H, -CH<sub>2</sub>), 1.17–1.12 (m, 2H, -CH<sub>2</sub>), 0.95–0.92 (m, 3H, -CH<sub>3</sub>), 0.88–0.86 (m, 6H, -CH(CH<sub>3</sub>)<sub>2</sub>) ppm; <sup>13</sup>C NMR (125 MHz, CDCl<sub>3</sub>):  $\delta$  = 166.8, 148.8 (2C), 143.4, 125.8, 109.7 (2C), 72.4, 52.2, 39.2, 37.3, 37.2, 29.8, 27.9, 24.6, 22.7, 22.6, 19.6 ppm; HRMS-ESI calculated for C<sub>18</sub>H<sub>28</sub>O<sub>5</sub> [M+H]<sup>+</sup>: 325.1937, found: 325.2020.

**5b:** Yield: 82%; <sup>1</sup>H NMR (500 MHz, CDCl<sub>3</sub>, TMS):  $\delta$  = 7.25 (s, 2H, Ar-*H*), 4.08–4.00 (m, 6H, -OCH<sub>2</sub>), 3.89 (s, 3H, -OCH<sub>3</sub>), 1.83–1.80 (m, 4H, -CH<sub>2</sub>), 1.67–1.63 (m, 2H, -CH(CH<sub>3</sub>)<sub>2</sub>), 1.52–1.44 (m, 6H, -CH<sub>2</sub>), 1.31–1.24 (m, 38H, -CH<sub>2</sub>), 0.92 (d, *J* = 6.5 Hz, 3H, -CH<sub>3</sub>), 0.89–0.85 (m, 12H, -CH(CH<sub>3</sub>)<sub>2</sub> + -CH<sub>3</sub>) ppm; <sup>13</sup>C NMR (125 MHz, CDCl<sub>3</sub>):  $\delta$  = 166.9, 152.9 (2C), 142.4, 124.7, 108.0 (2C), 71.7, 69.2 (2C), 52.1, 39.4, 37.5, 37.3, 31.9 (3C), 29.7 (12C), 29.5, 29.4 (2C), 28.0, 26.1 (2C), 24.7, 22.7 (2C), 22.6, 19.5, 14.1 (2C) ppm; HRMS-ESI calculated for C<sub>42</sub>H<sub>76</sub>O<sub>5</sub> [M+H]<sup>+</sup>: 661.5693, found: 661.5813.

**5c:** Yield: 83%; <sup>1</sup>H NMR (500 MHz, CDCl<sub>3</sub>, TMS):  $\delta$  = 7.19 (s, 2H, Ar-*H*), 3.95 (t, *J* = 6.0 Hz, 6H, -OCH<sub>2</sub>), 3.82 (s, 3H, -OCH<sub>3</sub>), 1.76–1.67 (m, 6H, -CH<sub>2</sub>), 1.48–1.41 (m, 6H, -CH<sub>2</sub>), 0.92–0.87 (m, 9H, -CH<sub>3</sub>) ppm; <sup>13</sup>C NMR (125 MHz, CDCl<sub>3</sub>):  $\delta$  = 166.9, 152.9 (2C), 142.5,



124.7, 108.1 (2C), 73.1, 68.9 (2C), 52.1, 32.3, 31.4 (2C), 19.3 (2C), 19.1, 13.8 (3C) ppm; HRMS-ESI calculated for C<sub>20</sub>H<sub>32</sub>O<sub>5</sub> [M+H]<sup>+</sup>: 353.2250, found: 353.2333.

**3.5.4. Synthesis of 3,4,5-trialkoxybenzoic acid (6):** In a general procedure, compound **5** (4.35 mmol, 1 equiv.) and solid KOH (13.1 mmol, 3 equiv.) were dissolved in distilled ethanol (60 mL) and was refluxed at 80 °C in a 250 mL round bottom flask for 12 h. After checking the completion of the reaction using TLC, the reaction mixture was then cooled to room temperature and the solvent was removed under reduced pressure. Then, the reaction mixture was acidified (pH = 2) with cold dilute HCl with continuous stirring and was extracted using chloroform. The organic layer was washed with brine thrice, dried over anhydrous Na<sub>2</sub>SO<sub>4</sub>, filtered, and the filtrate was concentrated under reduced pressure. The products formed was used for the next step without further purification.

**6a:** Detailed characterization data have been provided in Section 2.5.3. of Chapter 2.

**6b:** Yield: 90%; <sup>1</sup>H NMR (500 MHz, CDCl<sub>3</sub>, TMS): δ = 7.31 (s, 2H, Ar-H), 4.15–4.00 (m, 6H, -OCH<sub>2</sub>), 1.83–1.80 (m, 4H, -CH<sub>2</sub>), 1.76–1.69 (m, 2H, -CH(CH<sub>3</sub>)<sub>2</sub>), 1.59–1.44 (m, 6H, -CH<sub>2</sub>), 1.33–1.26 (m, 36H, -CH<sub>2</sub>), 1.16–1.03 (m, 2H, -CH<sub>2</sub>), 0.94–0.92 (m, 3H, -CH<sub>3</sub>), 0.9–0.84 (m, 12H, -CH(CH<sub>3</sub>)<sub>2</sub> + -CH<sub>3</sub>) ppm; <sup>13</sup>C NMR (125 MHz, CDCl<sub>3</sub>): δ = 170.8, 152.9 (2C), 143.0, 123.7, 108.5 (2C), 71.8, 69.2 (2C), 39.4, 37.4, 37.3, 31.9 (3C), 29.7 (12C), 29.4 (3C), 28.0, 26.1 (2C), 25.7, 24.7, 22.7 (2C), 19.6, 14.1 (2C) ppm; HRMS-ESI calculated for C<sub>41</sub>H<sub>74</sub>O<sub>5</sub> [M+Na]<sup>+</sup>: 669.5536, found: 669.5459.

**6c:** Yield: 89%; m.p.: 60-62 °C; <sup>1</sup>H NMR (500 MHz, CDCl<sub>3</sub>, TMS): δ = 7.25 (s, 2H, Ar-*H*), 3.99–3.95 (m, 6H, -OCH<sub>2</sub>), 1.77–1.64 (m, 6H, -CH<sub>2</sub>), 1.47–1.43 (m, 6H, -CH<sub>2</sub>), 0.93–0.88 (m, 9H, -CH<sub>3</sub>) ppm; <sup>13</sup>C NMR (125 MHz, CDCl<sub>3</sub>): δ = 171.8, 152.9 (2C), 143.2, 123.7, 108.6 (2C), 73.2, 68.9 (2C), 32.3, 31.3 (2C), 19.3 (2C), 19.1, 13.9, 13.8 (2C) ppm; HRMS-ESI calculated for C<sub>19</sub>H<sub>30</sub>O<sub>5</sub> [M+H]<sup>+</sup>: 339.2093, found: 339.2179.

**3.5.5. Synthesis of *N*-(2-aminoethyl)-3,4,5-trialkoxybenzamide (7):** In a general synthetic procedure, compound **6** (1.48 mmol, 1 equiv.) and BOP reagent (1.64 mmol, 1.11 equiv.) were dissolved in dry DCM (20 mL) in a 100 mL two-neck round bottom flask. Ethylenediamine (7.5 mmol, 5.1 equiv.) was added to the solution and the reaction mixture was stirred at room temperature for 3 h under inert atmosphere. The progress of the reaction was monitored using TLC. On completion of the reaction, solvent was evaporated under reduced pressure and the residue was extracted using chloroform. The organic layer was washed with brine thrice, dried over anhydrous Na<sub>2</sub>SO<sub>4</sub>, filtered and the filtrate was concentrated under reduced pressure. The obtained solid was dissolved in minimum amount of chloroform and was re-precipitated in methanol at 0 °C and the residue was collected upon filtration. The obtained crude product was then purified by column chromatography over silica gel to obtain **7a** (6% methanol/chloroform), **7b** (10% methanol/chloroform) and **7c** (5% methanol/chloroform) as colorless solids.

**7a:** Yield: 75%; m.p.: 137-139 °C; FT-IR (KBr): ν<sub>max</sub> = 3256 (s; ν<sub>str</sub>(N-H)), 2917 (s; ν<sub>as</sub>(-CH<sub>2</sub>)), 2847 (s; ν<sub>s</sub>(-CH<sub>2</sub>)), 1641 (s; ν<sub>str</sub>(C=O)), 1537 (s; ν<sub>def</sub>(N-H) + ν<sub>str</sub>(C-N)) cm<sup>-1</sup>; <sup>1</sup>H NMR (500 MHz, CDCl<sub>3</sub>, TMS): δ = 7.09 (s, 1H, -CONH), 7.04 (s, 2H, Ar-*H*), 4.03–3.96

(m, 6H, -OCH<sub>2</sub>), 3.53–3.50 (m, 2H, -NHCH<sub>2</sub>), 3.01 (t, *J* = 5.0 Hz, 2H, -CH<sub>2</sub>NH<sub>2</sub>), 1.49–1.43 (m, 6H, -CH<sub>2</sub>), 1.34–1.22 (m, 54H, -CH<sub>2</sub>), 0.90 (t, *J* = 6.5 Hz, 9H, -CH<sub>3</sub>) ppm; <sup>13</sup>C NMR (125 MHz; CDCl<sub>3</sub>): δ = 168.4, 153.0 (2C), 141.2, 128.4, 106.0 (2C), 73.5, 69.4 (2C), 40.3, 39.3, 31.9 (2C), 30.4, 29.8–29.4 (21C), 26.2 (2C), 26.1, 22.7 (3C), 14.1 (3C) ppm; HRMS-ESI calculated for C<sub>45</sub>H<sub>84</sub>N<sub>2</sub>O<sub>4</sub> [M+H]<sup>+</sup>: 717.6431, found: 717.6539.

**7b**: Yield: 62%; <sup>1</sup>H NMR (500 MHz, CDCl<sub>3</sub>, TMS): δ = 7.02 (s, 2H, Ar-*H*), 6.87 (s, 1H, -CONH), 4.07–3.99 (m, 6H, -OCH<sub>2</sub>), 3.52–3.48 (m, 2H, -NHCH<sub>2</sub>), 2.97 (t, *J* = 5.8 Hz, 2H, -CH<sub>2</sub>NH<sub>2</sub>), 1.81–1.76 (m, 4H, -CH<sub>2</sub>), 1.55–1.41 (m, 8H, -CH<sub>2</sub>), 1.33–1.21 (m, 38H, -CH<sub>2</sub>), 0.94–0.91 (m, 3H, -CH<sub>3</sub>), 0.89–0.85 (m, 12H, -CH(CH<sub>3</sub>)<sub>2</sub> + -CH<sub>3</sub>) ppm; <sup>13</sup>C NMR (125 MHz, CDCl<sub>3</sub>): δ = 167.8, 153.1 (2C), 141.1, 129.3, 105.7 (2C), 71.7, 69.3 (2C), 41.9, 41.2, 39.4, 37.5, 37.3, 31.9 (3C), 29.7 (12C), 29.5, 29.4 (2C), 28.0, 26.1 (2C), 24.7, 22.7, 22.6 (2C), 19.5, 14.1 (2C) ppm; HRMS-ESI calculated for C<sub>43</sub>H<sub>80</sub>N<sub>2</sub>O<sub>4</sub> [M+H]<sup>+</sup>: 689.6118, found: 689.6189.

**7c**: Yield: 79%; FT-IR (KBr): ν<sub>max</sub> = 3276 (s; ν<sub>str</sub>(N-H)), 2956 (s; ν<sub>as</sub>(-CH<sub>2</sub>)), 2870 (s; ν<sub>s</sub>(-CH<sub>2</sub>)), 1641 (s; ν<sub>str</sub>(C=O)), 1537 (s; ν<sub>def</sub>(N-H) + ν<sub>str</sub>(C-N)) cm<sup>-1</sup>; <sup>1</sup>H NMR (500 MHz, CDCl<sub>3</sub>, TMS): δ = 6.95 (s, 2H, Ar-*H*), 6.81 (s, 1H, -CONH), 3.95–3.91 (m, 6H, -OCH<sub>2</sub>), 3.45 (d, *J* = 5.5 Hz, 2H, -NHCH<sub>2</sub>), 2.91 (t, *J* = 5.5 Hz, 2H, -CH<sub>2</sub>NH<sub>2</sub>), 1.74–1.62 (m, 6H, -CH<sub>2</sub>), 1.48–1.39 (m, 6H, -CH<sub>2</sub>), 0.89 (m, 9H, -CH<sub>3</sub>) ppm; <sup>13</sup>C NMR (125 MHz; CDCl<sub>3</sub>): δ = 167.9, 153.1 (2C), 141.1, 129.3, 105.8 (2C), 73.1, 69.0 (2C), 41.7, 41.1, 32.3, 31.4 (2C), 19.3 (2C), 19.2, 13.9, 13.8 (2C) ppm; HRMS-ESI calculated for C<sub>21</sub>H<sub>36</sub>N<sub>2</sub>O<sub>4</sub> [M+H]<sup>+</sup>: 381.2675, found: 381.2754.

**3.5.6. Synthesis of *N*-(2-(3,5-diiodobenzamido)ethyl)-3,4,5-trialkoxybenzami**

**de (8):** Compound **7** (0.83 mmol, 1 equiv.), 3,5-diiodobenzoic acid<sup>[39]</sup> (0.96 mmol, 1.17 equiv.) and BOP reagent (0.92 mmol, 1.11 equiv.) were dissolved in dry DCM (20 mL) in a 250 mL two-neck round bottom flask. Dry triethylamine (0.92 mmol, 1.11 equiv.) was added to the reaction mixture and was allowed to stir at room temperature for 5 h under inert condition. The progress of the reaction was monitored by TLC. On completion of the reaction, the mixture of solvents was evaporated under reduced pressure and the residue was extracted using chloroform. The organic layer was washed with brine thrice, dried over anhydrous Na<sub>2</sub>SO<sub>4</sub>, filtered and the filtrate was concentrated under reduced pressure. The obtained crude product was then purified by column chromatography over silica gel to yield compound **8a** (4% methanol/chloroform), **8c** (1% methanol/chloroform) as colorless powders and **8b** (5% methanol/chloroform) as grey solid.

**8a:** Yield: 51%; m.p.: 108-110 °C; FT-IR (KBr):  $\nu_{\max}$  = 3273 (s;  $\nu_{\text{str}}(\text{N-H})$ ), 2919 (s;  $\nu_{\text{as}}(-\text{CH}_2)$ ), 2851 (s;  $\nu_{\text{s}}(-\text{CH}_2)$ ), 1641 (s;  $\nu_{\text{str}}(\text{C=O})$ ), 1537 (s;  $\nu_{\text{def}}(\text{N-H}) + \nu_{\text{str}}(\text{C-N})$ ) cm<sup>-1</sup>; <sup>1</sup>H NMR (500 MHz, CDCl<sub>3</sub>, TMS):  $\delta$  = 8.10 (s, 2H, Ar-*H*), 8.06 (s, 1H, Ar-*H*), 8.03 (s, 2H, -CONH), 6.93 (s, 2H, Ar-*H*), 3.96–3.91 (m, 6H, -OCH<sub>2</sub>), 3.62 (s, 4H, -NHCH<sub>2</sub>), 1.76–1.66 (m, 6H, -CH<sub>2</sub>), 1.42–1.38 (m, 6H, -CH<sub>2</sub>), 1.25–1.19 (m, 48H, -CH<sub>2</sub>), 0.81 (t, *J* = 6.0 Hz, 9H, -CH<sub>3</sub>) ppm; <sup>13</sup>C NMR (125 MHz, CDCl<sub>3</sub>):  $\delta$  = 169.2, 166.5, 153.2 (2C), 149.8, 138.2 (2C), 135.5 (2C), 132.8, 128.2, 105.7 (2C), 94.8, 73.5, 69.3 (2C), 41.5, 40.5, 31.9 (2C), 30.3, 29.7-29.4 (21C), 26.1 (2C), 26.0, 22.7 (3C), 14.1 (3C) ppm; HRMS-ESI calculated for C<sub>52</sub>H<sub>86</sub>I<sub>2</sub>N<sub>2</sub>O<sub>5</sub> [M+H]<sup>+</sup>: 1073.4626, found: 1073.4756.

**8b:** Yield: 39%; m.p.: 101-103 °C;  $^1\text{H}$  NMR (500 MHz,  $\text{CDCl}_3$ , TMS):  $\delta$  = 8.15 (s, 1H, Ar-H), 8.12 (s, 2H, Ar-H), 7.65 (s, 1H, -CONH), 7.13 (s, 1H, -CONH), 7.02 (s, 2H, Ar-H), 4.07-3.98 (m, 6H, -OCH<sub>2</sub>), 3.65 (s, 4H, -NHCH<sub>2</sub>), 1.85–1.77 (m, 4H, -CH<sub>2</sub>), 1.58–1.42 (m, 6H, -CH<sub>2</sub>), 1.30-1.23 (m, 38H, -CH<sub>2</sub>), 1.18-1.12 (m, 2H, -CH<sub>2</sub>), 0.92-0.85 (m, 15H, -CH(CH<sub>3</sub>)<sub>2</sub> + -CH<sub>3</sub>) ppm;  $^{13}\text{C}$  NMR (125 MHz,  $\text{CDCl}_3$ ):  $\delta$  = 169.0, 165.5, 153.2 (2C), 147.9, 141.3, 137.3, 135.6 (2C), 128.4, 105.6 (2C), 94.8 (2C), 71.8, 69.3 (2C), 41.5, 40.6, 39.4, 37.5, 37.3, 31.9 (2C), 29.7 (12C), 29.5, 29.4 (2C), 28.0, 26.2 (2C), 24.7, 22.7 (2C), 22.6 (2C), 19.6, 14.1 (2C) ppm; HRMS-ESI calculated for  $\text{C}_{50}\text{H}_{82}\text{I}_2\text{N}_2\text{O}_5$   $[\text{M}+\text{H}]^+$ : 1045.4313, found: 1045.4402.

**8c:** Yield: 75%; m.p.: 158-160 °C; FT-IR (KBr):  $\nu_{\text{max}}$  = 3275 (s;  $\nu_{\text{str}}(\text{N-H})$ ), 2959 (s;  $\nu_{\text{as}}(-\text{CH}_2)$ ), 2869 (s;  $\nu_{\text{s}}(-\text{CH}_2)$ ), 1642 (s;  $\nu_{\text{str}}(\text{C=O})$ ), 1537 (s;  $\nu_{\text{def}}(\text{N-H}) + \nu_{\text{str}}(\text{C-N})$ )  $\text{cm}^{-1}$ ;  $^1\text{H}$  NMR (500 MHz,  $\text{CDCl}_3$ , TMS):  $\delta$  = 8.38 (s, 1H, -CONH), 8.22 (s, 1H, Ar-H), 8.13 (s, 2H, Ar-H), 7.53 (s, 1H, -CONH), 7.04 (s, 2H, Ar-H), 4.06–4.01 (m, 6H, -OCH<sub>2</sub>), 3.70 (s, 4H, -NHCH<sub>2</sub>), 1.82 (t,  $J$  = 7.0 Hz, 6H, -CH<sub>2</sub>), 1.55–1.51 (m, 6H, -CH<sub>2</sub>), 1.01-0.96 (m, 9H, -CH<sub>3</sub>) ppm;  $^{13}\text{C}$  NMR (125 MHz,  $\text{CDCl}_3$ ):  $\delta$  = 168.8, 165.8, 153.1 (2C), 147.8, 141.1, 137.3, 135.7 (2C), 128.6, 105.6 (2C), 94.7 (2C), 73.1, 68.9 (2C), 41.1, 40.9, 32.3, 31.4 (2C), 19.3 (2C), 19.1, 13.9 (3C) ppm; HRMS (ESI) calculated for  $\text{C}_{28}\text{H}_{38}\text{I}_2\text{N}_2\text{O}_5$   $[\text{M}+\text{H}]^+$ : 737.0870, found: 737.0960.

**3.5.7. Synthesis of 4,4-difluoro-1,3,5,7-tetramethyl-8-(4-iodo)-4-bora-3a,4a-diaza-s-inadcene (11):** 4-Iodobenzoylchloride (**9**) (7.7 mmol, 1 equiv.) and 2,4-dimethyl pyrrole (**10**) (15.7 mmol, 2.04 equiv.) were dissolved in dry DCM. The color of

the mixture was immediately changed into bright red. After refluxing for 3 h at 35 °C under inert atmosphere, the reaction mixture was cooled down to room temperature. Et<sub>3</sub>N (5 mL) and BF<sub>3</sub>.Et<sub>2</sub>O (5 mL) were added and the reaction mixture was further refluxed for 30 minutes. On completion of the reaction (indicated by the bright greenish yellow fluorescence of the reaction mixture), the mixture of solvents was evaporated under reduced pressure and the residue was extracted using chloroform. The organic layer was washed with water thrice, dried over anhydrous Na<sub>2</sub>SO<sub>4</sub>, filtered, and the filtrate was concentrated under reduced pressure. The obtained crude product was then purified by column chromatography over silica gel (20% chloroform/*n*-hexane) to yield compound **11** as an orange solid.

**11:** Yield: 60%; m.p.: 225-227 °C; <sup>1</sup>H NMR (500 MHz, CDCl<sub>3</sub>, TMS): δ = 7.85 (d, *J* = 8.5 Hz, 2H, Ar-*H*), 7.05 (d, *J* = 8.5 Hz, 2H, Ar-*H*), 5.99 (s, 2H, Ar-*H*), 2.55 (s, 6H, Ar-CH<sub>3</sub>), 1.42 (s, 6H, Ar-CH<sub>3</sub>) ppm; <sup>13</sup>C NMR (125 MHz, CDCl<sub>3</sub>): δ = 154.9 (2C), 141.9 (2C), 139.1, 137.3 (2C), 133.6 (2C), 130.1, 129.0 (2C), 120.4 (2C), 93.7, 28.7, 13.6, 13.5, 10.2 ppm; HRMS-ESI calculated for C<sub>19</sub>H<sub>18</sub>BF<sub>2</sub>IN<sub>2</sub> [M+H]<sup>+</sup>: 451.0576, found: 451.0668.

### 3.5.8. Synthesis of 4,4-difluoro-1,3,5,7-tetramethyl-8-(4-(trimethylsilyl)ethynyl)-4-bora-3a,4a-diaza-s-indacene (**12**):

Compound **11** (0.502 mmol, 1 equiv.), Pd(PPh<sub>3</sub>)<sub>2</sub>Cl<sub>2</sub> (5 mol%) and CuI (5 mol%) were dissolved in a degassed (1:1) mixture of dry THF and triethylamine (30 mL) in a two-neck round bottom flask under inert atmosphere. Ethynyltrimethylsilane (0.63 mmol, 1.2 equiv.) was added dropwise and the reaction mixture was stirred at room temperature for 12 h. The progress of the reaction was

monitored using TLC. On completion of the reaction, the mixture of solvents was evaporated under reduced pressure and the residue was washed with 10% HCl solution to neutralize the remaining amount of triethylamine present within the medium. The residue was then extracted using chloroform, and the organic layer was washed thrice with brine, dried over anhydrous Na<sub>2</sub>SO<sub>4</sub>, filtered and the filtrate was concentrated under reduced pressure. The obtained crude product was then purified by column chromatography over silica gel (20% chloroform/*n*-hexane) to yield compound **12** as a dark orange solid.

**12:** Yield: 71%; m.p.: 202-204 °C; <sup>1</sup>H NMR (500 MHz, CDCl<sub>3</sub>, TMS): δ = 7.61–7.59 (m, 2H, Ar-*H*), 7.25–7.23 (m, 2H, Ar-*H*), 5.98 (s, 2H, Ar-*H*), 2.55 (s, 6H, Ar-CH<sub>3</sub>), 1.40 (s, 6H, Ar-CH<sub>3</sub>), 0.28 (s, 9H, Si-CH<sub>3</sub>) ppm; <sup>13</sup>C NMR (125 MHz, CDCl<sub>3</sub>): δ = 155.9 (2C), 143.1, 140.9, 135.3 (2C), 132.8 (2C), 131.3, 128.2 (2C), 124.1 (2C), 121.5 (2C), 104.3, 96.0, 14.7 (4C), 0.0 (3C) ppm; HRMS-ESI calculated for C<sub>24</sub>H<sub>27</sub>BF<sub>2</sub>N<sub>2</sub>Si [M+H]<sup>+</sup>: 421.2005, found: 421.2093.

**3.5.9. Synthesis of 4,4-difluoro-1,3,5,7-tetramethyl-8-(4-ethynyl)-4-bora-3a,4a-diaza-s-indacene (13):** Compound **12** (0.297 mmol, 1 equiv.) was dissolved in a mixture of MeOH (15 mL) and THF (15 mL) in a 100 mL round bottom flask. K<sub>2</sub>CO<sub>3</sub> (0.43 mmol, 1.45 equiv.) was added and the reaction mixture was stirred at room temperature for 1 h. The progress of the reaction was monitored using TLC. On completion, the reaction was immediately quenched with 15% aqueous NH<sub>4</sub>Cl (30 mL) and the residue extracted with chloroform. The organic layer was washed thrice with brine, dried over anhydrous Na<sub>2</sub>SO<sub>4</sub>, filtered, and the filtrate was concentrated under reduced pressure. The obtained

crude product was then purified by column chromatography over silica gel (50% chloroform/*n*-hexane) to yield compound **13** as a dark red solid.

**13**: Yield: 72%; m.p.: 239-241 °C; <sup>1</sup>H NMR (500 MHz, CDCl<sub>3</sub>, TMS): δ = 7.56 (d, *J* = 8.0 Hz, 2H, Ar-*H*), 7.20 (d, *J* = 8.0 Hz, 2H, Ar-*H*), 5.92 (s, 2H, Ar-*H*), 3.11 (s, 1H, -C≡C-*H*), 2.49 (s, 6H, Ar-CH<sub>3</sub>), 1.33 (s, 6H, Ar-CH<sub>3</sub>) ppm; <sup>13</sup>C NMR (125 MHz, CDCl<sub>3</sub>): δ = 154.8, 142.0, 139.1, 134.6, 131.9 (2C), 131.0 (2C), 127.2 (2C), 127.1 (2C), 121.9, 120.4, 112.2, 78.1, 77.5, 21.7, 13.6, 13.0, 12.2 ppm; HRMS-ESI calculated for C<sub>21</sub>H<sub>19</sub>BF<sub>2</sub>N<sub>2</sub> [M+H]<sup>+</sup>: 349.1609, found: 349.1694.

**3.5.10. Synthesis of Compounds 1-3**: In a general reaction procedure, compound **8** (0.20 mmol, 1 equiv.), Pd(PPh<sub>3</sub>)<sub>2</sub>Cl<sub>2</sub> (10 mol%) and CuI (10 mol%) were dissolved in a degassed (1:1) mixture of dry triethylamine and THF (15 mL) in a 100 mL two-neck round bottom flask under inert atmosphere. Compound **13** (0.48 mmol, 2.4 equiv.) dissolved in a degassed (1:1) mixture (5 mL) of dry triethylamine and THF, was added dropwise and the reaction mixture was refluxed at 70 °C for 18 h. The progress of the reaction was monitored using TLC. On completion of the reaction, the solvent mixture was evaporated under reduced pressure and the residue was washed with 10% HCl solution to neutralize the remaining amount of triethylamine present within the medium and the residue extracted using ethyl acetate. The organic layer was washed thrice with brine, dried over anhydrous Na<sub>2</sub>SO<sub>4</sub>, filtered and the filtrate was concentrated under reduced pressure. The obtained crude product was then purified by column chromatography over silica gel to yield



compound **1,3** (35% ethyl acetate/*n*-hexane) and **2** (40% ethyl acetate/*n*-hexane) as orange solid.

**1**: Yield: 23%; m.p.: 118-120 °C; FT-IR (KBr):  $\nu_{\max} = 3296$  (s;  $\nu_{\text{str}}(\text{N-H})$ ), 2926 (s;  $\nu_{\text{as}}(-\text{CH}_2)$ ), 2850 (s;  $\nu_{\text{s}}(-\text{CH}_2)$ ), 1642 (s;  $\nu_{\text{str}}(\text{C=O})$ ), 1513 (s;  $\nu_{\text{def}}(\text{N-H}) + \nu_{\text{str}}(\text{C-N})$ )  $\text{cm}^{-1}$ ;  $^1\text{H}$  NMR (500 MHz,  $\text{CDCl}_3$ , TMS):  $\delta = 7.99$  (s, 2H, Ar-*H*), 7.88 (s, 1H, Ar-*H*), 7.70 (d,  $J = 10.0$  Hz, 4H, Ar-*H*), 7.35 (d,  $J = 10.0$  Hz, 4H, Ar-*H*), 7.20 (s, 1H, -CONH), 7.02 (s, 2H, Ar-*H*), 6.91 (s, 1H, -CONH), 6.02 (s, 4H, Ar-*H*), 4.05–3.99 (m, 6H, -OCH<sub>2</sub>), 3.77 (bs, 4H, -NHCH<sub>2</sub>), 2.59 (s, 12H, Ar-CH<sub>3</sub>), 1.84-1.79 (m, 4H, -CH<sub>2</sub>), 1.76-1.72 (m, 2H, -CH<sub>2</sub>), 1.57 (s, 18H, -CH<sub>2</sub>), 1.46 (s, 12H, Ar-CH<sub>3</sub>), 1.27 (s, 36H, -CH<sub>2</sub>), 0.90 (t,  $J = 7.5$  Hz, 9H, -CH<sub>3</sub>) ppm;  $^{13}\text{C}$  NMR (125 MHz,  $\text{CDCl}_3$ ):  $\delta = 169.0$ , 167.1, 155.9 (2C), 153.2 (2C), 142.9 (6C), 141.2 (2C), 140.5 (2C), 135.6 (2C), 135.5 (2C), 132.5 (6C), 132.1 (2C), 131.2, 128.6 (2C), 128.4 (5C), 124.1 (2C), 123.4 (2C), 121.5 (2C), 105.5 (2C), 90.4 (2C), 88.9 (2C), 73.5, 69.2 (2C), 41.2, 40.9, 31.9 (3C), 29.7-29.6 (18C), 29.5, 29.4 (2C), 26.1 (3C), 22.7 (3C), 17.0 (2C), 16.1 (2C), 15.6 (2C), 14.9 (2C), 14.6, 14.1 (2C) ppm; MALDI-TOF calculated for  $\text{C}_{94}\text{H}_{122}\text{B}_2\text{F}_4\text{N}_6\text{O}_5$   $[\text{M-F}]^+$ : 1493.9609, found: 1494.0633.

**2**: Yield: 22%; m.p.: 119-121 °C;  $^1\text{H}$  NMR (500 MHz,  $\text{CDCl}_3$ , TMS):  $\delta = 7.91$  (s, 2H, Ar-*H*), 7.78 (s, 1H, Ar-*H*), 7.60 (d,  $J = 10.0$  Hz, 4H, Ar-*H*), 7.25 (d,  $J = 10.0$  Hz, 4H, Ar-*H*), 7.24 (s, 1H, -CONH), 6.93 (s, 2H, Ar-*H*), 6.91 (s, 1H, -CONH), 5.93 (s, 4H, Ar-*H*), 3.99–3.90 (m, 6H, -CH<sub>2</sub>), 3.67 (bs, 4H, -NHCH<sub>2</sub>), 2.49 (s, 12H, Ar-CH<sub>3</sub>), 1.75-1.71 (m, 4H, -CH<sub>2</sub>), 1.36 (s, 12H, Ar-CH<sub>3</sub>), 1.21-1.15 (m, 40H, -CH<sub>2</sub>), 1.07-1.03 (m, 6H, -CH<sub>2</sub>), 0.84-0.77 (m, 15H, -CH(CH<sub>3</sub>)<sub>2</sub> + -CH<sub>3</sub>) ppm;  $^{13}\text{C}$  NMR (125 MHz,  $\text{CDCl}_3$ ):  $\delta = 169.0$ , 167.0,

155.9 (2C), 153.2 (2C), 142.9 (6C), 140.6 (2C), 137.1 (2C), 135.6 (2C), 132.4 (6C), 131.1 (2C), 130.0, 128.8 (2C), 128.4 (5C), 123.4 (2C), 121.4 (2C), 105.6 (2C), 90.4 (2C), 88.9 (2C), 71.8, 69.3 (2C), 41.0, 40.9, 39.4, 37.5, 37.3, 31.9 (2C), 31.3 (2C), 29.7 (12C), 29.6, 29.4 (6C), 28.0, 26.1 (2C), 24.7, 22.7 (2C), 22.6 (2C), 19.5, 14.6 (6C), 14.1 (2C) ppm; MALDI-TOF calculated for  $C_{92}H_{118}B_2F_4N_6O_5$  [M-F]<sup>+</sup>: 1464.9286, found: 1465.910.

**3:** Yield: 25%; FT-IR (KBr):  $\nu_{\max}$  = 3297 (s;  $\nu_{\text{str}}(\text{N-H})$ ), 2956 (s;  $\nu_{\text{as}}(-\text{CH}_2)$ ), 2868 (s;  $\nu_{\text{s}}(-\text{CH}_2)$ ), 1652 (s;  $\nu_{\text{str}}(\text{C=O})$ ), 1541 (s;  $\nu_{\text{def}}(\text{N-H}) + \nu_{\text{str}}(\text{C-N})$ )  $\text{cm}^{-1}$ ; <sup>1</sup>H NMR (500 MHz, CDCl<sub>3</sub>, TMS):  $\delta$  = 7.99 (s, 2H, Ar-H), 7.88 (s, 1H, Ar-H), 7.70 (d,  $J$  = 5.0 Hz, 4H, Ar-H), 7.35 (d,  $J$  = 5.0 Hz, 4H, Ar-H), 7.24 (s, 1H, -CONH), 7.03 (m, 3H, Ar-H + -CONH), 6.02 (s, 4H, Ar-H), 4.06-4.00 (m, 6H, -OCH<sub>2</sub>), 3.77 (bs, 4H, -NHCH<sub>2</sub>), 2.59 (s, 12H, Ar-CH<sub>3</sub>), 1.80-1.70 (m, 6H, -CH<sub>2</sub>), 1.54-1.49 (m, 6H, -CH<sub>2</sub>), 1.46 (s, 12H, Ar-CH<sub>3</sub>), 0.97 (t,  $J$  = 7.5 Hz, 9H, -CH<sub>3</sub>) ppm; <sup>13</sup>C NMR (125 MHz, CDCl<sub>3</sub>):  $\delta$  = 168.9, 167.1, 158.4, 155.9 (2C), 155.1, 153.1 (2C), 144.9, 143.3, 143.0 (2C), 141.2, 140.3, 137.2, 135.6, 132.6 (4C), 132.4 (4C), 131.2 (2C), 130.1, 128.8 (2C), 128.4 (4C), 128.3 (4C), 123.7, 123.4, 122.5, 121.4 (2C), 105.5 (2C), 90.4, 90.3, 89.1, 88.9, 73.1, 68.9 (2C), 41.1, 41.0, 32.3, 31.4 (2C), 29.1, 19.3 (2C), 19.1, 16.9 (2C), 14.9, 14.6 (2C), 13.9 (4C), 11.6 ppm; MALDI-TOF calculated for  $C_{70}H_{74}B_2F_4N_6O_5$ [M-F]<sup>+</sup>: 1157.5853, found: 1157.4295.

## 3.6. Description on Experimental Techniques

### 3.6.1. Optical Measurements

Details of UV-vis absorption spectrophotometer and spectrofluorimeter instruments have been provided in Section 2.6.1. of Chapter 2. Deconvolution of broad absorption and

emission spectra was performed using the Fityk 0.9.8 software. Details of TCSPC system and calculation of different parameters have been reported in Section **2.6.1.** of Chapter 2.

### **3.6.2. Morphological Studies**

Details of TEM, SEM and fluorescence microscopy instruments have been provided in Section **2.6.2.** of Chapter 2. Samples for electron microscopy were prepared by dropcasting the aggregates of **1** and **2** from different solvents and solvent mixtures over carbon-coated copper grids (TEM), smooth aluminium foil (SEM) and then dried under air overnight. All the TEM images were obtained without staining. NTEGRA (NT-MDT) AFM operating in tapping mode regime was used to record the AFM images under ambient conditions and the offline mode was used to do AFM section analysis. Samples for AFM analysis were prepared by dropcasting the *n*-decane solution of **1** on a freshly cleaved mica surface followed by drying at ambient conditions.

### **3.6.3. Rheological Analysis**

Details of rheometer have been provided in Section **2.6.3.** of Chapter 2. *n*-Decane gels were directly put over the plate. In order to avoid the solvent evaporation, the plate was properly covered. The gap between the cone and the plate was kept fixed between 0.105 mm.

### **3.6.4. WAXS Analysis**

Details of WAXS instrument have been provided in Section **2.6.4.** of Chapter 2. Samples for WAXS analysis were prepared by dropcasting aggregates of **1** in *n*-decane or MCH ( $8 \times 10^{-3}$  M), followed by the complete removal of the solvents under high vacuum. These dried films were then used for the WAXS analysis.

### 3.6.5. Solvent Controlled Self-Assembly

In a typical experiment, the required BODIPY derivatives in linear (*n*-decane, *n*-heptane) or cyclic (*trans*-decalin, MCH) hydrocarbon solvents ( $3 \times 10^{-4}$  M, 300  $\mu$ L) were taken in a screw-capped 1 mm quartz cuvette and were cooled down from 363 to 283 K at a controlled rate (1 K/min) to form the self-assemblies and used for spectroscopy and microscopy studies. The spherical structures were created in MCH or *trans*-decalin by two different pathways; fast cooling followed by aging and controlled cooling at a rate of 1 K/min. The 2D sheets were obtained by controlled cooling (1 K/min) in *n*-decane or *n*-heptane. The thermodynamic parameters at different conditions were calculated from the cooling curves (obtained by controlled cooling at 1 K/min) at various concentrations and fitted to an equilibrium model. Fast cooling samples were prepared by immediately immersing the hot solution of **1** (363 K) at  $3 \times 10^{-4}$  M in MCH for 5 min and further utilized for DLS analysis and TEM imaging. For ultrasound stimulation experiments, aggregates of **1** initially prepared by controlled cooling in *n*-decane, were sonicated (37 kHz, bath temperature 293 K) for 10 min and used.

### 3.6.6. DLS Studies

DLS measurements were performed using Malvern type Zetasizer Nano ZSP. Samples for DLS studies were prepared by immediately immersing the hot solution (363 K) of **1** and **2** in MCH ( $3 \times 10^{-4}$  M) for 5 min in ice (fast cooling), and also by cooling at a controlled rate of 1 K/min from 363 to 283 K.

### 3.6.7. Time Resolved Emission and Anisotropy Studies

The samples prepared by controlled cooling of **1** or **2** (1 K/min) either in *n*-decane or MCH ( $3 \times 10^{-4}$  M) were utilized for these studies. The TRES and time-resolved fluorescence anisotropy data were obtained on UltraFast lifetime spectrofluorometer (Delta flex, Horiba Jobinyvon IBH Ltd.). The excitation source was provided by a DeltaDiode<sup>TM</sup> (Horiba) pulse laser diode with wavelength of 375 nm. TRES were obtained by uniformly incrementing the wavelength (5 nm) and measuring the time-resolved decay for equal periods of time. Fluorescence decay were then analyzed using EzTime decay analysis software by fitting common lifetimes to all of the individual decay curves. For the time-resolved anisotropy studies,  $\beta$  (angle between the excitation and emission transition dipole moment) has been calculated from the equation  $r_0 = (3\cos^2\beta - 1)/5$ ; where  $r_0$  is the initial anisotropy.

### 3.6.8. Reversible Control of Morphology and Cascade Energy Transfer

To check the reversibility of the morphological features and cascade energy transfer, solvent mixing experiments were performed. For the spherical to 2D sheets and the consequent change from single to multiple emission, different volume fractions of *n*-decane were mixed to a solution of **1** in MCH (v/v, 300  $\mu$ L) while maintaining the total concentration at  $3 \times 10^{-4}$  M. Similar procedure was also followed for the conversion of the 2D sheets to spherical structures and consequent change of the multiple emission to single emission by the addition of different volume fractions of MCH to a solution of **1** in *n*-decane. TEM, DLS and fluorescence spectral analyses were performed at different solvent

compositions ( $f = 0.02 - 0.98$ ) to establish the reversible morphology changes and emission behavior.

### 3.7. References

- [1] (a) H. W. Schmidt, F. Würthner, *Angew. Chem., Int. Ed.* **2020**, *59*, 8766–8775; (b) G. Vantomme, E. W. Meijer, *Science* **2019**, *363*, 1396–1397; (c) M. Aono, Y. Bando, K. Ariga, *Adv. Mater.* **2012**, *24*, 150–151.
- [2] (a) H. Zhang, Z. Zhao, A. T. Turley, L. Wang, P. R. McGonigal, Y. Tu, Y. Li, Z. Wang, R. T. K. Kwok, J. W. Y. Lam, et al., *Adv. Mater.* **2020**, *32*, 2001457; (b) V. K. Praveen, B. Vedhanarayanan, A. Mal, R. K. Mishra, A. Ajayaghosh, *Acc. Chem. Res.* **2020**, *53*, 496–507; (c) S. Varughese, *J. Mater. Chem. C* **2014**, *2*, 3499–3516; (d) L. Maggini, D. Bonifazi, *Chem. Soc. Rev.* **2012**, *41*, 211–241.
- [3] (a) P. K. Hashim, J. Bergueiro, E. W. Meijer, T. Aida, *Prog. Polym. Sci.* **2020**, *105*, 101250; (b) R. D. Mukhopadhyay, A. Ajayaghosh, *Science* **2015**, *349*, 241–242.
- [4] (a) B. Shen, Y. Kim, M. Lee, *Adv. Mater.* **2020**, *32*, 1905669; (b) K. Ariga, S. Watanabe, T. Mori, J. Takeya, *NPG Asia Mater.* **2018**, *10*, 90–106. (c) F. Ishiwari, Y. Shoji, T. Fukushima, *Chem. Sci.* **2018**, *9*, 2028–2041.
- [5] (a) M. Wehner, F. Würthner, *Nat. Rev. Chem.* **2020**, *4*, 38–53; (b) J. Matern, Y. Dorca, L. Sánchez, G. Fernández, *Angew. Chem. Int. Ed.* **2019**, *58*, 16730–16740; *Angew. Chem.* **2019**, *131*, 16884–16895; (c) A. Sorrenti, J. Leira-Iglesias, A. J. Markvoort, T. F. A. de Greef, T. M. Hermans, *Chem. Soc. Rev.* **2017**, *46*, 5476–5490.

- [6] (a) X. Jin, M. B. Price, J. R. Finnegan, C. E. Boott, J. M. Richter, A. Rao, S. M. Menke, R. H. Friend, G. R. Whittell, I. Manners, *Science* **2018**, *360*, 897–900; (b) Z. M. Hudson, D. J. Lunn, M. A. Winnik, I. Manners, *Nat. Commun.* **2014**, *5*, 3372.
- [7] (a) A. Sarkar, T. Behera, R. Sasmal, R. Capelli, C. Empereur-mot, J. Mahato, S. S. Agasti, G. M. Pavan, A. Chowdhury, S. J. George, *J. Am. Chem. Soc.* **2020**, *142*, 11528–11539; (b) W. Wagner, M. Wehner, V. Stepanenko, S. Ogi, F. Würthner, *Angew. Chem., Int. Ed.* **2017**, *56*, 16008–16012; (c) S. Ogi, K. Sugiyasu, S. Manna, S. Samitsu, M. Takeuchi, *Nat. Chem.* **2014**, *6*, 188–195.
- [8] (a) B. Adhikari, Y. Yamada, M. Yamauchi, K. Wakita, X. Lin, K. Aratsu, T. Ohba, T. Karatsu, M. J. Hollamby, N. Shimizu, et al., *Nat. Commun.* **2017**, *8*, 15254; (b) A. Gopal, M. Hifsudheen, S. Furumi, M. Takeuchi, A. Ajayaghosh, *Angew. Chem. Int. Ed.* **2012**, *51*, 10505–10509.
- [9] (a) G. Panzarasa, A. L. Torzynski, T. Sai, K. Smith-Mannschott, E. R. Dufresne, *Soft Matter* **2020**, *16*, 591–594; (b) H. A. M. Ardon, E. R. Draper, F. Citossi, M. Wallace, L. C. Serpell, D. J. Adams, J. D. Tovar, *J. Am. Chem. Soc.* **2017**, *139*, 8685–8692.
- [10] (a) T. K. Ellis, M. Galerne, J. J. Armao, A. Osypenko, D. Martel, M. Maaloum, G. Fuks, O. Gavat, E. Moulin, N. Giuseppone, *Angew. Chem. Int. Ed.* **2018**, *57*, 15749–15753; *Angew. Chem.* **2018**, *130*, 15975–15979; (b) J. Leira-Iglesias, A. Tassoni, T. Adachi, M. Stich, T. M. Hermans, *Nat. Nanotechnol.* **2018**, *13*, 1021–1027.
- [11] (a) H. He, W. Tan, J. Guo, M. Yi, A. N. Shy, B. Xu, *Chem. Rev.* **2020**, *120*, 9994–10078; (b) M. Kumar, N. L. Ing, V. Narang, N. K. Wijerathne, A. I. Hochbaum, R. V. Ulijn, *Nat. Chem.* **2018**, *10*, 696–703.

- [12] (a) X. Yu, L. Chen, M. Zhang, T. Yi, *Chem. Soc. Rev.* **2014**, *43*, 5346–5371; (b) J. M. Malicka, A. Sandeep, F. Monti, E. Bandini, M. Gazzano, C. Ranjith, V. K. Praveen, A. Ajayaghosh, N. Armaroli, *Chem. Eur. J.* **2013**, *19*, 12991–13001; (c) N. Komiya, T. Muraoka, M. Iida, M. Miyanaga, K. Takahashi, T. Naota, *J. Am. Chem. Soc.* **2011**, *133*, 16054–16061.
- [13] (a) P. Xing, Y. Li, Y. Wang, P.-Z. Li, H. Chen, S. Z. F. Phua, Y. Zhao, *Angew. Chem. Int. Ed.* **2018**, *57*, 7774–7779; (b) K. V. Rao, D. Miyajima, A. Nihonyanagi, T. Aida, *Nat. Chem.* **2017**, *9*, 1133–1139.
- [14] (a) A. Mishra, S. Dhiman, S. J. George, *Angew. Chem. Int. Ed.* **2020**, *59*, DOI:10.1002/anie.202006614; (b) B. Rieß, R. K. Grötsch, J. Boekhoven, *Chem* **2020**, *6*, 552–578.
- [15] (a) H.-J. Kim, T. Kim, M. Lee, *Acc. Chem. Res.* **2011**, *44*, 72–82; (b) J.-K. Kim, E. Lee, M. Lee, *Angew. Chem. Int. Ed.* **2006**, *45*, 7195–7198.
- [16] (a) Y. Kim, W. Li, S. Shin, M. Lee, *Acc. Chem. Res.* **2013**, *46*, 2888–2897; (b) Z. Huang, S.-K. Kang, M. Banno, T. Yamaguchi, D. Lee, C. Seok, E. Yashima, M. Lee, *Science* **2012**, *337*, 1521–1526.
- [17] C. Vijayakumar, V. K. Praveen, A. Ajayaghosh, *Adv. Mater.* **2009**, *21*, 2059–2063; (b) A. Ajayaghosh, C. Vijayakumar, R. Varghese, S. J. George, *Angew. Chem. Int. Ed.* **2006**, *45*, 456–460.
- [18] D. Tian, F. Qi, H. Ma, X. Wang, Y. Pan, R. Chen, Z. Shen, Z. Liu, L. Huang, W. Huang, *Nat. Commun.* **2018**, *9*, 2688.



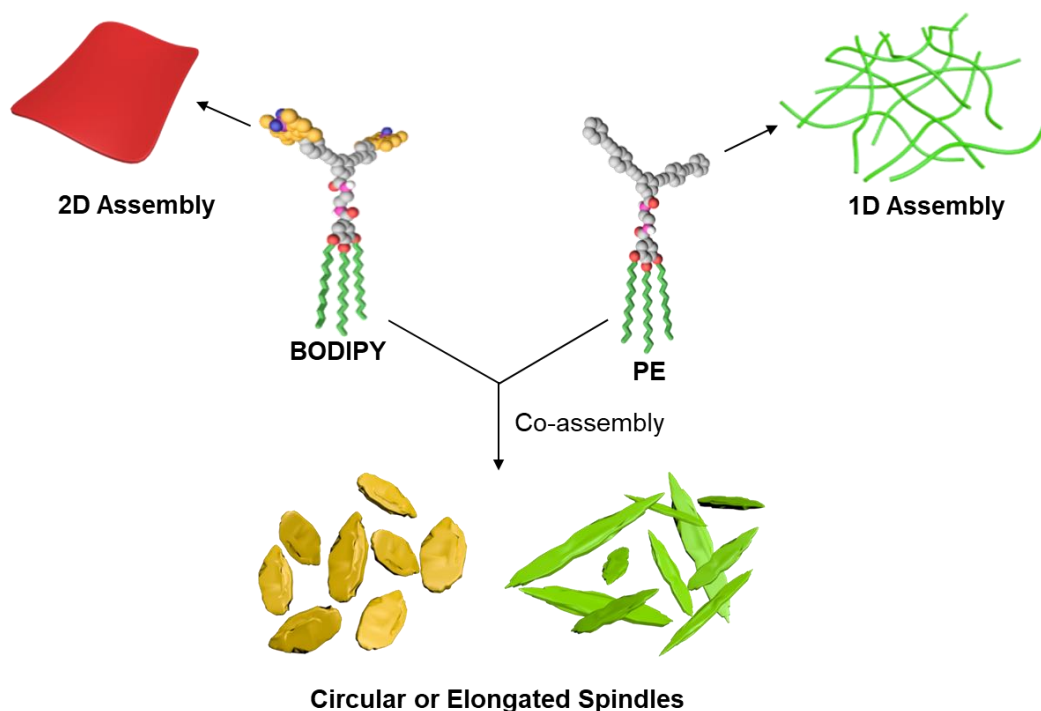
- [19] (a) N. Adir, S. Bar-Zvi, D. Harris, *Biochim. Biophys. Acta, Bioenerg.* **2020**, *1861*, 148047; (b) T. Brixner, R. Hildner, J. Köhler, C. Lambert, F. Würthner, *Adv. Energy Mater.* **2017**, *7*, 1700236; (c) K.-T. Wong, D. M. Bassani, *NPG Asia Mater.* **2014**, *6*, e116; (d) V. K. Praveen, C. Ranjith, N. Armaroli, *Angew. Chem. Int. Ed.* **2014**, *53*, 365–368; (e) Structure and Function of Phycobilisomes, M. Mimuro, H. Kikuchi, A. Murakami in *Concepts in Photobiology: Photosynthesis and Photomorphogenesis*, (Eds.: G. S. Singhal, G. RengeL S. K. Sopory, K.-D. Irrgang, Govindjee), Narosa Publishing House, New Delhi, **1999**.
- [20] (a) C. Giansante, C. Schäfer, G. Raffy, A. Del Guerzo, *J. Phys. Chem. C* **2012**, *116*, 21706–21716; (b) A. Ajayaghosh, V. K. Praveen, C. Vijayakumar, S. J. George, *Angew. Chem. Int. Ed.* **2007**, *46*, 6260–6265.
- [21] (a) J. Bañuelos, *Chem. Rec.* **2016**, *16*, 335–348; (b) G. Ulrich, R. Ziessel, A. Harriman, *Angew. Chem. Int. Ed.* **2008**, *47*, 1184–1201; (c) A. Loudet, K. Burgess, *Chem. Rev.* **2007**, *107*, 4891–4932.
- [22] (a) Z. Liu, Z. Jiang, M. Yan, X. Wang, *Front. Chem.* **2019**, *7*, 712. (b) A. V. Solomonov, Y. S. Marfin, E. V. Romyantsev, *Dye. Pigment.* **2019**, *162*, 517–542. (c) S. Cherumukkil, B. Vedhanarayanan, G. Das, V. K. Praveen, A. Ajayaghosh, *Bull. Chem. Soc. Jpn.* **2018**, *91*, 100–120.
- [23] (a) I. Helmers, G. Ghosh, R. Q. Albuquerque, G. Fernández, *Angew. Chem. Int. Ed.* **2020**, *59*, DOI: 10.1002/anie.202012710; (b) I. Helmers, B. Shen, K. K. Kartha, R. Q. Albuquerque, M. Lee, G. Fernández, *Angew. Chem. Int. Ed.* **2020**, *59*, 5675–5682; (c) I. Helmers, N. Bäumer, G. Fernández, *Chem. Commun.* **2020**, *56*, 13808–13811; (d) I. Helmers, M. Niehues, K. K. Kartha, B. J. Ravoo, G. Fernández, *Chem. Commun.* **2020**, *56*, 8944–8947; (e) J. Xia, E. Busby, S. N. Sanders, C. Tung, A. Cacciuto, M. Y. Sfeir, L. M. Campos, *ACS Nano* **2017**, *11*,

- 4593–4598; (f) S. Cherumukkil, S. Ghosh, V. K. Praveen, A. Ajayaghosh, *Chem. Sci.* **2017**, *8*, 5644–5649; (f) J.-H. Olivier, J. Widmaier, R. Ziessel, *Chem. Eur. J.* **2011**, *17*, 11709–11714.
- [24] (a) S. Radunz, W. Kraus, F. A. Bischoff, F. Emmerling, H. R. Tschiche, U. Resch-Genger, *J. Phys. Chem. A* **2020**, *124*, 1787–1797; (b) J. Gemen, J. Ahrens, L. J. W. Shimon, R. Klajn, *J. Am. Chem. Soc.* **2020**, *142*, 17721–17729; (c) Y. Zhang, P. Liu, H. Pan, H. Dai, X.-K. Ren, Z. Chen, *Chem. Commun.* **2020**, *56*, 12069–12072; (d) D. Okada, T. Nakamura, D. Braam, T. D. Dao, S. Ishii, T. Nagao, A. Lorke, T. Nabeshima, Y. Yamamoto, *ACS Nano* **2016**, *10*, 7058–7063; (e) S. Kim, J. Bouffard, Y. Kim, *Chem. Eur. J.* **2015**, *21*, 17459–17465; (f) N. K. Allampally, A. Florian, M. J. Mayoral, C. Rest, V. Stepanenko, G. Fernández, *Chem. Eur. J.* **2014**, *20*, 10669–10678;
- [25] (a) G. Das, R. Thirumalai, B. Vedhanarayanan, V. K. Praveen, A. Ajayaghosh, *Adv. Opt. Mater.* **2020**, *29*, 1703783; (b) B. Adelizzi, I. A. W. Filot, A. R. A. Palmans, E. W. Meijer, *Chem. Eur. J.* **2017**, *23*, 6103–6110. (c) H. M. M. ten Eikelder, A. J. Markvoort, T. F. A. de Greef, P. A. J. Hilbers, *J. Phys. Chem. B* **2012**, *116*, 5291–5301.
- [26] N. J. Hestand, F. C. Spano, *Chem. Rev.* **2018**, *118*, 7069–7163
- [27] (a) G. Liu, M. Cai, X. Wang, F. Zhou, W. Liu, *ACS Appl. Mater. Interfaces* **2014**, *6*, 11625–11632; (b) T. M. Ruhland, P. M. Reichstein, A. P. Majewski, A. Walther, A. H. E. Müller, *J. Colloid Interface Sci.* **2012**, *374*, 45–53.
- [28] (a) C. D. Jones, J. W. Steed, *Chem. Soc. Rev.* **2016**, *45*, 6546–6596; (b) S. Srinivasan, S. S. Babu, V. K. Praveen, A. Ajayaghosh, *Angew. Chem. Int. Ed.* **2008**, *47*, 5746–5749.

- [29] (a) S. Dhiman, R. Ghosh, S. Sarkar, S. J. George, *Chem. Sci.* **2020**, *11*, 12701–12709; (b) X. Xiao, H. Chen, X. Dong, D. Ren, Q. Deng, D. Wang, W. Tian, *Angew. Chem. Int. Ed.* **2020**, *59*, 9534–9541; (c) N. Sasaki, J. Yuan, T. Fukui, M. Takeuchi, K. Sugiyasu, *Chem. Eur. J.* **2020**, *26*, 7840–7846; (d) Yang, S.; Kang, S. Y.; Choi, T. L. *J. Am. Chem. Soc.* **2019**, *141*, 19138–19143. (e) Y. Liu, C. Peng, W. Xiong, Y. Zhang, Y. Gong, Y. Che, J. Zhao, *Angew. Chem. Int. Ed.* **2017**, *56*, 11380–11384; (f) M. E. Robinson, A. Nazemi, D. J. Lunn, D. W. Hayward, C. E. Boott, M. S. Hsiao, R. L. Harniman, S. A. Davis, G. R. Whittell, R. M. Richardson, et al., *ACS Nano* **2017**, *11*, 9162–9175.
- [30] (a) E. E. Greciano, J. Calbo, E. Ortí, L. Sánchez, *Angew. Chem. Int. Ed.* **2020**, *59*, 17517–17524; (b) A. Chakraborty, G. Ghosh, D. S. Pal, S. Varghese, S. Ghosh, *Chem. Sci.* **2019**, *10*, 7345–7351; (c) Y. Lin, M. Penna, M. R. Thomas, J. P. Wojciechowski, V. Leonardo, Y. Wang, E. T. Pashuck, I. Yarovsky, M. M. Stevens, *ACS Nano* **2019**, *13*, 1900–1909; (d) M. Pfeffermann, R. Dong, R. Graf, W. Zajaczkowski, T. Gorelik, W. Pisula, A. Narita, K. Müllen, X. Feng, *J. Am. Chem. Soc.* **2015**, *137*, 14525–14532; (e) M. Vybornyi, A. V. Rudnev, S. M. Langenegger, T. Wandlowski, G. Calzaferri, R. Häner, *Angew. Chem. Int. Ed.* **2013**, *52*, 11488–11493.
- [31] (a) M. Liu, L. Zhang, T. Wang, *Chem. Rev.* **2015**, *115*, 7304–7397; (b) V. K. Praveen, S. S. Babu, C. Vijayakumar, R. Varghese, A. Ajayaghosh, *Bull. Chem. Soc. Jpn.* **2008**, *81*, 1196–1211.
- [32] (a) M. F. J. Mabesoone, A. R. A. Palmans, E. W. Meijer, *J. Am. Chem. Soc.* **2020**, *142*, 19781–19798; (b) G. Ghosh, S. Ghosh, *Chem. Commun.* **2018**, *54*, 5720–5723; (c) C. Kulkarni, P. A. Korevaar, K. K. Bejagam, A. R. A. Palmans, E. W. Meijer, S. J. George, *J. Am. Chem. Soc.*

- 2017, 139, 13867–13875; (d) K. Baek, I. Hwang, I. Roy, D. Shetty, K. Kim, *Acc. Chem. Res.* **2015**, 48, 2221–2229; (e) Q. Jin, L. Zhang, M. Liu, *Chem. Eur. J.* **2013**, 19, 9234–9241.
- [33] B. Wittmann, F. A. Wenzel, S. Wiesneth, A. T. Haedler, M. Drechsler, K. Kreger, J. Köhler, E. W. Meijer, H.-W. Schmidt, R. Hildner, *J. Am. Chem. Soc.* **2020**, 142, 8323–8330.
- [34] Emission properties of the BODIPY has been reported to be controlled in mixed lipid monolayers by molecular compression at the air-water interface. T. Mori, H. Chin, K. Kawashima, H. T. Ngo, N. J. Cho, W. Nakanishi, J. P. Hill, K. Ariga, *ACS Nano* **2019**, 13, 2410–2419.
- [35] P. C. Nandajan, H. J. Kim, S. Casado, S. Y. Park, J. Gierschner, *J. Phys. Chem. Lett.* **2018**, 9, 3870–3877.
- [36] A. U. Neelambra, C. Govind, T. T. Devassia, G. M. Somashekharappa, V. Karunakaran, *Phys. Chem. Chem. Phys.* **2019**, 21, 11087–11102.
- [37] (a) C. Kulkarni, S. Balasubramanian, S. J. George, *ChemPhysChem* **2013**, 14, 661–673; (b) F. Würthner, S. Yao, U. Beginn, *Angew. Chem. Int. Ed.* **2003**, 42, 3247–3250.
- [38] A. Sarbu, L. Biniek, J. M. Guenet, P. J. Mésini, M. Brinkmann, *J. Mater. Chem. C* **2015**, 3, 1235–1242.
- [39] P. Rattanatraicharoen, Y. Tanaka, K. Shintaku, T. Kawaguchi, K. Yamabuki, T. Oishi, *J. Polym. Sci., Part A: Polym. Chem.* **2013**, 51, 1315–1322.

## Spindle-Shaped Supramolecular Copolymers with Controlled Excitation Energy Transfer



### 4.1. Abstract

*Spontaneous self-assembly of functional  $\pi$ -systems usually leads to 1D or 2D structures. In the previous chapter, we have reported the formation of 2D supramolecular sheets exhibiting multiple emission from a Y-shaped **BODIPY** molecule. In the present work, we found that self-assembly of a similar Y-shaped molecule, **PE** with a terminal moiety having different structural parameters when compared to **BODIPY**, can lead to 1D fibers under an identical experiential condition. In general, structurally mismatched*

monomers form homopolymers of narcissistically self-sorted assemblies instead of choosing a co-assembling pathway. Hence, it becomes challenging to copolymerize monomers that individually form 1D and 2D supramolecular polymers. Herein, we demonstrate the formation of an unusual spindle-shaped supramolecular structure by copolymerizing Y-shaped **PE** and **BODIPY** molecules under thermodynamic control. Detailed spectroscopy and microscopy studies reveal that copolymerization of 1:1 mixture of **BODIPY** and **PE** to elongated spindle-like co-assemblies (aspect ratio ~4-7) is initially driven by nucleation-elongation of **BODIPY**, followed by the secondary nucleation of **PE** monomers. Effect of initial nucleation of **BODIPY** monomers on morphology is also confirmed in the case of a 3:1 mixture of **BODIPY** and **PE**, which restricted the growth and controlled the length of the assembly to circular spindles having an aspect ratio of 1-2.5. However, when **PE** monomers initiated the nucleation process in the case of **BODIPY** and **PE** at a 1:3 composition, the control over the length for the resultant copolymer is lost and 1D structures with aspect ratio  $\geq 13-15$  are obtained. Finally, we demonstrate control over the cascade energy transfer process within **BODIPY** assembly by utilizing the hetero-energy migration process from **PE** donors to **BODIPY** acceptors within the copolymeric assemblies.

## 4.2. Introduction

Self-assembly of chromophoric  $\pi$ -systems is known to form a variety of supramolecular architectures such as particles, spheres, vesicles, tubes, fibers, and sheets;<sup>[1-4]</sup> which are

mainly formed by the involvement of various non-covalent interactions such as intermolecular H-bonding, van der Waals interaction,  $\pi$ -stacking or even amphiphilicity of the functional molecules. The aforementioned shapes of the supramolecular assemblies are quite usual and their formation mechanism has been well-explored with various experimental and theoretical models.<sup>[5]</sup> Nevertheless, chemists are keen to mimic some of the rare and aesthetic structures found in Nature. An example of such a biologically important structure found in Nature is ‘spindles’. The spindle shape, alternately known as ‘fusiform shape’, has an unusually wide portion in the middle and tapers at both ends.<sup>[6]</sup> This peculiar shape is commonly observed in human muscle cells present in the biceps brachii located in the upper arm area.<sup>[7]</sup> Even during mitosis and meiosis (the nuclear division process), the spindle formation has been found necessary in chromosomal segregation of a parental cell into daughter cells.<sup>[8]</sup> Furthermore, in the case of fast-flowing water, as observed in an open stream, fish becomes adaptive to the local environment and hence prefers to grow in a spindle-type fashion.<sup>[9]</sup> This particular shape helps a school of fish cleave through the water during fast swimming by protecting them from the opposite water-thrust. To understand the formation of such types of unusual morphological features in supramolecular assemblies, the structure and geometry of molecular building blocks must be properly chosen. Hence, in recent times, research in the field of supramolecular polymers has taken new dimensions by the clever design or selection of the monomeric  $\pi$ -systems and their polymerization protocol.<sup>[10]</sup>

The last couple of decades have witnessed how 1D supramolecular structures can be utilized to understand various mechanistic aspects of supramolecular polymerization. This knowledge has helped researchers to develop non-equilibrium systems useful to realize living and transient supramolecular polymerization.<sup>[11]</sup> To have overall control in the length and dispersity in the case of living supramolecular polymerization, the monomers have to be designed in such a way that an active living end always exists within the small oligomeric or polymeric systems, which have the propensity to attach with a new fraction of monomers after each new addition.<sup>[12]</sup> On the contrary, transient supramolecular polymerization requires a temporally controlled state alternatively known as the kinetically trapped or metastable state, which can be obtained by suitably imposing various self-assembly conditions such as rapid injection of the monomers from a good-to-bad solvent medium, rapid cooling of the monomer units from a high to low temperature and so on.<sup>[10,11,13]</sup> All of these processes can restrict the supramolecular polymerization to 0D structures before transforming into thermodynamically stable 1D supramolecular assemblies.<sup>[14]</sup> Furthermore, increasing the lateral interaction between the monomers by changing the length of the appended hydrophobic alkyl chains was introduced for preparing 2D supramolecular polymers.<sup>[15]</sup> Structural modification within the  $\pi$ -conjugated cores of the monomers has been reported to impart intrinsic curvature within the polymeric assembly and thereby leading towards the construction of well-defined topological features, starting from circular (toroidal) to randomly coiled or helically folded supramolecular polymers, and their stretched analogs with a high degree of



polymerization.<sup>[1a,16]</sup> Also, the utilization of a controlled secondary nucleation approach for supramolecular polymerization has been adopted as an effective strategy to create mechanically interlocked toroidal nanostructures.<sup>[17]</sup>

After gaining a detailed understanding of controlling the pathways associated with the supramolecular polymerization of single-component systems, there is a growing interest to explore the pathway complexity associated with the supramolecular polymerization of multi-component systems.<sup>[18]</sup> The co-assembly of different monomers can either retain their properties or offer a completely unexpected property to the resultant assembly. Hence, it becomes imperative to understand the sequential arrangement of various monomer units participating in copolymeric assembly. Recently, Manners, Winnick, and co-workers have demonstrated the formation of functionalized block copolymers with segments of different emission colors using the crystallization driven self-assembly approach.<sup>[12,19]</sup>

Co-assembly of two amphiphilic PBI dyes **PBI-1** and **PBI-2** functionalized with oligoethylene side chains have been reported by Würthner and co-workers (**Figure 4.1**).<sup>[20]</sup> The  $\pi$ -conjugated core of **PBI-1** was found to be planar, whereas twisted in the case of **PBI-2** (**Figure 4.1a**). Owing to the difference in their structural features, **PBI-1** has been found remarkably soluble in water, whereas **PBI-2** forms suspensions of small-size aggregates in water. TEM image of **PBI-1** indicated the formation of homogeneous and rigid segmented 1D nanorods at a concentration of 0.05 mM (**Figure 4.1b**) after a slow dissolution process in water, whereas TEM image of **PBI-2** revealed flexible and irregular nanoworm-like

aggregates ( $3 \times 10^{-5}$  M), when THF was slowly evaporated from the THF/water mixture of PBI-2 (**Figure 4.1c**). Difference in the morphology has been found to be associated with distinct aggregation behavior (**Figure 4.1d**), where PBI-1 and PBI-2 showed hypsochromic and bathochromic shift in the UV-vis absorption spectra, respectively with respect to their

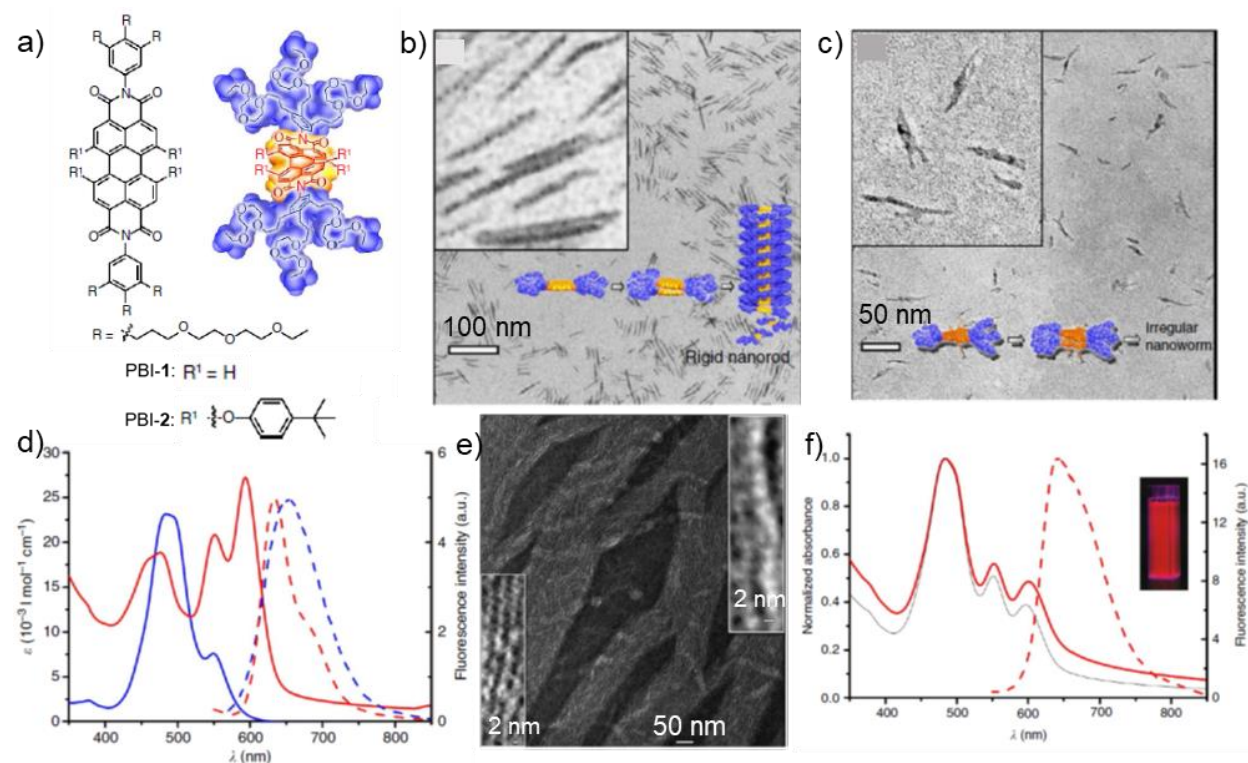


**Figure 4.1.** (a) Chemical structures and space-filling model of PBIs: PBI-1 and PBI-2. TEM images of the aggregates of (b) PBI-1 and (c) PBI-2 in water, schematic representation with space-filling models illustrate the self-assembly of PBI-1 and PBI-2. Insets for both the figures show the magnified TEM images of PBI-1 and PBI-2. (d) UV-vis absorption spectra (solid lines) and corresponding normalized fluorescence spectra (dashed lines) of PBI-1 (blue) and PBI-2 (red) in water; ( $1 \times 10^{-5}$  M,  $\lambda_{\text{ex}} = 470$  nm). (e) TEM images of the segmented nanowires formed by co-assembly of PBI-1 and PBI-2 (2:1 in molar ratio) in water. Inset shows the magnified TEM images of the single-molecule-thin nanowires. (f) Normalized absorption spectrum (red solid) and corresponding fluorescence spectrum (red dashed line,  $\lambda_{\text{ex}} = 480$  nm) of the nanowires formed by co-assembly of PBI-1 and PBI-2 (molar ratio of 2:1) compared with the linear sum of the absorption spectra (black solid) of PBI-1 and PBI-2 in water. Inset shows the photograph of a solution of the nanowires in water under illumination of UV light. (Adapted with permission from Ref 20).

monomers. Moreover, a large Stokes shift along with an excimer-like emission was noticed for PBI-1. However, the fluorescence spectrum of PBI-2 was found almost similar to that of the monomer emission with a marginal Stokes shift. Co-assembly of PBI-2 with PBI-1 was only possible upon evaporation of THF from the solvent mixture by a kinetically controlled assembly, which provided ultrathin and micrometer-long nanowires having uniform diameter of 3–4 nm (**Figure 4.1e**). Furthermore, the absorption spectrum of the co-assembly has been found to be in good agreement with the calculated one, suggesting that the aggregate mixture is composed of individual self-assembled alternating blocks of PBI-1 and PBI-2 (**Figure 4.1f**).

Palmans, Meijer and co-workers have demonstrated the formation of supramolecular block copolymers under thermodynamic control (**Figure 4.2**).<sup>[21]</sup> The microstructure of triarylamine triamide-based supramolecular block copolymer was elucidated with the help of various spectroscopy, microscopy and theoretical techniques. The monomers of TPyA-1 and TPA-2 (**Figure 4.2a**) were found to be ideal candidates for copolymerization studies owing to their similar molecular geometry and analogous aggregation behavior. The copolymer was formed following stepwise addition of the homopolymers of S-2 to S-1 at 40 °C (**Figure 4.2b**) and studied with the help of CD, and fluorescence spectroscopy techniques, where the characteristic spectrum for the copolymer was found non-identical in comparison to the spectrum obtained by linear combination of their individual components. Furthermore, the copolymerization ability of TPyA-1 and TPA-2 was tested following a thermodynamic approach, where the monomers formed at higher temperature

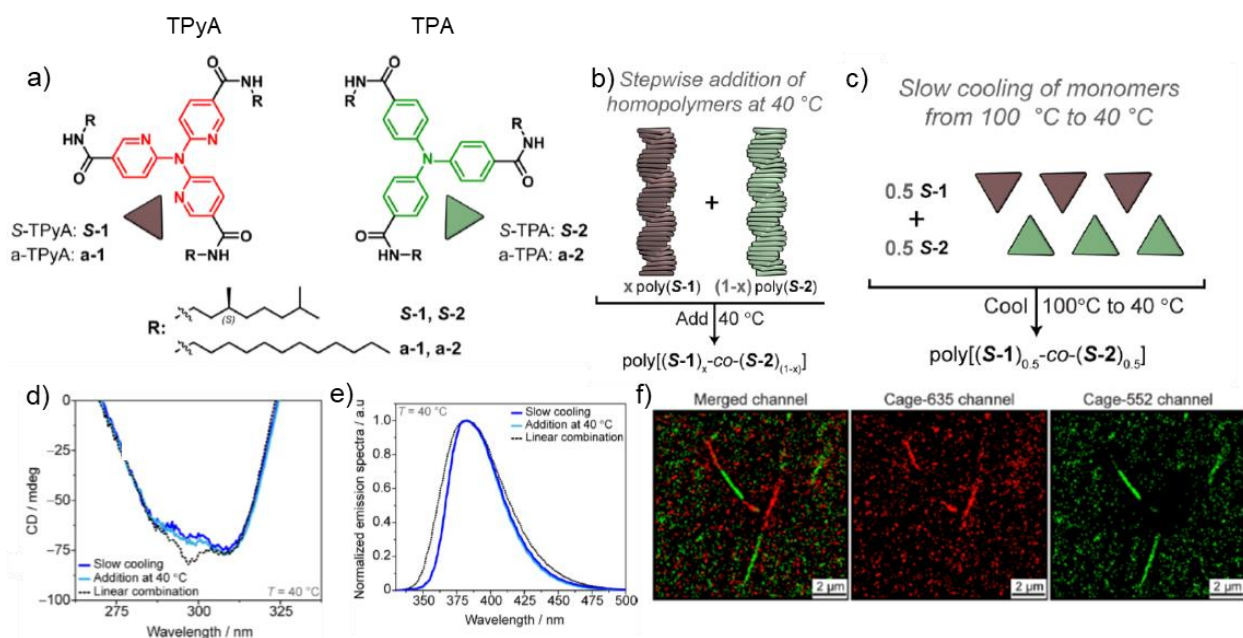


**Figure 4.2.** (a) Chemical structures of tri(pyrid-2-yl)amine triamide (TPyA-1) and triphenylamine triamide (TPA-2), substituted with a chiral (S)-3,7-dimethyloctyl (**S-1**, **S-2**) and achiral dodecyl chain (**a-1**, **a-2**). Schematic representation for the copolymerization achieved via (b) stepwise addition of supramolecular homopolymers or (c) slow cooling of the monomers. Comparison of (d) CD and (e) normalized emission spectra obtained by different copolymerization strategies: addition of homopolymers at 40 °C (light blue line), cooling of both the monomers from higher to lower temperature (violet line) with respect to the spectrum obtained by linear combination of the spectra for the homopolymers (black dotted lines) assuming no intermolecular interaction. (f) iPAINT images of supramolecular copolymer, reconstructed images of merged channels, and single Cage-635 (red) and Cage-552 (green) channels. (Adapted with permission from Ref 21).

were cooled together via a slow cooling rate (1 K/min) (**Figure 4.2c**). Here, formation of the copolymer has been confirmed from temperature-dependent CD cooling curves, exhibiting a single  $T_e$  and a completely different nature of the cooling spectrum in comparison to the linear sum of the respective homopolymers. Furthermore, it has been confirmed that the copolymer formed in two different ways are identical, as their CD and fluorescence spectra perfectly overlap with each other (**Figure 4.2d,e**). Theoretical studies introducing a mass balance model have further helped in unravelling the microstructure

analysis, confirming a stable multiblock supramolecular copolymer formation. The supramolecular block copolymers have been visualized by adapting a super-resolution microscopy technique, interface point accumulation for imaging in nanoscale topography, which exhibited the formation of block supramolecular structures in organic media (**Figure 4.2f**). Similar copolymerization methods have also been attempted for chiral and achiral molecules, where the kinetics of the copolymerization has been found to be slow along with a prominent chirality transfer from chiral to achiral derivative.

Sundaram, Agasti, Pavan, George and co-workers have shown that random, self-sorted, and block supramolecular copolymers can be achieved from two monomeric components by manipulating kinetic and thermodynamic pathways (**Figure 4.3a**).<sup>[22]</sup> For this purpose, cholesterol substituted NDI core functionalized with ethanethiol (NDI-1) and ethoxy (NDI-2) groups were designed and synthesized (**Figure 4.3b**). Spectroscopy studies have revealed that monomer NDI-1 and NDI-2 have distinct absorption (450-600 nm and 400-500 nm, respectively) and emission (570-750 nm and 450-570 nm, respectively) features, where a significant amount of spectral overlap between the emission spectrum of NDI-2 with the absorption spectrum of NDI-1 was noticed. Through proper utilization of various kinetic and thermodynamic self-assembly routes, an unprecedented control over the sequential arrangement of the monomers within the copolymer has been achieved, and their sequence have been characterized by comparing the spectroscopy features of the copolymer to that of the homopolymeric assembly. Detailed molecular dynamic simulations have further provided mechanistic insights into the strength of different

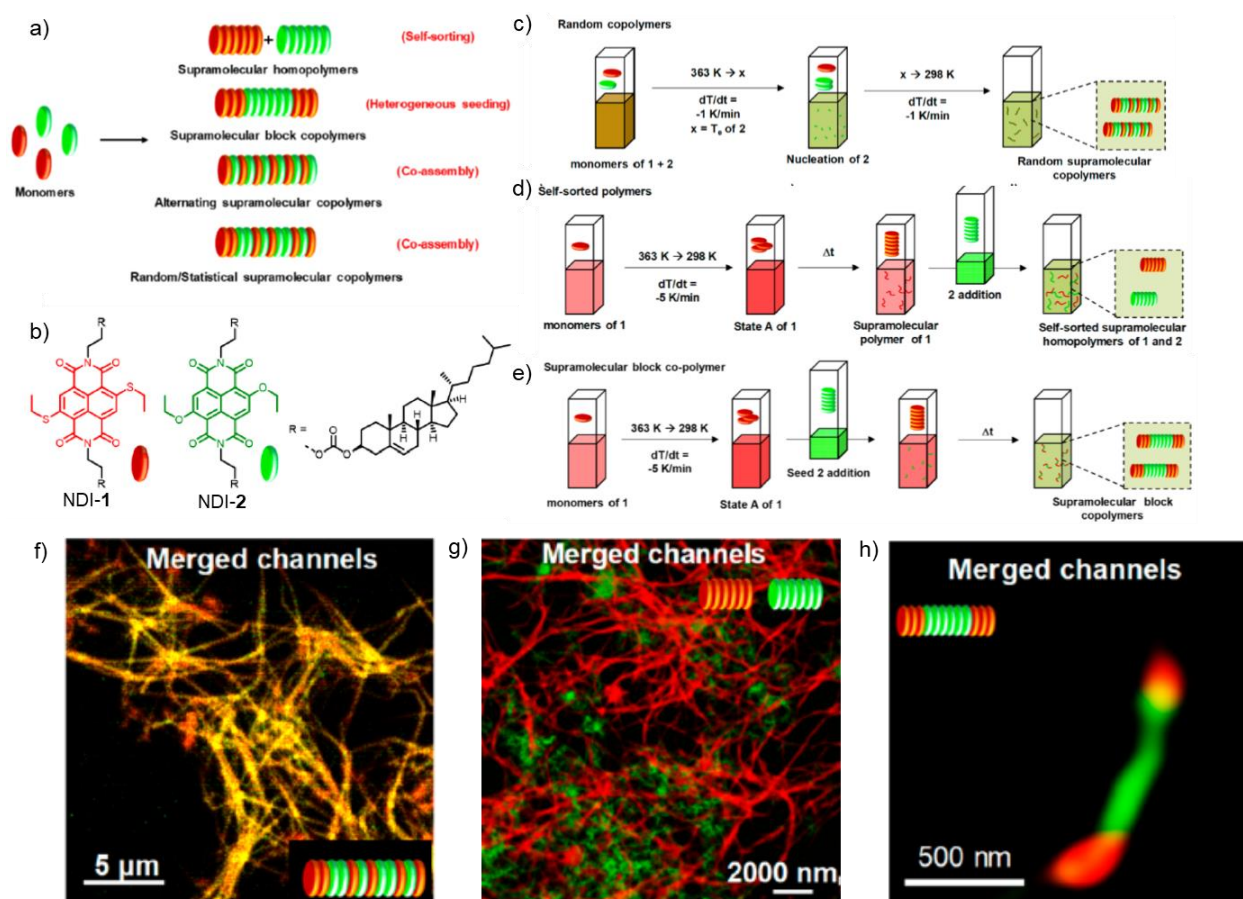


**Figure 4.3.** (a) Schematic representation demonstrating two-component supramolecular polymerization into narcissistically self-sorted supramolecular homo polymers, heterogeneously seeded supramolecular block copolymers and alternate or random/statistical supramolecular copolymers. (b) Molecular structures of NDI-1 and NDI-2 utilized for two-component supramolecular polymerization. Preparation protocols for the synthesis of (c) random supramolecular copolymer under thermodynamic control, (d) self-sorted homopolymers and (e) supramolecular block copolymers have been represented with the help of schematic representations. SIM images depicting the formation of (f) random, (g) spatially segregated (self-sorted) and (h) block supramolecular copolymers. (Adapted with permission from Ref 22).

intermonomeric interactions and the relative rate of the monomer exchange dynamics of these assemblies. Copolymerization of the monomers NDI-1 and NDI-2 following a thermodynamic approach, where both the monomers at higher temperature was together cooled at a controlled rate of 1 K/min resulted in the formation of random supramolecular

polymers (**Figure 4.3c**). On the other hand, self-sorted homopolymers of NDI-1 and NDI-2 was obtained by cooling monomers of NDI-1 at a cooling rate of 5 K/min followed by the subsequent addition of the aggregates of NDI-2 (**Figure 4.3d**). The block supramolecular copolymers with domains of NDI-1 and NDI-2 was created by heterogeneous seeded growth, where seed of NDI-2 was added to the aggregates of NDI-1 prepared by cooling at a rate of 5 K/min (**Figure 4.3e**). The spectroscopy results of the sequence controlled supramolecular copolymerization was further confirmed by structured illumination microscopy imaging of the resultant fibers for all the three distinct copolymeric assemblies (**Figure 4.3f-h**). Furthermore, cooperative supramolecular block copolymers obtained from the fluorescent core-substituted naphthalene diimide monomers have been utilized for the synthesis of functional axial organic heterostructures.<sup>[23]</sup>

From the aforementioned reports, it is obvious that monomers that form 1D homopolymers when copolymerized with a second monomer leads to a supramolecular copolymer with a marginal structural difference.<sup>[18]</sup> This aspect emphasizes the importance of the choice of monomers participating in supramolecular copolymerization for creating some of the rare and functional structures found in Nature. The supramolecular copolymerization of monomers forming 1D and 2D homopolymers could be a suitable approach with an extreme chance of achieving unusual supramolecular structures with emergent properties. To address this issue, we have selected a Y-shaped **BODIPY** (reported in Chapter 3), that forms 2D supramolecular sheets in *n*-decane (**Figure 4.4**) as one of the monomers for copolymerization studies. For the copolymer synthesis, we designed and synthesized a Y-shaped **PE**, as the second monomer (**Figure 4.4**). As



demonstrated in this chapter, the **PE** molecule forms 1D supramolecular polymers in an identical condition optimized for the self-assembly of **BODIPY**. This allowed us to copolymerize the Y-shaped **BODIPY** and the **PE** into a spindle-shaped supramolecular structure (**Figure 4.4**). The details of this interesting observation are discussed in this chapter.

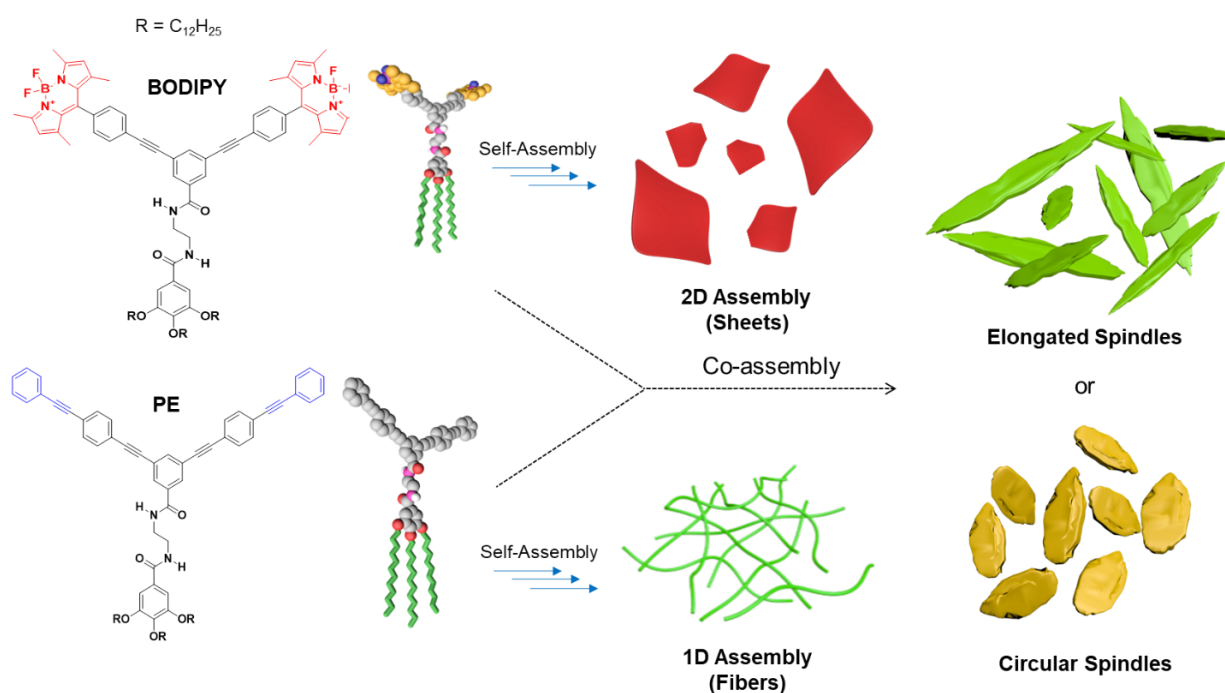


**Figure 4.4.** Schematic representation showing the molecular structures of the Y-shaped **BODIPY** and the **PE**-based monomers, forming 2D and 1D assembly, respectively and their copolymerization to form elongated or circular spindles.

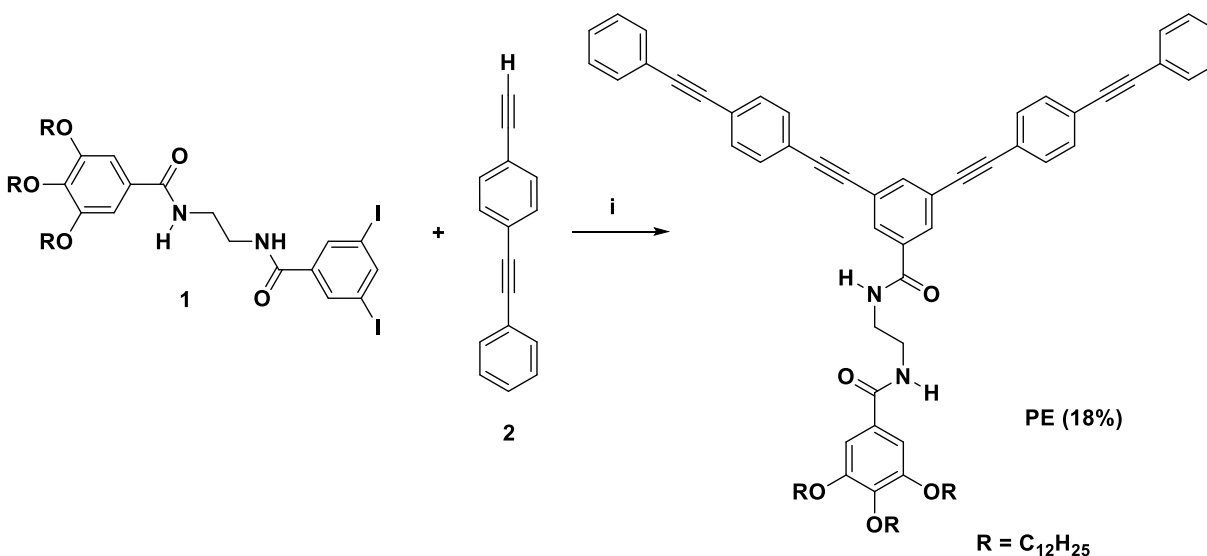
## 4.3. Results and Discussion

### 4.3.1. Synthesis of BODIPY and PE Derivatives

Synthesis of Y-shaped **BODIPY** has been reported in the section 3.5.3. to 3.5.10. of Chapter 3. A similar procedure was adopted for the synthesis of the Y-shaped **PE**, using



multistep palladium-catalyzed Sonogashira-Hagihara cross coupling reactions between *N*-(2-(3,5-diiodobenzamido)ethyl)-3,4,5-trialkoxybenzamide (**1**) and 1-ethynyl-4-(phenylethynyl)benzene (**2**), as mentioned in **Scheme 4.1**. Schemes, synthesis and characterization data related to the precursors (**1** and **2**) of **PE** are mentioned in Section 2.3.1., 2.5.7., 2.5.8. of Chapter 2 and in Section 3.3.1., 3.5.3.- 3.5.10. of Chapter 3. The final step was accomplished using Sonogashira-Hagihara cross coupling reaction between **1** and **2**, yielding the final compound **PE** with 18% yield (**Scheme 4.1**). The detailed procedure of synthesis and characterization data of **PE** are provided in the experimental section 4.5.3



**Scheme 4.1.** Synthesis of PE. Reagents and conditions: (i) PdCl<sub>2</sub>(PPh<sub>3</sub>)<sub>2</sub>, CuI, THF-Et<sub>3</sub>N (v:v 1:1), 70 °C, 20h.

#### 4.3.2. Structural Aspects of Y-Shaped BODIPY and PE

The Y-shaped **BODIPY** and **PE** selected for the present study have both structural similarities and differences, as depicted in **Figure 4.5**. Both molecules contain a diamide unit attached to a bulky solubilizing moiety. The similarities in the diamide linker and the

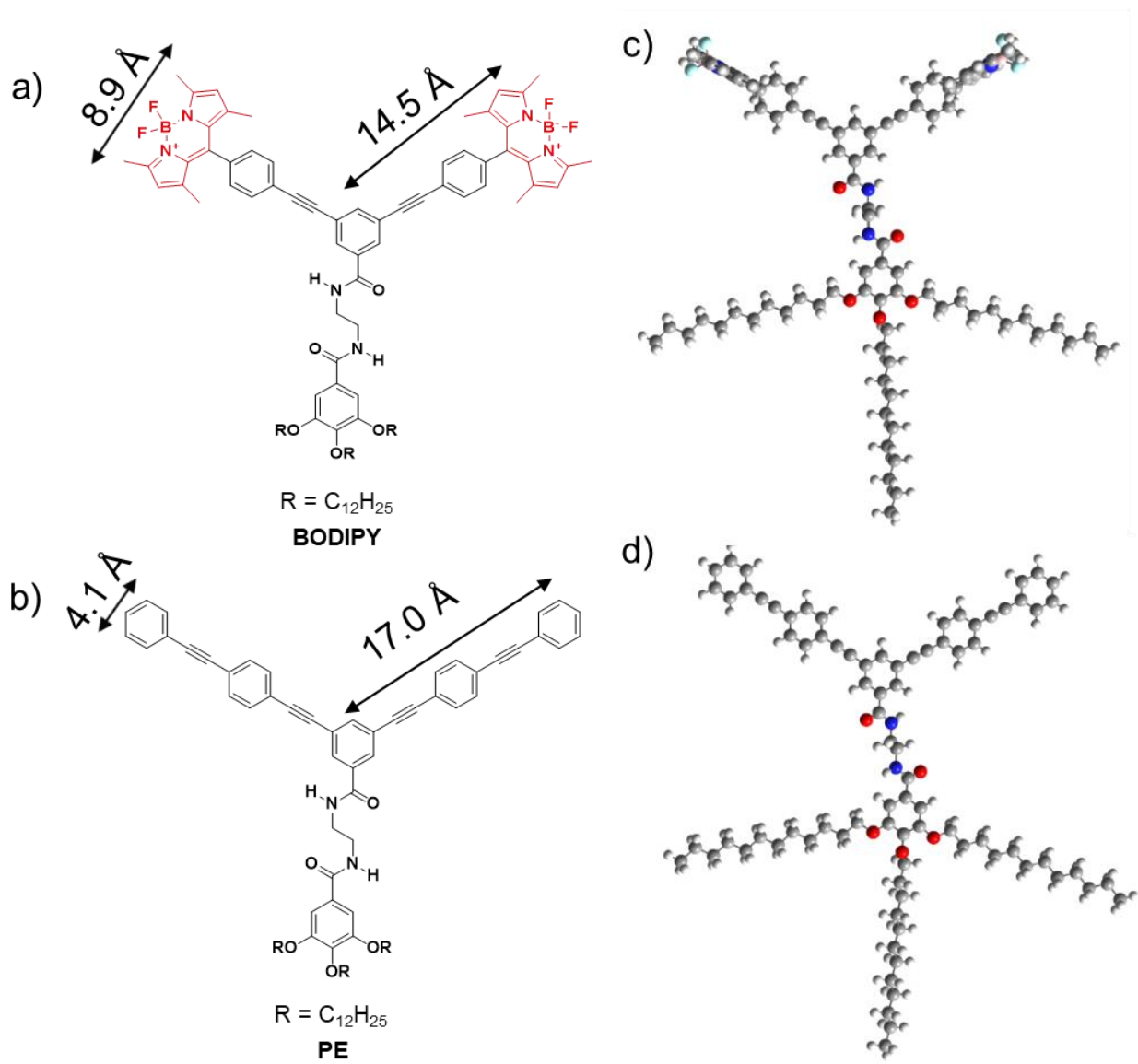


**Figure 4.5.** Molecular and energy minimized structures of the Y-shaped (a,c) **BODIPY** and (b,d) **PE**.

linear dodecyloxy chains are to facilitate an efficient H-bonding and van der Waals interaction between the monomers, respectively. However, from the energy minimized structure, it has been found that the length of the chromophoric arm is increased from 14.5 to 17.0 Å, and the width of the chromophore is reduced from 8.9 to 4.1 Å when ethynylbenzene moiety is replaced with the terminal Bodipy chromophoric units in the case

of the **PE** (Figure 4.5a,b). Moreover, it is clearly discernable from the energy minimized structure that the Bodipy chromophore in **BODIPY** remains perpendicular to the phenyl ring present in the *meso* position. In contrast, the terminal ethynylbenzene unit in **PE** are planar (Figure 4.5c,d). The **BODIPY** showed a high ground state dipole moment, ( $\mu_g = 7.53$  D) due to the presence of both electron-rich and deficient moieties, whereas the calculated ground state dipole moment,  $\mu_g$  of **PE** is 2.29 D.

### 4.3.3. Photophysical Properties and Self-Assembly

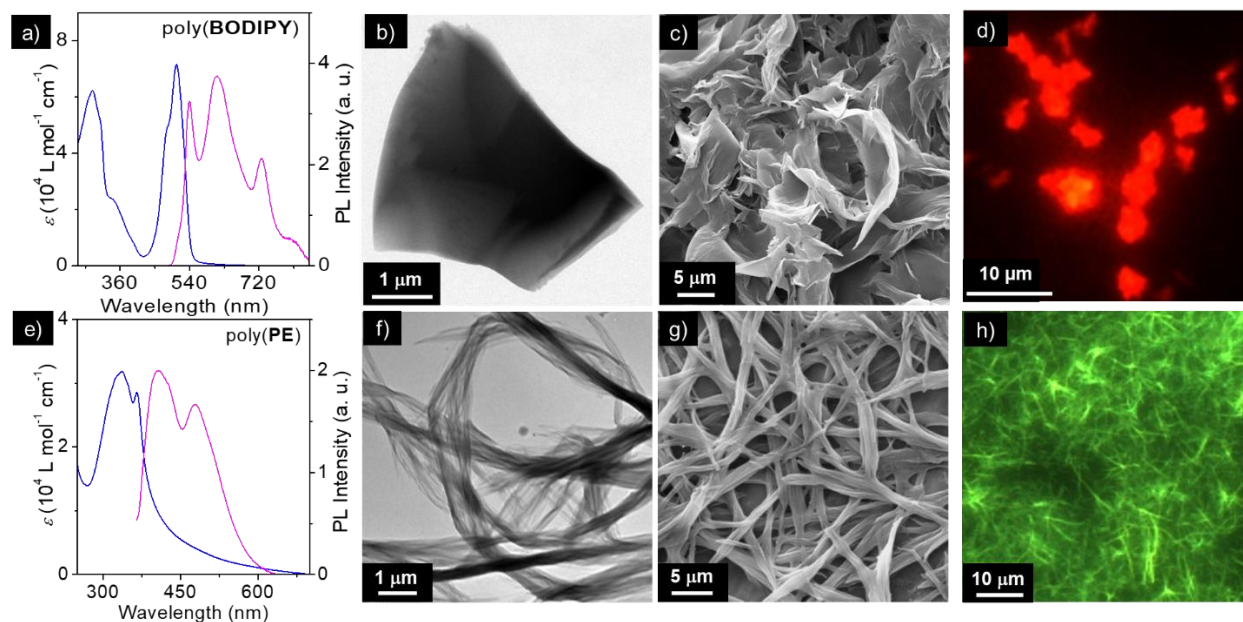


**Figure 4.6.** Absorption and emission spectra of (a) **BODIPY** ( $\lambda_{ex} = 475$  nm) and (e) **PE** ( $\lambda_{ex} = 380$  nm) in *n*-decane ( $3 \times 10^{-4}$  M). (b,f) TEM ( $3 \times 10^{-4}$  M), (c,g) SEM ( $1 \times 10^{-3}$  M) and (d,h) fluorescence microscopy ( $1 \times 10^{-3}$  M) images of the aggregates of (b-d) **BODIPY** and (f-h) **PE** in *n*-decane.

The aggregation behavior of **BODIPY** in *n*-decane at a concentration of  $3 \times 10^{-4}$  M are described in Section 3.3.2. of Chapter 3. The detailed photophysical studies describing the absorption and emission features of the **BODIPY** monomers and the aggregates are

reported in the same section. Details of the calculation for obtaining various thermodynamic parameters related to supramolecular polymerization of **BODIPY** in *n*-decane are previously mentioned in **Table 3.2.** and **Figure 3.9.** within Section **3.3.2.** of Chapter 3. The aggregates of **BODIPY** was then characterized using various microscopy techniques such as TEM, SEM and fluorescence microscopy, which are reported in Section **3.3.3.** of Chapter 3. In order to have a comparison between **BODIPY** and **PE**, the absorption and emission spectra of the monomers and aggregates of **BODIPY** along with the morphology of **BODIPY** aggregates obtained from various microscopy techniques are shown in **Figure 4.6a-d** and **4.7.**

The monomer **PE** was found to aggregate in *n*-decane at identical concentration ( $3 \times 10^{-4}$  M), when a similar polymerization method involving heating the solution to 363 K followed by controlled cooling at a rate of 1 K/min to 283 K. The UV-vis absorption spectrum of **PE** aggregates showed a strong  $\pi$ - $\pi^*$  absorption band with  $\lambda_{\max}$  at 336 nm ( $\epsilon = 3.2 \times 10^4 \text{ M}^{-1} \text{ cm}^{-1}$ ) along with a broad shoulder band noticed between 370-500 nm, indicating J-type aggregation of **PE** (**Figure 4.6e** and **4.8a**).<sup>[24]</sup> The self-assembly process in *n*-decane was further confirmed from variable temperature UV-vis absorption spectra, which exhibit a reversible transition between 363-283 K (**Figure 4.8c**). At 363 K, **PE** in *n*-decane displayed a sharp absorption band at 323 nm, whereas at 283 K, the  $\lambda_{\max}$  was red-shifted to 338 nm along with the formation of a new shoulder band at 365 nm (**Figure 4.8c**). In addition, the emission spectrum of **PE** aggregates was found to be broad with two distinct emission maxima at 442 and 528 nm, which is red-shifted with respect to the

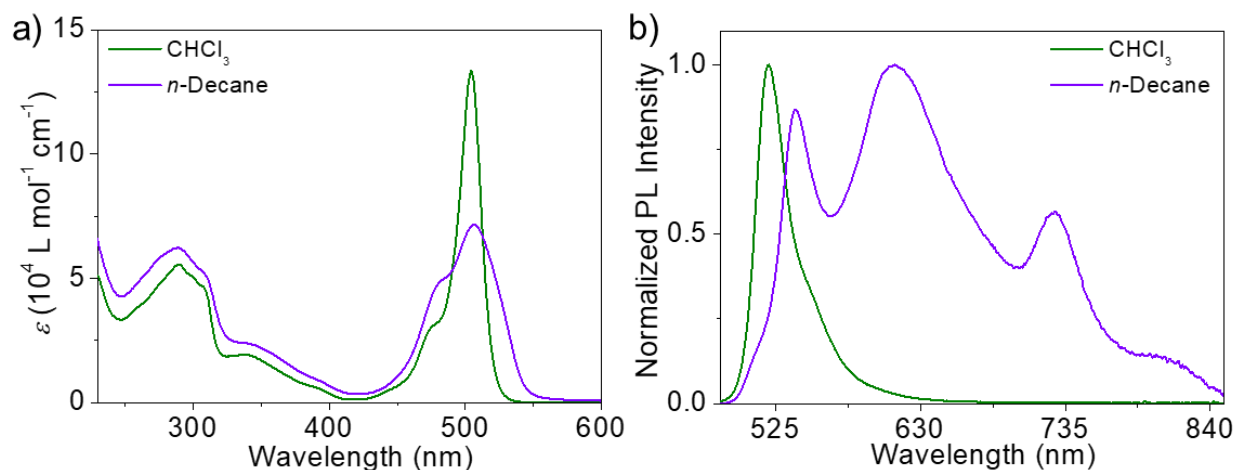


**Figure 4.7.** (a) Absorption and (b) normalized emission spectra of **BODIPY** in chloroform ( $1 \times 10^{-4}$  M,  $\lambda_{\text{ex}} = 340$  nm) and *n*-decane ( $3 \times 10^{-4}$  M,  $\lambda_{\text{ex}} = 475$  nm).

monomeric emission maximum obtained at 356 nm (**Figure 4.6e** and **4.8b**). Aggregation behavior of **PE** in *n*-decane was also confirmed from the temperature-dependent emission studies (**Figure 4.8d**). At 363 K, **PE** exhibited an emission maximum centered at 426 nm. Upon gradual reduction in temperature to 343 K, the intensity of the emission spectrum was increased with the appearance of a new peak at 520 nm. Further reduction in temperature to 283 K showed a gradual enhancement ( $\sim 3.3$  times) in the emission intensity with two distinct  $\lambda_{\text{em}}$  at 443 and 526 nm, indicating AIEE behavior of **PE**. To probe the self-assembly pathway of **PE** in *n*-decane, the changes in UV-vis absorption at 390 nm have been monitored for a wide range of concentrations starting from  $5 \times 10^{-5}$  to  $3 \times 10^{-4}$  M as a function of temperature (cooling rate 1 K/min, **Figure 4.9a** and **Table 4.1**), which followed an enthalpically driven nucleation-elongation supramolecular polymerization pathway.<sup>[25]</sup> The standard thermodynamic parameters  $\Delta H^\circ$  and  $\Delta S^\circ$  values estimated are

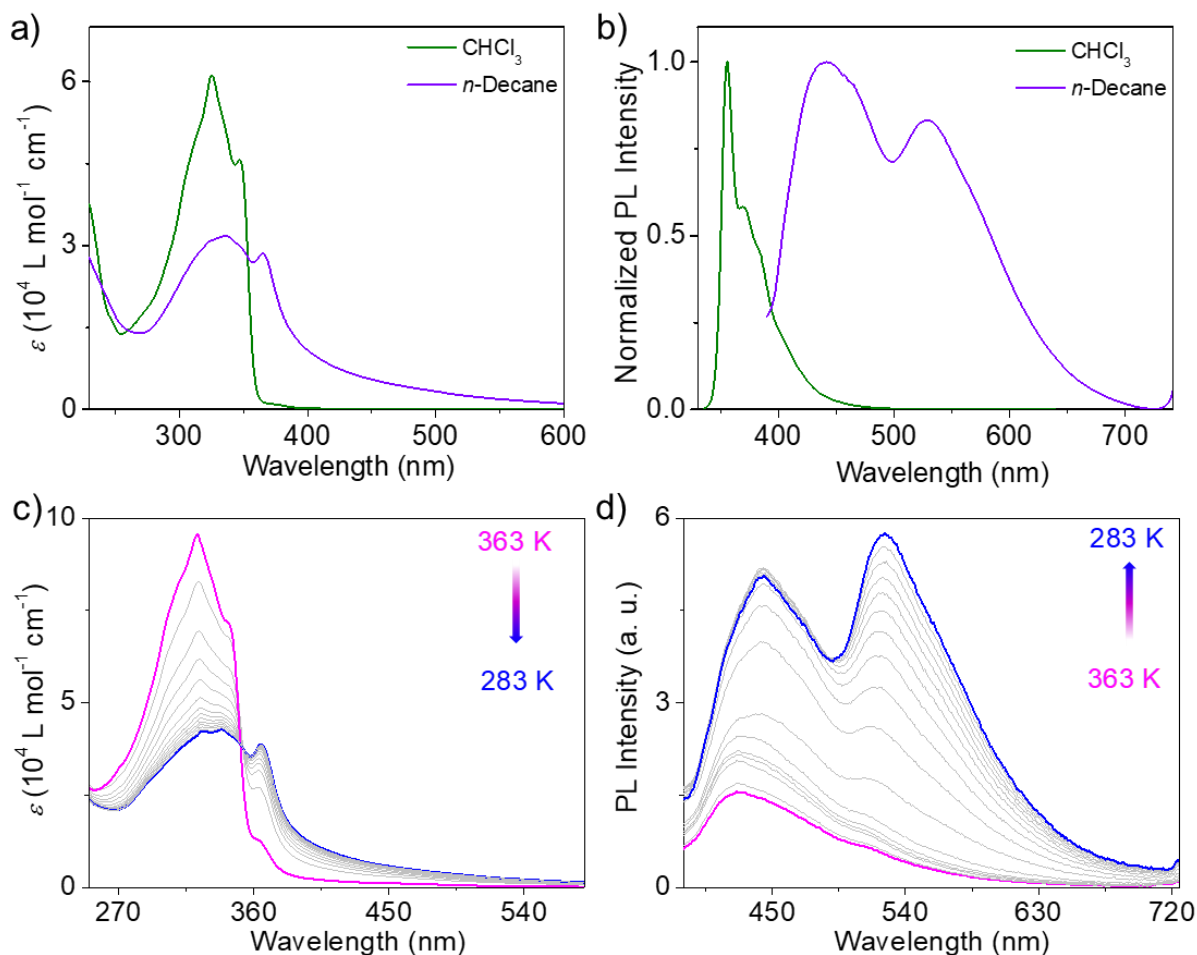


**Figure 4.8.** (a) Absorption and (b) normalized emission spectra of **PE** in chloroform ( $1 \times 10^{-4}$  M,  $\lambda_{\text{ex}} = 340$  nm) and *n*-decane ( $3 \times 10^{-4}$  M,  $\lambda_{\text{ex}} = 380$  nm). Temperature-dependent (c) absorption and (d) emission spectra of **PE** in *n*-decane ( $3 \times 10^{-4}$  M,  $\lambda_{\text{ex}} = 380$  nm).

$-79.11$  kJ/mol and  $-159.20$  J/mol K, respectively. With the help of these values,  $\Delta G^\circ$  was calculated as  $-31.67$  kJ/mol (**Figure 4.9b**). After having a detailed understanding over the self-assembly mechanism of **PE** in *n*-decane, we have investigated the morphological features of **PE**. In order to rule out the effect of substrate over the morphology of **PE** in *n*-decane, we have at first dropcast the aggregated solution ( $3 \times 10^{-4}$  M) over a carbon coated copper grid and imaged by TEM. Interestingly, TEM images showed the formation of

micrometer-sized 1D fibrillar morphology having width varying within the range from 500-800 nm (**Figure 4.6f**). The SEM analysis revealed the formation of micrometer long 1D fibers, having almost similar width as obtained from the TEM analysis (**Figure 4.6g**). Fluorescence microscopy image shown in **Figure 4.6h** indicate the formation of greenish-yellow emitting 1D fibers.

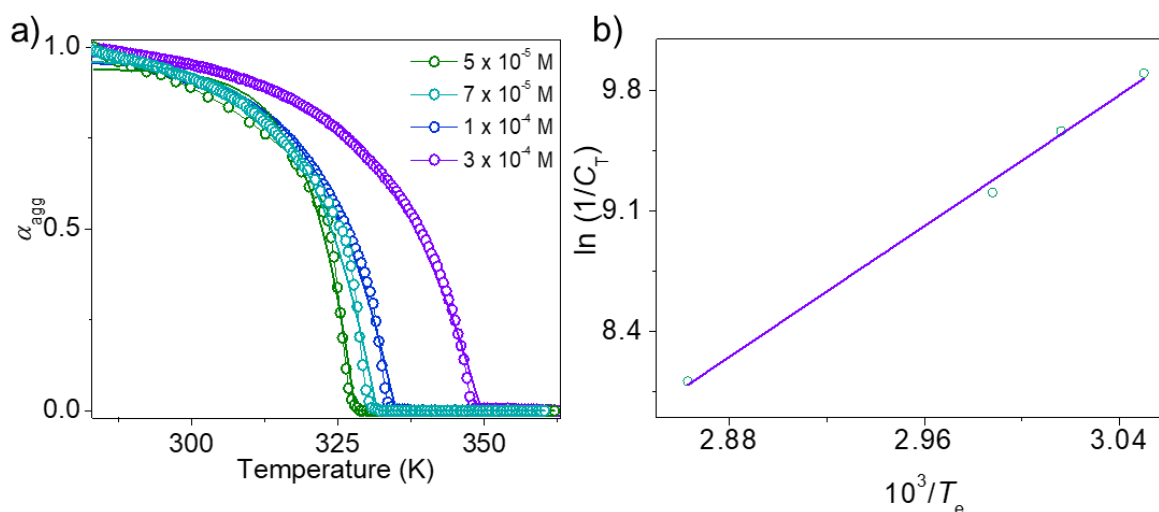


**Figure 4.9.** (a) The plot of  $\alpha_{agg}$  versus temperature at different concentrations of **PE** in *n*-decane;  $\alpha_{agg}$  has been calculated by monitoring changes in the absorbance at 390 nm. (b) van 't Hoff plot obtained through the controlled cooling experiments of **PE** in *n*-decane.

**Table 4.1.** Different thermodynamic parameters obtained by fitting temperature-dependent  $\alpha_{agg}$  of poly(**PE**) in *n*-decane (390 nm) to the equilibrium model.<sup>[25]</sup>

Conc. (M)	$\Delta H^\circ$ (kJmol <sup>-1</sup> )	$\Delta H^\circ$ (STD) (kJmol <sup>-1</sup> )	$\Delta S^\circ$ (kJmol <sup>-1</sup> K <sup>-1</sup> )	$\Delta S^\circ$ (STD) (kJmol <sup>-1</sup> K <sup>-1</sup> )	$\Delta H^\circ_{nucl}$ (kJmol <sup>-1</sup> )	$\Delta H^\circ_{nucl}$ (STD) (kJmol <sup>-1</sup> )	$T_e$ (K)	$T_e$ (STD)
$5 \times 10^{-5}$	-120.00	6.26	-0.283679	0.019315	-35.00	26.71	327.85	0.25
$7 \times 10^{-5}$	-84.57	2.68	-0.175524	0.008225	-35.00	19.82	331.55	0.26
$1 \times 10^{-4}$	-75.69	1.65	-0.149537	0.005044	-35.00	12.58	334.72	0.19
$3 \times 10^{-4}$	-62.93	1.10	-0.112753	0.003234	-35.00	8.21	349.24	0.21

$\Delta H^\circ$ : Enthalpy of elongation (kJ/mol);  $\Delta S^\circ$ : Entropy difference (kJ/mol K);  $\Delta H^\circ_{nucl}$ : Nucleation penalty (kJ/mol);  $T_e$ : Elongation temperature.

#### 4.3.4. Co-Assembly Studies of BODIPY and PE (1:1 ratio)

After confirming the supramolecular polymerization of **BODIPY** and **PE**-based monomers to poly(**BODIPY**) and poly(**PE**) at identical conditions to 2D-sheets and 1D-fibers,

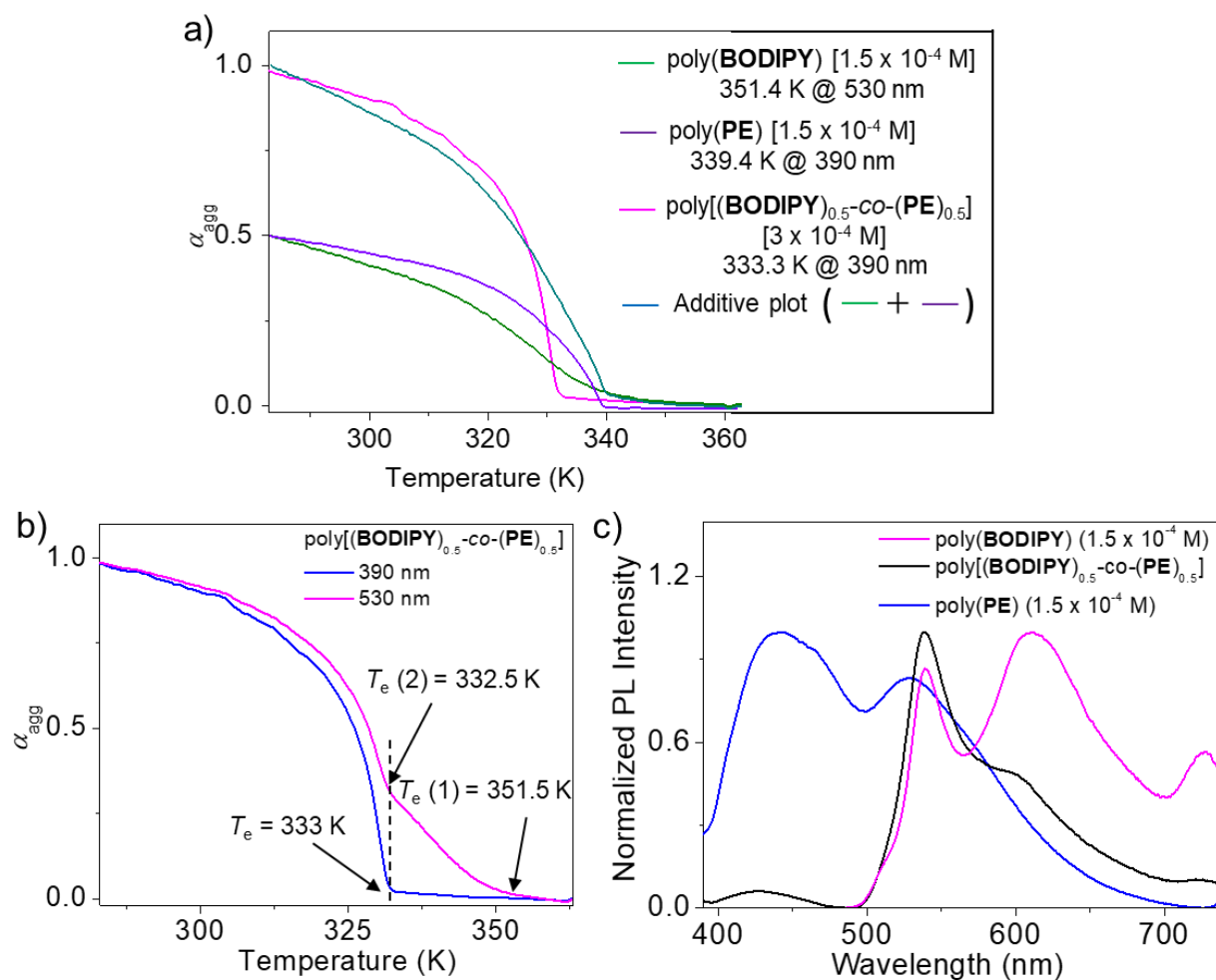


**Figure 4.10.** (a) Spectroscopy analysis (plot of  $\alpha_{agg}$  versus temperature) for the formation of supramolecular copolymer poly[(**BODIPY**)<sub>0.5</sub>-co-(**PE**)<sub>0.5</sub>] having 1:1 ratio of **BODIPY** and **PE**, achieved via a controlled rate of cooling (1 K/min) in *n*-decane. Cooling curves have been denoted as poly[(**BODIPY**)-co-(**PE**)] (magenta), poly(**BODIPY**) (green), poly(**PE**) (violet), and (poly(**PE**) + poly(**BODIPY**)) (light blue, assuming no interaction). (b) Plot of  $\alpha_{agg}$  versus temperature of poly[(**BODIPY**)<sub>0.5</sub>-co-(**PE**)<sub>0.5</sub>] in *n*-decane;  $\alpha_{agg}$  has been calculated by monitoring the changes in the absorbance at 390 (blue) and 530 nm. (c) Normalized emission spectra ( $\lambda_{ex} = 380$  nm) of poly[(**BODIPY**)<sub>0.5</sub>-co-(**PE**)<sub>0.5</sub>] in *n*-decane in comparison to the homopolymers, poly(**BODIPY**) and poly(**PE**).



Respectively, we attempted copolymerization of **BODIPY** and **PE**-based monomers in a 1:1 molar ratio (**Figure 4.10**). For this purpose, we have fixed the total concentration of the assembly as  $3 \times 10^{-4}$  M, where the individual concentration of **BODIPY** and **PE** is  $1.5 \times 10^{-4}$  M to have an identical mole fraction. For copolymerization, both the molecules were dissolved together as monomers at higher temperature (363 K) followed by cooling to 283 K by maintaining a controlled rate of cooling (1 K/min). In order to clearly differentiate copolymers based on their composition, they have been termed as poly[(**BODIPY**)<sub>x</sub>-co-(**PE**)<sub>(1-x)</sub>] in the present work; where x corresponds to the mole fractions of **BODIPY**-monomers present within the copolymer. **Figure 4.10a** shows the variation in  $\alpha_{\text{agg}}$  as a function of temperature, where we have separately monitored the cooling curves for **BODIPY** and **PE** at their individual concentrations and compared them with the cooling curve of the **BODIPY-PE** mixture. From the cooling curve of **BODIPY-PE** mixture (magenta line) monitored at 390 nm, a single  $T_e$  was obtained at 333.3 K (**Figure 4.10a**). Furthermore, the nature of this cooling curve was found to be entirely different from the independent cooling curves of poly(**BODIPY**) (green line,  $T_e = 351.4$  K) and poly(**PE**) (violet line,  $T_e = 339.4$  K) as estimated from the linear sum of the individual cooling curves (light blue line); which supports the formation of poly[(**BODIPY**)<sub>0.5</sub>-co-(**PE**)<sub>0.5</sub>].<sup>[21]</sup>

Monitoring the cooling curve for the copolymer at 390 nm indicated the involvement of **PE** molecules during aggregation, whereas to know the role of **BODIPY** molecules in the polymerization process we monitored the cooling curve at 530 nm (rate 1 K/min) corresponding to the **BODIPY** aggregation band (magenta line, **Figure 4.10b**). The cooling curve thus obtained clearly showed an initial nucleation at 351.5 K ( $T_e(1)$ ) almost

matching with the  $T_e$  of poly(BODIPY) at a concentration of  $1.5 \times 10^{-4}$  M. Another distinct change in the cooling curve has been observed at 332.5 K ( $T_e(2)$ ) from where a fast elongation was noticed. It is interesting to mention that  $T_e(2)$  almost matched with the  $T_e$  (333.3 K) obtained while monitoring the aggregation behavior at 390 nm (blue line, **Figure 4.10b**). Below this temperature, both cooling curves remained almost identical. These results imply that the formation of the initial assembly is mainly driven by nucleation-elongation of BODIPY, followed by the secondary nucleation of PE monomers.<sup>[26]</sup> Furthermore, the emission spectrum of poly[(BODIPY)<sub>0.5-co</sub>-(PE)<sub>0.5</sub>] exhibited multiple emission maxima at 427, 539 and 601 nm, whereas the peak at 725 nm was not clearly discernible (**Figure 4.10c**). Disappearance of the NIR emission peak for poly[(BODIPY)<sub>0.5-co</sub>-(PE)<sub>0.5</sub>] when compared to that of poly(BODIPY) corroborates to the fact that the homo-energy transfer process taking place within BODIPY has been restricted upto an extent of 600 nm.

TEM image of poly[(BODIPY)<sub>0.5-co</sub>-(PE)<sub>0.5</sub>] exhibited the formation of unusual morphological features having a wide portion in the middle and two sharp ends (tapers) at both the extremes, which are analogous to spindle (fusiform) shaped structures (**Figure 4.11a-e**). However, in our case, these spindle structures were found to be interconnected as seen from TEM and its magnified image (**Figure 4.11a,b**). The length and width of the spindles were found within the range of 1-1.5  $\mu\text{m}$  and 0.2-0.5  $\mu\text{m}$ , respectively and hence having an aspect ratio within 4-5. The spindle structures can be clearly visible from the SEM image (**Figure 4.11c,d**). Magnified SEM images have indicated the length and width

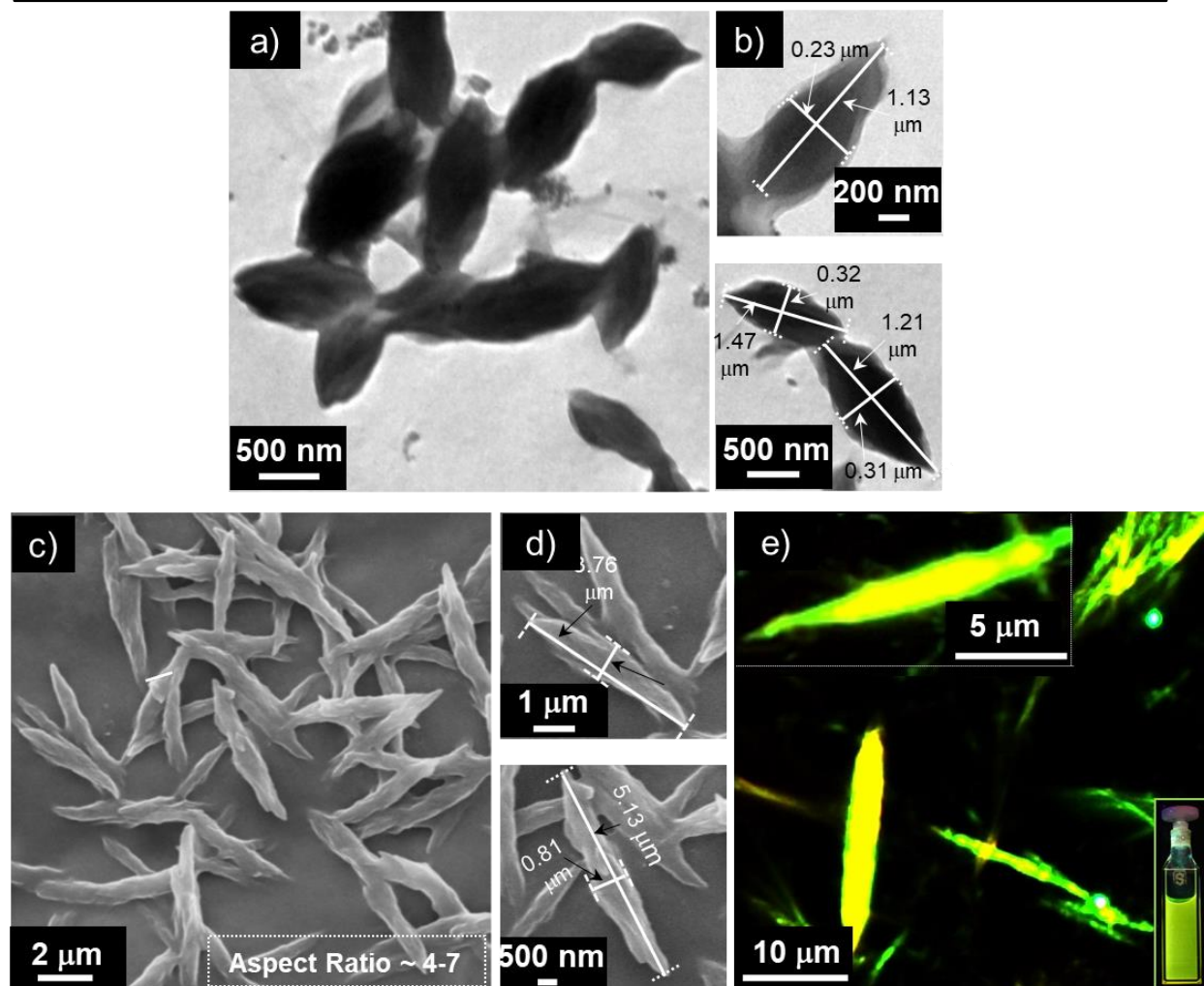


**Figure 4.11.** (a) TEM ( $3 \times 10^{-4}$  M), (c) SEM ( $1 \times 10^{-3}$  M) and (e) fluorescence microscopy ( $1 \times 10^{-3}$  M) images of poly[(BODIPY) $_{0.5}$ -co-(PE) $_{0.5}$ ]s in *n*-decane. Magnified (b) TEM and (d) SEM images of poly[(BODIPY) $_{0.5}$ -co-(PE) $_{0.5}$ ]. Inset in **Figure 4.11e** shows the photograph of poly[(BODIPY) $_{0.5}$ -co-(PE) $_{0.5}$ ] in *n*-decane under illumination of 365 nm UV light.

of these structures within 3-5  $\mu\text{m}$  and 0.6-0.8  $\mu\text{m}$  regime, respectively with an aspect ratio of 4-6 (**Figure 4.11d**). Though a minute difference in the length and width of the spindle structures has been noticed upon comparing the TEM and SEM studies, their aspect ratio is comparable. Formation of yellowish-green emitting spindle structures for poly[(BODIPY) $_{0.5}$ -co-(PE) $_{0.5}$ ] has been further confirmed from the fluorescence

microscopy image (**Figure 4.11e**), which matches with the emission color of the copolymer in *n*-decane (**Figure 4.11e**, inset).

#### 4.3.5. Importance of BODIPY Monomers in Co-Polymerization

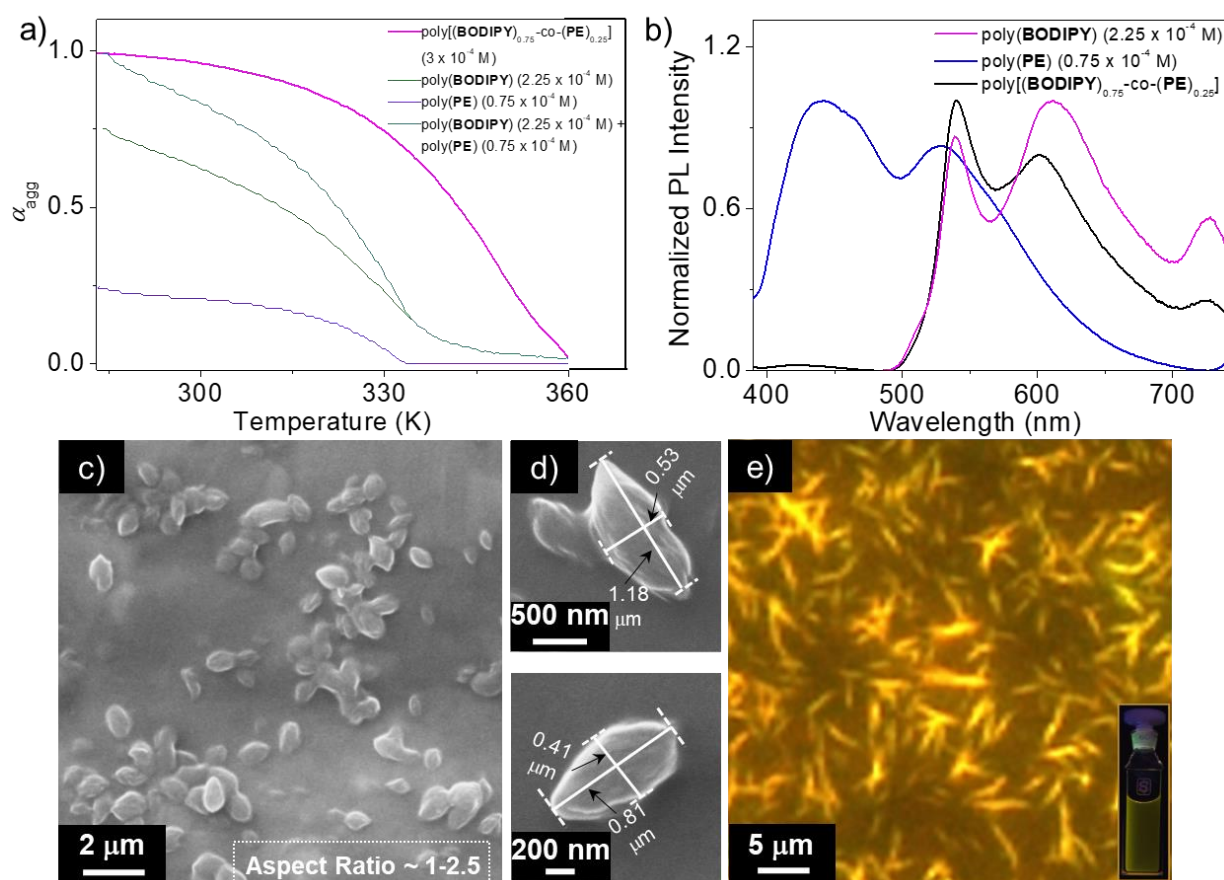


**Figure 4.12.** (a) Plot of  $\alpha_{agg}$  versus temperature for the formation of supramolecular copolymer poly[(BODIPY)<sub>0.75</sub>-CO-(PE)<sub>0.25</sub>] having 3:1 ratio of BODIPY and PE, achieved via a controlled rate of cooling (1 K/min) in *n*-decane. Cooling curves have been denoted as poly[(BODIPY)-co-(PE)] (magenta), poly(BODIPY) (green), poly(PE) (violet), and (poly(PE) + poly(BODIPY)) (light blue, assuming no interaction). (b) Normalized emission spectra ( $\lambda_{ex} = 380$  nm) of poly[(BODIPY)<sub>0.75</sub>-CO-(PE)<sub>0.25</sub>] ( $3 \times 10^{-4}$  M) in *n*-decane (black line) in comparison to the homopolymeric assemblies of poly(BODIPY) ( $2.25 \times 10^{-4}$  M) (magenta line) and poly(PE) (blue line) ( $0.75 \times 10^{-4}$  M). (c) SEM ( $1 \times 10^{-3}$  M) and (e) fluorescence microscopy ( $1 \times 10^{-3}$  M) images of poly[(BODIPY)<sub>0.75</sub>-CO-(PE)<sub>0.25</sub>] in *n*-decane. (d) Magnified SEM images of poly[(BODIPY)<sub>0.75</sub>-CO-(PE)<sub>0.25</sub>]. Inset in **Figure 4.12e** shows the photographs of poly[(BODIPY)<sub>0.75</sub>-CO-(PE)<sub>0.25</sub>] in *n*-decane under illumination of 365 nm UV light.

To understand the role of **BODIPY** molecules in the initial nucleation process and in the formation of unusual spindle shape structure, we have conducted copolymerization of **BODIPY** and **PE** monomers under different compositions. A 3:1 mixture of **BODIPY** and **PE** indicates their individual concentration as  $2.25 \times 10^{-4}$  and  $0.75 \times 10^{-4}$  M when the total concentration has been fixed to  $3 \times 10^{-4}$  M. In this case, we have found out that the cooling curve exhibited a single  $T_e$  (355.2 K) with significant difference from the linear sum of the individual cooling curves of **BODIPY** and **PE** at their respective concentrations, which supports formation of the copolymer poly[(**BODIPY**)<sub>0.75-*CO*</sub>-(**PE**)<sub>0.25</sub>] at this composition (**Figure 4.12a**).<sup>[21]</sup> Furthermore, from the thermal effect on the aggregation behavior, we have noticed that  $T_e$  for poly(**BODIPY**) ( $2.25 \times 10^{-4}$  M) and poly(**PE**) ( $0.75 \times 10^{-4}$  M) was obtained at 354.4 and 333.1 K, respectively. The coincidence of  $T_e$  (355.2 K) for poly[(**BODIPY**)<sub>0.75-*CO*</sub>-(**PE**)<sub>0.25</sub>] to that of poly(**BODIPY**) indicates that the initial nucleation event of the copolymer involves **BODIPY** monomers<sup>[21]</sup> and then elongates by copolymerizing with **PE** monomers. **Figure 4.12b** shows the emission profile of poly[(**BODIPY**)<sub>0.75-*CO*</sub>-(**PE**)<sub>0.25</sub>] exhibiting multiple emission maxima at 539, 610 and 725 nm. The appearance of NIR emission peak in the case of poly[(**BODIPY**)<sub>0.75-*CO*</sub>-(**PE**)<sub>0.25</sub>] indicates a possible long-range energy migration in comparison to that of poly[(**BODIPY**)<sub>0.5-*CO*</sub>-(**PE**)<sub>0.5</sub>] (**Figure 4.12b** and **4.10c**). SEM images of poly[(**BODIPY**)<sub>0.75-*CO*</sub>-(**PE**)<sub>0.25</sub>] showed the formation of circular-shaped spindles having length around 0.8-1.5  $\mu\text{m}$  and width ranging from 0.25-0.6  $\mu\text{m}$ , where the aspect ratio of the copolymer can be controlled within the range of 1-2.5 (**Figure 4.12c,d**). Fluorescence

microscopy images have also confirmed the formation of orange-red emitting circular spindles with reduced length (**Figure 4.12e**).

#### 4.3.6. Importance of PE Monomers in Co-Polymerization

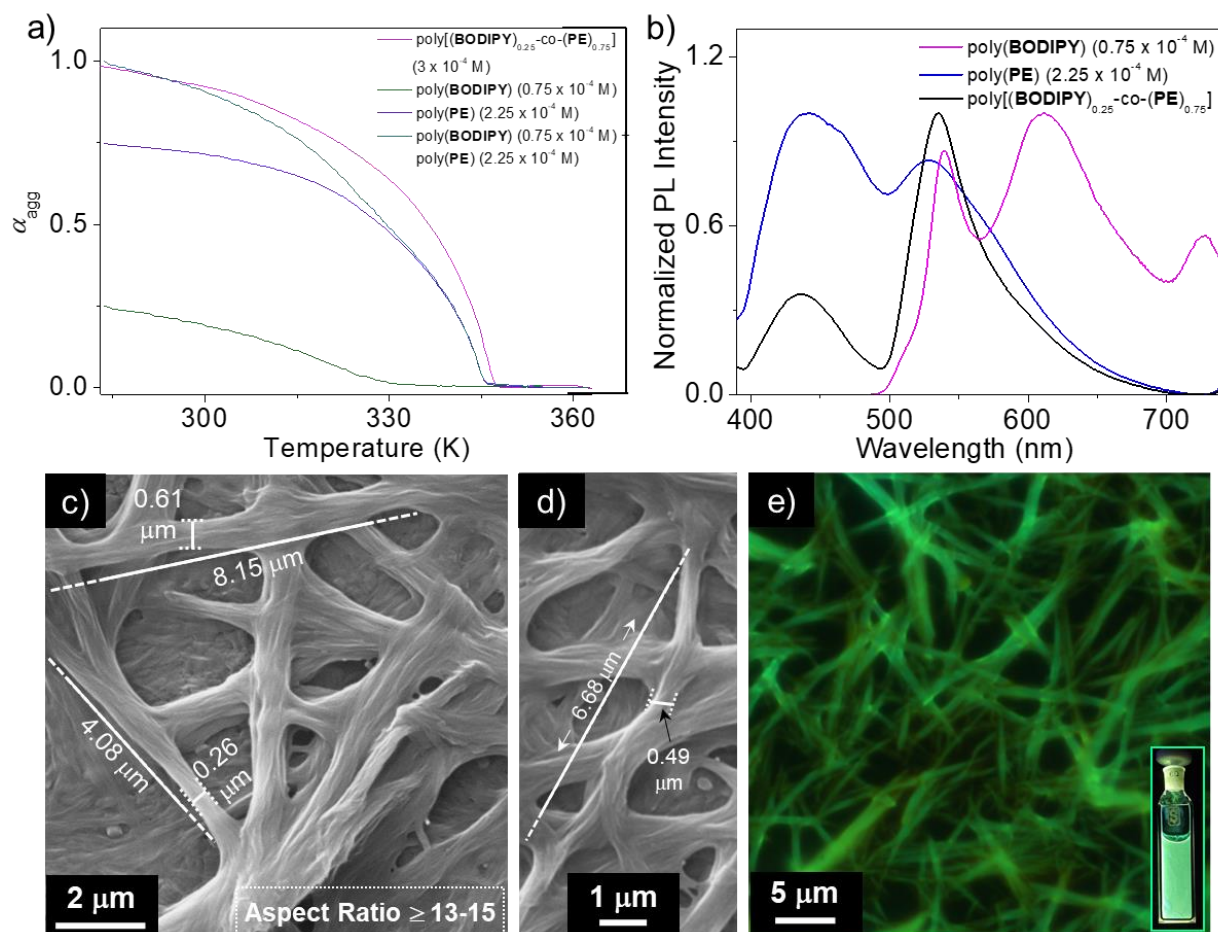


**Figure 4.13.** (a) Plot of  $\alpha_{agg}$  versus temperature for the formation of supramolecular copolymer poly[(BODIPY)<sub>0.25</sub>-co-(PE)<sub>0.75</sub>] having 1:3 ratio of BODIPY and PE, achieved via a controlled rate of cooling (1 K/min) in *n*-decane. Cooling curves have been denoted as poly[(BODIPY)-co-(PE)] (magenta), poly(BODIPY) (green), poly(PE) (violet), and (poly(PE) + poly(BODIPY)) (light blue, assuming no interaction). (b) Normalized emission spectra ( $\lambda_{ex} = 380$  nm) of poly[(BODIPY)<sub>0.25</sub>-co-(PE)<sub>0.75</sub>] ( $3 \times 10^{-4}$  M) in *n*-decane (black line) in comparison to the homopolymeric assemblies of poly(BODIPY) ( $0.75 \times 10^{-4}$  M) (magenta line) and poly(PE) (blue line) ( $2.25 \times 10^{-4}$  M). (c) SEM ( $1 \times 10^{-3}$  M) and (e) fluorescence microscopy ( $1 \times 10^{-3}$  M) images of poly[(BODIPY)<sub>0.25</sub>-co-(PE)<sub>0.75</sub>] in *n*-decane. (d) Magnified SEM images of poly[(BODIPY)<sub>0.25</sub>-co-(PE)<sub>0.75</sub>]. Inset in **Figure 4.13e** shows the photographs of poly[(BODIPY)<sub>0.25</sub>-co-(PE)<sub>0.75</sub>] in *n*-decane under illumination of 365 nm UV light.

To further demonstrate the role of **PE** molecules in controlling the aspect ratio, especially the length of the supramolecular copolymer, we studied the copolymerization of a 1:3 mixture of **BODIPY** and **PE**. Cooling curves obtained from the temperature-dependent absorption studies for the mixture assembly was then compared with the individual composition of **BODIPY** ( $0.75 \times 10^{-4}$  M) and **PE** ( $2.25 \times 10^{-4}$  M) (**Figure 4.13a**). Formation of the copolymer poly[(**BODIPY**)<sub>0.25</sub>-co-(**PE**)<sub>0.75</sub>] was confirmed from a single  $T_e$  (348.5 K) and also from the two emission maxima observed at 437 and 535 nm corresponding to aggregated **PE** and monomeric **BODIPY**, respectively (**Figure 4.13b**). Furthermore,  $T_e$  for poly[(**BODIPY**)<sub>0.25</sub>-co-(**PE**)<sub>0.75</sub>] was found to coincide with  $T_e$  (346.1 K) for poly(**PE**) ( $2.25 \times 10^{-4}$  M) and also remained almost unaltered irrespective of monitoring the cooling curve at **BODIPY** (530 nm) or **PE** (390 nm) aggregation band, which indicate the initial nucleation process taking place through **PE** (**Figure 4.14**). To our

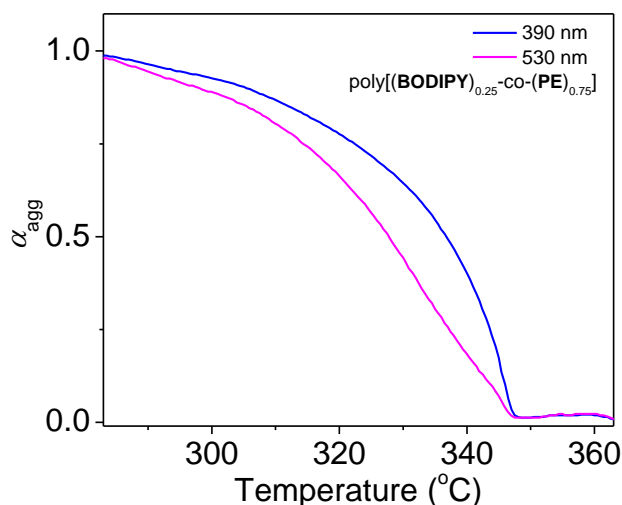


**Figure 4.14.** Plot of  $\alpha_{agg}$  versus temperature of poly[(**BODIPY**)<sub>0.25</sub>-co-(**PE**)<sub>0.75</sub>] in *n*-decane;  $\alpha_{agg}$  has been calculated by monitoring the changes in the absorbance at 390 (blue) and 530 nm (magenta).



surprise, poly[(**BODIPY**)<sub>0.25-co</sub>-(**PE**)<sub>0.75</sub>] formed green-emitting micrometer long 1D fibers (aspect ratio greater than 13-15) as confirmed by SEM and fluorescence microscopy studies (**Figure 4.13c-e**), indicating that the nucleation process originating with the help of 1D assembly forming monomers is unable to control the aspect ratio of the supramolecular copolymer, analogous to that of poly(**PE**).

#### 4.3.7. Excitation Energy Migration in Poly(**PE**)

Although the choice of selecting **BODIPY** and **PE**-based monomers in forming the copolymer was mainly decided based on their morphological features and identical self-assembling behavior, their photophysical properties especially the absorption and emission

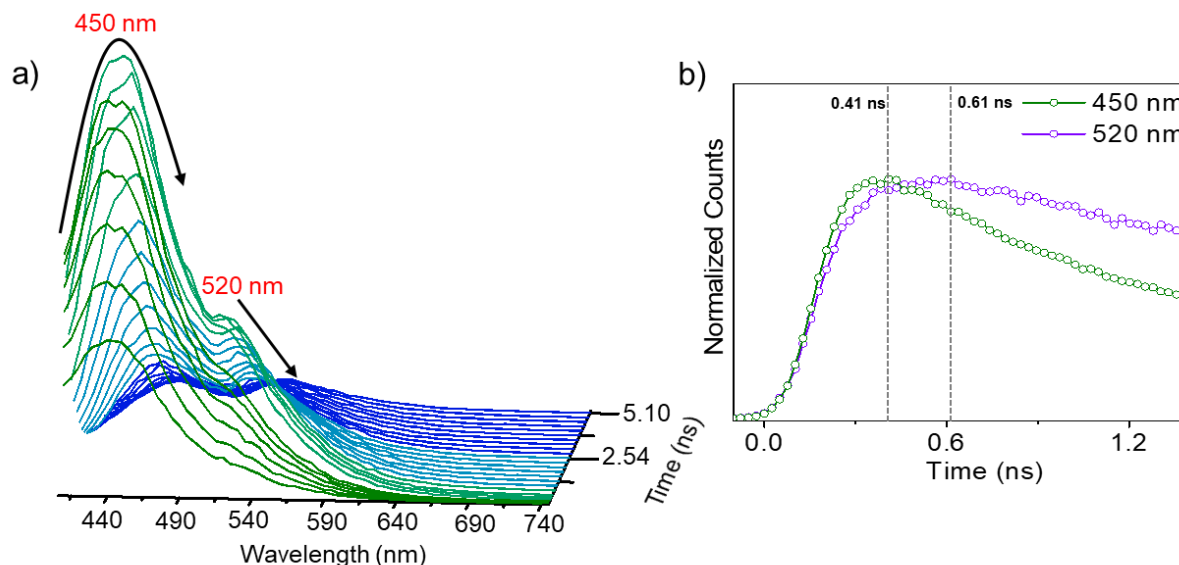


**Figure 4.15.** (a) TRES of poly(**PE**) in *n*-decane. (b) The normalized fluorescence decay curves for poly(**PE**) in *n*-decane; monitored at different emission wavelengths ( $3 \times 10^{-4}$  M,  $\lambda_{\text{ex}} = 375$  nm).

features have provided an additional opportunity to understand the controlled excitation energy migration property within the copolymer assemblies. Poly(**PE**) exhibited two



emission maxima at 442 and 528 nm ( $\lambda_{\text{ex}} = 380$  nm) in *n*-decane, which overlaps with the absorption maximum of poly(BODIPY) at 506 nm and hence an excitation energy transfer from PE donors to BODIPY acceptors is highly probable. The origin of two peaks in the case of poly(PE) was confirmed from the TRES studies (Figure 4.15). Upon excitation at 375 nm, the emission spectra of poly(PE) showed an initial growth profile at 450 nm within 10-264 ps (Figure 4.15a). With further increase in timescale from 391 ps to 2.57 ns, the intensity of 450 nm emission peak gradually decreased accompanying with a red shift in the emission peak to 520 nm. The peak at 520 nm initially showed a gradual growth in the emission intensity within 264 to 519 ps followed by a consecutive time-dependent decay. The time-dependent decay of the emission at 450 nm followed by the growth at 520 nm with dynamic red-shift of the emission can be considered as the characteristic of homo-energy migration.<sup>[27]</sup> Figure 4.15b reveals that the peak intensity at 450 nm reached maximum within 0.41 ns and then underwent rapid tri-exponential decay with time constants of 0.77 ns (28.37%), 1.98 ns (60.29%) and 4.65 ns (11.34%). On the other hand, the 520 nm emission peak is found to reach the maximum at 0.61 ns with a negative pre-exponential and the fitted rise time value of 0.32 ns. The rise time value at 520 nm correlates with the 0.11 ns decay component observed at 450 nm, that corroborates the homo energy transfer process. Previously, we have also reported a cascade homo energy transfer process taking place from 555 → 600 → 650 → 725 nm in the case of poly(BODIPY) in *n*-decane in Section 3.3.5. of Chapter 3.

### 4.3.8. Control over the Extent of Energy Migration in Co-Assembly

To understand the gradual disappearance of long wavelength emission peaks in the red (600 nm) and NIR region (725 nm) for poly[(BODIPY)<sub>0.25</sub>-CO-(PE)<sub>0.75</sub>] and poly[(BODIPY)<sub>0.5</sub>-CO-(PE)<sub>0.5</sub>], respectively, TRES studies were carried out for various BODIPY-PE copolymeric assemblies (Figure 4.16-4.18). Upon exciting poly[(BODIPY)<sub>0.75</sub>-CO-(PE)<sub>0.25</sub>] at 375 nm, emission of PE at 425 nm (donors) showed an

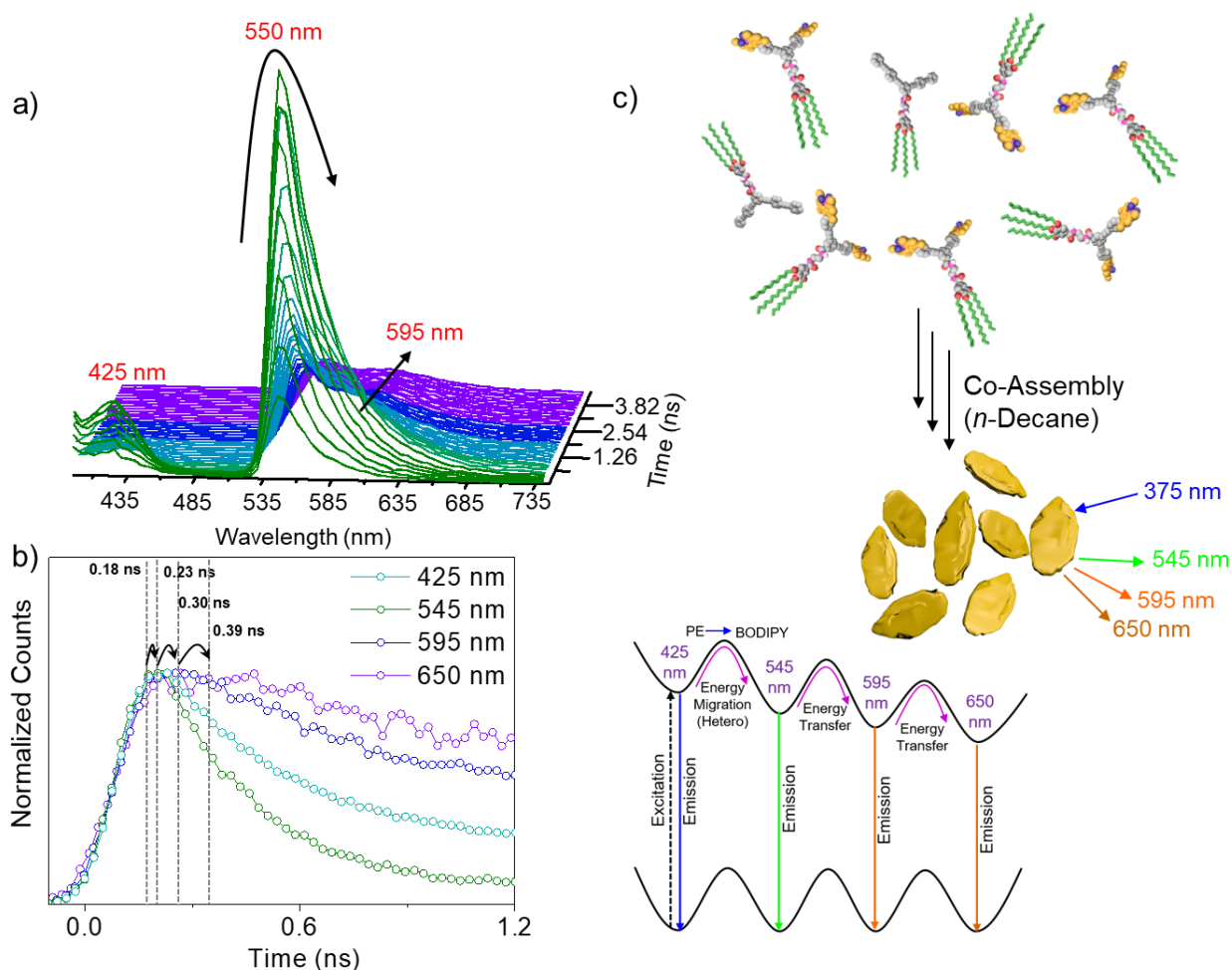


**Figure 4.16.** (a) TRES of poly[(BODIPY)<sub>0.75</sub>-CO-(PE)<sub>0.25</sub>] in *n*-decane. (b) The normalized fluorescence decay curves for poly[(BODIPY)<sub>0.75</sub>-CO-(PE)<sub>0.25</sub>] in *n*-decane; monitored at different emission wavelengths (3 × 10<sup>-4</sup> M, λ<sub>ex</sub> = 375 nm). (c) Schematic of the co-assembly of BODIPY and PE having 3:1 composition and the corresponding exciton deactivation within poly[(BODIPY)<sub>0.75</sub>-CO-(PE)<sub>0.25</sub>].

initial growth from 0 to 180 ps, which was completely diminished within 640 ps (**Figure 4.16a**). In addition, the emission profile at 550 nm was initially increased within 0-180 ps followed by a subsequent decrease in the intensity upto 2.56 ns along with the appearance of a new red-shifted peak at 595 nm at 1.79 ns. The 595 nm peak was then gradually decayed, showing a perfect correlation between 550 and 595 nm peaks. TRES studies demonstrate the probable energy transfer process from **PE** to **BODIPY** and subsequent homo energy transfer within poly[(**BODIPY**)<sub>0.75</sub>-CO-(**PE**)<sub>0.25</sub>]. **Figure 4.16b** shows the plot between the normalized emission counts of different emission peaks and the time scale for successive energy transfer process. The peak intensity of donor **PE** at 425 nm reached maximum within 0.18 ns followed by a decay, whereas the first peak of the acceptor **BODIPY** at 545 nm reached its maximum within 0.23 ns. Interestingly, the rise time value of 0.43 ns obtained for 545 nm was found to have a correlation with the decay component of 0.34 ns noticed in the case of 425 nm. Similarly, the 595 and 650 nm peak reached the maximum value of normalized emission counts within 0.30 and 0.39 ns, respectively followed by their decay. The negative pre-exponential factors obtained for 595 and 650 nm emission decay profiles confirm a step-wise energy transfer happening from 425 to 545 nm, 545 to 595 nm and probably a very weak energy transfer between 595 to 650 nm (**Figure 4.16c**).<sup>[27b,c,28]</sup>

TRES studies over poly[(**BODIPY**)<sub>0.5</sub>-CO-(**PE**)<sub>0.5</sub>] also showed similar enhancement in the emission intensity at 425 nm for the **PE** donors at the initial timescale of 0-180 ps, which gradually decayed upto 2.56 ns (**Figure 4.17a**). Moreover, a new red-shifted emission peak at 545 nm for **BODIPY** acceptor was found to gradually increase upto 257

ps followed by a successive decay until 3.2 ns. From the normalized counts versus timescale of energy transfer plot, it has been found that the decay profiles at 425, 545 and 595 nm emission reaches maximum within 0.25, 0.28 and 0.34 ns, respectively and then undergoes a consecutive/successive decay (**Figure 4.17b**). Furthermore, the rise time value (0.18 ns) obtained upon fitting the 545 nm decay profile was found to have a correlation with the decay component (0.22 ns) noticed at 425 nm. The dynamic red shift in the

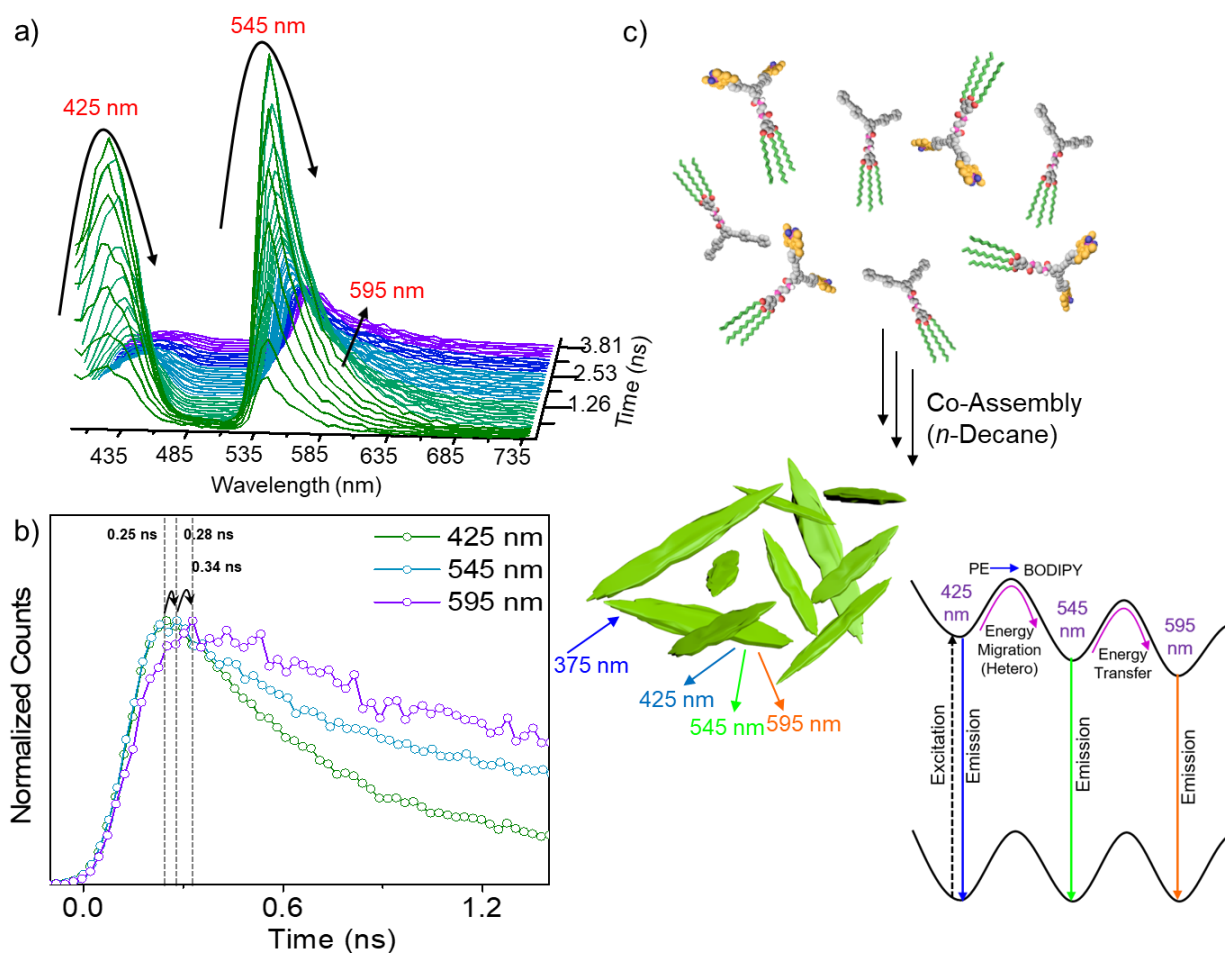


**Figure 4.17.** (a) TRES of poly[(BODIPY)<sub>0.5</sub>-CO-(PE)<sub>0.5</sub>] in *n*-decane. (b) The normalized fluorescence decay curves for poly[(BODIPY)<sub>0.5</sub>-CO-(PE)<sub>0.5</sub>] in *n*-decane; monitored at different emission wavelengths ( $3 \times 10^{-4}$  M,  $\lambda_{ex} = 375$  nm). (c) Schematic of the co-assembly of BODIPY and PE having 1:1 composition and the corresponding exciton deactivation within poly[(BODIPY)<sub>0.5</sub>-CO-(PE)<sub>0.5</sub>].

emission profile along with the correlation persisting between the consecutive emission peaks signify an energy migration from 425 to 545 nm and then from 545 to 595 nm (Figure 4.17c). However, further energy migration from 595 to 725 nm was not noticed, which may be the reason for the disappearance of 725 nm peak in the steady-state emission behavior.

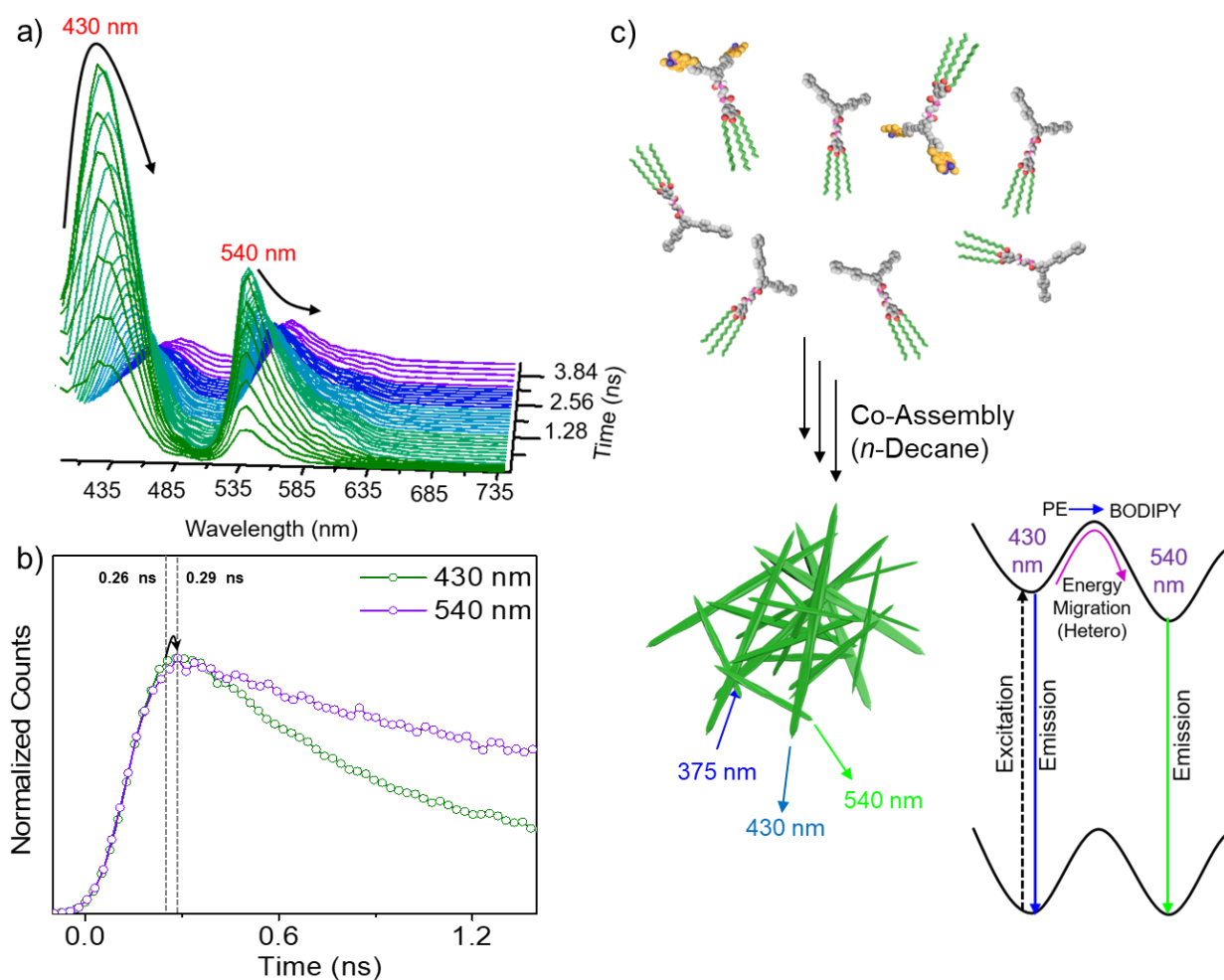


**Figure 4.18.** (a) TRES of poly[(BODIPY)<sub>0.25</sub>-CO-(PE)<sub>0.75</sub>] in *n*-decane. (b) The normalized fluorescence decay curves for poly[(BODIPY)<sub>0.25</sub>-CO-(PE)<sub>0.75</sub>] in *n*-decane; monitored at different emission wavelengths ( $3 \times 10^{-4}$  M,  $\lambda_{\text{ex}} = 375$  nm). (c) Schematic of the co-assembly of BODIPY and PE having 1:3 composition and the corresponding exciton deactivation within poly[(BODIPY)<sub>0.25</sub>-CO-(PE)<sub>0.75</sub>].

The disappearance of 595 nm emission peak for poly[(**BODIPY**)<sub>0.25-co</sub>-(**PE**)<sub>0.75</sub>] as seen in the steady state emission (**Figure 4.13b**) has been confirmed from the TRES analysis, which revealed the initial growth of the donor peak at 430 nm upto 201 ps followed by a gradual decay to 2.58 ns (**Figure 4.18a**). The acceptor peak at 540 nm reached maximum at 278 ps and gradually decayed till 1.30 ns. **Figure 4.18b** discloses that the peak intensity for 430 and 540 nm reaches the maximum of normalized counts within 0.26 and 0.29 ns, respectively before their decay and a correlation was found between the rise time (0.52 ns) of 540 nm peak to that of the decay component (0.31 ns) of 430 nm peak, which confirms the energy transfer process. However, the energy migration process was found limited within these two peaks and did not allow further energy transfer towards 595 and 725 nm (**Figure 4.18c**). Hence, we could demonstrate how a hetero-energy migration process between **PE** donors and **BODIPY** acceptors can be utilized to modulate the excited state properties of various **BODIPY-PE** co-assemblies and how to control the extent of homo-energy transfer process occurring within poly(**BODIPY**).

#### 4.4. Conclusions

In this study, we have demonstrated the formation of the spindle-shaped supramolecular polymers by a thermodynamically controlled supramolecular copolymerization of two distinct Y-shaped **BODIPY** and **PE** monomers, that form 2D and 1D supramolecular polymers, respectively. The cooling curves derived from the temperature-dependent UV-vis absorption spectra clearly discerned that copolymerization of a 1:1 mixture of **BODIPY** and **PE** to elongated spindle-like co-assemblies (aspect ratio ~ 4-7) is initially driven by

nucleation-elongation of **BODIPY**, followed by the secondary nucleation of **PE** monomers. The importance of the initial nucleation of **BODIPY** monomers in forming spindle structure with controlled length has been further confirmed by varying the composition of **BODIPY** and **PE** to 3:1 ratio, which restricted the growth and exhibited circular spindles having an aspect ratio of 1-2.5. Furthermore, it has also been demonstrated that when the initial nucleation occurs through 1D assembly forming **PE** monomers by changing the composition of **BODIPY** and **PE** to 1:3, the aspect ratio ( $\geq 13-15$ ) of the final supramolecular co-assembly structure could not be controlled. Finally, with the help of TRES analysis, we have established that the nature of the multiple emission peaks due to the hetero-energy migration from **PE** donors to **BODIPY** acceptors within the copolymeric assemblies could be controlled by varying the ratio between the two monomers. The present copolymeric system mentioned here is a rare example of spindle-shaped supramolecular polymers, the shape and optical properties of which could be controlled by varying the supramolecular copolymer composition.

## **4.5. Experimental Section: Synthesis**

### **4.5.1. General Procedure**

The details of the chemicals used, solvent purification, compound purification techniques etc. have been provided in the Section **2.5.1.** of Chapter 2 and also in the Section **3.5.1.** of Chapter 3. (4-Iodophenylethynyl)trimethylsilane and phenylacetylene were purchased from Sigma-Aldrich. Detailed synthesis of **BODIPY** is described in Chapter 3.

### 4.5.2. Characterization Techniques

The details of various characterization techniques have been provided in Section 2.5.2. of Chapter 2. Details of MALDI-TOF mass spectrometry have been provided in Section 3.5.2. of Chapter 3.

**4.5.3. Synthesis of PE:** Compound **1** (0.15 g, 0.14 mmol, 1 equiv.), Pd(PPh<sub>3</sub>)<sub>2</sub>Cl<sub>2</sub> (0.010 g, 10 mol%) and CuI (0.003 g, 10 mol%) were dissolved in a degassed mixture (1:1) of dry triethylamine and THF (15 mL) in a 100 mL two neck round bottom flask under inert atmosphere. Compound **2** (0.067 g, 0.34 mmol, 2.43 equiv.) dissolved in a degassed mixture (1:1) of dry triethylamine and THF (5 mL) was added dropwise and the reaction mixture was refluxed at 70 °C for 20 h. The progress of the reaction was monitored by TLC. On completion of the reaction, the solvent mixture was evaporated under reduced pressure and washed with 10% HCl solution to neutralize the remaining amount of triethylamine present within the medium and the residue extracted using ethyl acetate. The organic layer was washed thrice with brine, dried over anhydrous Na<sub>2</sub>SO<sub>4</sub>, filtered and the filtrate was concentrated under reduced pressure. The obtained crude product was purified using column chromatography over silica gel (33% ethyl acetate/*n*-hexane) to yield **PE** (0.031 g) as a colorless solid.

**PE:** Yield: 18%; m.p.: 151-153 °C; FT-IR (KBr):  $\nu_{\max}$  = 3275 (s;  $\nu_{\text{str}}(\text{N-H})$ ), 2922 (s;  $\nu_{\text{as}}(-\text{CH}_2)$ ), 2848 (s;  $\nu_{\text{s}}(-\text{CH}_2)$ ), 1641 (s;  $\nu_{\text{str}}(\text{C=O})$ ), 1513 (s;  $\nu_{\text{def}}(\text{N-H}) + \nu_{\text{str}}(\text{C-N})$ ) cm<sup>-1</sup>; <sup>1</sup>H NMR (500 MHz, CDCl<sub>3</sub>, TMS):  $\delta$  = 7.86 (s, 2H, Ar-*H*), 7.73 (s, 1H, Ar-*H*), 7.46–7.44 (m, 12H, Ar-*H*), 7.43 (s, 1H, -CONH), 7.30–7.28 (m, 6H, Ar-*H*), 6.97 (s, 1H, -CONH), 6.94



(s, 2H, Ar-*H*), 3.94–3.88 (m, 6H, -OCH<sub>2</sub>), 3.66 (s, 4H, -NHCH<sub>2</sub>), 1.72–1.62 (m, 8H, -CH<sub>2</sub>), 1.38–1.34 (m, 8H, -CH<sub>2</sub>), 1.21 (s, 44H, -CH<sub>2</sub>), 0.80 (t, *J* = 6.3 Hz, 9H, -CH<sub>3</sub>) ppm; <sup>13</sup>C NMR (125 MHz, CDCl<sub>3</sub>): δ = 168.9, 168.8, 153.1 (2C), 143.5, 137.1, 134.6, 131.7 (12C), 129.9 (2C), 128.4 (6C), 124.2 (2C), 123.8 (2C), 123.0 (3C), 122.3 (2C), 105.6 (2C), 91.6 (2C), 90.8 (2C), 89.4 (2C), 89.0 (2C), 73.5, 69.3 (2C), 41.1, 41.0, 31.9 (3C), 29.7–29.4 (21C), 26.1 (3C), 22.7 (3C), 14.1 (3C) ppm; MALDI-TOF calculated for C<sub>84</sub>H<sub>104</sub>N<sub>2</sub>O<sub>5</sub> [M+Na]<sup>+</sup>: 1243.7945, found: 1243.8060.

## 4.6. Description on Experimental Techniques

### 4.6.1. Optical Measurements

Details of UV-vis absorption spectrophotometer, spectrofluorimeter instruments have been provided in Section 2.6.1. of Chapter 2. Details of TCSPC system and calculation of different parameters have been reported in Section 2.6.1. of Chapter 2 and in Section 3.6.1., 3.6.7. of Chapter 3.

### 4.6.2. Morphological Studies

Details of TEM, SEM and fluorescence microscopy instruments have been provided in Section 2.6.2. of Chapter 2. Samples for electron microscopy were prepared by dropcasting the aggregates of **BODIPY**, **PE** and their mixtures of various compositions from *n*-decane over carbon-coated copper grids (TEM) or smooth aluminium foil (SEM), respectively and then dried under air overnight. TEM images were obtained without staining.

### 4.6.3. Preparation of Supramolecular Copolymeric Assemblies

For the preparation of copolymers poly[(**BODIPY**)-*co*-(**PE**)], required concentration (as mentioned below) of **BODIPY** and **PE** in *n*-decane were taken together in a screw-capped 1 mm quartz cuvette and cooled down from 363 to 283 K at a controlled rate of cooling (1 K/min). In a typical experiment, the total concentration of the co-assembly was kept fixed at  $3 \times 10^{-4}$  M. In the case of poly[(**BODIPY**)<sub>0.75</sub>-*co*-(**PE**)<sub>0.25</sub>], the concentration of **BODIPY** and **PE** was  $2.25 \times 10^{-4}$  and  $0.75 \times 10^{-4}$  M, respectively; whereas the individual concentration of **BODIPY** and **PE** was interchanged in poly[(**BODIPY**)<sub>0.25</sub>-*co*-(**PE**)<sub>0.75</sub>]. On the other hand, the concentration of both **BODIPY** and **PE** was  $1.5 \times 10^{-4}$  M in the case of poly[(**BODIPY**)<sub>0.5</sub>-*co*-(**PE**)<sub>0.5</sub>]. These samples were used further for spectroscopy and microscopy studies.

### 4.6.4. Time Resolved Emission Studies

The details of TCSPC instrument, excitation source and procedure to obtain TRES data have been reported in Section 3.6.7. of Chapter 3. The samples for TRES analysis were prepared by fixing the total concentration of the assembly as  $3 \times 10^{-4}$  M, where the concentration of **BODIPY** and **PE** was varied based on the mole fraction of the individual components. For copolymerization, both the molecules were mixed at a higher temperature (363 K) as monomers, followed by cooling to 283 K by maintaining a controlled rate of 1 K/min.

### 4.6.5. Theoretical Investigations

For an insight into the ground state geometry of the Y-shaped **BODIPY** and **PE**, the density functional theory (DFT) calculations were carried out using Gaussian 09 program package. The ground state geometries were optimized in gas phase at B3LYP level theory in conjunction with 6-311+g(d,p) basis set.

### 4.7. References

- [1] (a) S. Yagai, Y. Kitamoto, S. Datta, B. Adhikari, *Acc. Chem. Res.* **2019**, *52*, 1325–1335; (b) P. Xing, Y. Zhao, *Small Methods* **2018**, *2*, 1700364; (c) Y. Kim, T. Kim, M. Lee, *Polym. Chem.* **2013**, *4*, 1300–1308; (d) Y. Kim, T. Kim, M. Lee, *Polym. Chem.* **2013**, *4*, 1300–1308; (e) A. Kaeser, A. P. H. J. Schenning, *Adv. Mater.* **2010**, *22*, 2985–2997.
- [2] (a) T. Shimizu, W. Ding, N. Kameta, *Chem. Rev.* **2020**, *120*, 2347–2407; (b) S. S. Babu, V. K. Praveen, A. Ajayaghosh, *Chem. Rev.* **2014**, *114*, 1973–2129; (c) Y. Yamamoto, *Sci. Technol. Adv. Mater.* **2012**, *13*, 033001; (d) E. Krieg, M. M. C. Bastings, P. Besenius, B. Rybtchinski, *Chem. Rev.* **2016**, *116*, 2414–2477.
- [3] (a) B. Shen, Y. Kim, M. Lee, *Adv. Mater.* **2020**, *32*, 1905669; (b) K. Ariga, S. Watanabe, T. Mori, J. Takeya, *NPG Asia Mater.* **2018**, *10*, 90–106; (c) F. Ishiwari, Y. Shoji, T. Fukushima, *Chem. Sci.* **2018**, *9*, 2028–2041; (d) E. Moulin, J.-J. Cid, N. Giuseppone, *Adv. Mater.* **2013**, *25*, 477–487.
- [4] (a) X. Feng, B. Shen, B. Sun, J. Kim, X. Liu, M. Lee, *Angew. Chem. Int. Ed.* **2020**, *59*, 11355–11359; (b) H. Liu, Q. Pan, C. Wu, J. Sun, T. Zhuang, T. Liang, X. Mu, X. Zhou, Z. Li, Y. Zhao, *Mater. Chem. Front.* **2019**, *3*, 1532–1537; (c) A. Chakraborty, G. Ghosh, D. S. Pal, S. Varghese, S. Ghosh, *Chem. Sci.* **2019**, *10*, 7345–7351; (d) Y. Liu, C. Peng, W. Xiong, Y.

- Zhang, Y. Gong, Y. Che, J. Zhao, *Angew. Chem. Int. Ed.* **2017**, *56*, 11380–11384; (e) H. Qiu, Z. M. Hudson, M. A. Winnik, I. Manners, *Science* **2015**, *347*, 1329–1332. (f) M. Vybornyi, A. Rudnev, R. Häner, *Chem. Mater.* **2015**, *27*, 1426–1431; (g) M. Vybornyi, A. V. Rudnev, S. M. Langenegger, T. Wandlowski, G. Calzaferri, R. Häner, *Angew. Chem. Int. Ed.* **2013**, *52*, 11488–11493;
- [5] (a) T. F. A. de Greef, M. M. J. Smulders, M. Wolffs, A. P. H. J. Schenning, R. P. Sijbesma, E. W. Meijer, *Chem. Rev.* **2009**, *109*, 5687-5754. (b) T. F. A. de Greef, E. W. Meijer, *Nature* **2008**, *453*, 171-173; (c) C. Rest, R. Kandanelli, G. Fernández, *Chem. Soc. Rev.* **2015**, *44*, 2543-2572.
- [6] For the details of various spindle-shaped structures available in nature, kindly see the following link: [https://www.cactus-art.biz/note-book/Dictionary/Dictionary\\_F/dictionary\\_fusiform.htm](https://www.cactus-art.biz/note-book/Dictionary/Dictionary_F/dictionary_fusiform.htm)
- [7] (a) C. Österlund, J.-X. Liu, L.-E. Thornell, P.-O. Eriksson, *Anat. Rec. Adv. Integr. Anat. Evol. Biol.* **2011**, *294*, 683–693; (b) For details related to spindle shaped muscle cells, kindly see the following link: <https://courses.lumenlearning.com/suny-ap1/chapter/the-muscular-system/>.
- [8] (a) T. Potapova, G. Gorbsky, *Biology (Basel)* **2017**, *6*, 12; (b) C. B. O’Connell, A. L. Khodjakov, *J. Cell Sci.* **2007**, *120*, 1717–1722; (c) C. L. Rieder, A. Khodjakov, L. V. Paliulis, T. M. Fortier, R. W. Cole, G. Sluder, *Proc. Natl. Acad. Sci. USA* **1997**, *94*, 5107–5112.
- [9] J. E. Mank, *Science* **2009**, *326*, 1639–1640.
- [10] A. Sorrenti, J. Leira-Iglesias, A. J. Markvoort, T. F. A. de Greef, T. M. Hermans, *Chem. Soc. Rev.* **2017**, *46*, 5476-5490.
- [11] (a) S. Dhiman, S. J. George, *Bull. Chem. Soc. Jpn.* **2018**, *91*, 687-699; (b) R. D. Mukhopadhyay, A. Ajayaghosh, *Science* **2015**, *349*, 241–242.
- [12] (a) J. Kang, D. Miyajima, T. Mori, Y. Inoue, Y. Itoh, T. Aida, *Science* **2015**, *347*, 646-651;

- (b) Z. M. Hudson, C. E. Boott, M. E. Robinson, P. A. Rugar, M. A. Winnik, I. Manners, *Nat. Chem.* **2014**, *6*, 893–898; (c) Z. M. Hudson, D. J. Lunn, M. A. Winnik, I. Manners, *Nat. Commun.* **2014**, *5*, 3372.
- [13] (a) J. Matern, Y. Dorca, L. Sánchez, G. Fernández, *Angew. Chem. Int. Ed.* **2019**, *58*, 16730–16740; (b) E. Mattia, S. Otto, *Nat. Nanotechnol.* **2015**, *10*, 111–119; (c) A. T. Haedler, S. C. J. Meskers, R. H. Zha, M. Kivala, H. W. Schmidt, E. W. Meijer, *J. Am. Chem. Soc.* **2016**, *138*, 10539–10545.
- [14] (a) T. Fukui, M. Takeuchi, K. Sugiyasu, *Sci. Rep.* **2017**, *7*, 2425; (b) S. Ogi, V. Stepanenko, J. Thein, F. Würthner, *J. Am. Chem. Soc.* **2016**, *138*, 670–678; (c) S. Ogi, V. Stepanenko, K. Sugiyasu, M. Takeuchi, F. Würthner, *J. Am. Chem. Soc.* **2015**, *137*, 3300–3307. (d) S. Ogi, K. Sugiyasu, S. Manna, S. Samitsu, M. Takeuchi, *Nat. Chem.* **2014**, *6*, 188–195.
- [15] T. Fukui, S. Kawai, S. Fujinuma, Y. Matsushita, T. Yasuda, T. Sakurai, S. Seki, M. Takeuchi, K. Sugiyasu, *Nat. Chem.* **2017**, *9*, 493–499.
- [16] D. D. Prabhu, K. Aratsu, Y. Kitamoto, H. Ouchi, T. Ohba, M. J. Hollamby, N. Shimizu, H. Takagi, R. Haruki, S. Adachi, S. Yagai, *Sci. Adv.* **2018**, *4*, eaat8466.
- [17] S. Datta, Y. Kato, S. Higashiharaguchi, K. Aratsu, A. Isobe, T. Saito, D. D. Prabhu, Y. Kitamoto, M. J. Hollamby, A. J. Smith, R. Dalgliesh, N. Mahmoudi, L. Pesce, C. Perego, G. M. Pavan, S. Yagai, *Nature* **2020**, *583*, 400–405.
- [18] B. Adelizzi, N. J. Van Zee, L. N. J. de Windt, A. R. A. Palmans, E. W. Meijer, *J. Am. Chem. Soc.* **2019**, *141*, 6110–6121.
- [19] (a) H. Qiu, Z. M. Hudson, M. A. Winnik, I. Manners, *Science* **2015**, *347*, 1329–1332; (b) X. Wang, G. Guerin, H. Wang, Y. Wang, I. Manners, M. A. Winnik, *Science* **2007**, *317*, 644–647.

- [20] D. Görl, X. Zhang, V. Stepanenko, F. Würthner, *Nat. Commun.* **2015**, *6*, 7009.
- [21] B. Adelizzi, A. Aloï, A. J. Markvoort, H. M. M. Ten Eikelder, I. K. Voets, A. R. A. Palmans, E. W. Meijer, *J. Am. Chem. Soc.* **2018**, *140*, 7168–7175.
- [22] A. Sarkar, R. Sasmal, C. Empereur-mot, D. Bochicchio, S. V. K. Kompella, K. Sharma, S. Dhiman, B. Sundaram, S. S. Agasti, G. M. Pavan, S. J. George, *J. Am. Chem. Soc.* **2020**, *142*, 7606–7617.
- [23] A. Sarkar, T. Behera, R. Sasmal, R. Capelli, C. Empereur-mot, J. Mahato, S. S. Agasti, G. M. Pavan, A. Chowdhury, S. J. George, *J. Am. Chem. Soc.* **2020**, *142*, 11528–11539.
- [24] (a) R. Thirumalai, R. D. Mukhopadhyay, V. K. Praveen, A. Ajayaghosh, *Sci. Rep.* **2015**, *5*, 9842; (b) A. Ajayaghosh, R. Varghese, V. K. Praveen, S. Mahesh, *Angew. Chem. Int. Ed.* **2006**, *45*, 3261–3264; (c) A. Ajayaghosh, R. Varghese, S. Mahesh, V. K. Praveen, *Angew. Chem. Int. Ed.* **2006**, *45*, 7729–7732.
- [25] (a) G. Das, R. Thirumalai, B. Vedhanarayanan, V. K. Praveen, A. Ajayaghosh, *Adv. Opt. Mater.* **2020**, *29*, 1703783; (b) B. Adelizzi, I. A. W. Filot, A. R. A. Palmans, E. W. Meijer, *Chem. Eur. J.* **2017**, *23*, 6103–6110. (c) H. M. M. ten Eikelder, A. J. Markvoort, T. F. A. de Greef, P. A. J. Hilbers, *J. Phys. Chem. B* **2012**, *116*, 5291–5301.
- [26] M. Tornquist, T. C. T. Michaels, K. Sanagavarapu, X. Yang, G. Meisl, S. I. A. Cohen, T. P. J. Knowles, S. Linse, *Chem. Commun.* **2018**, *54*, 8667–8684.
- [27] (a) C. Giansante, C. Schäfer, G. Raffy, A. Del Guerzo, *J. Phys. Chem. C* **2012**, *116*, 21706–21716; (b) C. Vijayakumar, V. K. Praveen, A. Ajayaghosh, *Adv. Mater.* **2009**, *21*, 2059–2063; (c) A. Ajayaghosh, V. K. Praveen, C. Vijayakumar, S. J. George, *Angew. Chem. Int. Ed.* **2007**, *46*, 6260–6265.

- 
- [28] (a) X. Jin, M. B. Price, J. R. Finnegan, C. E. Boott, J. M. Richter, A. Rao, S. M. Menke, R. H. Friend, G. R. Whittell, I. Manners, *Science* **2018**, *360*, 897–900; (b) D. Okada, T. Nakamura, D. Braam, T. D. Dao, S. Ishii, T. Nagao, A. Lorke, T. Nabeshima, Y. Yamamoto, *ACS Nano* **2016**, *10*, 7058–7063; (c) D. Tian, F. Qi, H. Ma, X. Wang, Y. Pan, R. Chen, Z. Shen, Z. Liu, L. Huang, W. Huang, *Nat. Commun.* **2018**, *9*, 2688.

## ABSTRACT

Name of the Student: **Mr. Gourab Das**  
Faculty of Study: Chemical Sciences  
AcSIR academic centre/CSIR Lab: CSIR-National  
Institute for Interdisciplinary Science  
and Technology (CSIR-NIIST)

Registration No.: 10CC14A39001  
Year of Submission: 2021

Name of the Supervisor: Prof. A. Ajayaghosh

Title of the thesis: **Self-Assembly and Optical Properties of Phenyleneethynylene and BODIPY Based  $\pi$ -Systems**

Nature has been a source of inspiration to understand the complexities and functional properties of molecular assemblies and supramolecular polymers. Unlike covalent polymers, the prevalence of non-covalent interactions makes supramolecular polymers reversible, modular, adaptive, and stimuli-responsive. In the **First Chapter**, we summarize the recent developments in the field of supramolecular polymers by discussing the self-assembly behaviors of PE and PE-attached BODIPY chromophore assemblies in the context of their formation mechanism, diversity of morphology, intriguing ground and excited-state properties and applications.

Optical properties of  $\pi$ -systems are of great significance for a wide range of applications in materials and biology. Aggregation and self-assembly induced emission are one of such phenomena. In the **Second Chapter**, we report the self-assembly induced modulation of the emission of amide functionalized PE chromophores bearing linear achiral or branched chiral alkoxy chains. Self-assembled structures of both achiral and chiral-PEs from *n*-decane exhibit enhanced emission with  $\Phi_F$  values of 0.34 and 0.25, respectively, whereas these molecules are less-emissive in chloroform ( $\Phi_F = 0.02$ ). TEM and fluorescence microscopy studies reveal the formation of entangled blue-emissive fibers for achiral-PE and supercoiled helical blue-emissive fiber bundles for chiral-PE. At higher concentrations (8.8 mM for achiral-PE and 23.6 mM for chiral-PE) in *n*-decane, intense blue-emitting gels are obtained.

In the **Third Chapter**, we demonstrate creation and control of distinct supramolecular architectures and their energy landscape for the reversible control of the excited state emission processes through cascade energy transfer in chromophore assemblies, facilitated by an unprecedented solvent effect. In MCH, Y-shaped BODIPY molecule self-assembles to form an unusual spherical architecture of 400-1200 nm size, which exhibits a single emission at 540 nm upon 475 nm excitation through a normal excitation-deactivation process. However, in *n*-decane, the same BODIPY derivative forms 2D supramolecular sheets, exhibiting multiple emission peaks at 540, 610, 650, 725 and 790 nm with 475 nm excitation due to cascade energy transfer. Further control on the morphology and excitation energy transfer is possible with variable solvent composition and ultrasound stimulation, resulting in an enhanced NIR emission.

Spontaneous self-assembly of functional  $\pi$ -systems usually leads to 1D or 2D structures. In the previous Chapter, we have reported the formation of 2D supramolecular sheets exhibiting multiple emission from a Y-shaped **BODIPY** molecule. In continuation, we report that self-assembly of a similar Y-shaped molecule, **PE** with a terminal moiety having different structural parameters compared to BODIPY, can lead to 1D fibers under an identical experiential condition. In general, structurally mismatched monomers form homopolymers of narcissistically self-sorted assemblies instead of choosing a co-assembling pathway. In the **Fourth Chapter**, we demonstrate the formation of an unusual spindle-shaped (elongated or circular) supramolecular structures by copolymerizing Y-shaped **PE** and **BODIPY** molecules under thermodynamic control. Finally, we demonstrate control over the cascade energy transfer process within **BODIPY** assembly by utilizing the hetero-energy migration process taking place from **PE** donors to **BODIPY** acceptors within the copolymeric assemblies.



### **List of Publications from the Thesis Work**

1. **Das, G.**; Cherumukkil, S.; Padmakumar, A.; Banakar, V. B.; Praveen, V. K.; Ajayaghosh, A.  
Tweaking of an Unusual Spherical BODIPY Assembly to Two-Dimensional Supramolecular Sheets Facilitates Domino-Type Energy Transfer Assisted Multiple Emission  
*Angew. Chem. Int. Ed.* **2021**, *60*, 7851-7859.
2. **Das, G.**; Thirumalai, R.; Vedhanarayanan, B.; Praveen, V. K.; Ajayaghosh, A.  
Enhanced Emission in Self-Assembled Phenyleneethynylene Derived  $\pi$ -Gelators  
*Adv. Opt. Mater.* **2020**, *8*, 2000173.
3. **Das, G.**; Vedhanarayanan, B.; Padmakumar, A.; Praveen, V. K.; Ajayaghosh, A.  
Spindle-Shaped Supramolecular Block Polymers with Controlled Excitation Energy Transfer by Co-Polymerizing 2D- and 1D-Assembly Forming  $\pi$ -System Monomers  
(Manuscript under preparation)

### **List of Publications from Other Related Works**

1. Cherumukkil, S.; Vedhanarayanan, B.; **Das, G.**; Praveen, V. K.; Ajayaghosh, A.  
Self-Assembly of Bodipy-Derived Extended  $\pi$ -Systems  
*Bull. Chem. Soc. Jpn.* **2018**, *91*, 100–120.
2. Vedhanarayanan, B.; Praveen, V. K.; **Das, G.**; Ajayaghosh, A.  
Hybrid Materials of 1D and 2D Carbon Allotropes and Synthetic  $\pi$ -Systems  
*NPG Asia Mater.* **2018**, *10*, 107–126.
3. Mukhopadhyay, R. D.; **Das, G.**; Ajayaghosh, A.  
Stepwise Control of Host–Guest Interaction Using a Coordination Polymer Gel  
*Nat. Commun.* **2018**, *9*, 1987.
4. Santhini, P. V.; Krishnan R, A.; Babu, S. A.; Simethy, B. S.; **Das, G.**; Praveen, V. K.; Varughese, S.; John, J.  
One-Pot MCR-Oxidation Approach towards Indole-Fused Heteroacenes  
*J. Org. Chem.* **2017**, *82*, 10537–10548.

5. Vedhanarayanan, B.; Mukhopadhyay, R. D.; **Das, G.**; Shankar, S.; Ajayaghosh, A. A Superhydrophobic Coating for Faster and Fuel-Efficient Marine Transportation  
([Manuscript under preparation](#))
6. **Das, G.**; Mukhopadhyay, R. D.; Elizebath, D.; Praveen, V. K.; Ajayaghosh, A.  
Temporal Control over the Crystallinity of a Clay-Azobenzene Hybrid  
([Manuscript under preparation](#))

### **Book Chapters**

1. Mishra, R. K.; Das, S.; Vedhanarayanan, B.; **Das, G.**; Praveen, V. K.; Ajayaghosh, A.  
Stimuli-responsive Supramolecular Gels; In Molecular Gels: Structure and Dynamics, Weiss, R. G. (Ed.)  
[Monographs in Supramolecular Chemistry Series, RSC, 2018, pp-190-226.](#)

## List of Conference Presentations

1. **Das, G.**; Elizebath, D.; Praveen, V. K.; Ajayaghosh, A.  
Functional Supramolecular Polymers, [Polymer Conference for Young Researchers \(PCYR-18\)](#), November 17, 2018, CSIR-NIIST, Thiruvananthapuram, India. ([Invited Lecture](#)).
2. **Das, G.**; Mukhopadhyay, R. D.; Praveen, V. K.; Ajayaghosh, A.  
Heterogeneous Nucleation Mediated Assembly of a Photoresponsive Dye, [8<sup>th</sup> East Asia Symposium on Functional Dyes and Advanced Materials \(EAS8-2017\)](#), September 20-22, 2017, CSIR-NIIST, Thiruvananthapuram, India.
3. **Das, G.**; Mukhopadhyay, R. D.; Francy A.; Elizebath, D.; Praveen, V. K.; Ajayaghosh, A.  
Spatio-Temporal Control over the Crystallinity of a Clay-Azobenzene Hybrid, [24<sup>th</sup> CRSI National Symposium in Chemistry](#), February 8-10, 2019, CSIR-CLRI and IIT Madras, Chennai, India.
4. **Das, G.**; Mukhopadhyay, R. D.; Ajayaghosh, A.  
Controlling the Host-Guest Interaction in a Stepwise Manner Using a Coordination Polymer Gel, [CSIR-Inter Institutional Students Conference: Sustainable Chemistry for Health, Environment and Materials \(Su-CHEM YUVA-2019\)](#), July 24-26, 2019, CSIR-IICT, Hyderabad, India.
5. **Das, G.**; Mukhopadhyay, R. D.; Elizebath, D.; Praveen, V. K.; Ajayaghosh, A.  
Transient Crystallization of a Clay-Azobenzene Hybrid, [3<sup>rd</sup> International Conference on Advanced Functional Materials](#), December 9-10, 2019, CSIR-NIIST, Thiruvananthapuram, India.
6. **Das, G.**; Mukhopadhyay, R. D.; Elizebath, D.; Praveen, V. K.; Ajayaghosh, A.  
Control over Transient Crystallization of a Clay-Azobenzene Hybrid, [14<sup>th</sup> International Conference on Ecomaterials](#), February 5-7, 2020, CSIR-NIIST, Thiruvananthapuram, India.

# Enhanced Emission in Self-Assembled Phenyleneethynylene Derived $\pi$ -Gelators

Gourab Das, Rajasekaran Thirumalai, Balaraman Vedhanarayanan, Vakayil K. Praveen,\* and Ayyappanpillai Ajayaghosh\*

Optical properties of  $\pi$ -systems are of great significance for a wide range of applications in materials and biology. Aggregation and self-assembly induced emission are one of such phenomena. Herein, the self-assembly induced modulation of the emission of *p*-phenyleneethynylene (PE) chromophores bearing linear achiral (1) or branched chiral (2) alkoxy chains is reported. Self-assembled structures of both 1 and 2 from *n*-decane exhibit enhanced emission with fluorescence quantum yield ( $\Phi_F$ ) values of 0.34 and 0.25, respectively, whereas these molecules are less-emissive in chloroform ( $\Phi_F = 0.02$ ). Transmission electron microscopy and fluorescence microscopy studies reveal the formation of entangled blue-emissive fibers for 1 and supercoiled helical blue-emissive fiber bundles for 2. At higher concentrations ( $8.8 \times 10^{-3}$  M for 1 and  $23.6 \times 10^{-3}$  M for 2) in *n*-decane, intense blue-emitting gels are formed. Significant shift in the emission toward longer wavelength can be seen from solution state to aggregates to the gel state. The wide-angle X-ray scattering and fluorescence data indicate that the interdigitated lamellar assembly with weaker  $\pi$ -stacking and the resultant restriction of rotation of the PE chromophores are responsible for the enhanced emission of the self-assembled gel state.

## 1. Introduction

Fluorescence is one of the most sensitive optical properties of  $\pi$ -systems. Since fluorescence strongly depends upon the structural features, intermolecular interaction, and several external factors, fluorescent molecules are used for wide-ranging applications.<sup>[1–5]</sup> For example, fluorescent  $\pi$ -systems are used for sensing of analytes,<sup>[6–8]</sup> imaging,<sup>[9,10]</sup> and lighting applications.<sup>[11,12]</sup> However, in aggregated and solid states, most of the  $\pi$ -systems exhibit reduced quantum yield for emission due to

self-quenching phenomenon associated with strong  $\pi$ - $\pi$  interaction.<sup>[13]</sup> Therefore, it is necessary to prevent the fluorescence quenching by incorporating bulky terminal groups<sup>[14,15]</sup> or by modulating the viscosity of the medium<sup>[16]</sup> for any practical applications. Interestingly, in some cases, fluorescence is found to increase upon aggregation or self-assembly.<sup>[13,16,17]</sup> Though this phenomenon has been extensively studied in recent times as aggregation induced enhanced emission (AIEE), it is actually a manifestation of the previously known restricted rotation of chromophores in the solid and crystalline states.


Though several  $\pi$ -systems are known to exhibit AIEE, chromophores such as heteroatom-containing molecules,<sup>[18]</sup> cyano stilbenes,<sup>[19–21]</sup> distyrylanthracene,<sup>[22]</sup> tetraphenylethylenes,<sup>[23]</sup> excited state intramolecular proton transfer systems,<sup>[24]</sup> and so on are the best-studied systems.<sup>[6,16,17]</sup> In the case of AIEE-inac-

tive chromophores, the energy provided to excite the molecules is utilized for the rotational and vibrational motion of the molecules and thus nonradiative decay paths are found to be more effective to form less or nonemissive states. However, in the case of AIEE-active molecules, upon aggregation, intramolecular rotation and vibrational motion gets restricted and the radiative decay channels are activated to display enhanced emission.<sup>[13,16]</sup> Another interesting  $\pi$ -system that exhibit self-assembly induced enhanced emission (SIEE) is phenyleneethynylenes (PEs).<sup>[25–29]</sup> Due to the freedom of rotation of the phenyl rings around the triple bonds, they are less emissive in solution-state. However, properly functionalized PEs show strong fluorescence upon self-assembly. Garcia-Garibay and co-workers have demonstrated that variable optoelectronic properties of PEs can be achieved by controlling the extent of phenyl group rotation.<sup>[25,26]</sup> The emission spectrum of a PE remains structured when the phenyl rings are in the twisted confirmation or in the case of self-assembly induced planarization of the phenyl rings. However, the emission spectrum of PEs can be broadened and red-shifted upon the formation of cofacial planar PE assemblies. We have previously exploited this behavior of PEs to design fluorescent assemblies and organogels that respond to various stimuli.<sup>[8,30–35]</sup> For example, the weak blue fluorescence

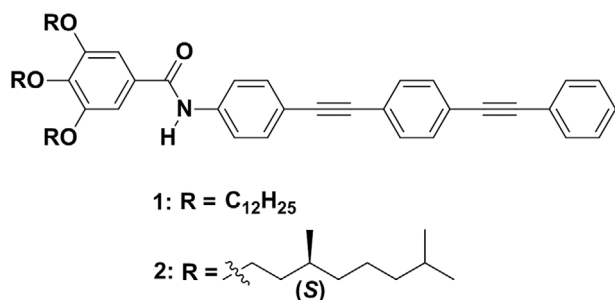
G. Das, Dr. R. Thirumalai, Dr. B. Vedhanarayanan, Dr. V. K. Praveen, Prof. A. Ajayaghosh  
Photosciences and Photonics Section  
Chemical Sciences and Technology Division  
CSIR-National Institute for Interdisciplinary Science and Technology (CSIR-NIIST)

Thiruvananthapuram, Kerala 695019, India  
E-mail: vkpraveen@niist.res.in; ajayaghosh@niist.res.in

G. Das, Dr. V. K. Praveen, Prof. A. Ajayaghosh  
Academy of Scientific and Innovative Research (AcSIR)  
Ghaziabad, Uttar Pradesh 201002, India

 The ORCID identification number(s) for the author(s) of this article can be found under <https://doi.org/10.1002/adom.202000173>.

DOI: 10.1002/adom.202000173



**Scheme 1.** Molecular structures of the PE-based achiral (**1**) and chiral (**2**) gelators.

of a PE attached with hydrophilic terminal groups has been shown to enhance upon contact with water, resulting in intense cyan emission.<sup>[33]</sup> In view of this observation, we have thought of investigating the role of the nature of the side chains<sup>[36–39]</sup> on the terminal moiety of PEs on their emission behavior. For this purpose, we have designed PEs **1** and **2**, in which the PE core is connected to a benzamide moiety bearing linear achiral or branched chiral alkoxy chains, respectively (**Scheme 1**). It is envisaged that the presence of solubilizing achiral and chiral side chains could modulate the amide H-bonding directed assembly of PE molecules and allow to explore their SIEE behavior in terms of small structural difference.

## 2. Results and Discussion

The molecules **1** and **2** were synthesized by multistep synthetic procedures using palladium-catalyzed Sonogashira–Hagihara cross-coupling reactions (Scheme S1, Supporting Information) and characterized using Fourier transform-infrared spectroscopy (FT-IR), NMR spectroscopy, and mass spectrometry techniques. In order to understand the aggregation properties, UV–vis absorption studies of **1** and **2** in chloroform and *n*-decane ( $5 \times 10^{-4}$  M) have been carried out. At 298 K in chloroform, **1** exists as monomers, which showed a strong  $\pi$ – $\pi^*$  absorption band with a maximum ( $\lambda_{\text{max}}$ ) at 333 nm (**Figure 1a**). In *n*-decane at 363 K, the absorption spectrum of **1** was almost similar to that in chloroform with  $\lambda_{\text{max}}$  at 332 nm, whereas at 283 K, the  $\lambda_{\text{max}}$  was found blue-shifted to 307 nm with the formation of a new shoulder band at 372 nm (**Figure 1a**). Similarly, in chloroform at 298 K, **2** showed a strong  $\pi$ – $\pi^*$  absorption band with  $\lambda_{\text{max}}$  at 334 nm, whereas in *n*-decane at 283 K, a decrease in the intensity with no shift of  $\lambda_{\text{max}}$  was observed (**Figure 1c**). Temperature-dependent absorption spectral changes of **1** in *n*-decane confirmed transition from the monomers at a higher temperature (363 K) to the aggregates at 283 K (**Figure 1a**). While gradually decreasing the temperature, a gradual decrease in the intensity of  $\lambda_{\text{max}}$  at 332 nm accompanied by a concomitant increase in the intensity of the shoulder band at 372 nm with an isobestic point at 364 nm was noticed. Similarly, the temperature-dependent absorption spectra of **2**

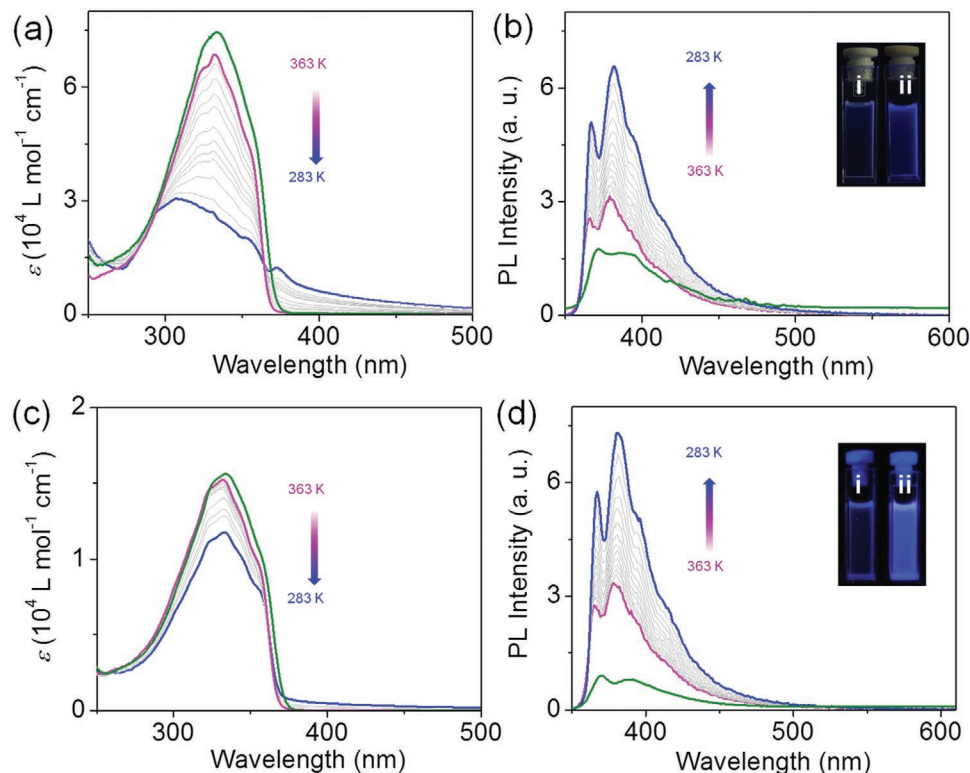


**Figure 1.** Absorption and emission ( $\lambda_{\text{ex}} = 340$  nm) spectra of a,b) **1** and c,d) **2** in chloroform (green curves) at 298 K. Temperature-dependent absorption and emission spectra of a,b) **1**<sub>agg</sub> and c,d) **2**<sub>agg</sub> in *n*-decane ( $5 \times 10^{-4}$  M from 363 K (magenta curves) to 283 K (blue curves). Inset shows the photographs of i) monomers and ii) aggregates emission of **1** and **2** under 365 nm UV light illumination.



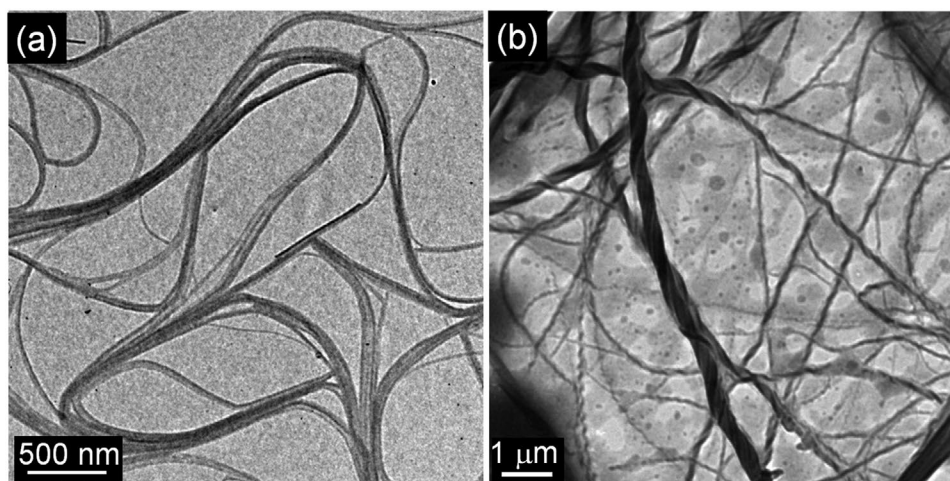


**Figure 2.** TEM images of a)  $1_{agg}$  and b)  $2_{agg}$  in *n*-decane ( $5 \times 10^{-4}$  M).

displayed a gradual decrease in the intensity of  $\lambda_{max}$  at 334 nm with a concomitant increase in the intensity of the band at 385 nm with an isosbestic point at 365 nm (Figure 1c).

The emission studies of **1** and **2** have also been carried out in chloroform and *n*-decane ( $5 \times 10^{-4}$  M). In case of **1** in chloroform (298 K), a very weak emission with maxima centered at 372 and 385 nm ( $\Phi_F = 0.02$ ) was observed (Figure 1b). However, in *n*-decane, aggregates of **1** ( $1_{agg}$ ) showed structured and enhanced emission with maxima at 367 and 382 nm ( $\Phi_F = 0.34$ ) with respect to monomeric chloroform solution. Similarly, **2** in the monomeric state also showed a weak emission in chloroform with maxima at 367 and 381 nm ( $\Phi_F = 0.02$ ), whereas in *n*-decane,  $2_{agg}$  exhibited enhancement in emission ( $\Phi_F = 0.25$ ) (Figure 1d). These observations indicate that both the molecules are SIEE active in their aggregated state. To further confirm the SIEE behavior, we have carried out temperature-dependent emission studies of  $1_{agg}$  and  $2_{agg}$ . Both **1** and **2** showed a gradual increase in the emission intensity while decreasing the temperature from 363 to 283 K. Around a twofold enhancement in emission was noticed upon comparing the emission intensities of *n*-decane solutions at 363 and 283 K (Figure 1b,d). Encouraged by these observations, we have carried out detailed studies on the effect of hierarchical self-assembly of **1** and **2** on their emission behavior.

Self-assembly pathway of both **1** and **2** in *n*-decane was probed by monitoring the changes in UV-vis absorption spectra as a function of temperature by maintaining a fixed cooling rate of  $1 \text{ K min}^{-1}$ . The plot of fraction of aggregates ( $\alpha_{agg}$ ) with respect to the gradual decrease in temperature revealed nonsigmoidal nature of the cooling curves for a wide range of concentrations for **1** ( $7 \times 10^{-4}$  to  $1.33 \times 10^{-3}$  M) and **2** ( $1 \times 10^{-3}$  to  $2 \times 10^{-3}$  M). For all the concentrations, the cooling curves could be fitted with an equilibrium model<sup>[40–42]</sup> characteristic of a co-operative self-assembly process (Figure S1a,b, Supporting Information).<sup>[35,39–46]</sup> A gradual shift in the elongation temperature ( $T_e$ ) to higher temperatures was observed upon increasing the concentration (Tables S1 and S2, Supporting Information). The plot between the natural logarithm of the reciprocal concentration of **1** against reciprocal of  $T_e$  exhibited a linear relationship (van 't Hoff plot),<sup>[44–46]</sup>

when  $T_e$  was gradually increased with the change in concentration (Figure S1c, Supporting Information). From the van 't Hoff plot, we have estimated the standard enthalpy ( $\Delta H^\circ$ ) and entropy ( $\Delta S^\circ$ ) values as  $-93.74 \text{ kJ mol}^{-1}$  and  $-251.07 \text{ J mol}^{-1} \text{ K}^{-1}$ , respectively. With the help of  $\Delta H^\circ$  and  $\Delta S^\circ$ , the standard Gibbs free energy  $\Delta G^\circ$  to be  $-18.92 \text{ kJ mol}^{-1}$  at 298 K for  $1_{agg}$  has been determined. Similar to this, the van 't Hoff plot for  $2_{agg}$  in *n*-decane also exhibited a linear relationship (Figure S1d, Supporting Information), from where the thermodynamic parameters such as  $\Delta H^\circ = -55.13 \text{ kJ mol}^{-1}$ ,  $\Delta S^\circ = -131.94 \text{ J mol}^{-1} \text{ K}^{-1}$ , and  $\Delta G^\circ = -15.81 \text{ kJ mol}^{-1}$  has been determined. The standard thermodynamic parameters obtained for both  $1_{agg}$  and  $2_{agg}$  in *n*-decane indicate the involvement of nucleation-elongation process as found in the case of H-bonded supramolecular polymers.<sup>[35,41,44,45]</sup>

To gain visual insight about the morphology of  $1_{agg}$  and  $2_{agg}$  in *n*-decane, samples were dropcast over carbon-coated copper grid and imaged using transmission electron microscopy (TEM). Images of  $1_{agg}$  showed micrometer long entangled fibers, whereas  $2_{agg}$  displayed the formation of right-handed micrometer long twisted helical fibers (Figure 2a,b). In both the cases, the width of the fibers is found within 50–200 nm. TEM image of  $1_{agg}$  reveals that the elongated fibers are formed by lateral bundling of thin fibrils of a few nanometers in width. In the case of  $2_{agg}$ , helical bundling of such thin helices resulted in superhelical fiber bundles.<sup>[35,47–49]</sup>

In order to further establish the formation of helical fibers of **2**, chiroptical properties were studied in comparison with **1** in chloroform and *n*-decane at 298 K (Figure S2, Supporting Information). As anticipated, both the compounds were circular dichroism (CD)-silent in chloroform ( $5 \times 10^{-4}$  M), indicating their existence as monomers. In addition,  $1_{agg}$  in *n*-decane ( $5 \times 10^{-4}$  M) did not show any CD activity since molecule is achiral (Figure S2a, Supporting Information). However, CD measurements of  $2_{agg}$  in *n*-decane ( $5 \times 10^{-4}$  M) exhibited a bisignate Cotton effect (Figure S2b, Supporting Information). In this case, an intense positive signal at 363 nm followed by two negative signals at 300 and 255 nm were noticed. The observed CD spectrum might be included the linear dichroism (LD) effect

**Table 1.** Critical gelator concentration (CGC) (in mM) of **1** and **2** in different solvents.

Compound <sup>a)</sup>	<i>n</i> -Decane	MCH	Cyclohexane	<i>n</i> -Hexane	Toluene
1	8.8 (G)	12.5 (G)	16.6 (G)	10.1 (G)	(S)
2	23.6 (G)	29.0 (G)	39.2 (G)	14.7 (G)	(S)

<sup>a)</sup>CGC is the minimum concentration required for the formation of a stable gel at room temperature. In parenthesis, G = gel and S = solution at room temperature.

associated with the fiber bundling (Figure S2c, Supporting Information).<sup>[42]</sup>

Interestingly, both **1** and **2** formed gels in *n*-decane above a critical concentration. Hence, gelation abilities of these molecules were examined in various hydrocarbon solvents and the results are summarized in Table 1. In all the solvents tested, the critical gelator concentration (CGC) values of **1** have been found to be lower than that of **2**. For instance, in *n*-decane, CGC of **1** is  $8.8 \times 10^{-3}$  M and that of **2** is  $23.6 \times 10^{-3}$  M, which implies that **1** having achiral dodecyloxy side chains is a better gelator in comparison to that of **2** containing branched chiral decyloxy side chains. This gelation ability has been further confirmed by studying the viscoelastic nature of the gels in *n*-decane (Figure 3). Dynamic frequency sweep experiments revealed that the storage modulus ( $G'$ ) and the loss modulus ( $G''$ ) values are independent of the oscillation frequency within the range of 1–100 rad  $s^{-1}$ , where the strain amplitude

( $\gamma$ ) has been kept fixed at 0.01 (Figure 3a,b). In both cases, the  $G'$  value is obtained to be an order of magnitude higher than  $G''$ , a characteristic feature of supramolecular gels.<sup>[50–52]</sup> Furthermore, the individual values of  $G'$  and  $G''$  of  $1_{\text{gel}}$  was found higher than that of the  $2_{\text{gel}}$ , which shows the ability of **1** to form a stronger gel in *n*-decane. Quantitative analysis of rheological studies showed that  $1_{\text{gel}}$  is 2.6 times stronger with respect to  $2_{\text{gel}}$  formed in *n*-decane, which almost matches the ratio ( $\approx 2.68$ ) of CGC values of **2** and **1** in *n*-decane. This behavior was found to remain unaltered when the nature of the nonpolar solvents was varied to other linear or cyclic solvents (Table 1).

Scanning electron microscopy (SEM) image of the dried  $1_{\text{gel}}$  revealed the formation of entangled fibers having a length of several micrometers (Figure 3c), which is found to be almost similar to that of the morphologies obtained by TEM at lower concentration (Figure 2a). On the contrary, SEM images of  $2_{\text{gel}}$  exhibited coiling of individual fibers to form right-handed supercoiled fibers (Figure 3d) having similarity with that of the TEM images obtained at lower concentration (Figure 2b). The observed morphologies of the gels are found to have correlation with the texture of the gel (insets of Figure 3c,d).  $1_{\text{gel}}$  and  $2_{\text{gel}}$  in *n*-decane under normal light are translucent and opaque in nature, respectively. The translucent nature of  $1_{\text{gel}}$  indicates less scattering of light as a result of bundling of thin fibers. On the other hand, coiling of helical fibrils forming thick supercoiled

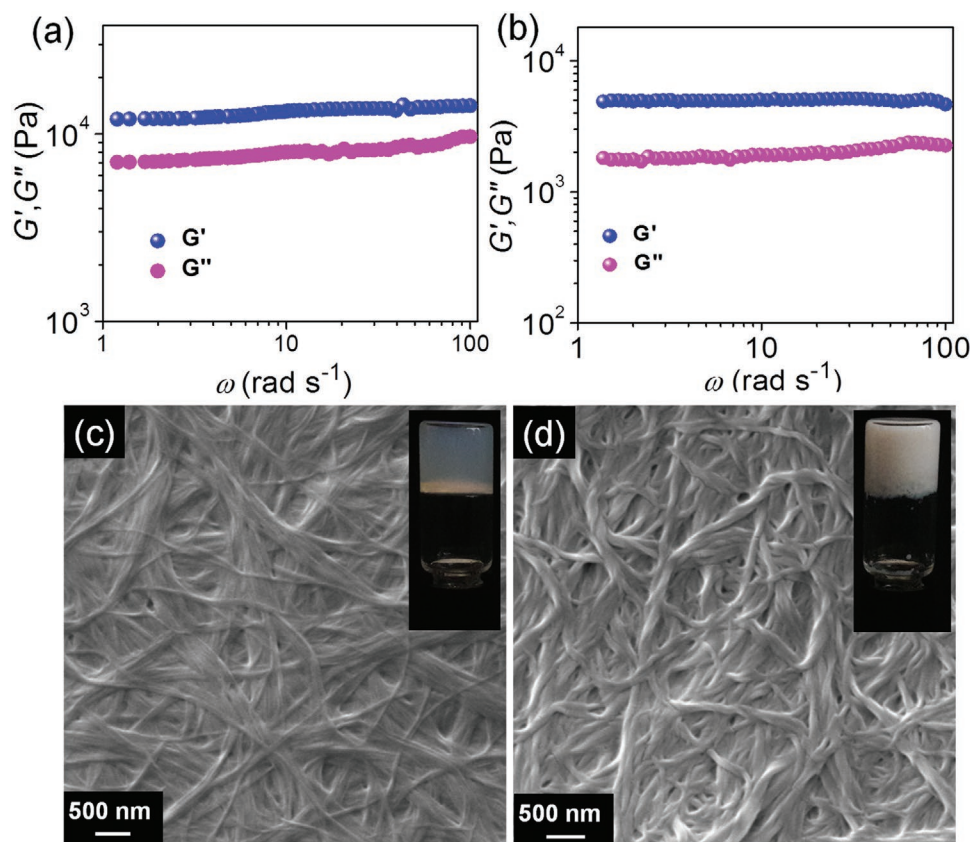


**Figure 3.** Plot of dynamic storage modulus ( $G'$ , blue) and loss modulus ( $G''$ , magenta) against angular frequency ( $\omega$ ) for a) **1** ( $8.8 \times 10^{-3}$  M) and b) **2** ( $23.6 \times 10^{-3}$  M) *n*-decane gels at 293 K, at a strain amplitude ( $\gamma$ ) of 0.01. SEM images of c) **1** and d) **2** *n*-decane gels. Inset shows the photographs of the corresponding *n*-decane gels under normal light.



fibers in  $2_{\text{gel}}$  scatter light in a greater extent and thus makes gel opaque.

Formation of nonhelical and helical 1D assemblies by **1** and **2** in *n*-decane, respectively, can be considered as a result of cooperative involvement of various noncovalent motifs including alkoxy side chains, amide functional group, and  $\pi$ -conjugated units. FT-IR spectrum of **1** revealed H-bonded N–H stretching frequency at  $3260\text{ cm}^{-1}$ , the amide I band at  $1643\text{ cm}^{-1}$ , and the amide II band at  $1518\text{ cm}^{-1}$ , indicating the involvement of intermolecular H-bonding in the assembly process (Figure S3 upper panel, Supporting Information).<sup>[36,53]</sup> However, the same peaks were shifted to  $3283$ ,  $1649$ , and  $1518\text{ cm}^{-1}$ , respectively, for **2** (Figure S3 lower panel, Supporting Information), which clearly signifies weakening of the amide H-bonding. Moreover, a significant shift in the amide I band was observed for xerogel films of **1** and **2** in comparison to their monomers in  $\text{CDCl}_3$ , corroborating to the intermolecular amide H-bonding in the gel state (Figure S4, Supporting Information). This observation was further supported by comparing the shift of symmetric and asymmetric  $-\text{CH}_2$  vibrations of both **1** and **2** xerogel films (Figure S5, Supporting Information). FT-IR spectrum of **1** displayed symmetric and asymmetric  $-\text{CH}_2$  vibrations around  $2848$  and  $2918\text{ cm}^{-1}$ , respectively. On the other hand, a shift in the symmetric and asymmetric  $-\text{CH}_2$  vibrations to  $2870$  and  $2924\text{ cm}^{-1}$ , respectively, was noticed in the case of **2**. These results indicate that linear alkoxy chains of **1** are in all *trans* configuration and

interdigitated, whereas the branched chiral alkoxy chains of **2** remain non-interdigitated.<sup>[53]</sup>

To understand the role of molecular packing on morphological properties and gel strength of **1** and **2**, we have carried out wide-angle X-ray scattering (WAXS) analysis. Figure 4a shows the WAXS pattern of **1** xerogel exhibiting two well-resolved peaks with a reciprocal *d*-spacing ratio of 1:2. The two intense sharp diffraction bands observed at  $50.7\text{ \AA}$  (001) and  $25.4\text{ \AA}$  (002) indicate a long-range lamellar type arrangement of the molecules.<sup>[53–56]</sup> The intense sharp peak at  $50.7\text{ \AA}$  corresponds to the width of a single 1D layer of the molecules, when two molecules of **1** are oriented from the opposite direction as shown in Figure 4b. In addition, the H-bonded intermolecular distance between the secondary amides is found to be  $\approx 4.3\text{ \AA}$ .<sup>[53,57,58]</sup> As seen in Figure 4c, the xerogel film of **2** shows a significant difference along with a larger set of reflections at  $34.6$ ,  $17.4$ ,  $15.3$ ,  $11.4$ ,  $5.2$ ,  $4.6$ , and  $4.2\text{ \AA}$ . The intense reflection at  $34.6\text{ \AA}$  (001) followed by a weak reflection at  $17.4\text{ \AA}$  (002) with a *d*-spacing ratio of 1:1/2 confirms lamellar arrangement of **2**. However, the first peak at  $34.6\text{ \AA}$  corresponds to the intercolumnar period as shown in Figure 4d<sup>[56]</sup> and the  $4.6\text{ \AA}$  peak to the H-bonded distance between the secondary amides. Furthermore, the lamellar arrangement of the molecules in **2** changes to a tilted fashion to allow for the  $\pi$ -stacking interaction and thereby leading to the formation of a long-range helical lamellar assembly. Comparison between the H-bonding distance between **1** and **2** clearly shows that the assembly of **1** is much stronger than that of **2**.

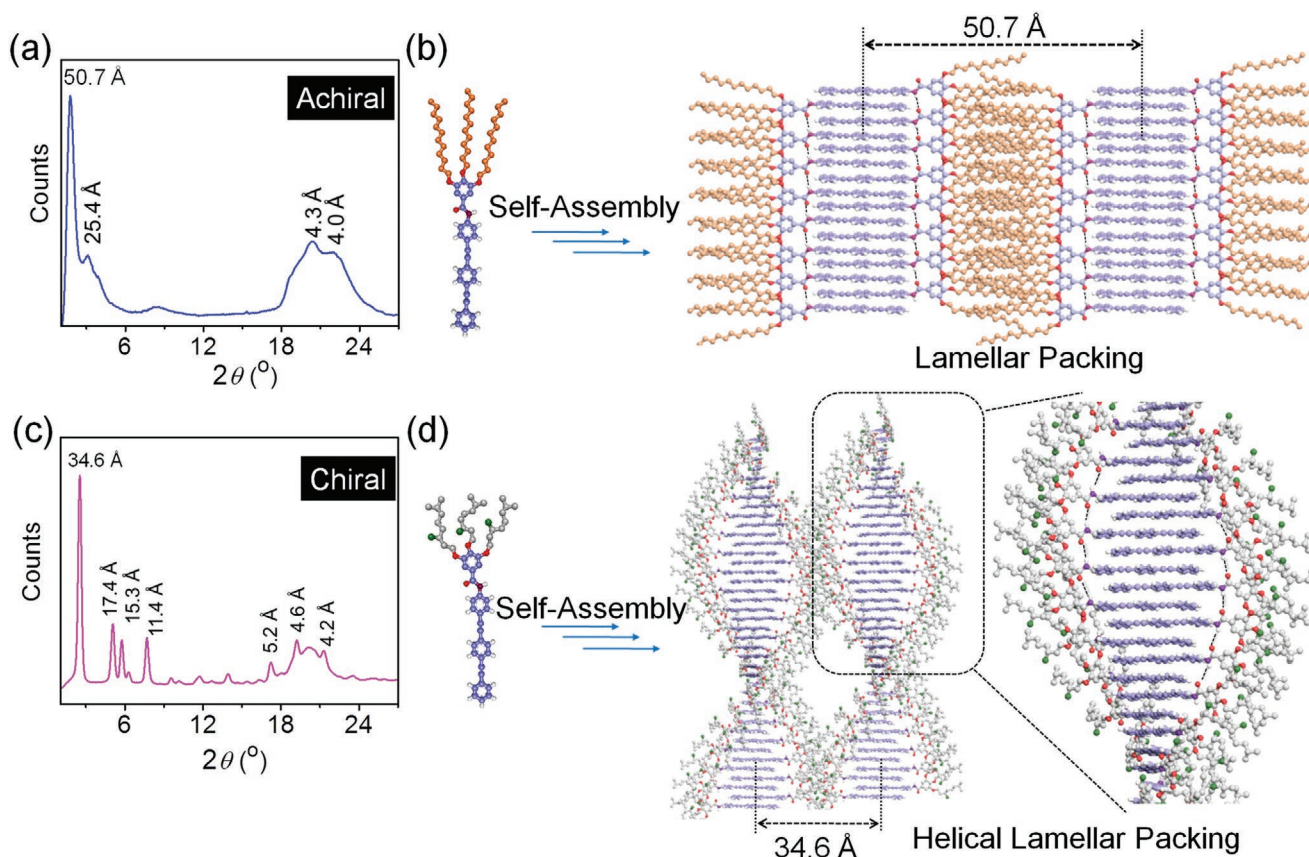


**Figure 4.** WAXS pattern of a)  $1_{\text{agg}}$  and c)  $2_{\text{agg}}$  in the xerogel state. Schematic representation of the *n*-decane assemblies of b)  $1_{\text{agg}}$  and d)  $2_{\text{agg}}$ .



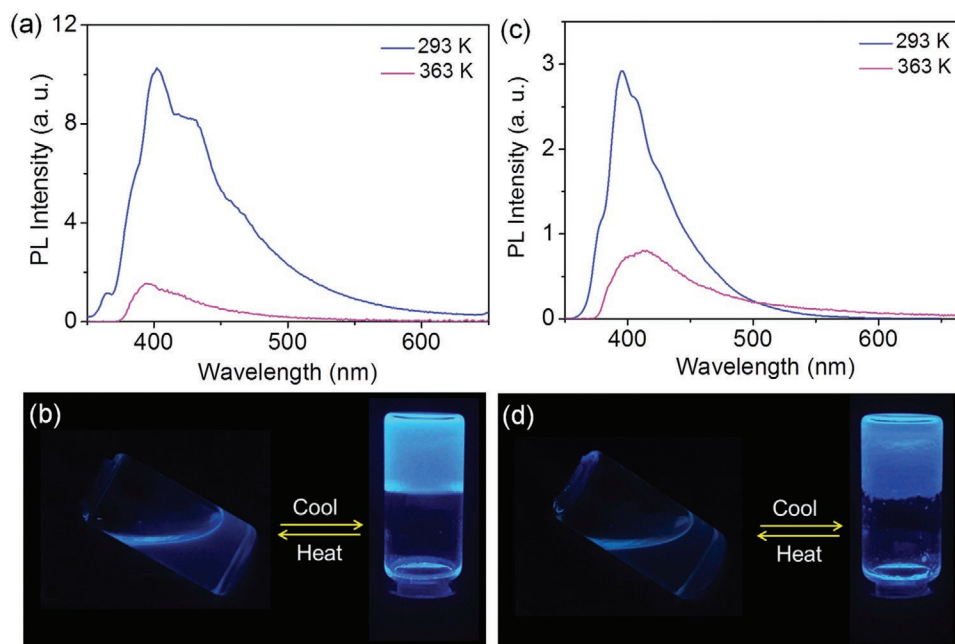


**Figure 5.** Emission spectra ( $\lambda_{\text{ex}} = 340$  nm) of *n*-decane gels (293 K) and the corresponding sols (363 K) of a) **1** and c) **2**. Photographs of the corresponding *n*-decane gels and sols of b) **1** and d) **2** under the illumination of 365 nm UV light.

Interestingly, the gels formed by both **1** and **2** are found to be emissive in the blue region (**Figure 5**). In comparison to the *n*-decane gel of **2** ( $\lambda_{\text{max}} = 395$  nm), the emission maximum of **1**<sub>gel</sub> was found to be slightly red-shifted ( $\lambda_{\text{max}} = 402$  nm), which points toward the stronger aggregation between the PE chromophores of the latter in presence of linear achiral alkoxy chains. However, in the case of **2**, the presence of asymmetric carbon centers reduces the interaction between the chromophores leading to the formation of a weak gel with a blue-shifted emission maximum. Furthermore, the solutions formed by heating the corresponding gels at higher temperature (363 K) were found to be less emissive (**Figure 5b,d**). In fact, the self-assembly induced sol to gel transition resulted in nearly 6.6 and 3.7 times enhancement in the emission

intensity of **1** and **2**, respectively, which indicate that the SIEE behavior of these molecules in the gel state<sup>[59–61]</sup> by preventing rotation of PE chromophore.<sup>[25–28]</sup> This has been further confirmed with the help of fluorescence microscopy studies, which revealed the strong solid-state emission of **1**<sub>gel</sub> and **2**<sub>gel</sub> (**Figure 6a,b**). Fluorescence microscopy images display the presence of blue emissive entangled fibers and densely coiled helical fibers for **1**<sub>gel</sub> and **2**<sub>gel</sub>, respectively.

The SIEE behavior of both **1** and **2** was further studied by measuring the fluorescence decay profiles of monomeric species in chloroform and self-assembled aggregates in *n*-decane (**Figure S6**, Supporting Information). **1**<sub>agg</sub> in *n*-decane exhibited a biexponential decay (emission monitored at  $\lambda_{\text{em}} = 382$  nm) having lifetimes of 0.15 (98.22%) and 1.10 ns (1.78%), whereas

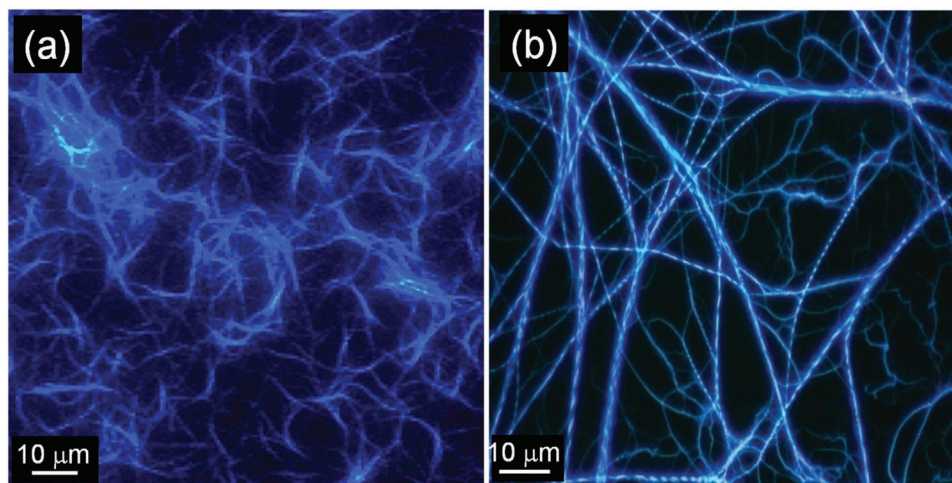


**Figure 6.** Fluorescence microscopy images of a) **1** and b) **2** *n*-decane xerogels.

**Table 2.** Photophysical parameters of **1** and **2** in different conditions.

Compound	$\Phi_f$	$\tau$ [ns]	$k_r$ [ $s^{-1}$ ] <sup>a)</sup>	$k_{nr}$ [ $s^{-1}$ ] <sup>b)</sup>	$k_r/k_{nr}$
1 in CHCl <sub>3</sub>	0.02	0.08	$2.67 \times 10^8$	$1.31 \times 10^{10}$	0.02
1 <sub>agg</sub> in <i>n</i> -decane	0.34	0.15 <sup>c)</sup>	$2.24 \times 10^9$	$4.34 \times 10^9$	0.52
2 in CHCl <sub>3</sub>	0.02	0.15	$1.38 \times 10^8$	$6.76 \times 10^9$	0.02
2 <sub>agg</sub> in <i>n</i> -decane	0.25	0.06 <sup>c)</sup>	$3.91 \times 10^9$	$1.17 \times 10^{10}$	0.33

<sup>a)</sup> $k_r$  is radiative decay rate; <sup>b)</sup> $k_{nr}$  is nonradiative decay rate; <sup>c)</sup>Average fluorescence lifetime ( $\tau_{av}$ ).

monomers of **1** in chloroform ( $\lambda_{em} = 372$  nm) exhibited a mono-exponential decay with lifetime of 0.075 ns (Figure S6a, Supporting Information). The increase in the lifetime values of **1**<sub>agg</sub> can be correlated to the formation of H-type aggregates in *n*-decane, which has also been confirmed from the blue shift in the absorption maximum from 333 to 307 nm (Figure 1a). As in the case of **1**<sub>agg</sub> in *n*-decane, the fluorescence decay profile of **2**<sub>agg</sub> in *n*-decane ( $\lambda_{em} = 381$  nm) was found to follow a biexponential decay with lifetime values 0.06 (81.76%) and 0.18 ns (18.24%) and a monoexponential decay with lifetime value of 0.15 ns in the monomeric state ( $\lambda_{em} = 367$  nm) (Figure S6b, Supporting Information). The decrease in lifetime value of the major emitting component of **2**<sub>agg</sub> in *n*-decane when compared to that of the monomer in chloroform indicates an assembly different from **1**<sub>agg</sub> in *n*-decane. The photophysical parameters of **1** and **2** in their monomeric and self-assembled states have been summarized in Table 2. These data reveal that the *n*-decane aggregates of both **1** and **2** exhibit higher  $k_r/k_{nr}$  values of 0.52, 0.33, respectively, than that of the monomeric state in CHCl<sub>3</sub> ( $k_r/k_{nr}$  values of 0.02, for both **1** and **2**), confirming the SIEE behavior.

### 3. Conclusion

In summary, we have established that the self-assembly of amide functionalized PE derivatives substituted with linear achiral **1** and branched chiral **2** alkoxy side chains result in highly luminescent gels comprising of 1D fibers. Absorption and emission spectroscopy studies have revealed that both the molecules undergo aggregation in *n*-decane at lower concentrations resulting in enhanced blue fluorescence. Above a critical concentration, self-assembly of both **1** and **2** led to gelation of linear and cyclic nonpolar solvents. The observed SIEE phenomenon in compounds **1** and **2** is attributed to the restriction of rotation of the PE chromophores in the gel state. Comparison of the optical properties between the gels of **1** and **2** revealed relatively stronger emission with the former having achiral side chains.

### Supporting Information

Supporting Information is available from the Wiley Online Library or from the author.

### Acknowledgements

A.A. is grateful to the DST-SERB, Government of India, for a J. C. Bose National Fellowship (SB/S2/JCB-11/2014). G.D. acknowledges

CSIR, Government of India, for a research fellowship. The authors thank Kiran Mohan and Harish Raj V. (CSIR-NIIST) for TEM and SEM measurements, respectively.

### Conflict of Interest

The authors declare no conflict of interest.

### Keywords

$\pi$ -systems, fluorescence, gels, helicity, molecular assembly

Received: January 30, 2020

Revised: March 5, 2020

Published online: April 30, 2020

- [1] L. Maggini, D. Bonifazi, *Chem. Soc. Rev.* **2012**, *41*, 211.
- [2] S. Varughese, *J. Mater. Chem. C* **2014**, *2*, 3499.
- [3] S. S. Babu, V. K. Praveen, A. Ajayaghosh, *Chem. Rev.* **2014**, *114*, 1973.
- [4] Y. Sagara, S. Yamane, M. Mitani, C. Weder, T. Kato, *Adv. Mater.* **2016**, *28*, 1073.
- [5] P. Data, Y. Takeda, *Chem. - Asian J.* **2019**, *14*, 1613.
- [6] M. Gao, B. Z. Tang, *ACS Sens.* **2017**, *2*, 1382.
- [7] P. Anees, V. K. Praveen, K. K. Kartha, A. Ajayaghosh, in *Comprehensive Supramolecular Chemistry II*, Vol. 9 (Ed: C. Raston), Elsevier Ltd., Amsterdam **2017**.
- [8] V. K. Praveen, B. Vedhanarayanan, A. Mal, R. K. Mishra, A. Ajayaghosh, *Acc. Chem. Res.* **2020**, *53*, 496.
- [9] L. D. Lavis, R. T. Raines, *ACS Chem. Biol.* **2014**, *9*, 855.
- [10] J. Schill, A. P. H. J. Schenning, L. Brunsveld, *Macromol. Rapid Commun.* **2015**, *36*, 1306.
- [11] G. Feng, R. T. K. Kwok, B. Z. Tang, B. Liu, *Appl. Phys. Rev.* **2017**, *4*, 021307.
- [12] *Photoluminescent Materials and Electroluminescent Devices* (Eds: N. Armaroli, H. J. Bolink), Topics in Current Chemistry Selections, Springer International Publishing, Switzerland **2017**.
- [13] Y. Chen, J. W. Y. Lam, R. T. K. Kwok, B. Liu, B. Z. Tang, *Mater. Horiz.* **2019**, *6*, 428.
- [14] S. S. Babu, V. K. Praveen, K. K. Kartha, S. Mahesh, A. Ajayaghosh, *Chem. - Asian J.* **2014**, *9*, 1830.
- [15] F. Lu, T. Nakanishi, *Adv. Opt. Mater.* **2019**, *7*, 1900176.
- [16] J. Mei, N. L. C. Leung, R. T. K. Kwok, J. W. Y. Lam, B. Z. Tang, *Chem. Rev.* **2015**, *115*, 11718.
- [17] J. Li, J. Wang, H. Li, N. Song, D. Wang, B. Z. Tang, *Chem. Soc. Rev.* **2020**, *49*, 1144.
- [18] P. Shen, Z. Zhuang, Z. Zhao, B. Z. Tang, *J. Mater. Chem. C* **2018**, *6*, 11835.
- [19] B. K. An, J. Gierschner, S. Y. Park, *Acc. Chem. Res.* **2012**, *45*, 544.
- [20] F. Aparicio, S. Cherumukil, A. Ajayaghosh, L. Sánchez, *Langmuir* **2016**, *32*, 284.
- [21] M. Martínez-Abadía, R. Giménez, M. B. Ros, *Adv. Mater.* **2018**, *30*, 1704161.
- [22] J. Zhao, Z. Chi, Z. Yang, Z. Mao, Y. Zhang, E. Ubba, Z. Chi, *Mater. Chem. Front.* **2018**, *2*, 1595.
- [23] D. D. La, S. V. Bhosale, L. A. Jones, S. V. Bhosale, *ACS Appl. Mater. Interfaces* **2018**, *10*, 12189.
- [24] V. S. Padalkar, S. Seki, *Chem. Soc. Rev.* **2016**, *45*, 169.
- [25] M. Levitus, K. Schmieder, H. Ricks, K. D. Shimizu, U. H. F. Bunz, M. A. Garcia-Garibay, *J. Am. Chem. Soc.* **2001**, *123*, 4259.
- [26] M. Levitus, G. Zepeda, H. Dang, C. Godinez, T. A. V. Khuong, K. Schmieder, M. A. Garcia-Garibay, *J. Org. Chem.* **2001**, *66*, 3188.

- [27] S. K. Albert, H. V. P. Thelu, M. Golla, N. Krishnan, S. Chaudhary, R. Varghese, *Angew. Chem.* **2014**, *126*, 8492; S. K. Albert, H. V. P. Thelu, M. Golla, N. Krishnan, S. Chaudhary, R. Varghese, *Angew. Chem. Int. Ed.* **2014**, *53*, 8352.
- [28] S. Roy, D. Samanta, P. Kumar, T. K. Maji, *Chem. Commun.* **2018**, *54*, 275.
- [29] D. S. Philips, K. K. Kartha, A. T. Politi, T. Krüger, R. Q. Albuquerque, G. Fernández, *Angew. Chem.* **2019**, *131*, 4782; D. S. Philips, K. K. Kartha, A. T. Politi, T. Krüger, R. Q. Albuquerque, G. Fernández, *Angew. Chem. Int. Ed.* **2019**, *58*, 4732.
- [30] A. Ajayaghosh, R. Varghese, V. K. Praveen, S. Mahesh, *Angew. Chem.* **2006**, *118*, 3339; A. Ajayaghosh, R. Varghese, V. K. Praveen, S. Mahesh, *Angew. Chem. Int. Ed.* **2006**, *45*, 3261.
- [31] A. Gopal, R. Varghese, A. Ajayaghosh, *Chem. - Asian J.* **2012**, *7*, 2061.
- [32] A. Gopal, M. Hifsudheen, S. Furumi, M. Takeuchi, A. Ajayaghosh, *Angew. Chem.* **2012**, *124*, 10657; A. Gopal, M. Hifsudheen, S. Furumi, M. Takeuchi, A. Ajayaghosh, *Angew. Chem. Int. Ed.* **2012**, *51*, 10505.
- [33] R. Thirumalai, R. D. Mukhopadhyay, V. K. Praveen, A. Ajayaghosh, *Sci. Rep.* **2015**, *5*, 09842.
- [34] S. Cherumukkil, S. Ghosh, V. K. Praveen, A. Ajayaghosh, *Chem. Sci.* **2017**, *8*, 5644.
- [35] M. Hifsudheen, R. K. Mishra, B. Vedhanarayanan, V. K. Praveen, A. Ajayaghosh, *Angew. Chem.* **2017**, *129*, 12808; M. Hifsudheen, R. K. Mishra, B. Vedhanarayanan, V. K. Praveen, A. Ajayaghosh, *Angew. Chem. Int. Ed.* **2017**, *56*, 12634.
- [36] F. García, L. Sánchez, *J. Am. Chem. Soc.* **2012**, *134*, 734.
- [37] A. Sandeep, V. K. Praveen, D. S. Shankar Rao, S. Krishna Prasad, A. Ajayaghosh, *ACS Omega* **2018**, *3*, 4392.
- [38] K. K. Kartha, V. S. Nair, V. K. Praveen, M. Takeuchi, A. Ajayaghosh, *J. Mater. Chem. C* **2019**, *7*, 1292.
- [39] R. van der Weegen, A. J. P. Teunissen, E. W. Meijer, *Chem. - Eur. J.* **2017**, *23*, 3773.
- [40] H. M. M. ten Eikelder, A. J. Markvoort, T. F. A. de Greef, P. A. J. Hilbers, *J. Phys. Chem. B* **2012**, *116*, 5291.
- [41] B. Adelizzi, I. A. W. Filot, A. R. A. Palmans, E. W. Meijer, *Chem. - Eur. J.* **2017**, *23*, 6103.
- [42] A. Langenstroer, K. K. Kartha, Y. Dorca, J. Droste, V. Stepanenko, R. Q. Albuquerque, M. R. Hansen, L. Sánchez, G. Fernández, *J. Am. Chem. Soc.* **2019**, *141*, 5192.
- [43] A. Sandeep, V. K. Praveen, K. K. Kartha, V. Karunakaran, A. Ajayaghosh, *Chem. Sci.* **2016**, *7*, 4460.
- [44] S. Ogi, V. Stepanenko, K. Sugiyasu, M. Takeuchi, F. Würthner, *J. Am. Chem. Soc.* **2015**, *137*, 3300.
- [45] M. Endo, T. Fukui, S. H. Jung, S. Yagai, M. Takeuchi, K. Sugiyasu, *J. Am. Chem. Soc.* **2016**, *138*, 14347.
- [46] D. D. Prabhu, K. Aratsu, Y. Kitamoto, H. Ouchi, T. Ohba, M. J. Hollamby, N. Shimizu, H. Takagi, R. Haruki, S.-i. Adachi, S. Yagai, *Sci. Adv.* **2018**, *4*, eaat8466.
- [47] E. E. Greciano, B. Matarranz, L. Sánchez, *Angew. Chem.* **2018**, *130*, 4787; E. E. Greciano, B. Matarranz, L. Sánchez, *Angew. Chem. Int. Ed.* **2018**, *57*, 4697.
- [48] F. Li, X. Li, Y. Wang, X. Zhang, *Angew. Chem.* **2019**, *131*, 18162; F. Li, X. Li, Y. Wang, X. Zhang, *Angew. Chem. Int. Ed.* **2019**, *58*, 17994.
- [49] A. Osypenko, E. Moulin, O. Gavot, G. Fuks, M. Maaloum, M. A. J. Koenis, W. J. Buma, N. Giuseppone, *Chem. - Eur. J.* **2019**, *25*, 13008.
- [50] S. Srinivasan, S. S. Babu, V. K. Praveen, A. Ajayaghosh, *Angew. Chem.* **2008**, *120*, 5830; S. Srinivasan, S. S. Babu, V. K. Praveen, A. Ajayaghosh, *Angew. Chem. Int. Ed.* **2008**, *47*, 5746.
- [51] K. V. Rao, K. K. R. Datta, M. Eswaramoorthy, S. J. George, *Adv. Mater.* **2013**, *25*, 1713.
- [52] R. D. Mukhopadhyay, G. Das, A. Ajayaghosh, *Nat. Commun.* **2018**, *9*, 1987.
- [53] J. M. Malicka, A. Sandeep, F. Monti, E. Bandini, M. Gazzano, C. Ranjith, V. K. Praveen, A. Ajayaghosh, N. Armaroli, *Chem. - Eur. J.* **2013**, *19*, 12991.
- [54] J. H. Ryu, E. Lee, Y. B. Lim, M. Lee, *J. Am. Chem. Soc.* **2007**, *129*, 4808.
- [55] H. Cao, Q. Yuan, X. Zhu, Y. P. Zhao, M. Liu, *Langmuir* **2012**, *28*, 15410.
- [56] A. Sarbu, L. Biniek, J.-M. Guenet, P. J. Mésini, M. Brinkmann, *J. Mater. Chem. C* **2015**, *3*, 1235.
- [57] F. D. Lewis, J.-S. Yang, C. L. Stern, *J. Am. Chem. Soc.* **1996**, *118*, 2772.
- [58] R. Abbel, R. van Der Weegen, W. Pisula, M. Surin, P. Leclère, R. Lazzaroni, E. W. Meijer, A. P. H. J. Schenning, *Chem. - Eur. J.* **2009**, *15*, 9737.
- [59] M. K. Nayak, B.-H. Kim, J. E. Kwon, S. Park, J. Seo, J. W. Chung, S. Y. Park, *Chem. - Eur. J.* **2010**, *16*, 7437.
- [60] P. Rajamalli, S. Atta, S. Maity, E. Prasad, *Chem. Commun.* **2013**, *49*, 1744.
- [61] Z. Wang, J. Nie, W. Qin, Q. Hu, B. Z. Tang, *Nat. Commun.* **2016**, *7*, 12033.

## Self-Assembly

# Tweaking a BODIPY Spherical Self-Assembly to 2D Supramolecular Polymers Facilitates Excited-State Cascade Energy Transfer

Gourab Das, Sandeep Cherumukkil, Akhil Padmakumar, Vijay B. Banakar, Vakayil K. Praveen,\* and Ayyappanpillai Ajayaghosh\*

In memory of Professor M. V. George

**Abstract:** Excited state properties such as emission, exciton transport, electron transfer, etc., are strongly dependent on the shape, size and molecular arrangement of chromophore based supramolecular architectures. Herein, we demonstrate creation and control of distinct supramolecular energy landscapes for the reversible control of the excited-state emission processes through cascade energy transfer in chromophore assemblies, facilitated by an unprecedented solvent effect. In methylcyclohexane, a tailor-made Y-shaped BODIPY derivative self-assembles to form an unusual spherical architecture of 400–1200 nm size, which exhibits a single emission at 540 nm upon 475 nm excitation through a normal excitation deactivation process. However, in *n*-decane, the same BODIPY derivative forms two-dimensional supramolecular sheets, exhibiting multiple emission peaks at 540, 610, 650, 725 and 790 nm with 475 nm excitation due to cascade energy transfer. Further control on the morphology and excitation energy transfer is possible with variable solvent composition and ultrasound stimulation, resulting in enhanced near-infrared emission with an overall pseudo Stokes shift of  $7105\text{ cm}^{-1}$ .

## Introduction

Creation of supramolecular architectures of different shapes, sizes and properties is the fundamental step to realize next generation complex multi-component systems with specific functions and applications.<sup>[1]</sup> In this context, chromophore based supramolecular systems have been at the center stage due to their reversible optoelectronic properties that can be modulated through the molecular assembly.<sup>[2]</sup> In recent times, several approaches have been introduced for the controlled assembly of  $\pi$ -conjugated molecules.<sup>[3–5]</sup> Living supramolecular polymerization,<sup>[3,5a]</sup> crystallization-driven


self-assembly<sup>[6]</sup> and seeded supramolecular polymerization<sup>[7]</sup> are examples that control the length and dimension of supramolecular structures through kinetic and thermodynamic control of self-assembly. While living supramolecular polymerization is undoubtedly a powerful tool for the precise control of molecular self-assembly, it cannot be applied as a general strategy. Therefore, different kinds of external stimuli such as light,<sup>[8]</sup> pH,<sup>[9]</sup> redox,<sup>[10]</sup> enzyme,<sup>[11]</sup> ultrasound,<sup>[12]</sup> and solvents,<sup>[13]</sup> have been exploited for controlled supramolecular polymerization of functional  $\pi$ -systems.<sup>[14]</sup>

Cascade energy transfer in supramolecular architectures is a fundamentally important process applicable to the biological and materials world.<sup>[15]</sup> For example, the phycobilisomes, which is the major light-harvesting complex in cyanobacteria and red algae, is considered one of the most efficient light-harvesting systems with more than 95% efficiency due to the cascade energy transfer.<sup>[15a,e]</sup> Though inferior to natural light-harvesting systems, the artificial supramolecular systems, due to the presence of aggregates of varying energy levels with large anisotropy, provides ample opportunities to simulate the natural light-harvesting processes. In this context, molecular assemblies of certain chromophores having the mixture of aggregates with different levels of electronic coupling have been shown to facilitate cascade energy transfer leading to red-shifted emission.<sup>[16]</sup> This red-shift can lead either to a broad emission, if aggregates of closely matching energy levels are involved or to multiple emission if aggregates of discrete energy levels are present in the hierarchical self-assembly. However, the latter type of molecular assembly resulting in multiple emission covering the entire visible-NIR region upon a single excitation remains a challenge.

Among different chromophores, 4,4-difluoro-4-bora-3a-4a-diaza-*s*-indacene (BODIPY) is an excellent choice for creating supramolecular optoelectronic materials due to their photostability, high molar absorptivity and sensitive fluorescence features.<sup>[17–20]</sup> Here, we demonstrate how distinct energy landscapes can be obtained by creating different morphological features that facilitate reversible modulation of emission behavior. This is possible by tweaking the self-assembly of *meso*  $\pi$ -extended BODIPY dyes **1–3** (Figure 1 a) with solvents as established in this work. The high ground state dipole moment ( $\mu_g = 7.53\text{ D}$ ) of Y-shaped **1** and **2** drives the self-assembly in cyclic nonpolar solvents such as methylcyclohexane (MCH) or *trans*-decalin, initially resulting in 10–20 nm spheres, which transform into large spheres of 600–800 nm with time as confirmed by dynamic light scattering

[\*] G. Das, Dr. S. Cherumukkil, A. Padmakumar, V. B. Banakar, Dr. V. K. Praveen, Prof. Dr. A. Ajayaghosh  
 Photosciences and Photonics Section, Chemical Sciences and Technology Division, CSIR-National Institute for Interdisciplinary Science and Technology (CSIR-NIIST)  
 Thiruvananthapuram, Kerala 695019 (India)  
 E-mail: vkpraveen@niist.res.in  
 ajayaghosh@niist.res.in

G. Das, A. Padmakumar, Dr. V. K. Praveen, Prof. Dr. A. Ajayaghosh  
 Academy of Scientific and Innovative Research (AcSIR)  
 Ghaziabad, Uttar Pradesh 201002 (India)

 Supporting information and the ORCID identification number(s) for the author(s) of this article can be found under <https://doi.org/10.1002/anie.202015390>.



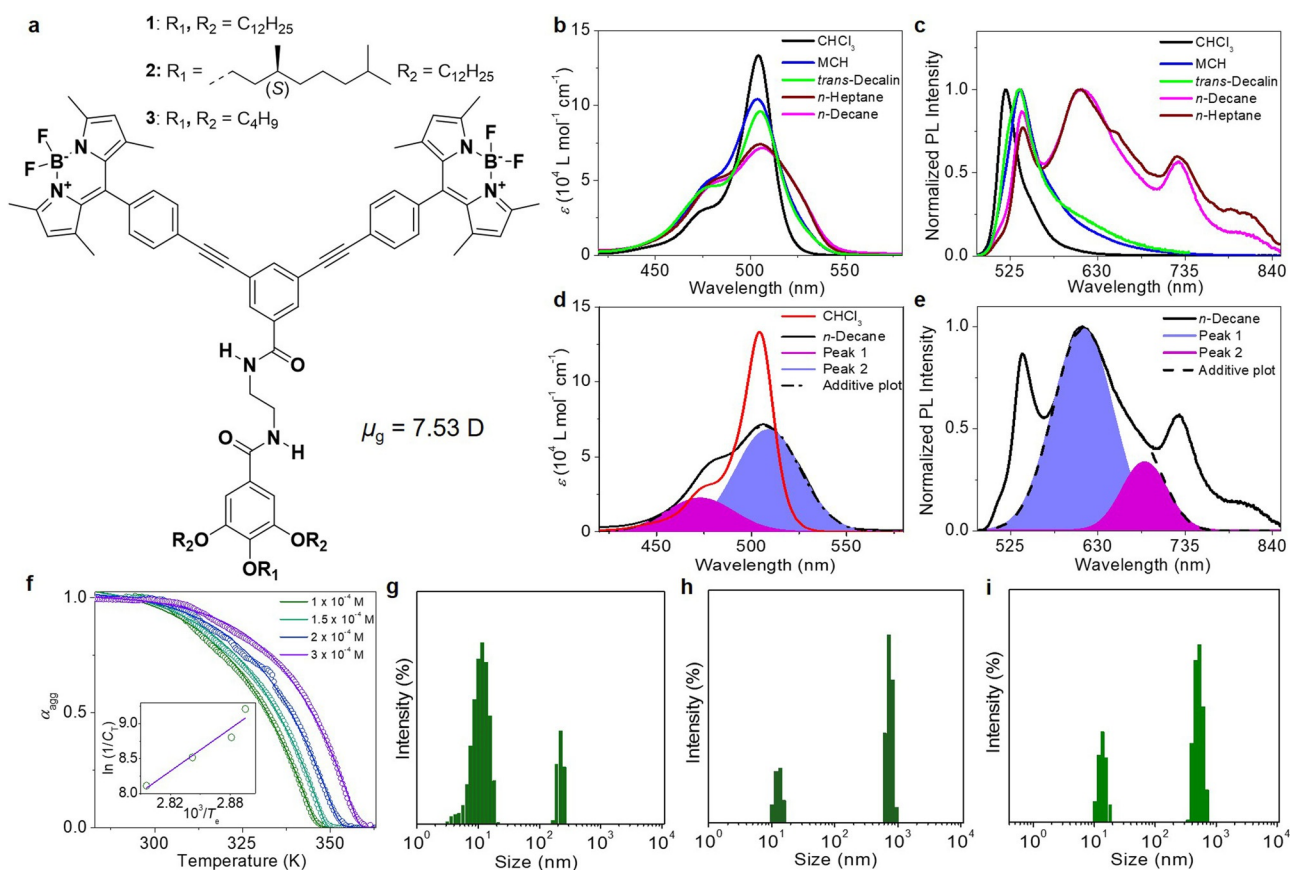


**Figure 1.** a) Molecular structures of the Y-shaped BODIPY derivatives **1–3**. b) Absorption (between 420–580 nm corresponding to the BODIPY chromophore) and c) normalized emission spectra ( $\lambda_{\text{ex}} = 475$  nm) of **1** in chloroform ( $1 \times 10^{-4}$  M), MCH, *trans*-decalin ( $3 \times 10^{-4}$  M) and *n*-decane, *n*-heptane ( $3 \times 10^{-4}$  M). Deconvoluted d) absorption and e) emission spectra of **1** in *n*-decane at 506 and 610 nm, respectively. f) The plot of  $\alpha_{\text{agg}}$  versus temperature at different concentrations of **1** in *n*-decane;  $\alpha_{\text{agg}}$  was calculated by monitoring the absorbance changes at 530 nm. Inset shows the van't Hoff plot obtained through the controlled cooling experiments of **1** in *n*-decane. DLS size distribution of **1** in MCH ( $3 \times 10^{-4}$  M): g) immediately after fast cooling, h) after aging the sample for 24 h, and i) after cooling at a controlled rate of  $1 \text{ K min}^{-1}$ .

(DLS) experiments. Evaporation of the MCH solution of **1** or **2** on a substrate resulted in an assembly of spherical structures, wherein each large sphere is surrounded by a layer of self-assembled nanospheres, appearing like a core-shell structure with an average size of 400–1200 nm. The spherical particles exhibited a normal emission spectrum with a single maximum at 540 nm. On the other hand, in linear nonpolar solvents such as *n*-heptane or *n*-decane, two-dimensional (2D) supramolecular sheets having broad emission comprising of 540, 610, 650, 725 and 790 nm bands are formed. Interestingly, the single and multiple emission could be reversibly controlled by tweaking the morphology between the spherical and 2D assemblies by changing the solvent composition. Molecule **3** having short alkyl chains failed to form either the spherical morphology or 2D sheets, revealing the importance of the alkyl chains in the self-assembly process. Ultrasound stimulation of the 2D sheets exhibited better efficiency for the successive energy transfer as evident by a 2.2-fold increase in the intensity of the near infrared (NIR) bands at 725 and 790 nm. The morphological features and the associated emission behavior described here are unprecedented and the origin of multiple emission ascribed is the manifestation of a cascade effect of the excitation energy

as established by time-resolved emission and anisotropy studies.

## Results and Discussion

After synthesizing **1–3** (Scheme S1–S3), we have studied their optical behavior and self-assembly processes (Figure 1 b,c and Figure S1). In  $\text{CHCl}_3$  ( $1 \times 10^{-4}$  M) at 295 K, the UV-vis absorption spectrum exhibited two maxima at 290 and 504 nm with a shoulder band around 475 nm. The broad absorption observed at 290 nm ( $\epsilon = 5.6 \times 10^4 \text{ M}^{-1} \text{ cm}^{-1}$ ) corresponds to the phenyleneethynylene moiety, whereas the narrow absorption feature at 504 nm ( $\epsilon = 1.3 \times 10^5 \text{ M}^{-1} \text{ cm}^{-1}$ ) implies the strong  $S_0 \rightarrow S_1$  electronic transition involving ( $0 \rightarrow 0$ ) vibrational states of the BODIPY chromophore. The band at 475 nm can be considered as the vibronic shoulder of  $S_0 \rightarrow S_1$  transition.<sup>[20]</sup> On the other hand, the absorption spectrum of **1** ( $3 \times 10^{-4}$  M) in MCH or *trans*-decalin, when heated to 363 K followed by cooling to 283 K at a rate of  $1 \text{ K min}^{-1}$ , exhibited an absorption maximum at 288 nm ( $\epsilon = 6.75 \times 10^4 \text{ M}^{-1} \text{ cm}^{-1}$ ), with a broad band ( $\lambda_{\text{max}} = 504 \text{ nm}$ ,  $\epsilon = 1.04 \times 10^5 \text{ M}^{-1} \text{ cm}^{-1}$ ) between 420–550 nm. Furthermore, **1** exhibits an emission

maximum at 520 nm ( $\Phi_F = 0.39$ ) in  $\text{CHCl}_3$ , whereas in MCH a red-shifted maximum at 540 nm ( $\Phi_F = 0.20$ ). These observations indicate aggregation of **1** in MCH as further confirmed by temperature-dependent  $^1\text{H}$  NMR, absorption and emission studies (Figures S2 and S3). Upon gradual reduction in temperature from 363 to 283 K, the intensity of the absorption maximum was reduced and the absorption spectrum corresponding to both BODIPY and phenyleneethynylene part became broad (Figure S3a). In contrast, the temperature-dependent emission studies showed a gradual increase in the intensity when **1** in MCH was cooled from 363 to 283 K, indicating aggregation-induced enhanced emission behavior (Figure S3b).<sup>[2a,21a]</sup> Since the phenyl ring attached at the *meso* position of BODIPY chromophore **1** is unsubstituted, rotational and vibrational motions are facilitated at higher temperature, leading to non-radiative deactivation of the excited state and less emission.<sup>[20a]</sup> However, upon gradual reduction in temperature, aggregation of **1** restricts the rotation and vibrational motion and activates radiative excited state decay to display enhanced emission. Aggregation of **1** in MCH at a concentration of  $3 \times 10^{-4}$  M was further confirmed from the plot of the fraction of aggregates ( $\alpha_{\text{agg}}$ ) of **1** with respect to temperature, revealing a non-sigmoidal cooling curve, which is characteristic of a co-operative self-assembly process (Figure S3c and Table S1).<sup>[21]</sup>

In *n*-decane or *n*-heptane ( $3 \times 10^{-4}$  M), the absorption spectra of **1** within 230–420 nm was almost similar to those in  $\text{CHCl}_3$  and MCH (Figure S1), however, the absorption corresponding to the BODIPY chromophore appeared much broader ( $\lambda_{\text{max}} = 506$  nm,  $\epsilon = 7.2 \times 10^4$  M $^{-1}$  cm $^{-1}$ ), with predominant shoulder bands in the lower and higher wavelength region (470 and 570 nm), indicating the formation of multiple aggregates (Figures 1b and S4). Surprisingly, the emission spectrum of **1** ( $3 \times 10^{-4}$  M) in *n*-decane or *n*-heptane exhibited an unusually broad band with multiple maxima at 540, 610, 650, 725 and 790 nm ( $\Phi_F = 0.14$ ). The peak at 650 nm is more resolved in *n*-heptane (Figure 1c). Deconvolution of the broad absorption peak (506 nm) obtained in *n*-decane shows two peaks at 473 and 509 nm, confirming the formation of aggregates (possibly mixture of both H- and J-type aggregates) (Figure 1d).<sup>[22]</sup> Deconvolution of the broad emission band at 610 nm in *n*-decane revealed two peaks at 612 and 686 nm (Figure 1e).

These observations were further confirmed from the temperature-dependent absorption and emission studies of **1** in *n*-decane (Figure S4, S5). At 363 K, **1** in *n*-decane displayed a sharp absorption band at 504 nm, which gradually reduced its intensity and became broad at 283 K (Figure S4a). The intensity of the emission spectrum of **1** in *n*-decane was initially found to increase with an appearance of a new peak at 725 nm upon reducing the temperature 363 to 348 K (Figure S5b, upper panel). Between 343 to 313 K, the emission intensity of the peak at 552 nm was found to gradually decrease with the appearance of a new peak at 600 nm (Figure S5b, middle panel). Further reduction in temperature to 283 K resulted in an overall enhancement in the intensity of emission profile with three distinct maxima at 552, 600 and 725 nm (Figure S5b, lower panel). A similar absorption and emission changes were also noticed at various

other concentrations of **1** in *n*-decane (Figure S4b–d, S5a). BODIPY derivatives are known to exhibit broad multiple emission in solid/semicrystalline powder form, however, not in any solvents.<sup>[19f,20d,e]</sup> While MCH and *n*-decane have more or less identical polarity, except for their difference in structure and shape (cyclic and linear), the observed difference in the emission behavior in these solvents could be associated with the hierarchical assembly of the BODIPYs.

Plots of  $\alpha_{\text{agg}}$  of **1** with respect to temperature revealed non-sigmoidal cooling curves for a wide range of concentrations ( $1 \times 10^{-4}$  to  $3 \times 10^{-4}$  M) in *n*-decane (Figure 1f and S4). The cooling curves thus obtained were fitted to an equilibrium model, characteristics of a co-operative self-assembly process.<sup>[21]</sup> Details of the thermodynamic parameters related to the fitting are summarized in Table S2. The plot of the natural logarithm of the reciprocal concentration of **1** against reciprocal of  $T_e$  exhibited a linear relationship (van't Hoff plot, Figure 1f inset). The thermodynamic parameters of **1** in *n*-decane were  $\Delta H^\circ = -84.26$  kJ mol $^{-1}$ ,  $\Delta S^\circ = -168.43$  J mol $^{-1}$  K $^{-1}$  and  $\Delta G^\circ = -34.07$  kJ mol $^{-1}$ , indicating that the self-assembly takes place through an enthalpically driven co-operative process. DLS experiments of **1** in MCH ( $3 \times 10^{-4}$  M) under fast cooling revealed the existence of two different bands with size distributions of 10–20 nm (80–90%) and 200–300 nm (10–20%) (Figure 1g). After aging for 24 h, the size of the aggregates increased to 600–800 nm (70%) while the population of the 10–20 nm size aggregates decreased to 30%, indicating a consecutive process taking place, where the initially formed smaller spherical aggregates were directly converted to bigger size assemblies without converting into the monomers (Figure 1h).<sup>[5b]</sup> However, a slow cooled ( $1$  K min $^{-1}$ ) solution exhibited almost similar size of the assemblies as obtained by aging (Figure 1i). No time-dependent changes were noticed in the case of aggregates of **1** in *n*-decane, implying that these aggregates have reached equilibrium when cooled at a controlled rate (Figure S6).

Transmission electron microscopy (TEM) images of the self-assembly in MCH ( $3 \times 10^{-4}$  M) exhibited a spherical morphology akin to a core-shell type structure<sup>[23]</sup> having broad size distributions of 400–1200 nm. The spheres from the fast-cooled solution of **1** in MCH have diameters between 400 and 600 nm (Figure 2a,b), which upon aging for 24 h showed a size increase of 600–1200 nm (Figure 2c,d). However, a slowly cooled solution ( $1$  K min $^{-1}$ ) resulted in spherical assemblies of 400–1000 nm (Figure S7). Magnified images of the spherical structures revealed a hyperdense core region having an average diameter of 200–900 nm (Figure 2b,d and S7b) and a less dense shell region of about 100–300 nm width. While these types of structures are common in the case of inorganic semiconductors, such structures are rare in the case of organic single molecular self-assembly. The solvent evaporation on the TEM grid may result in a thick core, around which excess nanospheres present in the mixture self-assemble to form a shell. On the other hand, from *n*-decane solution ( $3 \times 10^{-4}$  M), 2D sheet-like structures were obtained (Figure 2e,f and Figure S8). Cross-sectional analysis indicates an average height of  $1.9 \pm 0.1$  nm with marginal surface roughness. Upon increasing the concentration of **1** in *n*-decane ( $8 \times$

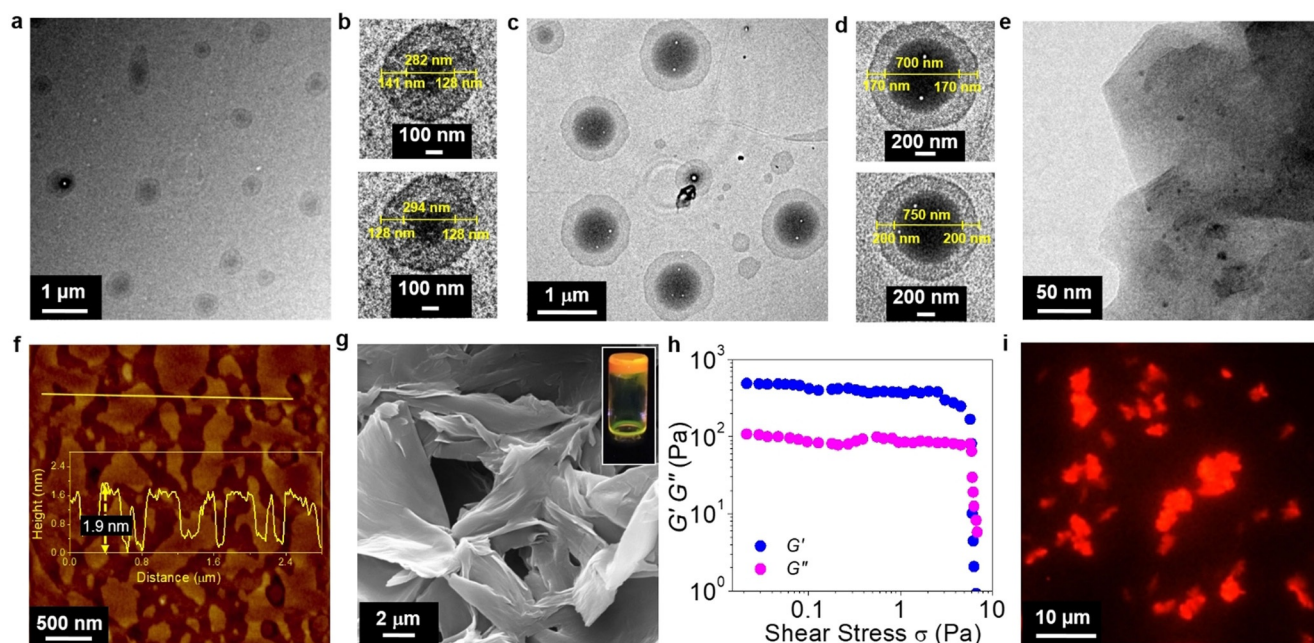


**Figure 2.** TEM images of **1** in MCH ( $3 \times 10^{-4}$  M), a) immediately after fast cooling and c) after aging the sample for 24 h. b, d) Magnified images corresponding to Figure 2a and c, respectively. e) TEM and f) AFM images of **1** in *n*-decane ( $3 \times 10^{-4}$  M). The height profile along the yellow line is shown in the inset of Figure 2f. g) SEM image of the *n*-decane gel ( $8 \times 10^{-3}$  M). Inset shows the photograph of the corresponding gel under the illumination of 365 nm UV light. h) The plot of dynamic storage ( $G'$ , blue) and loss modulus ( $G''$ , magenta) against shear stress ( $\sigma$ ) for *n*-decane gel ( $8 \times 10^{-3}$  M) at 298 K. Frequency ( $\nu$ ) was kept fixed at  $1 \text{ rad s}^{-1}$ . i) Fluorescence microscopy image of the diluted *n*-decane gel.

$10^{-3}$  M), the nanosheets were grown into large interconnected structures leading to an orange-red emitting gel (Figure 2g-i). However, **1** failed to form a gel in MCH (Figure S9). The viscoelastic nature of the *n*-decane gel is evident from the stress sweep experiments, which revealed the dependencies of storage modulus ( $G'$ ) and loss modulus ( $G''$ ) on the applied shear stress. Both the  $G'$  and  $G''$  were independent of applied stress up to 5.75 Pa, indicating the substantial elastic nature of the gel (Figure 2h).<sup>[24]</sup> These observations underpin the ability of **1** to undergo 2D supramolecular polymerization in *n*-decane.<sup>[4,25,26]</sup>

We hypothesized that, if the emission behavior is associated with morphological features, tweaking the spherical assembly to the 2D sheets may change the single emissive state to the multi-emissive one. Addition of different volume fractions ( $f = v/v$ ) of *n*-decane to **1** in MCH ( $3 \times 10^{-4}$  M), we found the spherical structure slowly changing to elongated sheets and then to large 2D sheets (Figure 3a-d). Upon increasing  $f$ , the intensity of the absorption of the BODIPY moiety ( $\lambda_{\text{max}} = 504 \text{ nm}$ ) gradually decreased with the appearance of a shoulder band at a higher wavelength. Interestingly, we could see multiple emission peaks at 600 and 725 nm in addition to the peak at 540 nm (Figure 3e). Similarly, upon addition of MCH to **1** in *n*-decane, the multiple emission changed to a single emission (Figure 3f). The reversibility in the emission feature along with the change in morphology underpins the role of the solvent-induced self-assembly<sup>[27]</sup> in perturbing the excited state properties.<sup>[28]</sup> Surprisingly, the intensities of the 540 and 600 nm bands were decreased while the intensity of the NIR emission band at 725 and 790 nm exhibited a 2.2 times enhancement upon sonication<sup>[12,24a,29]</sup> of

**1** in *n*-decane (Figure 3g). Similarly, the enhancement in NIR emission was also noticed when *n*-decane aggregates of **1** were cast as a film (Figure S10a). Upon sonication, the absorption intensity was slightly reduced (Figure S10b) and the formation of multilayered 2D structures was observed by TEM analysis (Figure S10c,d). In contrast, when sonication was applied to **1** aggregates in MCH, the emission profile remained almost unaltered (Figure 3h). The results of these studies indicate that sonication and film formation favor multilayered 2D assemblies of **1**, which enhance the NIR emission.

A deeper understanding of the origin of the multi-emission feature was possible with time-resolved emission spectral (TRES) studies of **1** in MCH and *n*-decane ( $3 \times 10^{-4}$  M) (Figure 4a-f). The emission spectra at different time scales in MCH ( $\lambda_{\text{ex}} = 375 \text{ nm}$ ) showed an increase in the intensity at 550 nm up to 280 ps followed by a gradual decrease in the intensity while retaining the nature of the emission profile up to 2.80 ns (Figure 4a). This observation indicates a normal excitation-deactivation process (Figure 4d). However, upon excitation in *n*-decane at 375 nm, a growth profile at 555 nm was observed within 32–210 ps (Figure 4b). With further increase in timescale up to 520 ps, the 555 nm emission intensity gradually decayed with a red-shift of the emission peak to 600 nm within the time scale of 950 ps. Thereafter, the emission peak at 600 nm showed a time-dependent decay up to a timescale of 2.40 ns. The time-dependent decay of the emission at a lower wavelength and the growth at the higher wavelength with dynamic red-shift of the emission are characteristic of energy migration from the excited states of lower-order aggregates (higher excited state



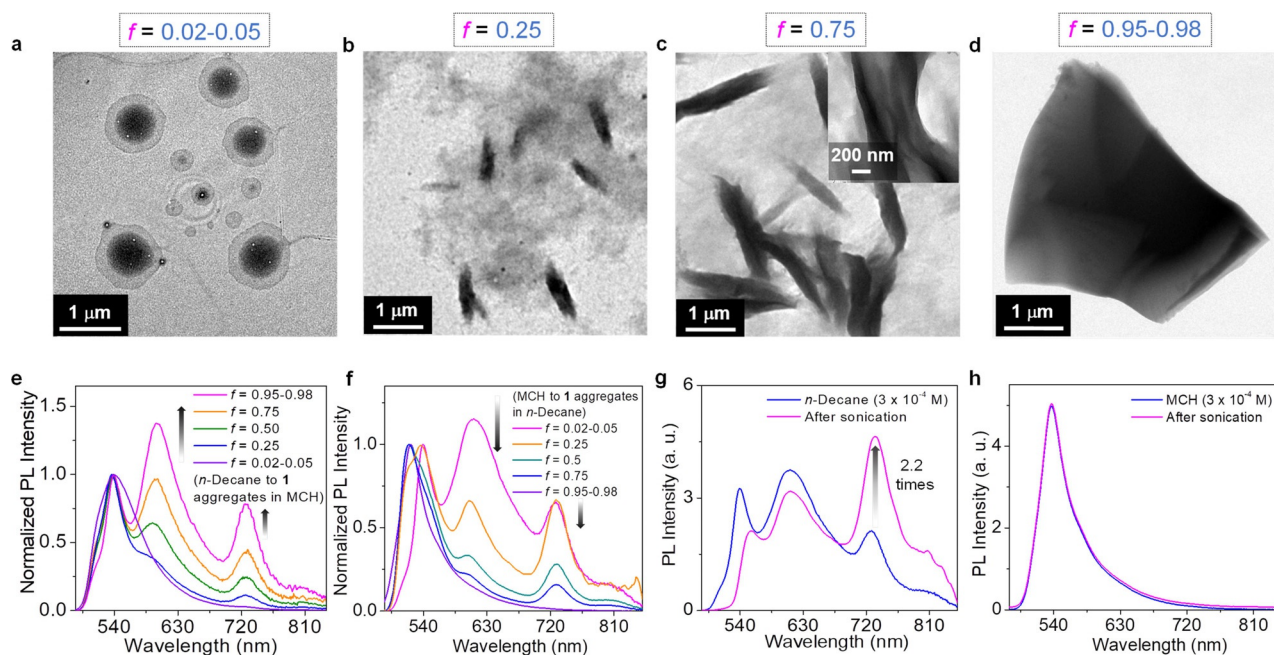


**Figure 3.** TEM images of aggregates of **1** upon increasing the volume fractions of *n*-decane in MCH (*f*): a) *f*=0.02–0.05, b) *f*=0.25, c) *f*=0.75 and d) *f*=0.95–0.98. Figure 3c inset shows the zoomed image. Changes in emission ( $\lambda_{\text{ex}}=475$  nm) upon varying the solvent compositions: e) addition of various fractions of *n*-decane to aggregates of **1** in MCH and f) addition of various fractions of MCH to aggregates of **1** in *n*-decane ( $3 \times 10^{-4}$  M). Emission spectra of **1** ( $\lambda_{\text{ex}}=475$  nm) in g) *n*-decane and h) MCH ( $3 \times 10^{-4}$  M), before (blue) and after (magenta) sonication.

energy) to the higher-order aggregates (lower excited state energy) leading to the multiple emission.<sup>[16]</sup> Figure 4e reveals that within 0.17 ns, the peak intensity at 555 nm reaches a maximum and then undergoes a rapid tri-exponential decay with time constants of 1.49 ns (44.76%), 5.82 ns (35.63%) and 0.25 ns (19.61%). The emission at 600 nm reaches the maximum at 0.25 ns with a negative pre-exponential. The fitted rise time value of 0.34 ns at 600 nm correlates with the 0.25 ns decay component observed at 555 nm, thus validating the energy migration process. Similarly, the 650 nm emission peak also reached the maximum at 0.35 ns, followed by a successive decay.

Since the multi-emissive nature is found to be strongly influenced by ultrasound, TRES analysis of the sonicated samples in *n*-decane was performed (Figure 4c). The initial increase in the emission profile at 555 nm within 30–160 ps exhibited a subsequent decrease in the intensity within a time scale of 390 ps, with the formation of a new red-shifted peak at 600 nm. The peak at 600 nm exhibited an increase in the emission intensity within 260–590 ps followed by a successive time-dependent decay. Within 650 ps, another peak at 725 nm (NIR region) was formed, which reached its maximum and then gradually decayed, showing a perfect correlation between 600 and 725 nm peaks, indicating energy transfer from the 600 nm emitting species. Plots of the normalized emission counts at different emission peaks and the time scale of the successive energy transfer is clear from Figure 4f. The peak intensity at 555 nm reached a maximum within 0.19 ns followed by decay, whereas the 600 nm emission reached its maximum at 0.41 ns. The rise time value (0.97 ns) obtained at 600 nm can be correlated with the decay component (0.81 ns) observed at 555 nm. In a similar fashion, 650 and 725 nm peak

reached their maximum within 0.49 and 0.56 ns, respectively and then decayed. A negative pre-exponential factor observed at 650 and 725 nm emission decays confirms the step-wise energy transfer from 555 to 600 nm, 600 to 650 nm, 650 to 725 nm and then a weak energy transfer from the 725 to 790 nm, suggesting multiple long-range cascade energy transfer.<sup>[6a,16b,c,20d,e]</sup> The BODIPY **2**, albeit having a chiral side chain, did not show any supramolecular chirality and exhibited the same behavior as of **1** with respect to the optical and morphological properties (Figures S11–S13).

Further insights on the cascade energy transfer could be obtained from time-resolved anisotropy studies (Figure 4g–i). In general, the loss of anisotropy of organized donors within an assembly occurs either through rotational motion or energy migration.<sup>[16,30]</sup> In *n*-decane, depolarization through rotational motion is less favored as spontaneous nucleation assists the formation of 2D assemblies and hence energy migration can be the possible pathway for depolarization.<sup>[16,30]</sup> At  $3 \times 10^{-4}$  M, **1** in *n*-decane exhibited an initial anisotropy value ( $r_0$ ) of 0.25 and reached the plateau region ( $r_\infty$ ) at 0.13 by losing the anisotropy with a decay time,  $\tau_r=45$  ps (Figure 4h). The  $r_0$  value of 0.25 at around zero time indicates that the initial orientation of the transition dipole moments has an angle of  $30^\circ$ .<sup>[31]</sup> On the other hand, at a similar concentration in MCH, the initial anisotropy ( $r_0$ ) was found to be 0.15, which reached the final anisotropy ( $r_\infty$ ) value of  $-0.04$  (Figure 4g). The difference in the initial anisotropy value indicates the random independent orientation of the chromophores in MCH, where a large angle ( $40^\circ$ ) exists between the excitation and emission dipole moments. Interestingly, the studies carried out in *n*-decane after sonication showed a higher initial anisotropy ( $r_0$ ) value of 0.32, where the angle ( $21^\circ$ )



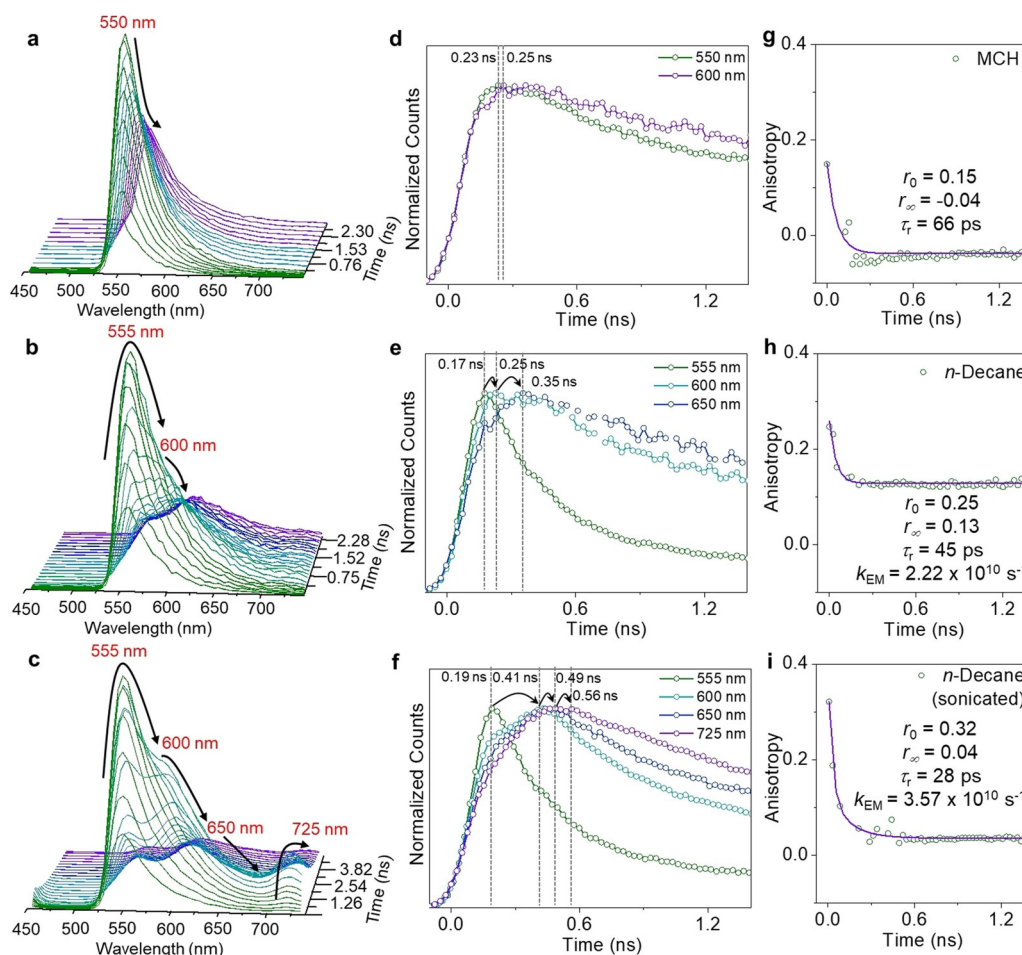


**Figure 4.** Time-resolved emission (TRES) of **1** in a) MCH, b) *n*-decane before sonication and c) after sonication. The normalized fluorescence decay curves in d) MCH, e) *n*-decane before sonication and f) after sonication; monitored at different emission wavelengths ( $3 \times 10^{-4}$  M,  $\lambda_{\text{ex}} = 375$  nm). Time-resolved fluorescence anisotropy decay in g) MCH ( $\lambda_{\text{em}} = 550$  nm), h) *n*-decane ( $\lambda_{\text{em}} = 555$  nm) before sonication and i) after sonication ( $3 \times 10^{-4}$  M,  $\lambda_{\text{ex}} = 375$  nm).

between the excitation and emission transition dipole moments was found to be much smaller in comparison to the other cases (Figure 4i). In addition, the final anisotropy ( $r_{\infty}$ ) value of 0.04 was reached within a short decay time ( $\tau_r$ ) of 28 ps. The anisotropy decay time  $\tau_r$ , which gives an estimation of the rate of energy migration ( $k_{\text{EM}}$ ) from the higher to the lower energy state,<sup>[16b,c]</sup> was found to be  $3.57 \times 10^{10}$  and  $2.22 \times 10^{10} \text{ s}^{-1}$  for sonicated and non-sonicated samples, respectively. The fast fluorescence depolarization and energy migration rate obtained in sonicated *n*-decane sample signify a fast interchromophore energy migration of a singlet exciton,<sup>[16,30]</sup> facilitating successive and partial energy transfer process within the aggregates having different HOMO–LUMO energy levels.

The solvent dependent origin of the distinct morphological features and the associated excited state property could be rationalized based on the difference in molecular packing (Figure 5) as evident from various experimental results. The antiparallel arrangement of the dipoles can lead to a centrosymmetric dimer structure,<sup>[32]</sup> as inferred from the *d*-spacing value of 56.2 Å obtained from the wide-angle X-ray scattering (Figure S14). These centrosymmetric dimers can further

involve in the nucleation process dictated by the nature of the solvent molecules (Figure 5).<sup>[27]</sup> In the case of MCH, the nucleation process was sluggish ( $T_c = 321$  K) in comparison to that in *n*-decane ( $T_c = 358$  K) due to the difference in the activation energy barriers (Figure 5). The fast nucleation-elongation process in *n*-decane resulted in 2D sheets stabilized by intermolecular H-bonding and interdigitated alkyl chains. Fourier transform-infrared (FT-IR) studies have shown that the 2D sheets formed in *n*-decane are stabilized by various non-covalent interactions (Figure S15). Film state FT-IR spectrum of **1** obtained from *n*-decane exhibited bands at 3288, 1640 and 1545  $\text{cm}^{-1}$ , suggesting intermolecular H-bonding.<sup>[12b,21a]</sup> On the other hand, the BODIPY **1** in  $\text{CDCl}_3$  displayed two bands at 3450 and 3348  $\text{cm}^{-1}$ , assigned as amide A bands. The amide I and II bands appeared at 1654 and 1543  $\text{cm}^{-1}$ , respectively. Intramolecular H-bonding was overruled based on the negligible hysteresis observed between cooling and heating curves for the *n*-decane aggregates and also from the identical cooling curves obtained when the cooling rate was varied from 1 to 5  $\text{K min}^{-1}$  (Figure S16). In addition, the symmetric and asymmetric  $-\text{CH}_2$  vibrations of **1** in the xerogel state were observed at 2852 and 2922  $\text{cm}^{-1}$ ,

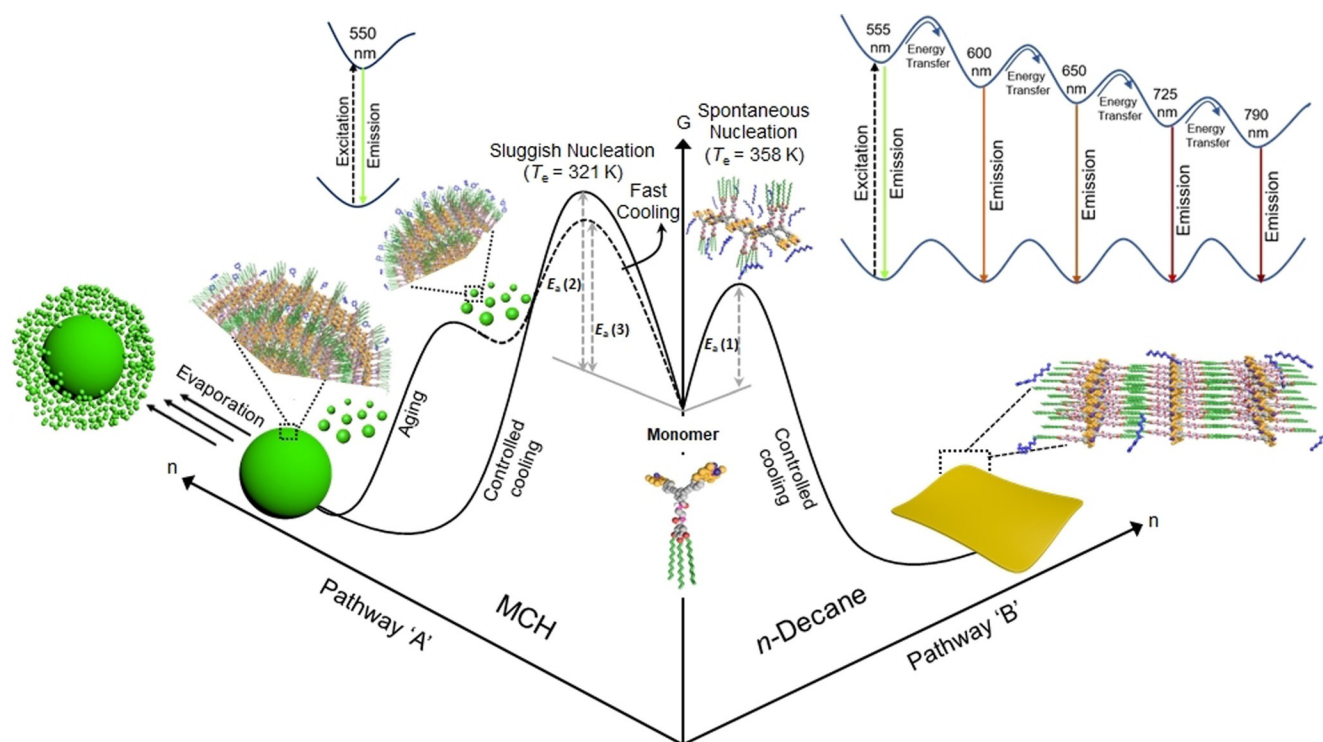


**Figure 5.** Schematic energy landscape diagram for the morphology dependent exciton deactivation in BODIPY assemblies. Self-assembly in MCH (left panel, pathway A) and *n*-decane (right panel, pathway B), forming spherical supramolecular structures and 2D sheets, leading to normal (single emission) and cascade energy transfer, respectively.

respectively and shifted towards the lower frequency region with respect to **1** in  $\text{CDCl}_3$  (Figure S17a), indicating that the dodecyl chains of **1** remain in all *trans* configuration and interdigitated in the 2D assembly forming aggregates.<sup>[12b]</sup> These sheets possess anisotropically organized aggregates of BODIPY chromophores with different energy band gaps leading to multi-emissive feature. In addition, the sluggish nucleation-elongation of **1** in MCH resulted in small particles (upon fast cooling) and their subsequent coalescence to large spheres with time, forming isotropically organized assembly of the BODIPY chromophores leading to a single emission peak. In this case, amide A, I and II bands were observed at 3289, 1637 and 1506  $\text{cm}^{-1}$ , respectively, suggesting the formation of intermolecular H-bonding between the molecules (Figure S15 and S16). However, FT-IR bands corresponding to symmetric and asymmetric  $-\text{CH}_2$  vibrations were almost indistinguishable in the case of **1** in MCH and  $\text{CDCl}_3$ , indicating randomly arranged dodecyl chains and thus unable to form gels (Figure S17b). The self-assembly of BODIPY derivative **3** having short butyl chains in *n*-decane ( $3 \times 10^{-4}$  M) resulted in a single emission maximum at 527 nm upon excitation at 475 nm (Figure S18a). Furthermore, failure of **3** to form a gel in *n*-decane ( $8 \times 10^{-3}$  M) and instead of forming spherical particle-like precipitates (Figure S18b) underpin the role of long hydrocarbon side chains in the observed 2D morphology of **1** and **2** in *n*-decane.

## Conclusion

The spherical morphology formed through the multistep assembly of the BODIPY **1** in MCH behaves like a normal chromophore assembly in terms of the excited state behavior; however, the 2D sheets formed in *n*-decane exhibits an unusual multi-emission associated with successive energy transfer within the energetically anisotropic chromophore assembly landscape. The long hydrocarbon chains in **1** and **2** are essential for forming 2D sheets, as illustrated with the inability of **3** to form such assembly in linear non-polar solvents. The transformation between the spherical assembly in MCH and 2D sheets in *n*-decane along with the changes from single to multiple emission underpin an assembly-dependent excited state behavior. Our results show that it is possible to reversibly control the excited state properties with two different stimuli such as solvent composition and ultrasound. Moreover, the effect of ultrasound stimulation of the 2D sheets on successive energy transfer with one of the largest observed pseudo Stokes-shift of 7105  $\text{cm}^{-1}$  may be useful for designing self-assembly based light-harvesting and photonic devices. Though there are many reports on cascade energy transfer, the present system is the only example available on intentionally modulated cascade energy transfer in a chromophore based supramolecular system, which can be reversibly controlled with solvents as a consequence of morphological change.

## Acknowledgements

A.A. is grateful to the DST-SERB, Govt. of India, for a J. C. Bose National Fellowship (SB/S2/JCB-11/2014). G.D. and A.P. acknowledges CSIR and UGC, Govt. of India for research fellowships, respectively. We acknowledge Dr. B. Vedhanarayanan and Dr. V. Karunakaran (CSIR-NIIST) for their support and scientific discussion at different stages of this work. We thank Kiran Mohan and Harish Raj V. (CSIR-NIIST) for TEM and SEM measurements, respectively.

## Conflict of interest

The authors declare no conflict of interest.

**Keywords:** BODIPY · fluorescence · organic dye · self-assembly · supramolecular polymer

- [1] a) H. W. Schmidt, F. Würthner, *Angew. Chem. Int. Ed.* **2020**, *59*, 8766–8775; *Angew. Chem.* **2020**, *132*, 8846–8856; b) G. Vantomme, E. W. Meijer, *Science* **2019**, *363*, 1396–1397; c) M. Aono, Y. Bando, K. Ariga, *Adv. Mater.* **2012**, *24*, 150–151.
- [2] a) H. Zhang, Z. Zhao, A. T. Turley, L. Wang, P. R. McGonigal, Y. Tu, Y. Li, Z. Wang, R. T. K. Kwok, J. W. Y. Lam, et al., *Adv. Mater.* **2020**, *32*, 2001457; b) V. K. Praveen, B. Vedhanarayanan, A. Mal, R. K. Mishra, A. Ajayaghosh, *Acc. Chem. Res.* **2020**, *53*, 496–507; c) S. Varughese, *J. Mater. Chem. C* **2014**, *2*, 3499–3516; d) L. Maggini, D. Bonifazi, *Chem. Soc. Rev.* **2012**, *41*, 211–241.
- [3] a) P. K. Hashim, J. Bergueiro, E. W. Meijer, T. Aida, *Prog. Polym. Sci.* **2020**, *105*, 101250; b) R. D. Mukhopadhyay, A. Ajayaghosh, *Science* **2015**, *349*, 241–242.
- [4] a) B. Shen, Y. Kim, M. Lee, *Adv. Mater.* **2020**, *32*, 1905669; b) K. Ariga, S. Watanabe, T. Mori, J. Takeya, *NPG Asia Mater.* **2018**, *10*, 90–106; c) F. Ishiwari, Y. Shoji, T. Fukushima, *Chem. Sci.* **2018**, *9*, 2028–2041.
- [5] a) M. Wehner, F. Würthner, *Nat. Rev. Chem.* **2020**, *4*, 38–53; b) J. Matern, Y. Dorca, L. Sánchez, G. Fernández, *Angew. Chem. Int. Ed.* **2019**, *58*, 16730–16740; *Angew. Chem.* **2019**, *131*, 16884–16895; c) A. Sorrenti, J. Leira-Iglesias, A. J. Markvoort, T. F. A. de Greef, T. M. Hermans, *Chem. Soc. Rev.* **2017**, *46*, 5476–5490.
- [6] a) X. Jin, M. B. Price, J. R. Finnegan, C. E. Boott, J. M. Richter, A. Rao, S. M. Menke, R. H. Friend, G. R. Whittell, I. Manners, *Science* **2018**, *360*, 897–900; b) Z. M. Hudson, D. J. Lunn, M. A. Winnik, I. Manners, *Nat. Commun.* **2014**, *5*, 3372.
- [7] a) A. Sarkar, T. Behera, R. Sasmal, R. Capelli, C. Empereur-mot, J. Mahato, S. S. Agasti, G. M. Pavan, A. Chowdhury, S. J. George, *J. Am. Chem. Soc.* **2020**, *142*, 11528–11539; b) W. Wagner, M. Wehner, V. Stepanenko, S. Ogi, F. Würthner, *Angew. Chem. Int. Ed.* **2017**, *56*, 16008–16012; *Angew. Chem.* **2017**, *129*, 16224–16228; c) S. Ogi, K. Sugiyasu, S. Manna, S. Samitsu, M. Takeuchi, *Nat. Chem.* **2014**, *6*, 188–195.
- [8] a) B. Adhikari, Y. Yamada, M. Yamauchi, K. Wakita, X. Lin, K. Aratsu, T. Ohba, T. Karatsu, M. J. Hollamby, N. Shimizu, et al., *Nat. Commun.* **2017**, *8*, 15254; b) A. Gopal, M. Hifsudheen, S. Furumi, M. Takeuchi, A. Ajayaghosh, *Angew. Chem. Int. Ed.* **2012**, *51*, 10505–10509; *Angew. Chem.* **2012**, *124*, 10657–10661.
- [9] a) G. Panzarasa, A. L. Torzynski, T. Sai, K. Smith-Mannschott, E. R. Dufresne, *Soft Matter* **2020**, *16*, 591–594; b) H. A. M. Ardoña, E. R. Draper, F. Citossi, M. Wallace, L. C. Serpell, D. J. Adams, J. D. Tovar, *J. Am. Chem. Soc.* **2017**, *139*, 8685–8692.
- [10] a) T. K. Ellis, M. Galerne, J. J. Armao, A. Osypenko, D. Martel, M. Maaloum, G. Fuks, O. Gavvat, E. Moulin, N. Giuseppone, *Angew. Chem. Int. Ed.* **2018**, *57*, 15749–15753; *Angew. Chem.* **2018**, *130*, 15975–15979; b) J. Leira-Iglesias, A. Tassoni, T. Adachi, M. Stich, T. M. Hermans, *Nat. Nanotechnol.* **2018**, *13*, 1021–1027.
- [11] a) H. He, W. Tan, J. Guo, M. Yi, A. N. Shy, B. Xu, *Chem. Rev.* **2020**, *120*, 9994–10078; b) M. Kumar, N. L. Ing, V. Narang, N. K. Wijerathne, A. I. Hochbaum, R. V. Uljin, *Nat. Chem.* **2018**, *10*, 696–703.
- [12] a) X. Yu, L. Chen, M. Zhang, T. Yi, *Chem. Soc. Rev.* **2014**, *43*, 5346–5371; b) J. M. Malicka, A. Sandeep, F. Monti, E. Bandini, M. Gazzano, C. Ranjith, V. K. Praveen, A. Ajayaghosh, N. Armaroli, *Chem. Eur. J.* **2013**, *19*, 12991–13001; c) N. Komiya, T. Muraoka, M. Iida, M. Miyanaga, K. Takahashi, T. Naota, *J. Am. Chem. Soc.* **2011**, *133*, 16054–16061.
- [13] a) P. Xing, Y. Li, Y. Wang, P.-Z. Li, H. Chen, S. Z. F. Phua, Y. Zhao, *Angew. Chem. Int. Ed.* **2018**, *57*, 7774–7779; *Angew. Chem.* **2018**, *130*, 7900–7905; b) K. V. Rao, D. Miyajima, A. Nihonyanagi, T. Aida, *Nat. Chem.* **2017**, *9*, 1133–1139.
- [14] a) A. Mishra, S. Dhiman, S. J. George, *Angew. Chem. Int. Ed.* **2021**, *60*, 2740–2756; *Angew. Chem.* **2021**, *133*, 2772–2788; b) B. Rieß, R. K. Grötsch, J. Boekhoven, *Chem* **2020**, *6*, 552–578.
- [15] a) N. Adir, S. Bar-Zvi, D. Harris, *Biochim. Biophys. Acta Bioenerg.* **2020**, *1861*, 148047; b) T. Brixner, R. Hildner, J. Köhler, C. Lambert, F. Würthner, *Adv. Energy Mater.* **2017**, *7*, 1700236; c) K.-T. Wong, D. M. Bassani, *NPG Asia Mater.* **2014**, *6*, e116; d) V. K. Praveen, C. Ranjith, N. Armaroli, *Angew. Chem. Int. Ed.* **2014**, *53*, 365–368; *Angew. Chem.* **2014**, *126*, 373–376; e) *Structure and Function of Phycobilisomes*, M. Mimuro, H. Kikuchi, A. Murakami in *Concepts in Photobiology: Photosynthesis and Photomorphogenesis*, (Eds.: G. S. Singhal, G. Rengel, S. K. Sopory, K.-D. Irrgang, Govindjee), Narosa Publishing House, New Delhi, **1999**.
- [16] a) C. Giansante, C. Schäfer, G. Raffy, A. Del Guerso, *J. Phys. Chem. C* **2012**, *116*, 21706–21716; b) C. Vijayakumar, V. K. Praveen, A. Ajayaghosh, *Adv. Mater.* **2009**, *21*, 2059–2063; c) A. Ajayaghosh, V. K. Praveen, C. Vijayakumar, S. J. George, *Angew. Chem. Int. Ed.* **2007**, *46*, 6260–6265; *Angew. Chem.* **2007**, *119*, 6376–6381.
- [17] a) J. Bañuelos, *Chem. Rec.* **2016**, *16*, 335–348; b) G. Ulrich, R. Ziessel, A. Harriman, *Angew. Chem. Int. Ed.* **2008**, *47*, 1184–1201; *Angew. Chem.* **2008**, *120*, 1202–1219; c) A. Loudet, K. Burgess, *Chem. Rev.* **2007**, *107*, 4891–4932.
- [18] a) Z. Liu, Z. Jiang, M. Yan, X. Wang, *Front. Chem.* **2019**, *7*, 712; b) A. V. Solomonov, Y. S. Marfin, E. V. Rummyantsev, *Dyes Pigm.* **2019**, *162*, 517–542; c) S. Cherumukkil, B. Vedhanarayanan, G. Das, V. K. Praveen, A. Ajayaghosh, *Bull. Chem. Soc. Jpn.* **2018**, *91*, 100–120.
- [19] a) I. Helmers, G. Ghosh, R. Q. Albuquerque, G. Fernández, *Angew. Chem. Int. Ed.* **2021**, *60*, 4368–4376; *Angew. Chem.* **2021**, *133*, 4414–4423; b) I. Helmers, B. Shen, K. K. Kartha, R. Q. Albuquerque, M. Lee, G. Fernández, *Angew. Chem. Int. Ed.* **2020**, *59*, 5675–5682; *Angew. Chem.* **2020**, *132*, 5724–5731; c) I. Helmers, N. Bäumer, G. Fernández, *Chem. Commun.* **2020**, *56*, 13808–13811; d) I. Helmers, M. Niehues, K. K. Kartha, B. J. Ravoo, G. Fernández, *Chem. Commun.* **2020**, *56*, 8944–8947; e) J. Xia, E. Busby, S. N. Sanders, C. Tung, A. Cacciuto, M. Y. Sfeir, L. M. Campos, *ACS Nano* **2017**, *11*, 4593–4598; f) S. Cherumukkil, S. Ghosh, V. K. Praveen, A. Ajayaghosh, *Chem. Sci.* **2017**, *8*, 5644–5649; g) J.-H. Olivier, J. Widmaier, R. Ziessel, *Chem. Eur. J.* **2011**, *17*, 11709–11714.
- [20] a) S. Radunz, W. Kraus, F. A. Bischoff, F. Emmerling, H. R. Tschiche, U. Resch-Genger, *J. Phys. Chem. A* **2020**, *124*, 1787–1797; b) J. Gemen, J. Ahrens, L. J. W. Shimon, R. Klajn, *J. Am. Chem. Soc.* **2020**, *142*, 17721–17729; c) Y. Zhang, P. Liu, H. Pan, H. Dai, X.-K. Ren, Z. Chen, *Chem. Commun.* **2020**, *56*, 12069–12072; d) D. Tian, F. Qi, H. Ma, X. Wang, Y. Pan, R. Chen, Z. Shen, Z. Liu, L. Huang, W. Huang, *Nat. Commun.* **2018**, *9*, 2688; e) D. Okada, T. Nakamura, D. Braam, T. D. Dao, S. Ishii, T.



- Nagao, A. Lorke, T. Nabeshima, Y. Yamamoto, *ACS Nano* **2016**, *10*, 7058–7063; f) S. Kim, J. Bouffard, Y. Kim, *Chem. Eur. J.* **2015**, *21*, 17459–17465; g) N. K. Allampally, A. Florian, M. J. Mayoral, C. Rest, V. Stepanenko, G. Fernández, *Chem. Eur. J.* **2014**, *20*, 10669–10678.
- [21] a) G. Das, R. Thirumalai, B. Vedhanarayanan, V. K. Praveen, A. Ajayaghosh, *Adv. Opt. Mater.* **2020**, *29*, 1703783; b) B. Adelizzi, I. A. W. Filot, A. R. A. Palmans, E. W. Meijer, *Chem. Eur. J.* **2017**, *23*, 6103–6110; c) H. M. M. ten Eikelder, A. J. Markvoort, T. F. A. de Greef, P. A. J. Hilbers, *J. Phys. Chem. B* **2012**, *116*, 5291–5301.
- [22] N. J. Hestand, F. C. Spano, *Chem. Rev.* **2018**, *118*, 7069–7163.
- [23] a) G. Liu, M. Cai, X. Wang, F. Zhou, W. Liu, *ACS Appl. Mater. Interfaces* **2014**, *6*, 11625–11632; b) T. M. Ruhland, P. M. Reichstein, A. P. Majewski, A. Walther, A. H. E. Müller, *J. Colloid Interface Sci.* **2012**, *374*, 45–53.
- [24] a) C. D. Jones, J. W. Steed, *Chem. Soc. Rev.* **2016**, *45*, 6546–6596; b) S. Srinivasan, S. S. Babu, V. K. Praveen, A. Ajayaghosh, *Angew. Chem. Int. Ed.* **2008**, *47*, 5746–5749; *Angew. Chem.* **2008**, *120*, 5830–5833.
- [25] a) S. Dhiman, R. Ghosh, S. Sarkar, S. J. George, *Chem. Sci.* **2020**, *11*, 12701–12709; b) X. Xiao, H. Chen, X. Dong, D. Ren, Q. Deng, D. Wang, W. Tian, *Angew. Chem. Int. Ed.* **2020**, *59*, 9534–9541; *Angew. Chem.* **2020**, *132*, 9621–9628; c) N. Sasaki, J. Yuan, T. Fukui, M. Takeuchi, K. Sugiyasu, *Chem. Eur. J.* **2020**, *26*, 7840–7846; d) S. Yang, S. Y. Kang, T. L. Choi, *J. Am. Chem. Soc.* **2019**, *141*, 19138–19143; e) Y. Liu, C. Peng, W. Xiong, Y. Zhang, Y. Gong, Y. Che, J. Zhao, *Angew. Chem. Int. Ed.* **2017**, *56*, 11380–11384; *Angew. Chem.* **2017**, *129*, 11538–11542; f) M. E. Robinson, A. Nazemi, D. J. Lunn, D. W. Hayward, C. E. Boott, M. S. Hsiao, R. L. Harniman, S. A. Davis, G. R. Whittell, R. M. Richardson, et al., *ACS Nano* **2017**, *11*, 9162–9175.
- [26] a) E. E. Greciano, J. Calbo, E. Ortí, L. Sánchez, *Angew. Chem. Int. Ed.* **2020**, *59*, 17517–17524; *Angew. Chem.* **2020**, *132*, 17670–17677; b) A. Chakraborty, G. Ghosh, D. S. Pal, S. Varghese, S. Ghosh, *Chem. Sci.* **2019**, *10*, 7345–7351; c) Y. Lin, M. Penna, M. R. Thomas, J. P. Wojciechowski, V. Leonardo, Y. Wang, E. T. Pashuck, I. Yarovsky, M. M. Stevens, *ACS Nano* **2019**, *13*, 1900–1909; d) M. Pfeiffermann, R. Dong, R. Graf, W. Zajaczkowski, T. Gorelik, W. Pisula, A. Narita, K. Müllen, X. Feng, *J. Am. Chem. Soc.* **2015**, *137*, 14525–14532; e) M. Vybornyi, A. V. Rudnev, S. M. Langenegger, T. Wandlowski, G. Calzaferri, R. Häner, *Angew. Chem. Int. Ed.* **2013**, *52*, 11488–11493; *Angew. Chem.* **2013**, *125*, 11702–11707.
- [27] a) M. F. J. Mabesoone, A. R. A. Palmans, E. W. Meijer, *J. Am. Chem. Soc.* **2020**, *142*, 19781–19798; b) G. Ghosh, S. Ghosh, *Chem. Commun.* **2018**, *54*, 5720–5723; c) C. Kulkarni, P. A. Korevaar, K. K. Bejagam, A. R. A. Palmans, E. W. Meijer, S. J. George, *J. Am. Chem. Soc.* **2017**, *139*, 13867–13875; d) K. Baek, I. Hwang, I. Roy, D. Shetty, K. Kim, *Acc. Chem. Res.* **2015**, *48*, 2221–2229; e) Q. Jin, L. Zhang, M. Liu, *Chem. Eur. J.* **2013**, *19*, 9234–9241.
- [28] B. Wittmann, F. A. Wenzel, S. Wiesneth, A. T. Haedler, M. Drechsler, K. Kreger, J. Köhler, E. W. Meijer, H.-W. Schmidt, R. Hildner, *J. Am. Chem. Soc.* **2020**, *142*, 8323–8330.
- [29] Emission properties of the BODIPY has been reported to be controlled in mixed lipid monolayers by molecular compression at the air–water interface. T. Mori, H. Chin, K. Kawashima, H. T. Ngo, N. J. Cho, W. Nakanishi, J. P. Hill, K. Ariga, *ACS Nano* **2019**, *13*, 2410–2419.
- [30] P. C. Nandajan, H. J. Kim, S. Casado, S. Y. Park, J. Gierschner, *J. Phys. Chem. Lett.* **2018**, *9*, 3870–3877.
- [31] A. U. Neelambra, C. Govind, T. T. Devassia, G. M. Somashekharappa, V. Karunakaran, *Phys. Chem. Chem. Phys.* **2019**, *21*, 11087–11102.
- [32] a) C. Kulkarni, S. Balasubramanian, S. J. George, *ChemPhysChem* **2013**, *14*, 661–673; b) F. Würthner, S. Yao, U. Beginn, *Angew. Chem. Int. Ed.* **2003**, *42*, 3247–3250; *Angew. Chem.* **2003**, *115*, 3368–3371.

Manuscript received: November 18, 2020

Accepted manuscript online: January 11, 2021

Version of record online: March 3, 2021